Intelligent and Reconfigurable Ultra-Wideband Spectrum Characterization at Sub-Nyquist Rate

A dissertation

submitted in partial fulfillment

of the requirements for the degree

Doctor of Philosophy

By

Himani Joshi

Advisor: Dr. Sumit J. Darak

Reading Committee:

Prof. Hongjian Sun (Durham University)

Prof. Neelesh B Mehta (Indian Institute of Science)

Prof. Manav Bhatnagar (Indian Institute of Technology Delhi)

Department of Electronics and Communication Engineering
Indraprastha Institute of Information Technology Delhi

New Delhi– 110020, India

November, 2021

Intelligent and Reconfigurable Ultra-Wideband Spectrum Characterization at Sub-Nyquist Rate

By

Himani Joshi

PhD-16103

under the guidance of

Dr. Sumit J. Darak

Associate Professor, IIIT Delhi

A Thesis

submitted in partial fulfillment of the requirements for the degree of

Doctor of Philosophy

to

Department of Electronics and Communication Engineering

Indraprastha Institute of Information Technology Delhi

November, 2021

To my loving family ...

Certificate

This is to certify that the thesis entitled "***Intelligent and Reconfigurable Ultra-Wideband Spectrum Characterization at Sub-Nyquist Rate***" being submitted by ***Himani Joshi*** to the Indraprastha Institute of Information Technology Delhi, for the award of the degree of Doctor of Philosophy, is an original research work carried out by her under my supervision. In my opinion, the thesis has reached the standard fulfilling the requirements of the regulations relating to the degree.

The results contained in this thesis have not been submitted in part or full to any other university or institute for the award of any degree or diploma.

Dr. Sumit J. Darak
Associate Professor,
Department of Electronics & Communication Engineering,
Indraprastha Institute of Information Technology Delhi,
New Delhi-110020, India
November, 2021

Declaration

This is certified that the thesis entitled "***Intelligent and Reconfigurable Ultra-Wideband Spectrum Characterization at Sub-Nyquist Rate***" being submitted by me to the Indraprastha Institute of Information Technology Delhi, for the award of degree of **Doctor of Philosophy**, is a bonafide work carried out by me. This research work has been carried out under the supervision of **Dr. Sumit J. Darak**. The study pertaining to this thesis has not been submitted in part or in full, to any other University or Institution for the award of any other degree.

Himani Joshi
PhD Scholar,
Department of Electronics & Communication Engineering,
Indraprastha Institute of Information Technology Delhi,
New Delhi-110020, India
November, 2021

Acknowledgements

I would like to take this opportunity to express my sincere gratitude and appreciation to a number of incredible people in my life. Without their tremendous guidance, mentoring, help, care, and love, I could not have been what I am today.

First and foremost, I would like to thank my advisor, **Dr. Sumit J. Darak** for his consistent support, guidance, motivation, and encouragement over these years. He chose me as his PhD student when I knew nothing about research. He has been phenomenal in nurturing my research capabilities. I remember how he pushed me at the right times and guided me in all technical matters like improving my communication and technical writing skills. On countless occasions, he boosted my confidence and has never failed to keep my optimism alive. I cannot thank him enough for the belief he showed in the moments of disappointment. He is probably one of the most energetic and passionate person I have ever seen. I admire many of his qualities, and no words can suffice my feelings of gratefulness towards him. I am fortunate to have him as my advisor.

I would also like to thank my supervisory committee members: Prof. Anubha Gupta and Dr. Shobha Sundar Ram, for their valuable advice, support and constructive feedbacks through these years. I have benefited from their knowledge and wisdom. The thesis has also been benefited from the comments and suggestions made by Dr Anchana Anil Kumar, Research Scientist at TCS Innovation lab in Bangalore, India, and Dr. Manjesh Kumar Hanawal, Associate Professor at IIT Bombay, India. I take this opportunity to thank them. I would like to thank Dr Bhavani Shankar Mysore Rama Rao, Senior Research Scientist, and Dr. Mohammad Alaee-Kerahroodi, Research Scientist, for their support and guidance during my internship at the University of Luxembourg. Their continuous suggestions helped me to complete the hardware implementation of my work.

I would like to give a special thanks to my lab mates and friends: Rohit, Neelam and Niharika. Researching with them have been full of fun and excitement. They have helped me broaden my horizons too. I very much appreciate Mr. Khagendra Joshi for the help and support in providing the resources required that has made an invaluable contribution towards my PhD.

I must also express gratitude to my parents and husband to give me the motivation at low times and make my journey memorable. I have never felt time passing faster than when I am talking with them. I owe them special thanks. Finally, I would like to thank the Indraprastha Institute of Information Technology-Delhi for providing excellent infrastructure and research environment. I would also like to thank CSIR-JRF/SRF scheme for sponsoring my research.

Abstract

Historically, throughput is one of the key performance indicators driving the transition to next-generation cellular networks. The throughput per square kilometer depends on three factors: 1) Available spectrum, 2) Base station density, and 3) Spectrum utilization efficiency. The mmWave spectrum (24 GHz - 100 GHz) is actively being explored to augment the sub-6 GHz spectrum (450 MHz – 6000 MHz) due to the availability of a wide spectrum and low auction cost. However, it has limited coverage and range, limiting its usefulness in indoor short-range mobile broadband services. This makes the sub-6 GHz spectrum a preferred candidate for outdoor communications and network coverage services. The high auction cost of the sub-6 GHz spectrum limits the licensed spectrum, and base station density is constrained due to infrastructure cost, handover overhead, and interference constraints. Thus, innovative ways to utilize the sub-6 GHz spectrum efficiently needs to be explored.

One promising solution is dynamic spectrum sharing which is now a de-facto approach in cellular networks. For instance, 5G supports the deployment in shared (2.3 GHz Europe / 3.5 GHz USA) and unlicensed (2.4 GHz / 5-7 GHz / 57-71 GHz global) spectrums along with licensed non-contiguous spectrum. Joint radar-communication systems are being explored to improve the utilization of a large section of the sub-6 GHz spectrum allocated to radar applications. Similarly, IEEE 802.15.4 for industrial internet-of-things (IIoT) networks support deployment in 250-740 MHz, 3.1-4.8 GHz and 6 - 11.6 GHz. To enhance spectrum efficiency, multi-antenna systems are being explored, allowing multiple users to communicate simultaneously over a given frequency band. This demands wideband spectrum analyzer (WSA) for the digitization of ultra-wide non-contiguous spectrum (UWNS), and capability to identify the transmission opportunities in time, frequency and spatial domains reliably. The traditional approaches need complex hardware and signal processing algorithms that question their suitability for real-time requirements.

In this thesis, we focus on the sub-Nyquist sampling (SNS) and sparse antenna-array based intelligent and reconfigurable WSA for the digitization and spatial sensing of UWNS using low-rate analog-to-digital converters (ADCs). In the first contribution, we explore reconfigurable SNS, which allows the digitization of a non-contiguous spectrum. The non-contiguous nature demands learning the occupancy of various parts of the spectrum since spectrum digitization can fail when the number of occupied bands in a digitized spectrum is higher than that of ADCs. On the other hand, high throughput requirement demands digitization of as wide spectrum as possible. We address such a trade-off via Multi-Play Multi-Armed Bandit (MPMAB) framework. The functionality of the proposed intelligent and reconfigurable WSA is validated using real radio signals via universal software radio peripheral (USRP) testbed.

After successful digitization and identification of vacant spectrum, the next contribution deals with the characterization of the occupied spectrum. We extend the WSA using a multi-antenna approach to enable blind identification of carrier frequency, angle of arrival and modulation scheme. It is referred to as ultra-wideband angular spectrum sensing (UWASS). The UWASS receiver overcomes the limitation of existing methods in which the number of antennas depends on the spectrum sparsity making it computationally efficient. The performance of the UWASS receiver is analyzed for uniform and sparse antenna arrays. In the third contribution, we develop a realistic multi-antenna USRP testbed to demonstrate the functional correctness of the UWASS receiver for various parameters such as signal-to-noise ratio (SNR), spectrum sparsity, antenna array, and its size.

Recently, deep learning has outperformed conventional statistical and machine learning based spectrum characterization methods. In the fourth and last contribution, we explored various deep learning approaches for spectrum reconstruction and characterization. Specifically, we propose a novel non-iterative wideband deep learning-based modulation classification (WDLMC) which can simultaneously identify the frequency band status and the modulation scheme of all the frequency bands in the digitized spectrum compared to existing iterative approaches. We also propose deep learning based spectrum reconstruction for UWASS as an alternative to the conventional orthogonal matching pursuit (OMP) approach. In-depth performance analysis validates the functional correctness and superiority of the proposed approach over state-of-the-art approaches in terms of computational complexity and execution time.

To summarize, the proposed intelligent and reconfigurable WSA offer efficient and hardware friendly solutions to improve the utilization of the sub-6 GHz spectrum by identifying the spectrum opportunities in time, frequency and spatial domains.

Keywords: Automatic modulation classification, direction-of-arrival, multi-play multi-armed bandit, non-contiguous sensing, sub-Nyquist sampling, universal software radio peripheral, wideband spectrum analyzer

Publications

Journals

J1. Mansi, S. Sharma, **H. joshi** and S. J. Darak,"Reconfigurable Architecture for Spatial Sensing in Wideband Radio Front-End " in *IEEE Transactions on Circuits and Systems*, Oct. 2021. (Early Access)

J2. S. Chandhok, **H. Joshi**, A V Subramanyam and S. J. Darak, "Novel Deep Learning Framework for Wideband Spectrum Characterization at Sub-Nyquist Rate," accepted in *Springer: Wireless Networks*, Oct. 2021. (S. Chandhok and H. Joshi are joint first author) (Early Access)

J3. **H. Joshi**, S. Santra, S. J. Darak, M. K. Hanawal and S. V. S. Santosh, "Multi-play Multi-Armed Bandit Algorithms For Wideband Spectrum Analysis," in *IEEE Transactions on Industrial Informatics*, Aug. 2021. (Early Access)

J4. **H. Joshi**, S. J. Darak, M. Alaee-Kerahroodi and Bhavani Shankar Mysore Rama Rao, "Reconfigurable and Intelligent Ultra-Wideband Angular Sensing: Prototype Design and Validation," in *IEEE Transactions on Instrumentation and Measurement*, vol. 70, Art no. 5501415, pp. 1-15, Jan. 2021.

J5. **H. Joshi**, S. J. Darak and A. A. Kumar, "Low-Complexity Reconfigurable and Intelligent Ultra wideband Angular Sensing," in *IEEE Systems Journal*, vol. 14, no. 4, pp. 4931-4942, Dec. 2020.

J6. **H. Joshi**, S. J. Darak, A. A. Kumar and R. Kumar, "Throughput Optimized Non-Contiguous Wideband Spectrum Sensing via Online Learning and Sub-Nyquist Sampling" in *IEEE Wireless Communication Letter*, vol. 8, no. 3, pp. 805-808, Jan. 2019.

J7. **H. Joshi**, S. J. Darak and Y. Louet,"Spectrum Blind Recovery and Application in Non-Uniform Sampling Based Automatic Modulation Classi-

fier," in *Springer: Circuits, Systems, and Signal Processing (CSSP)*, vol. 7, pp. 3457–3486, Aug. 2018.

Demo

D1. **H. Joshi**, M. Alaee-Kerahroodi, Bhavani Shankar Mysore Rama Rao, S. J. Darak, S. Kumar, and Kumar Vijay Mishra, "Learning based Reconfigurable Wideband Non-Contiguous Spectrum Characterization for 5G Applications," presented in *45th IEEE International Conference on Acoustics, Speech, and Signal Processing (ICASSP)*, Barcelona, Spain, May 2020. Demo Link

D2. **H. Joshi**, M. Alaee-Kerahroodi, Bhavani Shankar Mysore Rama Rao and S. J. Darak, "Learning based Reconfigurable Wideband Non-Contiguous Spectrum Characterization for 5G Applications," presented in *IEEE 5G World Forum*, Bangalore, India, Sep. 2020. Demo Link

Conferences

C1. **H. Joshi**, M. A. Kerahroodi, A. A. Kumar, B. S. M. RamaRao and S. J. Darak, "Learning based Reconfigurable Sub-Nyquist Sampling Framework for Ultra-Wideband Angular Sensing" in *IEEE International Conference on Acoustics, Speech, and Signal Processing (ICASSP)*, pp. 4637-4641, Barcelona, Spain, May 2020.

C2. N. Agrawal, **H. Joshi**, S. J. Darak and F. Bader, "USRP Testbed and Performance Analysis of New Reconfigurable LDACS In Presence of DME Interference," in *IEEE International Symposium on Wireless Communication Systems (ISWCS)*, pp. 400-405, Oulu, Finland, August 2019.

C3. **H. Joshi** and S. J. Darak, "Review: Wideband Spectrum Sensing for Next Generation Wireless Networks," in *URSI Asia-Pacific Radio Science Conference (AP-RASC)*, Delhi, India, March 2019.

C4. **H. Joshi**, R. Kumar, A. Yadav and S. J. Darak, "Distributed Algorithm for Dynamic Spectrum Access in Infrastructure-less Cognitive Radio Network," in *IEEE Wireless Communications and Networking Conference (WCNC)*, pp. 1-6, Barcelona, Spain, April 2018.

C5. **H. Joshi** and S. J. Darak, "Sub-Nyquist Sampling and Machine Learning based Online Automatic Modulation Classifier for Multi-carrier Waveform" in *32nd Union Radio Scientific International General Assembly and Scientific Symposium (URSI GASS)*, pp. 1-4, Montreal, Canada, Aug. 2017.

Posters

P1. S. Chandhok, **H. Joshi**, S. J. Darak and A. V. Subramanyam, "LSTM Guided Modulation Classification and Experimental Validation for Sub-Nyquist Rate Wideband Spectrum Sensing," in *IEEE International Conference on Communication System & Networks (COMSNET)*, pp. 458-460, Jan. 2019, Bangalore, India **(Best Poster Runner-up Award)**

P2. R. Verma, S. J. Darak, V. Tikkiwal, **H. Joshi** and R. Kumar, "Countermeasures Against Jamming Attack in Sensor Networks with Timing and Power Constraints," in *IEEE International Conference on Communication System & Networks (COMSNET)*, pp. 485-488, Jan. 2019, Bangalore, India.

Achievements

1. Awarded National Instruments (NI) Academic Research Grant in July 2017 (USD 2,000).
2. Received Best Graduate Forum Presenter Award and Second-best poster award in COMSNETS 2019.

Contents

List of Figures

List of Tables

List of Abbreviations

ADC Analog Digitial Converter

AFE Analof Front End

AMC Automatic Modulation Classifier

AP Amplitude Phase

AWGN Additive White Gaussian Noise

BMP Bayesian Matching Pursuit

BPSK Binary Phase Shift Keying

CASCADE Compressed Carrier and DOA Estimation

CMAB Combnitorial Multi Armed Bandit

CNN Convolutional Neural Network

DFE Digital Front End

DL Deep Learning

DLDR Deep Learning based Digital Reconstruction

DLMC Deep Learning based Modulation Classifier

DLWSS Deep Learning based Wideband Spectrum Sensing

DoA Direction of Arrival

DNN Dense Neural Network

DTFT Discrete Time Fourier Transform

DSS Dynamic Spectrum Sharing

ED Energy Detector

ESPIRIT Estimation of Signal Parameters via Rotational Invariant Technique

FPGA Field Programmable Gated Array

FRI Finite Rate of Innovation

IQ In-phase Quadrature-phase

KNN k-nearest neighbor

LAA License Assisted Access

LDM Learning and Decision Making

LPF Low Pass Filter

LSTM Long Short Term Memory

LTE Long Term Evolution

MCS Multi-Coset Sampling

MDP Markovian Decision Process

MIMO Multiple Input Multiple Output

mMIMO massive MIMO

MPMAB Multi Play Multi Armed Bandit

MP-TS Multi Play Thompson Sampling

MUSIC MUltiple SIgnal Classification

MWC Modulated Wideband Converter

NCEE Normalized Carrier Frequency Estimation Error

NDEE Normalized DoA Estimation Error

NDLMC Narrowband DLMC

NR New Radio

OFDM Orthogonal Frequency Division Multiplexing

OMP Orthogonal Matching Pursuit

PAM Pulse Amplitude Modulation

PDSCH Physical Downlink Shared Channel

PPS Pulse per second

PRS Phase Reference Signal

PTRS Phase Tracking and Reference Signal

QAM Quadrature Amplitude Modulation

QPSK Quadrature Phase Shift Keying

RD Random Demodulator

RF Radio Frequency

SAA Sparse Antenna Array

SC-FDMA Single Carrier Frequency Division Multiple Access

SNR Signal to Noise Ratio

SNS Sub-Nyquist Sampling

SS Synchronization Signal

SSS Secondary Synchronization Signal

SVM State Vector Machine

TI-ADC Time Interleaved ADC

UCB Upper Confidence Bound

UDS User Data Signal

ULA Uniform Linear Array

USRP Universal Software Radio Peripheral

UWASS Ultra-Wideband Angular Spectrum Sensing

UWNS Ultra Wideband Non-Contiguous Spectrum

WAS Wideband Angular Sensing

WDLMC Wideband DLMC

WSA Wideband Spectrum Analyzer

WSS Wideband Spectrum Sensing

List of Symbols

Symbols	Definitions
$x(t)$	Received wideband signal
$X(f)$	Fourier transform of $x(t)$
f_{max}	Maximum frequency of $x(t)$
N	Total number of channels (or frequency bands) in $X(f)$
M	Number of occupied/busy channels (or active transmission) in $x(t)$
B	Bandwidth of a channel (or) Maximum possible bandwidth of an active transmission
T	Nyquist period of $x(t)$
f_s	Nyquist frequency of $x(t)$
K	Number of ADCs in MCS (or) MWC (or) FRI SNS architecture
β	A set of frequency bands for non-contiguous sensing
$m_k(t)$	Mixing function of k^{th} analog branch of MWC or FRI SNS technique
$\alpha_{k,i}$	Scaling coefficient for the i^{th} band of k^{th} branch in FRI SNS technique
$\mathbf{A}$	Sampling matrix of a SNS technique
$\tilde{y}_k(t)$	Output of the k^{th} mixer
$y_k(t)$	Output of the k^{th} low pass filter
$y_k[n]$	Sub-Nyquist samples at the k^{th} branch
$\mathbf{Y}$	DTFT of the sub-Nyquist samples matrix
β^*	Optimal channel subset
$[N]$	A set of the indices of channels
$\mathbf{s}$	A $1 \times N$ binary vector containing occupancy status of N channels
$\mathbf{s}_\beta$	A $1 \times \lvert\beta\rvert$ binary vector containing occupancy status of β channels
Q_β	A power-set containing all possible values of $\mathbf{s}_\beta$
$\boldsymbol{p}$	A $1 \times N$ vector storing vacancy probability of N channels
$\boldsymbol{p}_{u,v}$	A $1 \times N$ vector storing channel transitional probability of going from state u to v
$\zeta_{\mathbf{s}_\beta}$	Reconstruction/Characterization failure event for β channel subset
t_s	Index indicating the current learning time slot
β_v	A set of vacant channels of β

Symbols	Definitions
β_{t_s}	β selected at t_s time slot
P	Total number of learning time slots
$\mathcal{S}$	A power-set containing all possible values of β
γ	A channel subset containing common channels of β and $\mathcal{S}(i)$
γ_c	A channel subset containing $\mathcal{S}(i) - \beta$ channels
T_c	A $1 \times N$ vector denoting number of times each channel is selected
X_c	A $1 \times N$ vector denoting number of times each channel sensed to be vacant
Q_c	A $1 \times N$ vector storing the quality index of each channel
T_s	A $1 \times \lvert\mathcal{S}\rvert$ vector denoting the number of times each channel-subset of $\mathcal{S}$ is selected
X_s	A $1 \times \lvert\mathcal{S}\rvert$ vector denoting the number of times each channel-subset of $\mathcal{S}$ does not face characterization failure
Q_s	A $1 \times \lvert\mathcal{S}\rvert$ vector storing the quality index of each channel-subset of $\mathcal{S}$
O_β	Number of occupied channels in β
V_β	Number of vacant channels in β
$\boldsymbol{\omega}$	Immediate probability of vacancy
$s_n(t_s)$	Status of the n^{th} channel at t_s time slot
$c_i(t)$	Amplitude of the i^{th} narrowband signal
f_i	Carrier frequency of i^{th} narrowband signal
θ_i	DoA of i^{th} narrowband signal
$x_l(t)$	Wideband signal received at l^{th} antenna
$\tau_l(\theta_i)$	Time delay observed by the i^{th} narrowband signal at l^{th} antenna
$\boldsymbol{\psi}_n$	Center frequency of n^{th} channel
L	Total number of antennas
J	Total number of ADCs used in the WSA
$\mathbf{E}$	Steering matrix of size $L \times M$
$\mathbf{E}_c$	Over-complete steering matrix of size $L \times 180$
$u(t)$	Narrowband SC-FDMA signal
$\mathbf{b}$	Set-Reset bit vector
$a(t)$	Transmitted SC-FDMA signal
$p(t)$	Reference signal for phase calibration
$z(t)$	Received wideband signal at the input of an USRP
$z[n]$	A digitized wideband signal at the output of an USRP
$\tilde{z}[n]$	Output of phase calibration & synchronization unit
β_{busy}	Index of busy channels in β

Symbols	Definitions
$C_q(e^{j2\pi f})$	DTFT of the narrowband signal present in q^{th} channel
Q	Number of sub-Nyquist samples at the output of an ADC
$\mathbf{D}$	$\beta_{busy} \times Q$ matrix with $D_q(e^{j2\pi f}) = \alpha_{1,q}\, C_i(e^{j2\pi f})$ as its q^{th} row
U	Number of observations/examples for DLMC dataset
V	Number of modulated symbols in DLMC
W	Number of modulation schemes in DLMC
$h_i(t)$	Channel response for the i^{th} modulated signal
f_d	Doppler frequency
$\tilde{\mathbf{X}}(f)$	$N \times Q$ pseudo reconstructed matrix
$\tilde{\mathbf{X}}_d(f)$	$N \times Q \times 2$ higher dimensional reconstructed matrix
$\tilde{\mathbf{X}}_n(f)$	$N \times Q \times 2$ higher dimensional reconstructed matrix normalized between $[0, 1]$
$\hat{\mathbf{w}}$	$N \times W + 1$ label matrix denoting status and modulation scheme classified by DLMC
ϕ_{ss}	Learned network parameters for DLWSS
ϕ_c	Learned network parameters for DLMC
$\hat{\mathbf{X}}_s$	Modulated symbols recovered from symbol recovery block
$\mathcal{T}$	Throughput obtained by an LDM algorithm
$\mathcal{R}$	Regret achieved by an LDM algorithm
$\hat{v}$	Estimated value of a variable v
$\delta(.)$	Kronecker delta function
$\mathbb{E}[.]$	Expectation operator
$\mathbb{P}(.)$	Probability operator
$C(.,.)$	Combination operator
$PMF(.)$	Probability mass function operator
$\lvert.\rvert$	Cardinality operator
$\lvert\lvert.\rvert\rvert_1$	l_1-norm operator

Chapter 1

Introduction

1.1 Background

The rapid evolution of wireless communication from low-speed text and voice based communication to today's high-speed and reliable video and multimedia based communication make it an integral and indispensable part of our daily activities. Its impact on economic progress is huge due to the ubiquitous capacity of multimodal and interactive communication, which has made the applications such as massive internet of things (IoT) networks, smart industry, smart cities, intelligent transportation systems and wearable devices reality today. It has also played a vital role in making human life more secure and healthy. Even during the unprecedented lockdown due to the Covid-19 pandemic, wireless communication enabled the rapid transition to remote learning, work from home offices, tele-medicine, and multimedia services, making social distancing a little less lonely. Its usefulness in contact tracing and vaccine supply chain logistics is crucial in the ongoing fight against Covid-19 and sustainable life thereafter.

Significant research and innovation efforts are needed to bring next-generation wireless technologies that make the envisioned futuristic services such as remote healthcare, autonomous driving, the large-scale artificial intelligence of things (AIoT), extended reality, flying cars etc., a reality. In this direction, various studies, experiments and standardization activities are being carried out for next-generation networks such as 5G and 6G. As shown in Table 1.1, these networks are expected to support a wide range of use cases compared to broadband based services in existing networks.

Table 1.1: Features of 4G, 5G and 6G, the future generation wireless standard. AR: augmented reality, ELPC: extremely low power consumption, eMBB: enhanced mobile broadband, ERLLC: extremely reliable and low latency communications, FeMBB: further eMBB, HD: high definition, LDHMC: long distance and high mobility communication, MBB: mobile boradband, mMTC: massive machine type communication, umMTC: ultra mMTC, URLLC: ultra reliable low latency communications, UHD: ultra high definition, VR: virtual reality, IoT: internet of things, V2X: vehicle to everything.

Key Features	**4G**	**5G**	**6G**
Use Cases	MBB	eMBB, URLLC, mMTC	FeMBB, ERLLC, umMTC LDHMC, ELPC
Applications	HD Video Streaming Mobile TV Mobile Pay Mobile Internet	AR/VR UHD Video streaming V2X, IoT Smart Cities/Home/Industry	Tactile Internet Fully Automated Driving Internet of Bio-Nano Things Industrial Internet
Peak Data Rate	100 $Mbps$	20 $Gbps$	≥ 1 $Tbps$
Spectrum Efficiency	$1\times$	$3\times$	$15-30\times$
Network Energy Efficiency	$1\times$	$10-100\times$	$100-10,000\times$
Device Density	10^5 devices/Km^2	10^6 devices/Km^2	10^7 devices/Km^2
Latency	10 ms	1 ms	$10-100$ μs

Throughput is one of the important performance metrics of a cellular network. Historically, switching to next-generation cellular networks is economically feasible only when it offers at least 100-factor improvement per square kilometre throughput. The throughput depends on three parameters: 1) Avail-

able spectrum, 2) Base station density and 3) Spectrum utilization efficiency. The mmWave spectrum (24 GHz - 100 GHz) is actively being explored beyond 4G networks due to the availability of a wide spectrum and low auction cost. However, it has limited coverage and range, limiting its usefulness in indoor short-range mobile broadband only. Thus, making the sub-6 GHz spectrum a preferred candidate for outdoor communications and network coverage. Infrastructure cost, handover overhead, and interference constraints limit the base station density. A sharp rise in the auction price of the sub-6 GHz spectrum demands innovative ways to utilize the sub-6 GHz spectrum efficiently.

One promising solution is dynamic spectrum sharing (DSS) which is now a de-facto approach in recent and upcoming networks. For instance, as shown in Fig. 1.1, in the subsequent deployment of 4G cellular networks, various paradigms such as LTE-Unlicensed, Licensed Assisted Access (LAA), LTE WLAN Link Aggregation (LWA), LTE WLAN radio level integration with IPsec tunnel (LWIP), MulteFire, Wi-Fi (802.11ac/ .11ad /.11ax/.11ay) are explored to make unlicensed sub-6 GHz spectrum available for cellular networks without compromising on QoS [1]. The IEEE 802.15.4 for industrial internet-of-things (IIoT) networks support deployment in 250-740 MHz, 3.1-4.8 GHz and 6 - 11.6 GHz. Since the majority of the sub-6 GHz spectrum is allocated for radar services, joint radar-communication systems are being developed to improve the spectrum utilization [2].

The upcoming 5G network follows a revolutionary path of the DSS. For instance, a non-contiguous shared (2.3 GHz Europe / 3.5 GHz USA) and unli-

censed (2.4 GHz / 5-7 GHz / 57-71 GHz global) spectrum in addition to the licensed spectrum [3–5] are explored in 5G new radio (NR) to allow opportunistic spectrum access over time and geographies. 5G has extended LAA to anchored NR-U and standalone NR-U. The anchored NR-U combines the unlicensed spectrum with both the licensed and shared spectrum, whereas standalone NR-U allows the usage of unlicensed spectrum for the 5G cellular connection. 5G also supports DSS between the 4G and 5G cellular users over the same frequency bands. The ultra-wide and non-contiguous sub-6 GHz spectrum (UWNS) makes the characterization, i.e. identification of spectrum opportunities, challenging. To enhance the spectrum efficiency, multi-antenna massive MIMO (mMIMO) systems are being explored, which allows multiple users to communicate simultaneously over a given frequency band via beamforming [5]. Hence, a dedicated wideband spectrum analyzer (WSA) for spatial sensing of UWNS is desired and the focus of the work presented in this thesis.

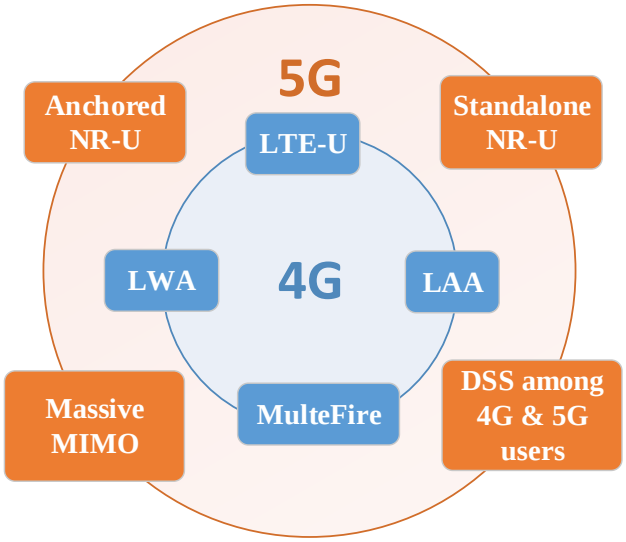

Figure 1.1: Various DSS technologies in 4G and 5G Networks.

1.2 Motivation

The design of WSA for spatial sensing of UWNS involves three important tasks: 1) Digitization of UWNS, 2) Spectrum conditioning, and 3) Spectrum characterization. Most of the existing works focus on narrowband spatial sensing. The desired narrowband spectrum is digitized via Nyquist-sampling based approach, which is then filtered to remove interference and noise. The resultant signal is then characterized to determine its status (vacant or busy), modulation scheme, angle-of-arrival etc. Various spectrum characterization methods such as energy detector [7, 8], matched filter [9], cyclostationary detector [10, 11], wavelet based detector [12, 13], maximum-likelihood estimation [14, 15] and machine learning/deep learning algorithms [16, 17] have been studied in the literature. The energy detector utilizes the signal energy to characterize the spectrum. Its performance has been analyzed for various channels models like Rayleigh, Rician, Nakagami, $k-\mu$ and $k-\mu$ extreme fading channels [7]. Improved energy detector utilizing the p^{th} power of the absolute sample is also discussed for cooperative spectrum sensing scenario in [8]. By maximizing the signal to noise ratio (SNR) of the received signal, the matched filter [9] has shown better performance than the energy detector based spectrum sensing at low SNR case. But due to the requirement of prior knowledge of the signal parameters like modulation scheme, pulse shaping, etc., matched filtering is not preferred for spectrum characterization [10]. Cyclostationary feature detection determines the spectral correlation function of the received wide sense stationary signal, thus enabling

the cyclostationary detector to determine the spectrum parameters like carrier frequency, direction of arrival (DoA), modulation scheme under low SNR conditions [10]. Cyclostationary detectors along with high order cumulants are further used to determine the modulation schemes of higher-order modulation schemes [11]. The wavelet transform based spectrum sensing method proposed in [12] has shown higher sensing accuracy the energy and cyclostationary detectors. Furthermore, wavelet transform along with the classification methods is used to perform spectrum characterization [13].

The maximum likelihood method proposed in [14] used a collaborative log-likelihood function to determine the status of the narrowband spectrum. A hypothesis for each modulation scheme is considered in [15], and a hypothesis having the highest value of likelihood function is selected to determine the modulation scheme of the spectrum. Recently, an intelligent machine and deep learning spectrum characterization method, showing better performance than the feature-based and likelihood-based characterization methods, have been studied in the literature. Deep learning in various applications of wireless communication is studied [16]. Here, deep learning techniques like dense neural networks, long short term memory and detection network have been studied for wireless channel estimation, modulation classification and MIMO detection, respectively. Two convolutional neural networks, AlexNet and GoogLeNet, are discussed in [17] to perform the modulation scheme characterization.

Although the characterization methods discussed in [7–17] can be extended for WAS on UWNS of bandwidth up to a few GHz, but they require pro-

hibitively high Nyquist rate analog to digital converters (ADCs) for wideband signal digitization. Such ADCs are cost, area and power hungry. For example, the narrowband channel bandwidth in WiFi bands ($2.4\ GHz$ and $5\ GHz$) ranges from $20\ MHz$ to $160\ MHz$ [6], whereas the bandwidth of a wideband spectrum for 5G use cases can range from $700\ MHz$ to $7\ GHz$ [19]. Thus, as shown in Table 1.2, increases the cost, power and area requirement by 1232%, 1266% and 864%, respectively. Hence there is a need for efficient WSA methods [18].

Table 1.2: Comparison of Nyquist sampling and sub-Nyquist sampling digitization techniques.

Characteristics	**RF-Nyquist Sampling**	**Sub-Nyquist Sampling**
Analog Bandwidth	$\sim 8\ GHz$	$10 - 200\ MHz$
Number of ADCs	Single ADC	Multiple ADCs
Power Consumption	High ($> 8200mW$)	Low ($28 - 600mW$)
Area Requirement	High ($> 781mm^2$)	Low ($67 - 81mm^2$)
Cost (in USD)	High (> 2451)	Low ($34 - 184$)

Due to the under-utilization of the spectrum in the temporal and spatial horizon, the wideband spectrum exhibits sparse characteristics. By exploiting the sparse nature, sub-Nyquist sampling (SNS) based WSA techniques have been studied in the last decade [23–29,31,36–42,54,55]. SNS digitization techniques employ multiple low rate ADCs such that the average sampling rate is below the Nyquist rate of the wideband signal [56]. For example, as shown in Fig. 1.2, a received wideband signal, $x(t)$ of maximum frequency f_{max}, is divided into N frequency bands (or channels) of bandwidth $B\ Hz$. If M out of these N frequency bands are occupied, and $M << N$, then the minimum sampling rate

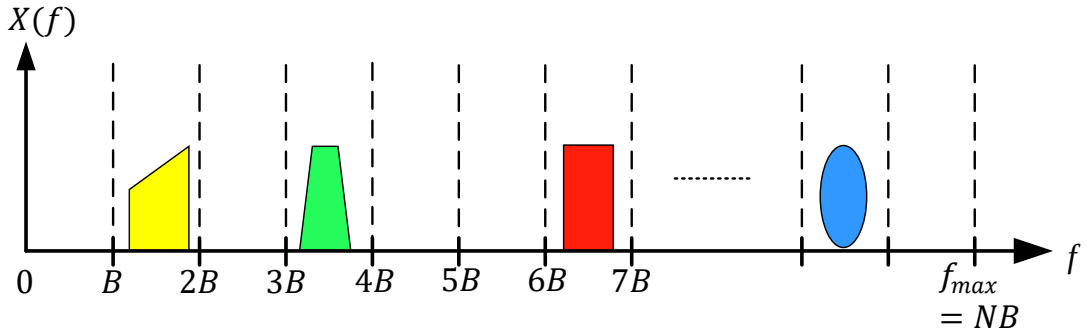

Figure 1.2: Wideband spectrum with N channels (or frequency bands).

required to sample and reconstruct a multiband signal is given by Landau's theorem, and it is equal to MB [57]. Various SNS digitization techniques are designed to achieve this rate with fewer ADCs, and computationally efficient analog front-end.

The multi-coset sampling (MCS) and modulated wideband converter (MWC) are state-of-the-art SNS techniques and studied widely in the literature [56]. MCS [58, 59] uniformly samples the received wideband signal, $x(t)$, via K parallel synchronized ADCs at a distinct time offset w.r.t. the initial sample. The sampling rate of all K ADC is $\frac{1}{NT}$, where $K << N$ and T is the Nyquist period of $x(t)$. MCS follows a straightforward approach to generate low rate samples, but it suffers from various limitations. First, due to time delays of order pico-second, it is difficult to achieve accurate time-offsets. Second, due to the processing of direct radio frequency (RF) signal, it requires ADCs with high analog bandwidth of Nyquist frequency (i.e. in GHz) [60]. The MWC SNS technique has been explored in [60] to overcome these drawbacks. It uses a specific analog mixing function, followed by a low pass filter and a low rate ADC at every analog branch. Thus, it avoids the need for accurate time off-

sets. Furthermore, to validate the functionality of MWC, a hardware prototype is developed in [61] to perform MWC based SNS on a wideband spectrum of bandwidth 2 GHz. However, the existing MCS and MWC SNS techniques digitize the entire wideband spectrum, and hence they are categorized as contiguous SNS techniques. But these contiguous SNS techniques suffer from two major limitations:

1. The number of low rate ADCs is directly proportional to the number of active transmissions in the sensed spectrum. Since the number of ADCs is fixed in the SNS architecture, the contiguous SNS technique incurs reconstruction failure when the number of active transmissions becomes larger than ADCs.

2. The upcoming wireless cellular networks are expected to operate on the non-contiguous wideband spectrum. The existing contiguous SNS is not capable of skipping the digitization of undesired frequency bands. Thus, by sensing the active transmissions present in the undesired bands, the contiguous SNS leads to inefficient utilization of hardware resources.

To overcome the above limitations, a non-contiguous SNS technique that can offer complete control over the number and location of sensed bands needs to be explored. The finite rate of innovation (FRI) architecture of SNS [62, 63] is similar to the architecture of MWC. But instead of digitizing all N frequency bands, FRI digitizes a set of non-contiguous frequency bands, β. To perform this, the FRI uses unique mixing functions at each analog branch. Due to this,

the DTFT of samples generated at the output of every analog branch is a linear combination of shifted copies of all frequency bands present in β. However, the determination of β is a challenging task as the increase in the size of β may increase the number of vacant frequency bands in β. However, it also increases the probability of characterization failure at WSA. Hence, there is a need for a learning and decision making (LDM) algorithm. By balancing the trade-off between the size of β and characterization failure, the LDM algorithms can select the best set of frequency bands for the digitization of UWNS. Furthermore, there is a need for characterization techniques that can determine the occupancy status and parameters (like carrier frequency, DoA, modulation scheme, etc.) of occupied bands directly from the sub-Nyquist samples of the UWNS. Motivated by these open research problems, the work presented in this thesis focuses on the design of a reconfigurable and intelligent WSA for the characterization of the sub-Nyquist sampled UWNS.

1.3 Research Objectives and Major Contribution

The work presented in this thesis aims to address the research challenges related to the design of reconfigurable and intelligent WSA for UWNS and efficiently implement the proposed WSA on the hardware testbed. These challenges will be addressed via the following research objectives:

- Design a subset selection algorithm, which balances the trade-off between the channel (or frequency bands) subset size and characterization failure,

and allows selection of the best channel subset such that total throughput is maximized. Note that the throughput is the number of vacant bands in the sensed spectrum.

- Develop a universal software radio peripheral (USRP) hardware testbed to validate the performance of the proposed subset selection algorithms for different spectrum statistics.
- Perform SNS based characterization of the UWNS by determining the vacant and occupied frequency bands and parameters like carrier frequencies, direction of arrivals and modulation schemes of occupied bands.
- Develop a muti-antenna USRP testbed to perform ultra-wideband angular sensing and study its performance analysis for various sparsity levels of the signal, antenna array configuration and the number of antennas.
- Develop a USRP hardware testbed to determine the modulation scheme parameter of the occupied frequency bands at the sub-Nyquist rate for different modulation schemes and channel conditions.

Various contributions of this thesis to meet the above research objectives are summarised as follows:

C1. Our first contribution is to propose a multi-play multi-armed bandit (MPMAB) algorithm to select a channel subset to perform non-contiguous digitization. As the selection of subset results in the loss of feedback whenever the number of active transmissions is higher than the number of ADCs,

the channel subset selection becomes a non-trivial problem. We develop various MPMAB algorithms to meet the above requirement [J5, J3]. The first algorithm, $K-$SL ($K-$subset learning), shows the learnability of the MPMAB problem for the channel statistics of Bernoulli distribution [J5]. Here, the algorithm always selects a subset of size the same as the number of ADCs and hence, failure does not happen. We then extend the K-SL algorithm to the K^+-SSL (K^+- subset shared learning) algorithm, which identifies the optimal subset that gives the best possible throughput (i.e. the number of vacant channels) and could have a size potentially larger than the number of ADCs. Next, we propose K^+-SSLE (K^+-SSL via subset size estimation) to reduce the computational complexity due to a large number of subsets. By learning the channel statistics, K^+-SSLE determines the size of the best subset. But to perform accurate learning, K^+-SSLE requires the knowledge of the minimum difference between the channel statistics. So, then we propose K^+-BSSLE (Blind SSLE) to overcome the drawback of K^+-SSL [J3]. It considers Markov channel distribution where the current occupancy status of channels depends on their previous status, and hence, it is more realistic than the Bernoulli channel distribution. Later the performance of the proposed MPMAB has been verified on the USRP hardware testbed.

C2. By using the proposed MPMAB algorithm, our next work develops an intelligent reconfigurable UWASS receiver architecture, and it is the second contribution of this thesis [J2]. The proposed receiver follows a multi-

antenna array followed by a non-contiguous SNS digitization technique. The estimation algorithms then utilize the sub-Nyquist samples to determine the occupancy status of sensed channels and carrier frequency and DoA of the occupied channels. The performance analysis of this work is done for the different number of sub-Nyquist samples, ADCs and antennas.

C3. As the third contribution of the thesis, we develop a multi-antenna USRP hardware testbed for UWASS [J1]. At the transmitter, we develop a multi-directional multi-band wireless traffic signal consisting of SC-FDMA signals at every channel. These SC-FDMA signals occupy the channels with user-defined occupancy statistics, and it is unknown at the receiver. The receiver consists antenna array followed by the proposed MPMAB and parameter estimation techniques discussed in points C1 and C2. We validate the performance of the developed UWASS USRP testbed for various antenna array configurations, including sparse and uniform antenna array and different occupancy statistics of the generated multi-directional multi-band wireless traffic signal.

C4. The fourth and last contribution of the thesis is the designing of deep learning based modulation classification (DLMC)[J6, P1]. Here, we consider two approaches. The first one uses the conventional approach where DLMC is applied sequentially on all occupied frequency bands (or channels) transmissions. However, in the proposed approach, the DLMC is applied for the first time on the symbols reconstructed from the sub-Nyquist samples. To validate the performance of the proposed sequential DLMC

approach on the real radio signal, we also develop a USRP testbed [P1].

Whereas in the second approach, we introduce a unified deep learning model for WSA to accomplishes two tasks: 1) Reconstruct the signal directly from the sub-Nyquist samples, and 2) Identify the occupancy status and modulation scheme of all bands [J6]. The proposed non-iterative approach based reconstruction provides the occupancy status of all bands in a single forward pass leading to significant improvement in execution time over state-of-the-art iterative methods. In addition, the proposed approach does not need complex signal conditioning between reconstruction and characterization. We extensively compare the performance of our framework for a wide range of modulation schemes, SNR and channel conditions. A single unified deep-learning framework makes the proposed method a good candidate for reconfigurable platforms.

1.4 Outline of the thesis

The rest of the thesis is organized as follows. Chapter 2 gives an overview of the state-of-the-art SNS digitization techniques and challenges faced by them. A literature review of the existing MPMAB algorithms and wideband spectrum characterization is provided. Later the survey of the hardware implementation of various wideband spectrum digitization and characterization algorithm is discussed. Chapter 3 presents the proposed MPMAB for the selection of the best channel subset for Bernoulli and Markovian channel distribution. The performance analysis is also presented, along with the description of the proposed

USRP hardware testbed. An intelligent and reconfigurable UWASS receiver architecture is proposed, and its performance is analyzed for various number of antennas, ADCs and SNR in Chapter 4. The designing of the multi-antenna USRP testbed for the verification of the UWASS receiver proposed in Chapter 4 is explained in Chapter 5. The hardware validation is done extensively for different antenna array configurations and sparsity of the spectrum. Chapter 6 discusses the proposed DLMC techniques along with the study of their performance analysis for various deep learning models. Chapter 7 concludes the thesis with some possible future directions.

Chapter 2

Literature Review: Wideband Spectrum Digitization & Characterization

In this chapter, we review the state-of-the-art wideband signal digitization and characterization techniques. We begin with the detailed study of sub-Nyquist sampling (SNS) techniques, followed by the discussion on channel subset selection algorithms and various wideband spectrum sensing and parameter estimation techniques. In the end, we present the hardware prototypes for the wideband signal digitization and characterization.

2.1 Wideband Signal Digitization Techniques

This section discusses the state-of-the-art low rate wideband digitization techniques.

2.1.1 Time Interleaved ADC

Time interleaved ADCs (TI-ADC) [64] considers a wideband signal, $x(t)$, divided into N number of frequency bands (or channels). It consists of N number of parallel ADCs, as shown in Fig. 2.1. The sampling rate of each ADC is $\frac{f_s}{N}$, where f_s is the Nyquist frequency of $x(t)$. As shown in Fig. 2.1, every k^{th} ADC has a phase offset of $k\frac{2\pi}{N}$. The output of each ADC is then combined by a multiplexer working at a clock frequency of $f_s\ Hz$ to produce high Nyquist rate samples. TI-ADC follows a straightforward approach to generate Nyquist rate samples via low rate ADCs, but it suffers from various limitations. First, due to the requirement of time delays of $\frac{1}{f_s}$ (i.e. in pico-second), it is difficult to achieve synchronization between ADCs. Second, due to the processing of direct radio frequency (RF) signal, ADCs require high analog bandwidth. Third, the number of ADCs increases with an increase in frequency bands in a wideband spectrum. But due to the sparse nature of the wideband spectrum, the minimum sampling rate required to perform blind (i.e. the location of carrier frequencies is unknown) reconstruction of the spectrum is twice Landau's rate, i.e. equal to the occupied bandwidth in the spectrum [57]. Thus, to perform digitization below the Nyquist rate, several sub-Nyquist sampling techniques have been studied.

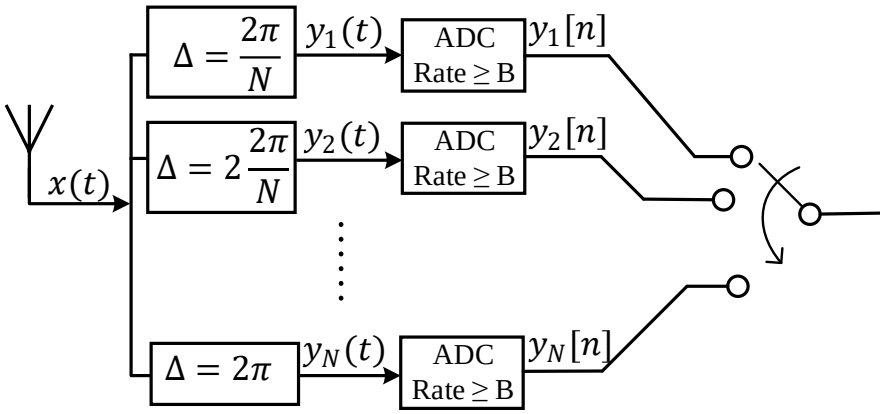

Figure 2.1: Block diagram of time interleaved ADC [64].

2.1.2 Multi-Coset Sampling (MCS)

MCS [58, 59] uses the concept of time interleaved ADCs [64] to generate sub-Nyquist samples of a wideband signal, $x(t)$. As shown in Fig. 2.2, MCS uniformly samples $x(t)$ via K parallel ADCs at a rate of $B = \frac{1}{NT}$ where $K << N$. All ADCs are synchronized with each other and samples at a distinct time offset, $c_k \in \{1, 2, .., N\} \; \forall \; k = \{1, 2, \cdots, K\}$ w.r.t. initial sample. The sub-Nyquist samples generated by the k^{th} ADC can be represented as

$$y_k[n] = x(nT) \sum_{m \in Z} \delta(n - (mN + c_k)) \qquad 1 \leq k \leq K \tag{2.1}$$

where $\delta(.)$ is a Kronecker delta function. For a given c_k, the output of each ADC is an active coset of Nyquist rate samples. For example, as shown in Fig. 2.3, the output of three ADCs will be samples produced at time instances, $t = \{0, 5 * T, 10 * T, 15 * T, ...\}$, $t = \{2 * T, 7 * T, 12 * T, 17 * T, ...\}$ and $t = \{3 * T, 8 * T, 13 * T, ...\}$,, where $T = \frac{1}{f_s}$. Using the Poisson summation formula, the discrete time Fourier transform (DTFT) of k^{th} active coset, $y_k[n]$,

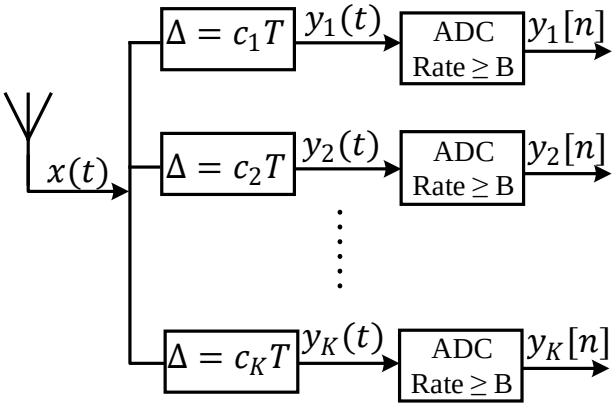

Figure 2.2: Block diagram of multi-coset sampler [60].

can be computed as

$$Y_k(e^{j2\pi fT}) = \frac{1}{NT}\sum_{i=0}^{N-1} X\left(f + \frac{i}{NT}\right) e^{j2\pi c_k i/N} \tag{2.2}$$

The DTFT of all active cosets can be represented as

$$\mathbf{Y}(f) = \mathbf{A}\mathbf{X}(f) \qquad \forall f \in \left[0, \frac{1}{NT}\right) \tag{2.3}$$

where $\mathbf{Y}(f)$ represents $K \times 1$ vector with $Y_k(e^{j2\pi fT})$ as its k^{th} row, $\mathbf{A}$ is $K \times N$ matrix with $\frac{1}{NT}e^{(j2\pi c_k i/N)}$ as $(k,i)^{th}$ element and $\mathbf{X}(f)$ is a $N \times 1$ vector with

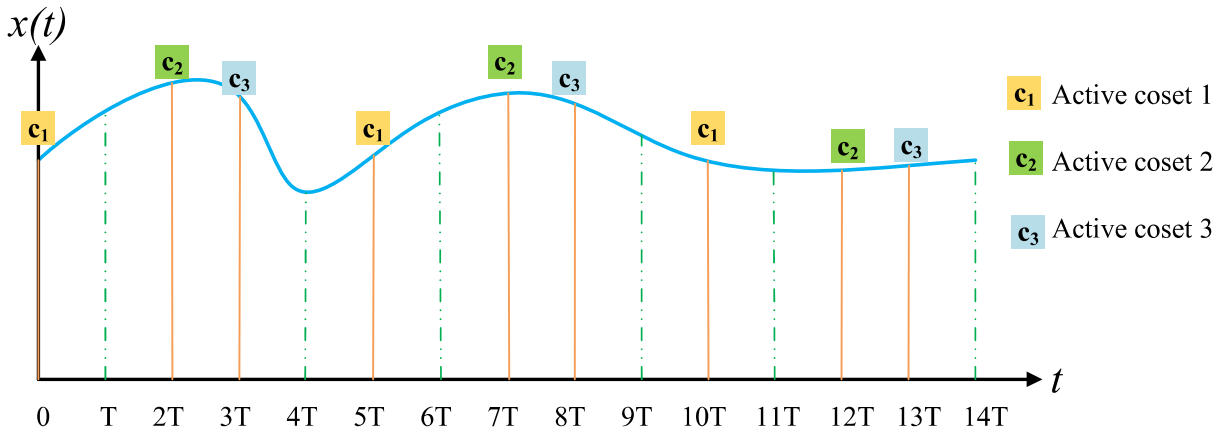

Figure 2.3: MCS for N = 5, K=3 and $c_k = \{0, 2, 3\}$.

$X\left(f+\frac{i}{NT}\right)$ as its i^{th} row.

Although MCS performs digitization at a sub-Nyquist rate, it suffers from similar drawbacks as TI-ADCs. Furthermore, the number of ADCs increases proportionately with the number of occupied frequency bands (or channels). Random demodulator, discussed in the next section, overcomes some of these limitations.

2.1.3 Random Demodulation (RD)

RD [65] is another SNS digitization technique that aims to achieve Landau's rate. As shown in Fig. 2.4, the block diagram of RD has a pseudo-random sequence generator, a mixer, an accumulator and an ADC. The RD demodulates a multi-tone wideband signal, $x(t)$, by mixing it with a pseudo-random sequence of ± 1 generated at a Nyquist rate, f_s, of $x(t)$. The demodulated signal is then passed through an accumulator and ADC to generate sub-Nyquist samples at a rate of $R\ Hz$, which is defined as

$$R \geq CM(\log f_s)^6 \tag{2.4}$$

where C is a positive constant, M is the maximum possible number of active tones in $x(t)$. The accumulation step corresponds to an integrate and dump operation where the demodulated signal is integrated for the duration, $\frac{1}{R}$, and then reset to its initial value. The major limitation of RD is that it is valid only for a multi-tone signal. Since wideband signals are analog in nature and contain an infinite number of tones, RD based digitization becomes computationally

expensive. A modulator wideband converter overcomes this drawback of RD.

2.1.4 Modulated Wideband Converter (MWC)

MWC [60] is another blind SNS technique that works on the concept of RF demodulation. As shown in Fig. 2.5, it multiplies the received wideband signal, $x(t)$, with K parallel mixing functions, $m_k(t), 1 \leq k \leq K$, in the analog front-end. The $m_k(t)$ is a digital signal of amplitude either +1 or -1 and is periodic with a period, $T_p = \frac{1}{f_p} \leq \frac{N}{f_s}$. Being a periodic signal, the Fourier series expansion of $m_k(t)$ is given as

$$m_k(t) = \sum_{i=-\infty}^{+\infty} b_{k,i} e^{j2\pi i f_p t} \tag{2.5}$$

where $b_{k,i}$ is the Fourier series coefficient. The Fourier transform of the mixed

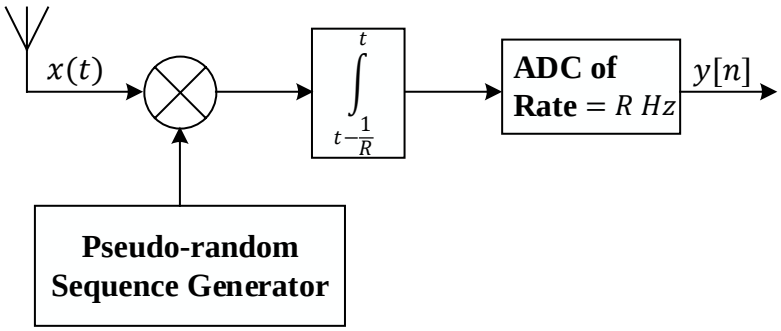

Figure 2.4: Block diagram of random demodulator [65].

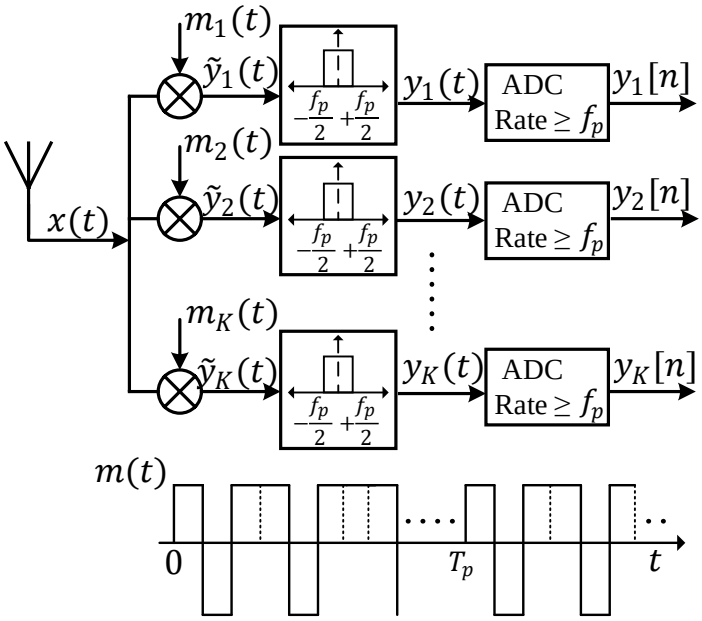

Figure 2.5: Block diagram of modulated wideband converter [60].

signal at k^{th} branch will be

$$\begin{aligned}\tilde{Y}_k(f) &= \int_{-\infty}^{+\infty} x(t) \left(\sum_{i=-\infty}^{+\infty} b_{k,i} e^{j2\pi i f_p t} \right) e^{-j2\pi f t} dt \\ &= \sum_{i=-\infty}^{+\infty} b_{k,i} \int_{-\infty}^{+\infty} x(t) e^{-j2\pi (f - i f_p) t} dt \\ &= \sum_{i=-\infty}^{+\infty} b_{k,i} X(f - i f_p)\end{aligned} \tag{2.6}$$

It can be observed from Eq. 2.6 that the output of the k^{th} multiplier is the linear combination of the shifted copies of spectrum, $X(f)$, where every shift is an integer multiple of f_p and $X(f)$ is the Fourier transform of the received wideband signal, $x(t)$. The mixed aliased signal is then bandlimited to $[-f_p/2, f_p/2]$ via a low pass filter (LPF) to remove the higher frequency components. All synchronized ADCs of K branches now perform uniform sampling at a rate of f_p. As shown in Fig. 2.6, the DTFT of the sub-Nyquist samples obtained at every

k^{th} branch contains the aliased images of all N frequency bands and is defined as

$$Y_k(e^{j2\pi fT_s}) = \sum_{i=-\frac{N}{2}}^{+\frac{N}{2}} b_{k,i} X(f - if_p), \quad f \in [-f_p/2, +f_p/2] \tag{2.7}$$

The DTFT of the output of all ADCs can be written as

$$\mathbf{Y}(f) = \mathbf{A}\mathbf{X}(f) \tag{2.8}$$

where $\mathbf{Y}(f)$ represents $K \times 1$ vector with $Y_k(e^{j2\pi fT_s})$ as its k^{th} row, $\mathbf{A}$ is $K \times N$ matrix with $b_{k,i}$ as $(k,i)^{th}$ element and $\mathbf{X}(f)$ is a $N \times 1$ vector with $X\,(f - if_p)$ as its i^{th} row.

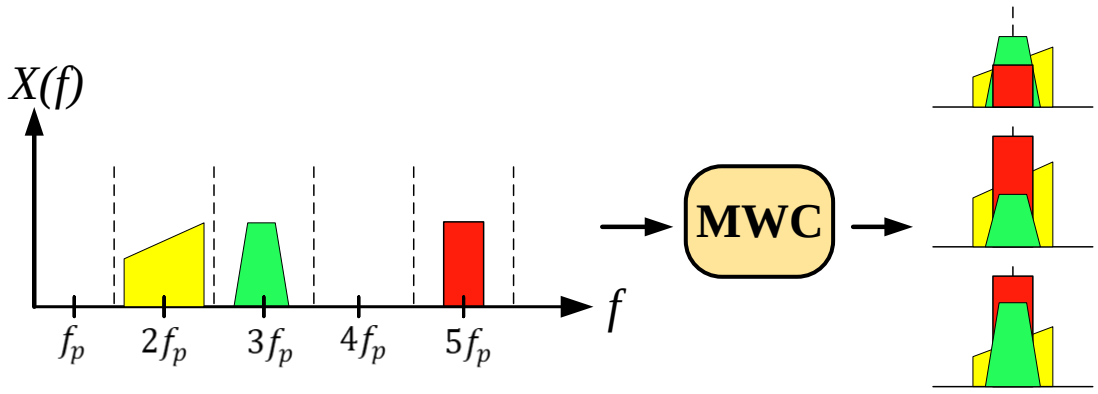

Figure 2.6: Input and output spectrum of three branch MWC.

2.1.5 Finite Rate of Innovation (FRI)

Similar to MWC, the FRI sampling technique [62] uses RF analog front end. But unlike MCS and MWC, FRI allows sampling over non-contiguous frequency bands of a wideband signal. As shown in Fig. 2.7, the FRI architecture consists of K parallel branches where a wideband signal, $x(t)$, is passed

through a branch dependent analog mixing function, $m_k(t)$, given by

$$m_k(t) = \sum_{i \in \beta} \alpha_{k,i}\ e^{-j2\pi(i-1)Bt} \tag{2.9}$$

where β is a set of frequency bands (or channels) over which SNS is to be performed, $\alpha_{k,i}$ is a unique scaling coefficient of β frequency bands, and B is the bandwidth of a frequency band. The Fourier transform of a mixed-signal, $\tilde{y}_k(t) = x(t)\ m_k(t)$, produced at the output of k^{th} mixer can be written as

$$\tilde{Y}_k(f) = \sum_{i \in \beta} \alpha_{k,i} \int_{-\infty}^{+\infty} x(t) e^{-j2\pi(f+(i-1)B)t} dt \tag{2.10}$$

$$= \sum_{i \in \beta} \alpha_{k,i} X(f + (i-1)B) \tag{2.11}$$

where $X(f)$ is the Fourier transform of $x(t)$. Since the mixed-signal, as shown in Fig. 2.8, is an aliased signal of β frequency bands, the mixed-signal $\tilde{y}_k(t)$ is then bandlimited by an LPF followed by the digitization via ADCs of rate $B = \frac{1}{NT}$ Hz. The DTFT of samples generated at the k^{th} ADC is given by

$$Y_k(e^{j2\pi fT}) = \sum_{i \in \beta} \alpha_{k,i} X\left(f + \frac{(i-1)}{NT}\right)\ \forall f \in \left[0, \frac{1}{NT}\right] \tag{2.12}$$

The sub-Nyquist samples of all K ADCs can be collectively represented as

$$\mathbf{Y}(f) = \mathbf{A}\mathbf{X}_\beta(f) \qquad \forall f \in \left[0, \frac{1}{NT}\right] \tag{2.13}$$

where $\mathbf{X}_\beta(f)$ represents $|\beta| \times 1$ vector containing Fourier transform of β fre-

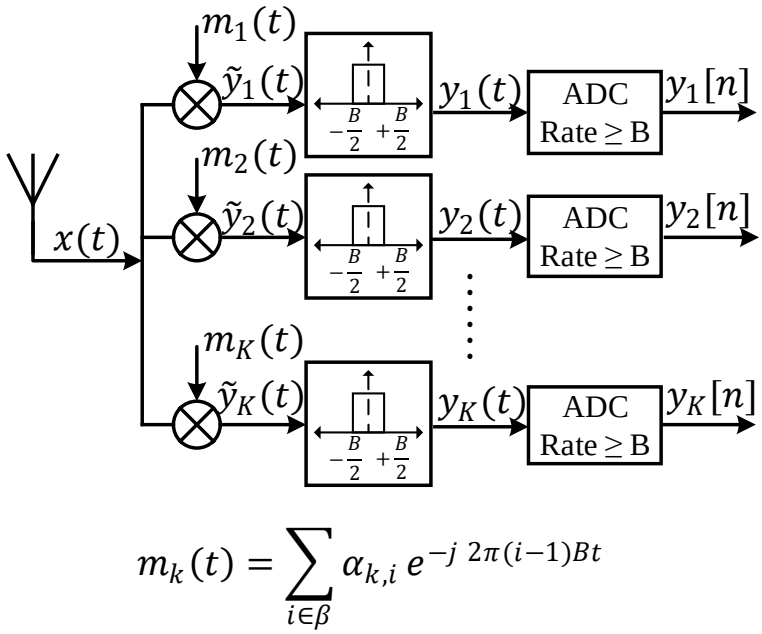

Figure 2.7: Block diagram of finite rate of innovation based SNS [63].

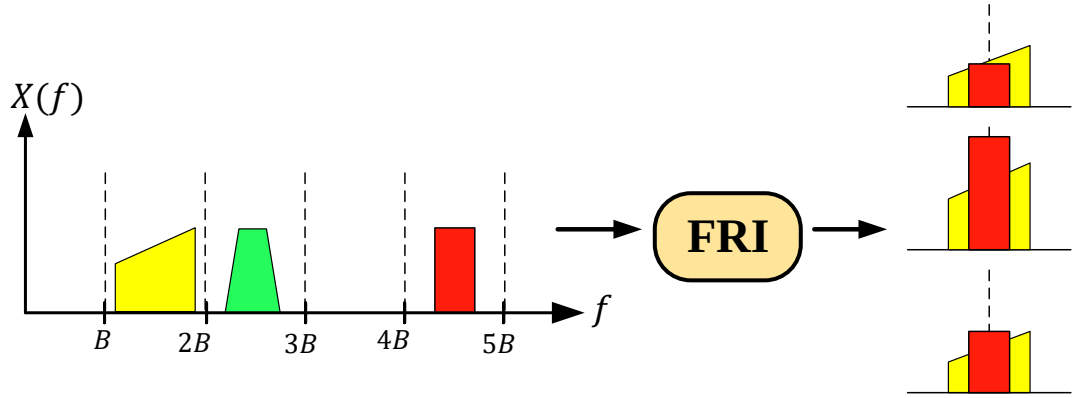

Figure 2.8: FRI based SNS for multiband signal.

quency bands and **A** is a $K \times |\beta|$ matrix containing $\alpha_{k,i}$ as its $(k,i)^{th}$ entry. However, the main challenge in the FRI SNS technique is the determination of the frequency band set β.

The summary of the wideband signal digitization techniques is discussed in Table 2.1. It can be observed that to sample a wideband signal of N frequency bands, TI-ADC requires N ADCs of sampling rate $B\ Hz$. Hence, the TI-ADC sampling technique can be applied to both sparse and non-sparse sig-

Table 2.1: Comparison of state-of-the-art wideband techniques.

Sampling Techniques	Number of ADCs	Sampling Rate	ADC Analog Bandwidth	Sampling Strategy	Characterization Failure
TI-ADC	N	B	f_s	Contiguous	No
MCS	K	B	f_s	Contiguous	$M > K$
RD	1	$R < f_s$	$R < f_s$	Contiguous	Eq. 2.4 not valid
MWC	K	B	B	Contiguous	$M > K$
FRI	K	B	B	Non-Contiguous	$M_\beta > K$

nals. Whereas MCS, MWC and FRI employ $K < N$ ADCs of sampling rate $B\ Hz$. Hence, they can be applied to the sparse wideband signal. Unlike TI-ADC, MCS, MWC and FRI, RD uses one ADC of sampling rate, $R < f_s$ (defined in Eq. 2.4). But RD can work only for multi-toe signal, and hence, it is not applicable for analog signal which has an infinite number of tones. The analog bandwidth of ADCs in TI-ADC and MCS sampling techniques is the same as the Nyquist frequency, f_s. But in the case of MWC and FRI techniques, the ADC analog bandwidth is $B = \frac{f_s}{N}$. Hence, making MWC and FRI better sampling techniques than TI-ADC and MCS. It can be observed that MCS and MWC follow the contiguous sampling approach. Hence, they incur characterization failure whenever the number of active transmissions, M goes beyond K. To overcome this drawback of MWC, FRI based sampling techniques performs digitization over the selected subset of frequency bands, β and hence, incurs failure only when the number of active transmissions in β, i.e. M_β is higher than K. However, the selection of β is a critical step because if we increase the size of β, then the throughput (i.e. the number of vacant bands in β) may increase, but it also increases the probability of characterization failure. Thus there is a need for a decision making algorithm to select the best frequency bands subset.

2.2 Learning and Decision Making (LDM) Algorithms

The decision of selecting the best subset of frequency bands (or channels) requires prior knowledge of the spectrum statistics like occupancy probabilities of frequency bands. Since the information of spectrum statistics is unknown to WSA, a learning and decision making (LDM) algorithm capable of learning statistics as well as making the decision of best channel subset is desired. Multi-Armed Bandits (MAB) algorithms are extensively studied LDM algorithms [66–68]. The performance of these algorithms is expressed in terms of regret. Regret is defined as a difference between cumulative throughput obtained by MAB algorithms and an oracle policy that plays the optimal frequency band in each time slot. By accurately learning the spectrum statistics, these algorithms select the best frequency band. But the accurate learning requires the MAB algorithms to explore each frequency band sufficiently. This leads to the selection of sub-optimal frequency bands (also referred to as arms in MAB algorithms) for a larger duration, incurring higher regret. However, the exploitation of a good quality frequency band from the beginning of the learning process will reduce the exploration duration and hence, results in lower regret. But lower exploration duration might also lead to incorrect selection of band if the learning is incorrect and therefore collects a linear regret, which is undesired. Thus, there is a need for the MAB algorithm, which balances the trade-off between the exploration and exploitation duration. Furthermore, the MAB algorithms select only a single frequency band. The extensions of MAB, named as Multi-

Play MAB (MPMAB) and combinatorial MABs (CMAB) [69, 70, 75, 76], are proposed where in each time slot, an LDM is applied on a subset of frequency bands to learn the optimal subset.

Upper confidence bound (UCB) based algorithms for multi-play scenario is developed in [69]. Here the players can select a subset of frequency bands in each time slot. The authors show that their algorithm, named CMAB, achieves logarithmic regret. However, the constant terms match the lower bound. [70] extends Thompson sampling for multi-players setting when the learner can play a subset of fixed size in each time slot. The authors show that when the throughput (also called as reward in MAB algorithms) distributions are Bernoulli, their Multi-Play Thompson Sampling (MP-TS) algorithm achieves optimal regret. [75] generalizes the work of [70] by allowing subsets of size less than a specific size in each time slot. Using the matroid bandits set-up, they show that the regret bound of their algorithm matched with that in [70]. Furthermore, [75] considers the prior distribution of the means of all frequency bands as the beta distribution, and its extension in [76] provides the tight regret bounds for multi-variate Gaussian distribution priors of frequency bands.

All the MPMAB algorithms (also referred to as CMAB in the literature) [69,70,75,76] consider fixed-size subsets, say K. The main assumption in these works is that whenever a subset is played, throughput from all the frequency bands in the subsets are observed, i.e., there is no loss of feedback. However, in the SNS based WSA with K ADCs, the selection of a subset of size larger than K may lead to the reconstruction failure. Hence, resulting in the collection

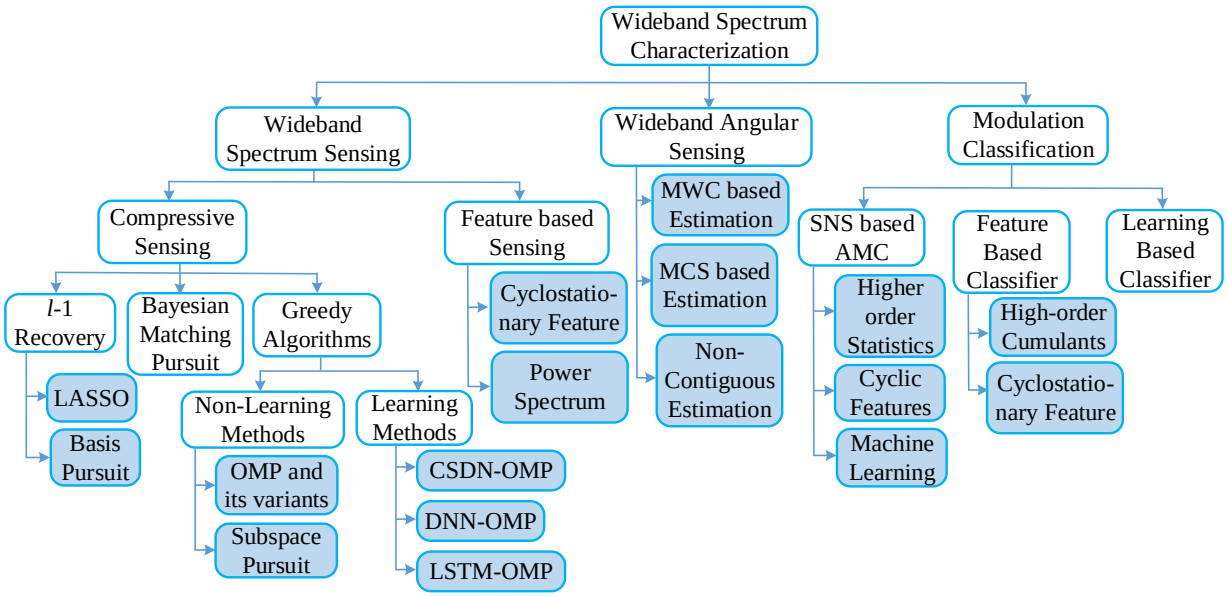

Figure 2.9: Various wideband spectrum characterization techniques.

of no feedback. Thus the algorithm developed for MPMAB or combinatorial bandits cannot be directly applied to our setting.

2.3 Wideband Spectrum Characterization at WSA

The sub-Nyquist samples generated in the previous section can be utilized in different ways to perform the characterization of a wideband signal. The characterization aims to estimate parameters like occupancy status of the frequency bands of a wideband spectrum and transmission directions, i.e., the direction of arrival (DoA) and modulation scheme of occupied frequency bands of a wideband spectrum at sub-Nyquist rate. Fig. 2.9 shows the various SNS based wideband spectrum characterization techniques. In the following sub-sections, we discuss these characterization techniques in detail.

2.3.1 Wideband Spectrum Sensing (WSS)

The determination of the occupancy status of the frequency bands of a wideband signal is referred to as wideband spectrum sensing (WSS) [20, 21]. The SNS based WSS approaches studied in the literature are:

2.3.1.1 Compressive Sensing

The next step after performing SNS is the reconstruction of the wideband signal in the digital domain. Various reconstruction approaches have been explored in the literature [77]. We can broadly classify these approaches into three categories: 1) Greedy algorithms [78], 2) l_1-minimization algorithms [78], and 3) Bayesian algorithms [79]. The l_1-minimization based algorithms like basis pursuit and LASSO (least absolute shrinkage and selection operator) offer better reconstruction and hence, wideband sensing accuracy than greedy and Bayesian algorithms. But l_1-minimization is not feasible for real-time applications due to high computation time and complexity. Bayesian algorithms offer lower computational complexity than l_1-minimization algorithms and have better reconstruction accuracy than greedy algorithms [80]. But Bayesian algorithms require prior knowledge of the probability distribution of the information signal transmitted in the wideband spectrum.

The greedy algorithm, such as orthogonal matching pursuit (OMP) [81], is widely used due to lower computational complexity. OMP follows the iterative approach where each iteration performs four operations: 1) Matching, 2)

Identification, 3) Least squares, and 4) Approximation. Deep learning based OMP methods have been proposed in [82–84] to improve the performance of OMP. [82], [83] and [84] methods replace the matching operation of OMP with convolutional deep stacking networks (CSDN), multi-layer deep neural network (DNN) and long short term memory (LSTM) deep learning approaches, respectively. But all these algorithms [81–84] require prior knowledge of the number of occupied bands. The compressive WSS method discussed in [85] performs blind SNS sensing. Here, a residual energy-based detector is proposed, which uses the derived decision threshold to make a series of binary hypotheses.

The Bayesian approach is used in [86] for WSS. It divides the wideband range into multiple bands, creates an observation window, and applies random sampling. [86] reconstructs the frequency spectrum for every observation periods and takes their average to perform spectrum estimation and sensing. Finally, the status of the spectrum bands is determined by applying classical binary hypothesis testing on every frequency sub-band.

2.3.1.2 Feature Detection

Feature-based WSS has two significant advantages over compressive reconstruction based spectrum sensing. Firstly, the signal transmitted over an occupied frequency band exhibits unique features like modulation scheme, stationary and cyclostationary properties. These features have a fewer degree of freedom than the reconstruction of the signal. Hence, feature-based WSS is applicable even if the signal's sparsity is low. Secondly, features are more robust to noise,

such as the cyclostationary feature is independent of the stationary noise and hence, can work under low SNR. Recently, SNS based feature detection has been proposed [30–41] to reconstruct features from the sub-Nyquist samples followed by the parameter estimation technique [51–53] to determine the carrier frequency and bandwidth of occupied frequency bands.

Power spectrum based WSS [31–35] assume the transmissions in a wideband signal are uncorrelated wide-sense stationary. In [30], the wideband spectrum is divided into multiple sub-bands, and wavelet transform is applied on each sub-band to detect the irregularities in the power spectral densities of the sub-bands. [31] employs binary hypothesis testing on the power spectrum of each frequency band of a wideband spectrum. The performance of the power detector is analyzed with simple FFT, windowed FFT and multitap windowed FFT for frequency domain power detection. [31] is extended to a multitap power detector with adaptive sensing time and threshold [32]. But, both [31] and [32] require high Nyquist rate ADCs for digitization. To overcome this drawback, [33] introduces a minimum sparse ruler based multicoset sampling and performs the recovery of the power spectrum of the wideband spectrum from the sub-Nyquist samples. Similar to [33], [34, 35] also perform the direct recovery of the power spectrum from the sub-Nyquist samples. But unlike [33], [35] provides the proof for the universal sampling pattern of multicoset sampling. It considers both sparse and non-sparse signal models and derives the minimum sampling rate for perfect power spectrum reconstruction. Furthermore, [35] also presented the WSS techniques to achieve the minimum sampling rate.

Cyclostationary based WSS takes advantage of the statistical periodicity of the modulated signal because of which the signal behaves as a cyclostationary process [36, 37, 40, 41]. Thus by finding the spectral correlation, the desired signal can be separated from the noise making the cyclostationary based WSS more robust to noise. The sub-Nyquist sampling based cyclostationary detector presented in [36] is the first work that utilizes the sub-Nyquist samples generated via MCS or MWC sampling technique. Whereas [37] performs the reconstruction of the two-dimensional Nyquist spectral correlation function from the sub-Nyquist samples. To reconstruct the spectral correlation function, [37] uses regularized least square approach. The reconstruction of the sparse two-dimensional cyclic spectrum does not follow linear recovery relation with the sub-Nyquist samples.

In [38], the vectorized cyclic spectrum is reformulated into linear autocorrelation of the sub-Nyquist samples. Furthermore, a cyclic feature based detector capable of simultaneously identifying all active transmissions is developed in [38]. The sampling rate compression is done in [37, 40] depend on the second-order statistics. But in [39], the prior spectral information of active frequency bands is also exploited along with the second-order statistics to reduce the sampling rate further. Similar to [37–39], [40] also reconstruct the spectral correlation function from the sub-Nyquist samples. But [40] performs reconstruction of both sparse and non-sparse signals and develops the blind and non-blind detection method for sparse signal. Apart from reconstructing the cyclic spectrum, [41] number of active transmissions in a wideband signal and their carrier frequen-

cies and bandwidth. Also, [41] derives the lower bound on the sampling rate to reconstruct the cyclic spectrum perfectly. It is shown that for a non-sparse and sparse wideband signal, the minimum sampling rate required to reconstruct the cyclic spectrum perfectly is $4/5$ times of the Nyquist rate and $8/5$ times of the Landau's rate, respectively. The wideband receiver impairments due to low noise amplifier and mixer are analyzed in [42]. It is shown that due to the nonlinearities of the receiver, the performance of WSS suffers degradation. The impact of cyclic frequency and sampling clock offsets on the conventional cyclostationary WSS detector is examined in [43]. A multi-frame test statistic determining the optimal frame length such that the detection performance can be maximized for the given sensing time is proposed to reduce the effect of these offsets.

2.3.1.3 Collaborative WSS

The sensing performance of the spectrum analyzer degrades under shadowing/deep fading scenarios. To improve the sensing accuracy in such situations, collaborative spectrum sensing, which collectively processes the sensing information from different sensor nodes, has been studied [44]. The collaborative spectrum sensing can be performed in two manners: 1) Centralized collaborative sensing where sensing information of each node is sent to a fusion center to make the final decision; 2) Decentralized collaborative sensing where each node makes its own decision and share the results with the neighbouring nodes. But due to hardware limitations, it is not possible to perform WSS at every sen-

sor node. Various collaborative WSS techniques have been studied in the last decade [45–49]. [45] proposes to use a frequency-selective filter at every sensor node and send the linear combined multi-channel information to the fusion center. Thus, the fusion center gets the diverse information of all channels in the wideband signal from the sensor nodes to decide on spectrum occupancy status. SNS based collaborative spectrum sensing is discussed in [46–48]. Each sensor node has a wideband filter to remove the undesired frequency component followed by the sub-Nyquist sampler. The sampling rate of each sampler is decided by the fusion center, which is relatively prime among all the nodes. Then the FFT and energy detector blocks determine the energy of the sub-Nyquist samples. The energy output of each sensor node is sent to the fusion center to determine the occupancy status of all bands of a wideband spectrum. [47] extends the work of [46] to perform multi-rate SNS based collaborative spectrum sensing under Rayleigh and log-normal fading channel distributions. [48] also performed SNS based collaborative spectrum sensing, but its every node performs MCS with relatively prime sampling rate followed by signal recovery. The recovery block takes the multi-coset samples and the recovered carrier frequencies and power spectral densities of neighbouring sensor nodes to determine the average carrier frequency and power spectral density information. In [49], the superposition property of the wireless channel is utilized to reduce the computational cost at the fusion center. Here, the sensor nodes perform interleaved sampling at a low rate. The sensor nodes then perform modified DFT and transmit the samples in a synchronized manner. The transmitted samples

are then combined over the air and processed by the fusion center to perform WSS. The work presented in [50] exploits the spectrum occupancy behaviour to perform cooperative WSS. By utilizing the block-like spectrum occupancy, [50] uses machine learning with the proposed weighted compressive sampling to determine the wideband occupancy information efficiently.

2.3.2 Wideband Angular Spectrum Sensing (WAS)

Determination of the direction of users is a critical step to perform spatial multiplexing. Thus apart from performing WSS in the temporal domain, there is a need for wideband angular sensing (WAS) techniques that can perform spectrum sensing in both temporal and spatial domains. The work presented in [22–27] explored WAS. [22] proposes a distributed WAS where every base station of a small cell is assigned a set of spectrum for spatio-temporal sensing. Then the base stations share the sensing report to other base stations to obtain the occupancy status of a wideband spectrum. The work presented in [23–27] performed a joint estimation of the carrier frequency and directional of arrival (DoA) of active transmissions present in the sensed spectrum. The WAS requires multi-antenna SNS architecture for the digitization of wideband signal, $x(t)$. In this discussion, we consider the L number of antennas in the receiver architecture. A nested array architecture with a delayed branch at every antenna of the dense array is proposed in [23]. Though it offers wideband spectrum digitization via low-rate ADCs, there are two major drawbacks: 1) The delay in each branch must be identical and of the order of Nyquist period (i.e.

in nano seconds), and 2) Each antenna needs two ADCs (one at delayed and direct branch) of an analog bandwidth of Nyquist rate, which is significantly wide. Both the requirements are difficult to meet in AFE, making [23] difficult to realize in practice. The condition of identical delay in each branch is relaxed in [24]. Compressed carrier and DoA estimation (CASCADE) architecture based on well-known MWC [60] based SNS overcomes drawbacks [25]. CASCADE uses an L-shaped antenna array, and similar to MWC, the AFE of each antenna consists of an analog mixing function followed by an LPF and ADC. Since the mixer down-coverts each frequency band to the baseband, the analog bandwidth of ADC is reduced to the bandwidth of a frequency band. All these works [23–25] are based on contiguous SNS, which may not be suitable for next-generation wireless networks.

Ideally, digitization architecture should characterize as many busy frequency bands in the digitized spectrum as possible. However, SNS restricts the number of allowable busy frequency bands in the digitized spectrum for a given number of antennas. For example, the number of busy bands must be less than the number of antennas in [23–25]. By creating the virtual antennas, the architectures in [26, 27] allow characterization of the higher number of busy frequency bands than the number of antennas. To achieve this, [26] uses a uniform rectangular array having L antennas with one antenna containing K multiple delayed branches. On performing 3-D spatial smoothing and rank enhancement, [26] creates $L_s > L$ antennas (i.e. the sum of physical and actual antennas) and allows sensing of up to $\frac{KL}{4}$ busy frequency bands. In [27], the architecture is

based on the integration of ULA with MCS [59]. It sparsely activates only a few antennas of ULA to estimate DoA. The hardware complexity comparison of the existing WAS methods [23–27], when they are implemented on the AFE, is shown in Table 2.2. It can be observed that for M number of active transmissions, [26] and [27] require fewer antennas and ADCs. This happens due to the sparse antenna architecture of WAS receiver architecture of [26] and [27]. Also, because of the sparse antenna array, [26] and [27] incur characterization failure only when the number of active transmissions is higher than the total number of antennas, i.e. $M > L_s$. But since [25] uses MWC based AFE, it does not require precise delay elements of the order of nano-seconds. Furthermore, the analog bandwidth of the ADCs of [25] is as low as the bandwidth of a frequency band, i.e. $B = \frac{f_s}{N}$, whereas in [23, 24, 26, 27], the analog bandwidth is as high as the Nyquist frequency, f_s. But all the WAS techniques [23–27] are based on contiguous SNS. Thus, there is a need for an architecture that allows non-contiguous SNS based WAS.

Table 2.2: Hardware complexity comparison of different UWASS approaches.

Characteristics	**[23]**	**[24]**	**[25]**	**[26]**	**[27]**
Number of Antennas	$M+1$	$M+1$	$2M+1$	$4M/K$	$< M+1$
Number of ADCs	$2M+1$	$M+1$	$2M+1$	$(4M+K-1)/K$	$< (M+1)K$
Analog BW of ADCs	High	High	Low	High	High
Precise delay	Required	Not required	Not required	Required	Required
Sensing Failure ($M \geq L$)	Fails	Fails	Fails	Fails when $M \geq L_s$	Fails when $M \geq L_s$

2.3.3 Automatic Modulation Classifier (AMC)

In the underlay dynamic spectrum sharing approach, the information of parameters like power, modulation schemes, etc., of licensed users is desired to keep the inference level below the acceptable threshold [87]. In this section, we discuss the various automatic modulation classification (AMC) techniques such as likelihood ratio based classifier [91], feature-based classifier [92, 93] and intelligent learning classifiers [94–107] to determine the modulation schemes of the active transmissions present in the wideband signal. Likelihood ratio based classifiers [91] treat AMC as a multiple-composite hypothesis testing problem, and parameters are determined by applying the maximum likelihood estimation (MLE) criteria. The drawback of this approach is that the accuracy depends on the knowledge of the distribution of active transmissions and noise, which vary dynamically in the real environment. Feature-based classification methods [88–90] are explored to overcome this drawback. This classification method analyzes a variety of statistical features such as higher-order moments, cumulants [88] and cyclostationary features [93] of the received spectrum. Extensive research has been focused on the usefulness and performance analysis of these methods for AMC [92, 93]. In [92], various normalized fourth-order cumulants are explored. Then the relationship between these cumulants and multipath fading effects is developed to improve the AMC performance for the fading channel condition. The performance of various algorithms using the cyclostationary feature is reviewed in [93]. Later, the cyclostationary feature is utilized

by different classifiers like neural networks and hidden Markovian models to perform AMC.

Recently, various intelligent learning based AMC exploiting features along with learning algorithms such as support vector machine (SVM) [94], k-nearest neighbor (KNN) [95], random forest (RF) [96] and neural networks [94–107] has shown to offer a significant improvement in performance with limited prior knowledge of spectrum. An SVM classifier based AMC for varying channel noise is explored in [94]. In this, twenty five types of features are extracted, out of which four features that are insensitive varying channel noise are selected for the training of the SVM classifier. Genetic programming along with the KNN classifier is used in [95] to classify BPSK, QPSK, QAM16 and QAM64. Cumulants features are used for genetic programming to distinguish between BPSK, QPSK and QAM. After that, KNN is used to further improve the performance by classifying QAM16 and QAM64. A random forest machine learning classifier is studied in [96] to classify various analog and digital modulation schemes for various SNR ranges. A dictionary learning based AMC is studied in [97]. A block coordinate descent dictionary learning is proposed to learn a sparse dictionary for modulation classification, and it is shown to outperform other machine learning AMCs like SVM [94] and KNN [95]. Among various intelligent learning classifiers, neural networks based AMC are state-of-the-art classification methods [98–107]. Neural networks are DL models which work as function approximators and extract desirable patterns from the underlying relationships in data. A MAXNET neural network consisting of a multilayer lin-

ear perceptron network for every modulation scheme class is discussed in [98]. The performance of a dense neural network is analyzed for AMC application in [99]. Twenty-one features with widely separated distribution are considered an input to the dense neural network with three hidden layers. Its trained model considers samples from all channel conditions, i.e. additive white Gaussian noise and Rician fading channel. A state-of-the-art neural network architecture, i.e. a convolutional neural network (CNN) model, with only two layers is studied in [103]. It is shown that the proposed CNN based AMC significantly outperforms the expert feature-based AMC methods. In [100, 101], the principle architectures used for image recognition are utilized for the AMC along with an extensive analysis to study the effect of network depth, filter sizes and the number of filters on the accuracy of classification.

The representation of input signal for DL algorithms is analyzed in [102], and it is shown that the use of amplitude-phase samples with LSTM learning algorithm outperforms the real and imaginary sample based CNN AMC [103]. The time-frequency feature is also considered as an input to the CNN model in [104] to improve the accuracy. Thus, the selection of an appropriate input format is essential for AMC. A fusion-based CNN AMC is considered in [105] to improve the accuracy of simple CNN-based classification. Three fusion methods, namely: voting based fusion, confidence based fusion and feature based fusion methods, are employed in [105] to improve classification performance. Similarly, another feature fusion method for AMC using CNN is studied in [106]. It uses eight handcrafted features and two image features extracted by apply-

ing smooth pseudo Wigner Ville and Born-Jordan time-frequency distribution to CNN models. These ten features are then used by multi-modality fusion to improve AMC performance. Although the intelligent learning based AMC has higher performance than conventional AMCs, they have high computational complexity. [107] presents the light weight AMC, which offers a smaller model size and faster computation speed. It determines the redundant neurons of CNN and removes them. This results in a slight reduction of the performance of AMC, but it significantly reduces the model size and accelerates the computation.

All the AMC methods studied above [91–107] work on the Nyquist samples and hence, they are applicable only for a narrowband signal. The extension of narrowband AMC to wideband AMC is non-trivial due to the need for SNS, digital reconstruction, channelization and characterization algorithms, and integration. [54, 55, 108, 109] are the only work that consider wideband AMC. But they do not consider state-of-the-art SNS approaches and need tunable channelizers to convert wideband spectrum to multiple narrowband signals for characterization using narrowband methods. Thus, wideband AMC is needed to determine the modulation schemes of all occupied frequency bands concurrently.

2.4 Hardware Implementation

This section presents the hardware implementation of the MWC SNS technique of wideband signal digitization and various wideband characterization algorithms like MAB learning algorithm, WSS, WAS and AMC techniques.

2.4.1 MWC Digitization Implementation

MWC is the only SNS technique that has been implemented and successfully tested on the real-time wideband signal [61]. The hardware testbed of MWC is able to process a wideband signal of Nyquist frequency, $f_s = 6\ GHz$ and spectrum occupancy of $200\ MHz$ at a sampling rate of $480\ MHz$. The block diagram of the hardware prototype of MWC is shown in Fig. 2.10. The received RF signal first passed through the splitter and preprocessor, which duplicates the RF signal for four parallel RF chains and preprocesses it to perform equalization, impedance correction and gain adjustment. The preprocessed signal is then amplified by a low noise amplifier (LNA). The amplified signal of every RF branch is then modulated by a unique mixing sequence of ± 1 such that all mixing functions are uncorrelated. Now, the modulated signal is passed through an anti-aliasing LPF followed by an amplifier and attenuator. Finally, to generate sub-Nyquist samples, the filtered signal is digitized by the synchronized ADCs of RF branches. The digitized low rate samples are then fed to software-defined digital signal processing block to perform digital processing tasks like signal recovery, detection, demodulation, etc., as per the application.

2.4.2 LDM Algorithms Implementation

Various experiments implementing MAB algorithms have been performed to select the best frequency band from a set of frequency bands [110–113]. The USRP and GNU radio hardware demonstration performed in [110] shows the

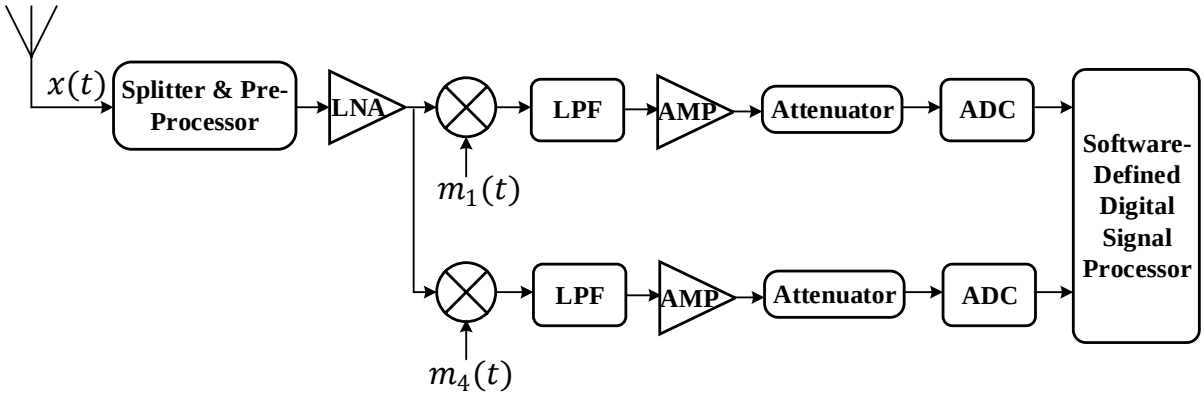

Figure 2.10: Hardware prototype of MWC.

learning capability of the UCB algorithm on the real radio environment. The demonstration allows the secondary/unlicensed user to pick the frequency band of maximum probability of vacancy by learning the occupancy statistics. Similarly, an intelligent IoT network is developed in [111, 112]. They create a decentralized learning mechanism where multiple intelligent users can improve access to the available network spectrum. A trekking based multi player distributed algorithm is developed in [113], and it is shown that the algorithm offers a significantly lower number of secondary users collision while selecting the best frequency bands. All the demonstrations performed in [110–113] aim to either select a single best quality frequency band or multiple good quality frequency bands for more than one secondary user. No demonstration is done to validate the selection of a set of frequency bands which is the primary requirement of the non-contiguous wideband signal digitization.

2.4.3 WSS Implementation

Various spectrum sensing methods are being developed and validated on the hardware testbeds [61, 114–121]. In [114], a histogram based spectrum seg-

mentation method is proposed to detect the spectral boundaries of primary (or licensed) users. Whereas the performance of spectrum sensing methods like discriminant analysis [115], energy detector and cyclo-stationary detector [116] are validated in [115, 116]. Furthermore, the performance of the cyclo-stationary detector for LTE SC-FDMA signal is analyzed for different channel conditions in [117]. The hardware set-up used in [114–117] consists of a vector signal generator to generate the licensed user traffic signals. Then via the Ethernet cable, this signal is then passed to the processing unit and vector signal analyzer to perform spectrum sensing. For validating the performance of the energy detector under the non-ideal behaviour of the AFE of the receiver, [118] uses software defined radio for the reception of signal. But similar to [114–117], [118] also performs wired transmission of the signal. To analyze spectrum sensing performance for over the air transmission, [119, 120] use USRPs for the wireless transmission and reception of the signal. In [119], a cognitive radio network is developed to perform spectrum sensing, followed by dynamic spectrum access on the detected spectrum opportunities. In contrast, a method identifying the secondary (unlicensed) user, which does not contribute to collaborative spectrum sensing, is proposed in [120]. In [121], a spectrum sensing receiver with Analog Devices frontend AD9361RF and Xilinx Kintex-7 FPGA is developed. The analog frontend allows the sensing of frequency bands in the range of 70 MHz to 6 GHz, and the energy detector based spectrum sensing is implemented on FPGA in the pipelined manner. Although the spectrum sensing methods discussed in [114–121] validate different spectrum sensing meth-

ods under various channels conditions and non-ideal behaviour of transmitter and receiver RF AFE, they all assume the Nyquist sampling based digitization. Hence, [114–121] are not applicable to perform WSS. A BigBand technology capable of sensing a wideband spectrum in real-time via low rate ADCs is developed in [122]. It senses a wideband spectrum of $0.9\ GHz$ bandwidth via 3 USRPs with SBX daughter board. To sense the wideband bandwidth, the low pass filter of daughter board is removed. The sampling rate of all synchronized ADCs of three USRPs is set to $50MS/s$. Thus, the sampling rate is six times slower than the sensing bandwidth. The MWC prototype developed in [61] is also extended to perform WSS. But both [61, 122] implement contiguous SNS followed by determining the status of every frequency band.

2.4.4 WAS Implementation

The main role in WAS is to determine the carrier frequency and DoA of the active transmissions present in the occupied frequency bands of the wideband signal. In [123, 124], the localization of a single transmission under various hardware impairments like multi-path channel, non-ideal antenna array and non-ideal RF AFE is discussed. To perform this task, single input multiple output testbed is developed for the DoA estimation. In [125], DoA estimation at high altitude is accomplished via a multi-antenna spherical array testbed. In [126], an interesting DoA estimation approach via a single antenna receiver on the high-speed train environment is demonstrated. By considering the uniform speed of the train, virtual ULA is realized by considering the samples received

at different time instants along with space alternating generalized expectation-maximization principle [127] for DoA estimation. For DoA estimation, MUSIC and ESPIRIT are widely used algorithms, and among them, MUSIC is shown to offer higher accuracy [128]. All these methods [123–128] perform DoA estimation of only single-user transmission, i.e. narrowband DoA estimation.

Very few works consider the DoA estimation of the wideband spectrum and prototype design. The hardware testbeds discussed in [123–129] use the uniform array for the DoA estimation and hence can not determine the DoAs when the number of transmissions is more than the number of antennas. In [129], DoA estimation testbed for two and three transmissions with the help of four and eight antennas ULA respectively is demonstrated. It employs Cholesky and LDL decomposition on the FPGA platform. [130] uses a co-prime antenna array to receive the signal and employs MUSIC, Capon and Least Absolute Shrinkage and Selection Operator (LASSO) methods to perform DoA estimation. Although [130] considers DoA estimation of multi-tone signal, all the tones have the same DoA.

To summarize, existing works can perform the DoA estimation on Nyquist sampled signal and have limitations on the digitization bandwidth and the number of possible DoAs. Furthermore, none of the existing works offers an end-to-end prototype for WAS.

2.4.5 AMC Implementation

The blind estimation of the modulation scheme is a key requirement of future generation intelligent radios. Various AMC methods have been studied in the literature to meet this demand, and a few works have been done to validate these AMC methods on the real radio signals [131–134]. A NI-LabVIEW and USRP hardware testbed for cyclostationary feature based AMC is developed in [131]. Upon receiving the modulated signal, the receiver extracts the cyclostationary feature and apply the trained neural network to classify BPSK, QPSK, FSK and MSK modulation scheme. A centralized framework for AMC is developed in [132]. Multiple sensors send the information to the fusion center, which applies likelihood ratio classification to determine the modulation scheme.

A hardware demonstration of blind hierarchical AMC is studied in [133]. It applies the energy detector to perform coarse estimation of the signal and then applies cumulants, cyclostationary detector and Kupier test to detect amplitude modulation (AM), frequency modulation (FM), and QAM, PAM and PSK modulation schemes, respectively. An artificial neural network based AMC hardware testbed is developed in [134] to enhance classification accuracy. It employs Nesterov accelerated adaptive moment estimation technique to enhance the performance of the developed AMC further. All the AMC testbeds developed in [131–134] utilize the Nyquist rate samples and are applicable for a single modulated signal. But due to SNS based digitization of a wideband signal, there is a need to develop an AMC testbed that can perform simultaneous

AMC on all the active transmissions of a wideband signal.

2.5 Summary

In this chapter, a brief review of the existing wideband spectrum digitization and characterization techniques is presented. We also discuss the hardware prototype of the wideband signal digitization method and various testbeds for the validation of the wideband spectrum characterization techniques.

Future generation radios are expected to perform dynamic spectrum sharing over a wide range of non-contiguous unlicensed and shared spectrum. In order to provide the area, power and cost effectively wideband signal digitization, several sampling techniques employing low rate analog to digital converters (ADCs) are studied in the first section of the chapter. In which we have reviewed time interleaved ADC (TI-ADC), multi-coset sampling (MCS), random demodulator (RD), modulated wideband converter (MWC), and finite rate of innovation (FRI) based sub-Nyquist sampling (SNS) techniques, which employ low rate ADCs for the digitization of wideband signal. It is shown that TI-ADC, MCS, RD and MWC techniques perform the digitization of the entire wideband spectrum, which is not desired. Hence, the FRI SNS technique, which can perform non-contiguous digitization of the spectrum, is explored in the latter part of the first section.

While FRI SNS technique is most compatible with the wideband signal digitization for future generation wireless networks, it requires the intelligence

of selecting non-contiguous frequency bands for digitization. The multi-play multi-armed bandit (MPMAB) algorithms, which provide this decision making capability, is discussed in the second section of the chapter. The existing MPMAB algorithms select a set of best frequency bands, but all these algorithms select a fixed number of frequency bands and always receive feedback on the frequency band selection. Whereas for the desired non-contiguous SNS set-up, the wireless network incurs a loss of feedback (i.e. reconstruction or characterization failure) when the number of active transmissions is higher than the number of ADCs. Hence, the need for a new MPMAB algorithm is also discussed in detail.

Next, various wideband spectrum characterization techniques, including wideband spectrum sensing (WSS), wideband angular sensing (WAS) and automatic modulation classification (AMC) technique, are presented in the third section of the chapter. Under WSS, we have discussed compressive sensing and feature based spectrum sensing techniques. Here, we have reviewed the compressive sensing methods like l_1-minimization, Bayesian and greedy algorithms, which determine the status of frequency bands of the wideband spectrum directly from the sub-Nyquist samples. Whereas in feature based WSS, we have discussed cyclostationary feature and power spectrum based WSS methods. The comparison is made on the various multi-antenna WAS architectures to extend the WSS in the spatial domain. Here, we have classified the WAS architectures into MCS and MWC SNS based WAS approaches. But both the WAS approaches are dependent on the number of antennas. So, the need for an intelligent and recon-

figurable WAS receiver architecture is discussed at the end of WAS techniques. Finally, various AMC techniques to blindly detect the modulation schemes of the active transmissions present in the wideband spectrum are reviewed. Here, we have discussed several feature based AMCs, including likelihood ratio, cyclostationary feature, cumulants and intelligent machine/deep learning methods. However, in the literature, the performance analysis of all these AMCs is limited to the classification of narrowband signals. So, the need for SNS based AMC is discussed at the end of the third section of the chapter.

Lastly, we have done a detailed review of the existing hardware prototypes of the wideband signal digitization and characterization techniques in the fourth section. It is shown that MWC is the only SNS technique that is successfully implemented and tested on the real-time wideband signal. Finally, we have explained the various universal software radio peripheral (USRP) hardware testbeds for signal characterization techniques. These testbeds comprise WSS hardware testbeds for cognitive radio and IoT networks, multi-antenna hardware testbeds for the direction of arrival estimation for WAS, and hardware prototypes for cyclostationary feature, cumulant and artificial neural network based AMCs. Although various hardware testbeds are developed to validate existing characterization algorithms, all these testbeds are validated on Nyquist sampled signal and hence, applicable for narrowband signals.

In the next chapter, we discuss the proposed MPMAB algorithms, which incorporate the feedback loss due to the characterization failure and their hardware validation on the developed USRP hardware testbed.

Chapter 3

MPMAB Algorithms for Non-Contiguous Channels Selection

The non-contiguous wideband signal digitization demands learning the channel (or frequency band) occupancy status as the selection of channels is not fixed and varies based on licensed user activity. Further, the identification of channel status (reconstruction) can fail when the number of non-vacant channels in a selected channel subset is higher than that of ADCs. This failure probability increases with the subset size. Whenever a failure occurs, the channel state is unknown. Thus the goal is to identify a subset with more vacant channels on average without a reconstruction failure for sparse wideband spectrum. The problem of learning the best subset is modelled as a Multi-Play Multi-Armed Bandit (MPMAB). This chapter focuses on developing subset learning and selection algorithms that balance the trade-off between the subset size and reconstruction failure for two different channel statistics: 1) Bernoulli distribution model and 2) Markov decision process. Later, we develop a USRP hardware

testbed to validate the efficacy of the proposed MPMAB algorithms on the real radio environment.

3.1 System Model: Bernoulli Distribution Model

Consider an ultra-wideband spectrum consisting of N non-overlapping channels (or frequency bands). The occupancy status of the channels is modelled as independent Bernoulli distribution as in [68–70,75,76]. Let $\boldsymbol{p}$ be a vector storing the vacancy probabilities of N channels and is unknown to the wideband signal analyzer (WSA). Let a set of channels be denoted by $[N] = \{1, 2, \ldots, N\}$. WSA is based on the FRI digitization approach with a fixed number of ADCs, K. In each time slot, WSA selects a subset of channels from the wideband spectrum, digitizes them and updates the channel occupancy estimates. Let β be a subset storing the indices of selected channels, and $|\beta|$ denotes its size. Let $\mathbf{s}$ be a $1 \times N$ binary vector storing the occupancy status of all N channels. If i^{th} channel is vacant, then $s(i) = 0$. Otherwise, $s(i) = 1$. Then, $\mathbf{s}_\beta \subset \mathbf{s}$ is a $1 \times |\beta|$ vector storing the occupancy status of all channels in β. We denote a power set containing all possible realizations of $\mathbf{s}_\beta$ as Q_β. Thus the number of elements in Q_β is $2^{|\beta|}$. As the occupancy status of channels is independent, the realization $\mathbf{s}_\beta$ occurs with probability $\mathbb{P}(\mathbf{s}_\beta) = \prod_{i \in \beta} ((1 - \mathbf{s}(i))\boldsymbol{p}(i) + \mathbf{s}(i)(1 - \boldsymbol{p}(i)))$.

The mean throughput (or reward) of a subset β is defined as the expected

number of vacant channels observed by WSA, given by

$$\mathcal{T}(\beta) = \sum_{\mathbf{s}_\beta \in \mathcal{Q}_\beta} \mathbb{P}(\zeta_{\mathbf{s}_\beta} = 0)\ ||1 - \mathbf{s}_\beta||_1 \tag{3.1}$$

where $||1 - \mathbf{s}_\beta||_1$ gives the number of vacant channels in β and $\mathbb{P}(\zeta_{\mathbf{s}_\beta} = 0)$ is probability successful reconstruction, i.e.,

$$\mathbb{P}(\zeta_{\mathbf{s}_\beta} = 0) = \begin{cases} 0, & \text{if } ||\mathbf{s}_\beta||_1 > K \\ \mathbb{P}(\mathbf{s}_\beta) & \text{otherwise.} \end{cases} \tag{3.2}$$

The aim of the WSA is to select a subset that maximizes the expected throughput, i.e., β^* expressed as

$$\beta^* = \arg\max_{\beta \subset [N]} \mathcal{T}(\beta). \tag{3.3}$$

The size of the optimal channel subset β^* can have any value between K and N. Learning the optimal subset β^* is a non-trivial task. When selected subset β is such that $|\beta| > K$, reconstruction failure could occur and no feedback (or throughput) is observed if the number of occupied channels in β is more than K, i.e., $||\mathbf{s}_\beta||_1 > K$. Hence, resulting in collection of no throughput i.e. loss of feedback. On the other hand, if the selected subset β is such that $|\beta| \leq K$, no reconstruction failure occurs and feedback is observed, but subsets of size K need not be optimal, resulting in the collection of lower throughput (i.e. the number of vacant channels in the sensed wideband spectrum).

An oracle with prior knowledge of $\boldsymbol{p}$ can compute the optimal value of β^*

using Eq. 3.3 and play it in each time slot to get the best possible throughput. Whereas a learner having no prior knowledge of spectrum statistics estimates $\boldsymbol{p}$ by repeated selection of the subsets. Let β_{t_s} denote the selected subset at time slot t_s. We compare the performance of the learner over P time slots in terms of the regret defined as follows:

$$\mathcal{R} = P\mathcal{T}(\beta^*) - \sum_{t_s=1}^{P} \mathcal{T}(\beta_{t_s}), \tag{3.4}$$

where the first term denotes the cumulative throughput/reward obtained from the oracle and the second term denotes the cumulative throughput/reward obtained by the learner. The goal of the learner is to minimize the expected regret, $\mathbb{E}[\mathcal{R}]$, where the expectation is with respect to randomness in the selection of β_{t_s} induced by the channel status observed. For simplicity of expressing the results, we assume that the spectrum statistics, $\boldsymbol{p}$, are arranged in the descending order of their probability of vacancy. This ordering is unknown to the learner.

Next, we discuss the proposed algorithms which offer better performance and compare their computational complexity. For the ease of exposure, first algorithm is where the learner selects subsets of size K in each time slot so that there is no feedback loss. Then the next algorithm selects subsets of a size larger than K and carefully handles the issue of feedback loss.

3.1.1 K-Subset Learning (K-SL) Algorithm

The proposed K-SL algorithm aims to identify the optimal subset among all subsets with the channel subset size fixed to K. Let a power-set of all possible subsets consisting of K channels be denoted by $\mathcal{S}$. Hence, the number of such subsets, $|\mathcal{S}|$, is given by

$$|\mathcal{S}| = C(N, K) = \frac{N!}{K!\,(N-K)!} \tag{3.5}$$

The K-SL algorithm is inspired by the multi play Thompson sampling (MP-TS) algorithm [70]. Its pseudo-code is given in Algorithm 1. In each time slot, the quality index, Q_c, of all the channels are calculated via Thompson Sampling based MAB approach, i.e. using the beta distribution $Beta(X_c(n), T_c(n))$ [71] (Algorithm 1: Line 2). Here $X_c(n)$ denotes the reward collected over the n^{th} channel till time slot t_s and $T_c(n)$ denotes the number of times n^{th} channel is selected for digitization till time slot t_s. Using X_c and T_c, the quality index, Q_s, of all subsets in $\mathcal{S}$ are calculated (Algorithm 1: Line 3). Then, the subset with the maximum value of Q_s is selected, and all the channels in the selected subset are digitized via FRI based approach. The selected subset is denoted by β. Next, an energy detector (ED) based sensing is used to estimate the status, $\mathbf{s}_\beta$, of channels present in β. The estimated status, $\hat{\mathbf{s}}_\beta$, is used to determine the number of vacant channels, V_β, in β, and is calculated as the l_1 norm of the complement of $\hat{\mathbf{s}}_\beta$. At the end of the time slot, parameters such as instantaneous throughput, $\mathcal{T}(t_s)$, X_c and T_c are updated.

Algorithm 1 K-SL Algorithm

Input: $P, N, [N], \mathcal{S}$
Initialize: $X_c = [1]_{1\times N}, T_c = [1]_{1\times N}$
Output: β (for digitization)

for $t_s = 1, 2, \cdots, P$ **do**
  Update $Q_c(n) \sim Beta(X_c(n), T_c(n)) \; \forall \; n \in [N]$
  Determine $Q_s(v) = \sum_{n\in\mathcal{S}(v)} Q_c(n) \; \forall \; v \in \{1, 2, \cdots, |\mathcal{S}|\}$
  Select a subset, β, of maximum value of Q_s
  Determine $\hat{\mathbf{s}}_\beta$, of β channels via ED
  Determine the number of vacant channels, $V_\beta = ||1 - \hat{\mathbf{s}}_\beta||_1$
  Store indices of vacant channels of β in β_v
  $\mathcal{T}(t_s) = V_\beta/N$ ▷ Instantaneous throughput
  $X_c(n) = X_c(n) + 1 \; \forall \; n \in \beta_v$
  $T_c(n) = T_c(n) + 1 \; \forall \; n \in \beta$
end for

3.1.1.1 Regret Analysis

Since no feedback loss occurs when subsets of size K are selected, K-SL is same as the MP-TS algorithm. Then the analysis in [70] yields the following result.

Theorem 1 *Under the bounded reward and error free sensing, the regret of K-SL is upper bounded as*

$$\mathbb{E}(\mathcal{R}(P)) \leq \mathcal{O}\left(\sum_{i\in[N]\setminus\beta^*} \frac{\Delta_{i,K}\log(P)}{d(p_i, p_K)}\right), \tag{3.6}$$

where $d(p_i, p_K) = p_i \log(p_i/p_K) + (1 - p_i)\log((1 - p_i)/(1 - p_K))$ is the KL divergence between the two Bernoulli distributions of mean p_i and p_K, $\Delta_{i,K} = p_K - p_i$ is the increase in regret when instead of K^{th} optimal channel, i^{th} sub-optimal channel is drawn, and p_i and p_K are the vacancy probability of i^{th} and K^{th} channel, respectively. The performance of K-SL is optimal as the above

upper bound matches with the lower bound for MPMAB in [72]. Hence, the $K - SL$ algorithm will converge at time, $t \to \inf$.

When the spectrum is sparse, restricting the channel subset size to K may not result in optimal throughput as the size of optimal β^*, i.e. $|\beta^*|$, could be larger than K. The Fig. 3.1 shows the regret comparison of K-SL for two instances: 1) When $|\beta^*| = K$ and 2) When $|\beta^*| > K$. The comparison is done for number of bands, $N = 8$, number of ADCs, $K = 4$, and number of times slots, $P = 5,00,000$.

In both cases, the oracle plays an optimal subset. As seen, the regret of the K-SL algorithm saturates when $|\beta^*|$ is K, thereby demonstrating the learnability of the optimal subset. For the second scenario, K-SL incurs linear regret as it restricts subset size to K while the optimal subset size is $K + 1$. On increasing the optimal subset size beyond $K + 1$, the slope of linear regret also increases. To exploit the sparsity of spectrum, we next allow a subset of size larger than K to be played in each time slot. However, in this case, feedback loss occurs, and one needs to use the available feedback efficiently to identify the optimal subset quickly.

3.1.2 K^+-Shared Subset Learning (K^+-SSL) Algorithm

K^+-Shared Subset Learning (K^+-SSL) is a variant of K-SL, where any subset of size K or higher can be selected in each time slot. Let $|\mathcal{S}|$ denotes the number

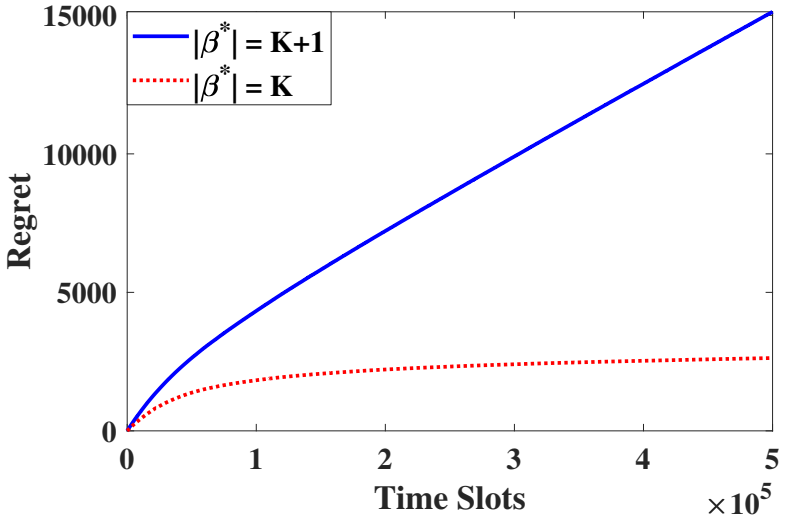

Figure 3.1: Regret plot of K-SL algorithm when $|\beta^*|$ is K (sub-linear regret) and $K+1$ (linear regret).

of such subsets and is given as

$$|\mathcal{S}| = 2^N - \sum_{k=0}^{K-1} C(N,k) \tag{3.7}$$

With respect to the K-SL algorithm, the K^+-SSL algorithm differs in calculating the subset quality index. Instead of individual channel quality index, the subset quality index is calculated via Thompson Sampling based MAB algorithm. Specifically, Q_s is calculated for all subsets in $\mathcal{S}$ via beta function i.e. $Beta(X_s(v), T_s(v))$, where $X_s(v)$ is the reward collected over the v^{th} subset when it was selected $T_s(v)$ number of times. Furthermore, subset parameters $X_s(v)$ and $T_s(v)$ are also updated whenever a subset containing common channels is selected for the digitization. The proposed K^+-SSL algorithm is given in Algorithm 2. It consists of the characterization stage (Line 2) to determine the appropriate subset followed by the update parameter stage to update the channel parameters of the selected subset (Lines 4-9) and subset parameters of the subsets having at least one common channel with the selected subset (Lines

11-26).

The characterization stage described using Subroutine 1 calculates the quality index, Q_s, for all $|\mathcal{S}|$ subsets, selects a subset having the highest Q_s and determines the status of the channels in the selected subset along with the number of occupied and vacant channels. Initially, each subset is selected once (Subroutine 1: Lines 1-2). After $|\mathcal{S}|$ number of time slots, the quality index of each subset is determined using Thompson Sampling based MAB (Subroutine 1: Line 4). Then, the subset with the highest value of Q_s is selected for digitization via FRI based approach. The selected subset is denoted by β, i.e. β stores the indices of channels present in the selected subset (Subroutine 1: Line 5). After digitization, the status, $\hat{\mathbf{s}}_\beta$, of selected channels is determined as follows:

$$\hat{\mathbf{s}}_\beta = \begin{cases} \text{ED} & |\beta| \leq K \\ \text{BMP} & \text{otherwise} \end{cases} \tag{3.8}$$

When $|\beta| \leq K$, the SNS sampled signal present in the occupied channels of β is reconstructed directly via inverse operation, and ED is applied to determine their status [73]. When $|\beta| > K$, spectrum reconstruction is formulated as a sparse signal recovery problem [77]. Since the spectrum statistics, $\hat{\boldsymbol{p}} = \frac{X_c}{T_c}$ is learnt, the Bayesian Matching Pursuit (BMP) algorithm [74] is applied for sparse signal recovery and determination of the channel status. In the end, the number of occupied channels, O_β, and the number of vacant channels, V_β, are calculated for β(Subroutine 1: Lines 8-9). After the characterization stage, the

Algorithm 2 K^+-SSL Algorithm

Initialize: X_s=$[1]_{1\times|\mathcal{S}|}$, T_s=$[1]_{1\times|\mathcal{S}|}$, X_c=$[1]_{1\times N}$, T_c=$[1]_{1\times N}$
Input: $P, K, N, \mathcal{S}$
Output: β (for digitization)

for $t_s = 1, 2, \cdots, P$ **do**
  $[\beta, \hat{\mathbf{s}}_\beta, O_\beta, V_\beta] =$ ***Characterization***$(t_s, X_s, T_s, \mathcal{S})$
  Form a set β_v containing vacant channels of β
  if $O_\beta \leq K$ **then** ▷ Reconstruction Success
    $\mathcal{T}(t_s) = V_\beta/N$ and $X_c(n) = X_c(n) + 1 \; \forall \; n \in \beta_v$
  else ▷ Reconstruction Failure
    $\mathcal{T}(t_s) = 0$
  end if
  $T_c(n) = T_c(n) + 1 \; \forall \; n \in \beta$
  for $i = 1 : |\mathcal{S}|$ **do** ▷ Update: Subset Parameters
    Update γ with common channels in β and $\mathcal{S}(i)$
    if $|\gamma| > 0$ **then**
      if $O_\beta \leq K$ **then** ▷ Reconstruction Success
        Determine $O_\gamma = ||\hat{\mathbf{s}}_\gamma||_1$ for γ subset
        Update a subset γ_c with $\{\mathcal{S}(i)\} - \{\gamma\}$ channels
        Find $\hat{\boldsymbol{p}}_{\gamma_c} = \frac{X_c(\gamma_c)}{T_c(\gamma_c)}$ of γ_c channels
        $O_{\gamma_c} =$ ***Shared_Occupancy***$(\gamma_c, \hat{\boldsymbol{p}}_{\gamma_c})$
        Calculate S via Eq. 3.12
        $X_s(i) = X_s(i) + S \cdot \mathbb{1}_{O_{\gamma_c} + O_\gamma \leq K}$, $T_s(i) = T_s(i) + 1$
      else ▷ Reconstruction Failure
        Find $\hat{\boldsymbol{p}}_s = \frac{X_c(\mathcal{S}(i))}{T_c(\mathcal{S}(i))}$ of $\mathcal{S}(i)$ channels
        $F =$ ***Shared_Failure***$(\mathcal{S}(i), \beta, \hat{\boldsymbol{p}}_s)$
        $T_s(i) = T_s(i) + F$
      end if
    end if
  end for
end for

Subroutine 1: Characterization

Input: $t_s, X_s, T_s, \mathcal{S}$
Output: $\beta, \hat{\mathbf{s}}_\beta, O_\beta, V_\beta$

if $t_s \leq |\mathcal{S}|$ **then**
  Select a subset, β, as $\mathcal{S}(t_s)$
else
  Update $Q_s(v) \sim Beta(X_s(v), T_s(v)) \; \forall \; v \in \{1, 2, \cdots, |\mathcal{S}|\}$
  Select a subset, β, having maximum value of Q_s
end if
Determine $\hat{\mathbf{s}}_\beta$ via Eq. 3.8
Determine the number of occupied channels, $O_\beta = ||\hat{\mathbf{s}}_\beta||_1$
Determine the number of vacant channels, $V_\beta = ||1 - \hat{\mathbf{s}}_\beta||_1$

selected subset's channel parameters are updated depending on reconstruction status (Algorithm 2: Lines 4-9).

Next, the parameters of subsets having common channels with the selected subset are updated (Algorithm 2: Lines 11-26). Let γ contains the indices of common channels between β and i^{th} subset, $\mathcal{S}(i)$. When $|\gamma|> 0$ and reconstruction of β channel subset is successful, then $X_s(i)$ and $T_s(i)$ of i^{th} subset of $\mathcal{S}$ are incremented by S and 1, respectively. On the other hand, when $|\gamma|> 0$ and reconstruction of β channels fails, only $T_s(i)$ is incremented by F.

To calculate parameter S for $\mathcal{S}(i)$, we find the number of occupied channels, O_γ, in γ and set of channels, γ_c, present in $\mathcal{S}(i)$ but not in γ. Using the learnt probability, $\hat{\boldsymbol{p}}_{\gamma_c}$, of γ_c channels, the estimate of the number of occupied channels, O_{γ_c}, in γ_c is calculated using Subroutine 2. To estimate O_{γ_c}, a power-set, $\mathcal{Q}_{\gamma_c}$, containing all possible status of γ_c channels is considered (subroutine 2: Line 1). A random variable, Y_{γ_c}, denoting the number of occupied channels in γ_c is generated. Thus, the possible values of Y_{γ_c} are $\{0, 1, .., |\gamma_c|\}$. Now, the probability mass function (PMF) of Y_{γ_c} is calculated as

$$\mathbb{P}(Y_{\gamma_c} = y) = PMF(y, \mathcal{Q}_{\gamma_c}, \hat{\boldsymbol{p}}_{\gamma_c}) = \sum_{\substack{\boldsymbol{q}\in\mathcal{Q}_{\gamma_c},\\ ||\boldsymbol{q}||_1=y}} \mathbb{P}(\boldsymbol{q}) \tag{3.9}$$

where $\mathbb{P}(\boldsymbol{q})$ is the probability of getting the status $\boldsymbol{q}$ for γ_c channels. Note that similar to $\boldsymbol{s}_\beta$, $\boldsymbol{q}$ is a binary vector storing the status of γ_c channels. Thus, $\mathbb{P}(\boldsymbol{q})$ is

calculated as

$$\mathbb{P}(\boldsymbol{q}) = \prod_{j=1}^{|\gamma_c|}(1-\boldsymbol{q}(j))\hat{\boldsymbol{p}}_{\gamma_c}(j) + \boldsymbol{q}(j)(1-\hat{\boldsymbol{p}}_{\gamma_c}(j)) \tag{3.10}$$

Based on the PMF, the probability regions are defined in Fig. 3.2. The Region y corresponds to the $\mathbb{P}(Y_{\gamma_c} = y)$ (i.e. the probability of y number of occupied channels in γ_c), and their decision boundaries are calculated as

$$\Delta_y = \sum_{k=0}^{y} \mathbb{P}(Y_{\gamma_c} = k) \tag{3.11}$$

The number of occupied channels, O_{γ_c}, in γ_c is y whenever a uniform random variable ρ lies in Region y. If $(O_\gamma + O_{\gamma_c}) \leq K$ (i.e. successful sensing) then the throughput, S, is calculated as

$$S = \frac{V_{\gamma_c} + V_\gamma}{N} \tag{3.12}$$

where $V_{\gamma_c} = |\gamma_c| - O_{\gamma_c}$ and $V_\gamma = |\gamma| - O_\gamma$ are the number of vacant channels in γ_c and γ.

The calculation of the parameter F is explained using Subroutine 3. When $\mathcal{S}(i)$ is the same as the selected subset β, then $F = 1$ indicating reconstruction

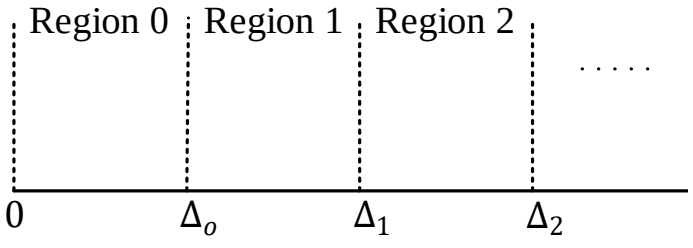

Figure 3.2: Probability region.

Subroutine 2: Shared_Occupancy

Input: γ_c,$\hat{\boldsymbol{p}}_{\gamma_c}$
Output: O_{γ_c}

1: Let $\mathcal{Q}_{\gamma_c}$ stores all possible status of γ_c channels
2: Let Y_{γ_c} be a random variable of values $\{0, 1, ..., |\gamma_c|\}$
3: Determine $\mathbb{P}(Y_{\gamma_c} = y) = PMF(y, \mathcal{Q}_{\gamma_c}, \hat{\boldsymbol{p}}_{\gamma_c}) \; \forall \; y \in \{0, 1, ..., |\gamma_c|\}$ as per Eq. 3.9
4: Generate ρ from uniform distribution of range $[0, 1]$
5: Define probability regions as per Eq. 3.11 and Fig. 3.2.
6: **if** ρ lies in Region y where $y \in \{0, 1, .., |\gamma_c|\}$ **then**
7: $\quad O_{\gamma_c} = y$
8: **end if**

failure. F is determined based on the learnt probability of vacancy, $\hat{\boldsymbol{p}}_s$, of $\mathcal{S}(i)$ subset channels for other subsets. Similar to Subroutine 2, a power-set, $\mathcal{Q}_s$, containing all possible status of $\mathcal{S}(i)$ channels and a random variable, Y_s, denoting the number of occupied channels in $\mathcal{S}(i)$ are defined. The possible values of Y_s are $\{0, 1, .., |\mathcal{S}(i)|\}$. Now, based on the $P(Y_s = y) = PMF(y, \mathcal{Q}_s, \hat{\boldsymbol{p}}_s)$, the Failure probability, f_p, is determined as

$$f_p = \sum_{y=K+1}^{|\mathcal{S}(i)|} \mathbb{P}(Y_s = y) \tag{3.13}$$

If a random variable, ρ, generated from the uniform random distribution is lower than f_p, then $F = 1$, otherwise $F = 0$.

As N increases, the number of subsets increased exponentially, resulting in a significant rise in exploration time and poor regret performance, as demonstrated later in Section 3.1.4. From an architecture perspective, many subsets result in a significant increase in memory requirements since the parameters of each subset need to be stored separately. A subset elimination approach has been explored to gradually reduce the number of active subsets (Refer to Sec-

Subroutine 3: Shared_Failure

Input: $\mathcal{S}(i), \beta, \hat{\boldsymbol{p}}_s$

Output: F

if $\mathcal{S}(i)$ is same as β **then**
    $F = 1$
else
    Let $\mathcal{Q}_s$ stores all possible status of $\mathcal{S}(i)$ channels
    Let Y_s be a random variable of values $\{0, 1, ..., |\mathcal{S}(i)|\}$
    Determine $\mathbb{P}(Y_s = y) = PMF(y, \mathcal{Q}_s, \hat{\boldsymbol{p}}_s)\ \forall\ y \in \{0, 1, ..., |\mathcal{S}(i)|\}$ as per Eq. 3.9
    Determine failure probability, f_p, as per Eq. 3.13
    Generate ρ from uniform distribution of range $[0, 1]$
    if $\rho < f_p$ **then** ▷ Failure Estimation
        $F = 1$
    else
        $F = 0$
    end if
end if

tion 3.1.4 for more details). But from the computational complexity perspective, the subset learning approach incurs huge complexity due to quality index calculation and parameter update requirement for each subset in each time slot. To overcome these issues and develop a low complexity hardware-friendly algorithm for WSA, a novel approach to estimate the subset size has been proposed.

The analysis of MAB of multi play and combinatorial bandits cannot be adapted to K^+-SSL due to the feedback loss incurred. One needs to take into the impact of feedback loss carefully and how it affects the learning rate. The analysis of K^+-SSL algorithm has been left for future work, and its empirical performance is evaluated in Section 3.1.4.

3.1.3 K^+-SSL via Subset Size Estimation (K^+-SSLE)

The main idea behind K^+-SSLE is to decide the subset size at the beginning of each time slot and then, among the subsets of the chosen size, select the

one with the highest quality index. The optimum subset size, $|\beta^*|$, needs prior knowledge of channel statistics, and it is given as

$$|\beta^*| = \arg\max_{|\beta'| \geq K} \sum_{\mathbf{s}_{\beta'} \in \mathcal{Q}_\beta} \mathbb{P}(\zeta_{\mathbf{s}_{\beta'}} = 0) \, ||1 - \mathbf{s}_{\beta'}||_1 \tag{3.14}$$

where $\mathbb{P}(\zeta_{\mathbf{s}_\beta} = 0)$ is calculated as in Eq. 3.2. Once $|\beta^*|$ is calculated, the number of candidate subsets is reduced from $2^N - \sum_{k=0}^{K-1} C(N,k)$ to $\mathcal{S} = C(N, |\beta^*|)$. Furthermore, as discussed in the K-SL algorithm (Algorithm 1), the quality index of each subset is the normalized sum of the quality index of all the channels in that subset. Thus, the proposed approach reduces the number of quality index calculations per slot from $|\mathcal{S}|$ to at most N, resulting in huge savings in complexity and latency.

The challenge in the above approach is that the channel statistics, $\boldsymbol{p}$, are unknown. To learn the channel statistics accurately, the pure exploration phase is introduced where the subsets of size K are sequentially chosen as follows:

$$\beta = \{(i-1)K + 1, (i-1)K + 2, \cdots, \min\{iK, N\}\} \tag{3.15}$$

where i is reset to 1 whenever $min\{iK, N\} = N$. Since the subset size is the same as the number of ADCs, there is no reconstruction failure, and hence, channel feedback is guaranteed. As shown in Theorem 2, the duration of the exploration phase, W, is selected such that it guarantees μ-correct estimation of $\boldsymbol{p}$ with δ probability and it is given by, $W = \frac{2}{\mu^2} \ln\left(\frac{2N}{\delta}\right)$ time slots, where μ is a lower bound on the smallest optimally gap.

Theorem 2 *: If the minimum gap between p_m and p_n is $\mu, \forall m, n \in \{1, .., N\}$ and $m \neq n$, then the exploration time slots, $W \geq \frac{4}{\mu^2}\left\lceil \frac{N}{K} \right\rceil \ln\left(\frac{2N}{\delta}\right)$ to achieve $\mu-$correct estimation with a probability of at least $1-\delta$.*

Proof: *Let J be an event denoting each band has been observed minimum Q times. Then we can upper bound the probability of no $\mu-$correct estimation given the event J as*

$$\mathbb{P}\left(\textit{No } \mu - \textit{ correct estimation} | J\right) < \delta \tag{3.16}$$

Mathematically, it can be represented as

$$\mathbb{P}\left(\exists\, n \in \{1 \cdots N\}\ s.t.\ |\hat{p}_n - pn| > \frac{\mu}{2} \mid J\right)$$

$$\leq \sum_{n=1}^{N} \mathbb{P}\left(|\hat{p}_n - p_n| > \frac{\mu}{2} \mid J\right) \qquad \text{(By Union Bound)}$$

$$= \sum_{n=1}^{N} \sum_{q=Q}^{\infty} \mathbb{P}\left(|\hat{p}_n - p_n| > \frac{\mu}{2}\right) \mathbb{P}\left(q \textit{ observations} | q \geq Q\right) \tag{3.17}$$

$$\leq \sum_{n=1}^{N} 2\exp\left(\frac{-Q\mu^2}{2}\right) \sum_{q=Q}^{\infty} \mathbb{P}\left(q \textit{ observations} | q \geq Q\right)$$

(By Hoeffding's inequality)

$$\leq 2N \exp\left(\frac{-Q\mu^2}{2}\right) \tag{3.18}$$

From Eq. 3.16, the above equation can be written as

$$2N \exp\left(\frac{-Q\mu^2}{2}\right) < \delta \implies Q > \frac{2}{\mu^2} \ln\left(\frac{2N}{\delta}\right) \tag{3.19}$$

Since $\mathbb{P}$(*No* $\mu-$*correct estimation*$|J) < \delta$ *implies* $\mathbb{P}(\mu-$*correct estimation*$|J) \geq 1-\delta$, *therefore* Q *should be greater than* $\frac{2}{\mu^2}\ln\left(\frac{2N}{\delta}\right)$ *for* $\mu-$*correct estimation. As in every* $2\left\lceil\frac{N}{K}\right\rceil$ *time slots, only one observation of each frequency band is obtained. Thus the number of time slots required to obtain* Q *observations of all bands (i.e.* $\mu-$*correct estimation),* $W \geq 2Q\left\lceil\frac{N}{K}\right\rceil$.

Once all channels are sampled W times, the subset size is calculated via Eq. 3.14, by using the learnt statistics. Then we update the power-set, $\mathcal{S}$, with the subsets of size $|\beta|$. Next, the quality index, Q_c, of every channel is calculated via the beta function i.e. $Beta(X_c(n), T_c(n))$. Then the quality index, Q_s, of all subsets of $\mathcal{S}$ is determined (Algorithm 3, line 9). Finally, the subset having the highest quality index is selected for sensing. Similar to Algorithm 2, K^+-SSLE determines the status, $\mathbf{s}_\beta$, as shown in Eq. 3.8, and similar to Algorithm 1, it determines the number of vacant bands, V_β, and updates the instantaneous throughput, $\mathcal{T}(t_s), X_c$ and T_c.

3.1.4 Simulation Results: Bernoulli Distribution Model

The performance metrics used for the comparison are Reward/throughput, $\mathcal{T}$, and regret, $\mathcal{R}$, collected over the entire time horizon, P. An illustrative comparison of the proposed algorithms is shown in Table 7.1. In addition to the

Algorithm 3 K^+-SSLE Algorithm

Initialize: X_c=$[1]_{1\times N}$, T_c=$[1]_{1\times N}$
Input: $P, W, K, N, \mathcal{S}, [N]$
Output: β (for digitization)

for $t_s = 1, 2, \cdots, P$ **do**
  if $t_s < \lceil N/K \rceil * W$ **then**
    $|\beta| = K$ ▷ Exploration phase
    Select a subset, β, via Eq. 3.15
  else
    Determine the subset size, $|\beta|$, via Eq. 3.14 and $\hat{\boldsymbol{p}}$
    Update the power-set, $\mathcal{S}$, with subsets of size $|\beta|$
    Update $Q_c(n) \sim Beta(X_c(n), T_c(n)) \; \forall \; n \in [N]$
    Determine $Q_s(v) = \sum_{n \in \mathcal{S}(v)} Q_c(n) \; \forall \; v \in \{1, 2, \cdots, |\mathcal{S}|\}$
    Select a subset, β, of maximum value of Q_s
  end if
  Determine the status, $\hat{\mathbf{s}}_\beta$, via Eq. 3.8
  Determine number of occupied channels, $O_\beta = ||\hat{\mathbf{s}}_\beta||_1$
  Determine number of vacant channels, $V_\beta = ||1 - \hat{\mathbf{s}}_\beta||_1$ and store their indices in β_v
  if $O_\beta \leq K$ **then** ▷ Reconstruction Success
    $\mathcal{T}(t_s) = V_\beta / N$ and $X_c(n) = X_c(n) + 1 \; \forall \; n \in \beta_v$
  else ▷ Reconstruction Failure
    $\mathcal{T}(t_s) = 0$
  end if
  $T_c(n) = T_c(n) + 1 \; \forall \; n \in \beta$
end for

proposed K-SL, K^+-SSL and K^+-SSLE algorithms, two other algorithms are also considered: 1) K^+-SL and 2) K^+-RSSL. K^+-SL is an extension of K-SL with subset sizes ranging from K to N, and does not include shared subset learning. Whereas K^+-RSSL is an extension of K^+-SSL where the number of active subsets is reduced dynamically over time using the Eliminate subroutine given in Subroutine 4. The first step is to determine the mean reward of all subsets, $\mathbb{P}(\mathcal{S}) = X_s/T_s$. Then, the size of power-set, $\mathcal{S}$, is reduced by eliminating half of the subsets having the lowest $\mathbb{P}(\mathcal{S})$. In the end, parameters X_s, T_s and $[N]$ are updated. We consider the following parameters for comparison:

- **Subset Size** ($|\beta|$): All algorithms except $K-$SL explore subsets of size

Table 3.1: Comparison of various subset learning algorithms.

Parameters	**K-SL**	K^+**-SL**	K^+**-SSL**	K^+**-RSSL**	K^+**-SSLE**
Subset Size, $\lvert\beta\rvert$	K	$K \leq \lvert\beta\rvert \leq N$	$K \leq \lvert\beta\rvert \leq N$	$K \leq \lvert\beta\rvert \leq N$	$K \leq \lvert\beta\rvert \leq N$
No. of Subsets, $\lvert\mathcal{S}\rvert$	$C(N,k)$	$2^N - \sum_{k=0}^{K-1} C(N,k)$	$2^N - \sum_{k=0}^{K-1} C(N,k)$ after W time slots	• $2^N - \sum_{k=0}^{K-1} C(N,k)$ • Reduces by 50%	• Depends on $\lvert\beta\rvert$, Eq 3.14
$\lvert\beta\rvert$ **Estimation**	No	No	No	No	Yes
No. of Subset updates in each slot	One i.e. β subset	One i.e β subset	All	All	One i.e β subset
Complexity	Lowest	High	Highest	High	Low

ranging from K to N compared to the fixed subset size of K in $K-$SL.

- **Number of Subsets,** $|\mathcal{S}|$**, and** $|\beta|$ **Estimation**: K^+-SL, K^+-SSL and K^+-RSSL explore the maximum number of subsets and hence, need large exploration time compared to K^+-SSLE, which minimizes the exploration time via a novel subset size estimation approach.

- **Number of Subset Updates:** K^+-SSL and K^+-RSSL algorithms need to update the parameters of multiple subsets in each time slot. This makes them computationally complex. With an increase in N, the number of subsets increases substantially, leading to a significant increase in the complexity of K^+-SL, K^+-SSL and K^+-RSSL compared to the K^+-SSLE algorithm.

First we present the simulation results comparing the regret performance of the proposed algorithms. We consider the four cases:

Case 1: $N = 8,\ K = 2,\ \boldsymbol{p} = [0.6\ \ 0.65\ \ 0.7\ \ 0.75\ \ 0.8\ \ 0.85\ \ 0.9\ \ 0.95]$

Case 2: $N = 8,\ K = 4,\ \boldsymbol{p} = [0.6\ \ 0.65\ \ 0.7\ \ 0.75\ \ 0.8\ \ 0.85\ \ 0.9\ \ 0.95]$

Subroutine 4: Eliminate

Input: $\mathcal{S}, [N], X_s, T_s$

Output: $\mathcal{S}, [N], X_s, T_s$

1: Determine $\mathbb{P}(\mathcal{S}) = X_s/T_s$
2: Update I with indices of $\left\lceil \frac{|\mathcal{S}|}{2} \right\rceil$ maximum values of $\mathbb{P}(\mathcal{S})$
3: Update $\mathcal{S} = \mathcal{S}(I)$
4: Update $X_s = X_s(I)$
5: Update $T_s = T_s(I)$
6: $[N]$ = channels present in $\mathcal{S}$

Case 3: $N = 12,\ K = 2,\ \boldsymbol{p} = [0.4\ \ 0.45\ \ 0.5\ \ 0.55\ \ 0.6\ \ 0.65\ \ 0.7\ \ 0.75\ \ 0.8\ \ 0.85\ \ 0.9\ \ 0.95]$

Case 4: $N = 12,\ K = 4,\ \boldsymbol{p} = [0.4\ \ 0.45\ \ 0.5\ \ 0.55\ \ 0.6\ \ 0.65\ \ 0.7\ \ 0.75\ \ 0.8\ \ 0.85\ \ 0.9\ \ 0.95]$

The regret comparison for Case 1 to Case 4 is shown in Fig. 3.3. These results are averaged over ten experiments, and each experiment consists of $P = 1,00,000$-time slots. As expected, K-SL offers poor performance since optimal $|\beta| > K$ in all cases. Furthermore, K^+-SL offers sub-linear regret in Case 1 and Case 2, indicating the identification of the optimal subset, but its performance degrades for Case 3 and Case 4. As discussed in Section 3.1.2, this happens because the number of subsets grows from 503 to 4083 when N increases from 8 to 12 with $K = 2$. Thus, resulting in a large exploration time. Due to the proposed shared subset learning, K^+-SSL, K^+-RSSL, and K^+-SSLE outperform conventional subset learning approaches.

Among K^+-SSL and K^+-RSSL, the regret of the latter algorithm is slightly better than the former due to the subset elimination approach resulting in further savings in exploration time. The performance of the K^+-SSLE improves with

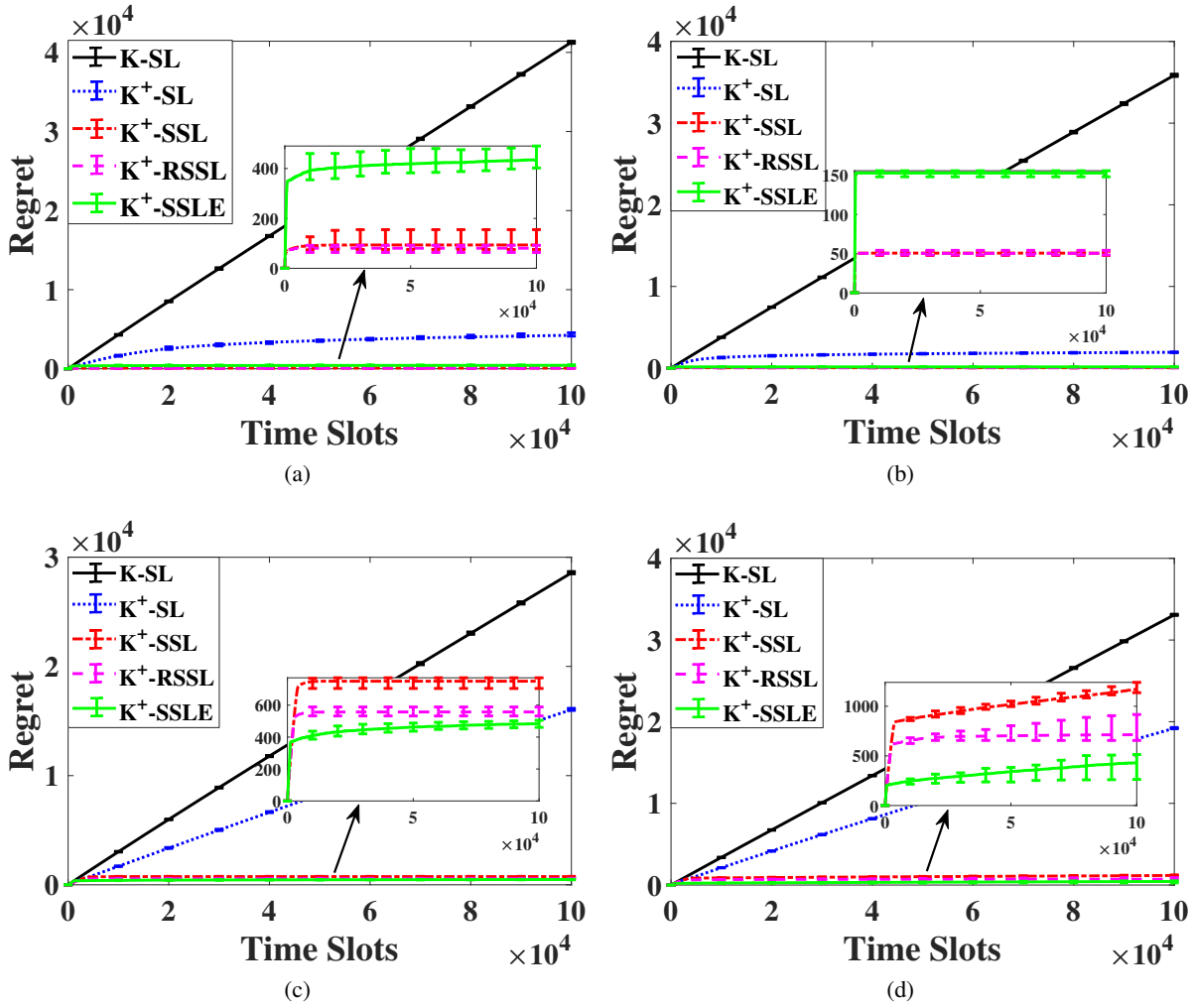

Figure 3.3: Regret analysis of K-SL, K^+-SL, K^+-SSL, K^+-RSSL and K^+-SSLE for a) Case 1 (i.e. $N = 8$, $K = 2$) (b) Case 2 (i.e. $N = 8$, $K = 4$) (c) Case 3 (i.e. $N = 12$, $K = 2$) and (d) Case 4 (i.e. $N = 12$, $K = 4$).

an increase in N due to the novel subset size estimation approach. Due to the initial exploration phase, K^+-SSLE regret is higher when N is small. In practice, N is expected to be greater than 10 for WSA deployed in ultra-wideband spectrum. Next, the above simulations are repeated for four cases with randomly chosen spectrum statistics, $\boldsymbol{p}$ in each experiment. All the results are averaged over 100 experiments, and the average regret is shown in Fig. 3.4. The results are similar to Fig. 3.3, validating the performance of the proposed algorithms in a wide variety of spectrum environments.

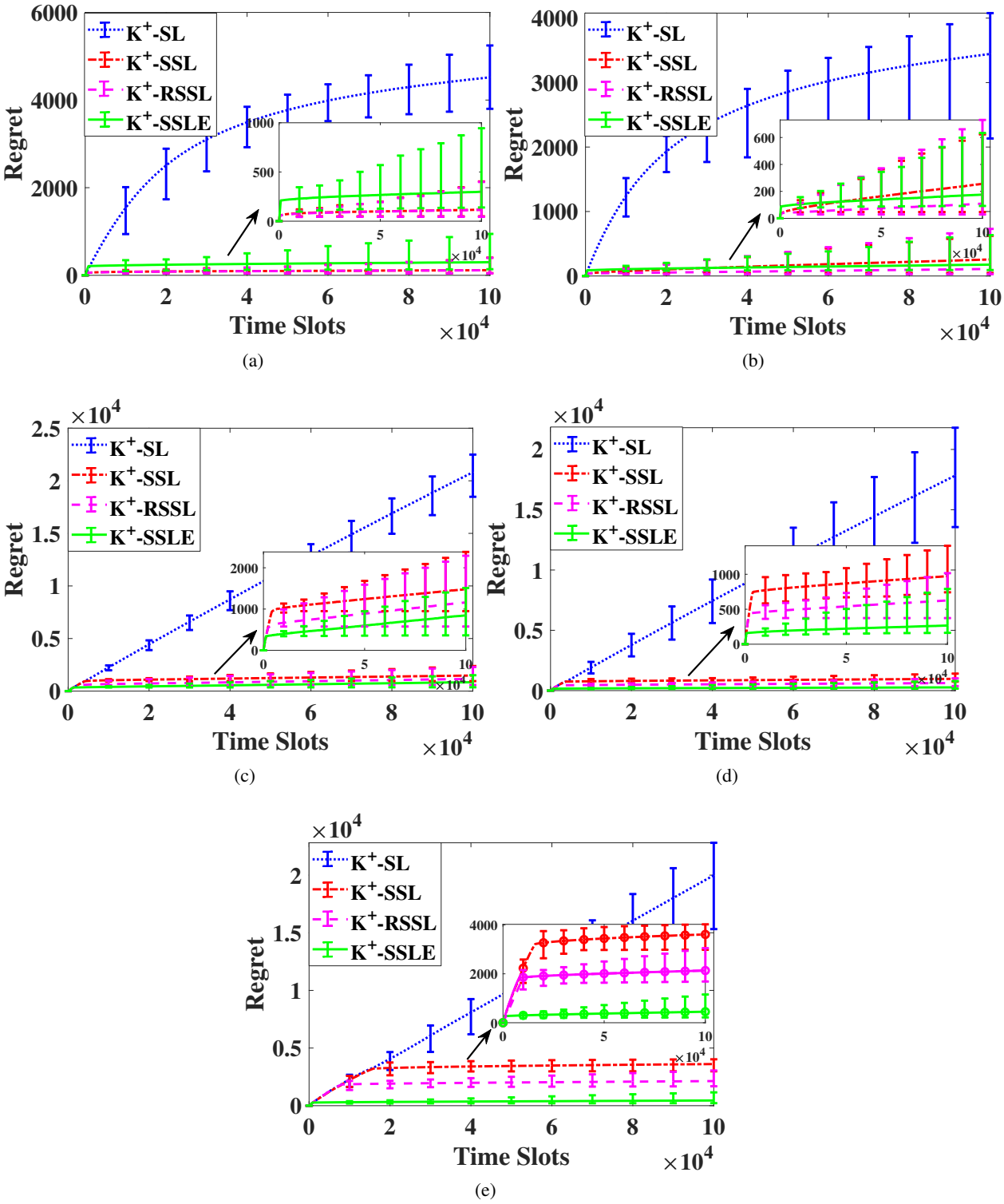

Figure 3.4: Regret of random values of $\boldsymbol{p}$ for (a) $N = 8$ and $K = 2$, (b) $N = 8$ and $K = 4$ (c) $N = 12$ and $K = 2$, (d) $N = 12$ and $K = 4$ and (e) $N = 14$ and $K = 4$.

The final throughput achieved at the end of the horizon for a different number of channels, N, and ADCs, K, is shown in Fig. 3.5(a) and (b), respectively. As

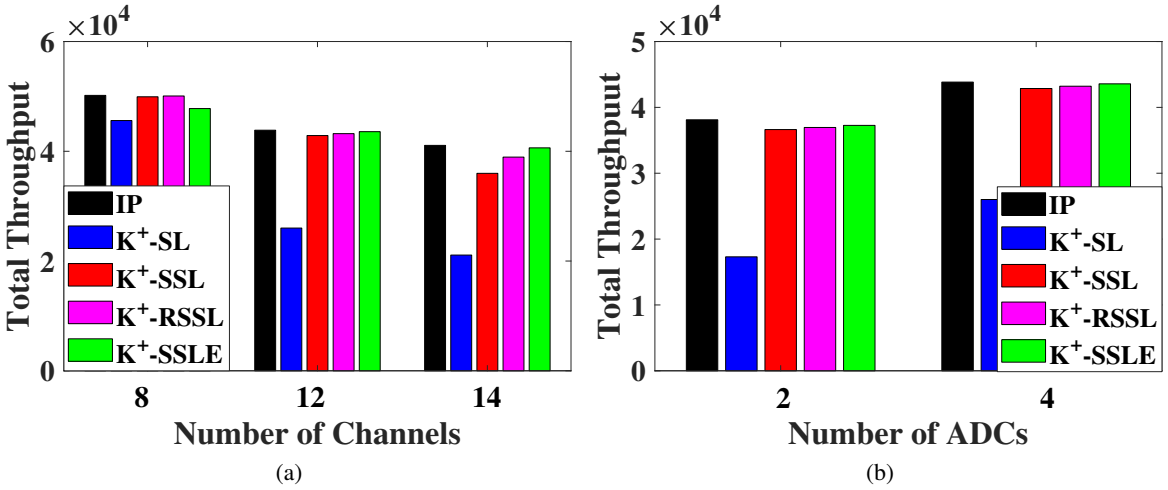

Figure 3.5: Total throughput achieved for different values of (a) channels, N and (b) ADCs, K.

expected, ideal policy (IP) achieves the highest throughput due to prior knowledge of channel statistics and hence, there is no loss due to exploration. Among the algorithms, the throughput of the K^+-SSLE is highest due to the subset size estimation, and hence, it incurs lower regret. Due to the fewer subsets, K^+-RSSL offers higher throughput than the K^+-SSL algorithm. K^+-SL achieves the lowest throughput due to the large number of subsets, which in turn needs long exploration. Furthermore, it can be observed that the throughput of all algorithms increases with an increase in K. Whereas, it decreases with the increase in N. It happens because the number of reconstruction failures increases with N, which further leads to a decrease in the throughput of all algorithms, including IP. Furthermore, the throughput increases with K, because the size of β, i.e. $|\beta|$ increases with K. This allows sensing of a higher number of channels, leading to an increase in throughput.

In Table 3.2, the number of reconstruction failures is compared, i.e. number of time slots out of 10^4 slots during which digitization fails. Hence, WSA cannot

Table 3.2: Comparison of number of reconstruction failures.

Spectrum Statistics	**K-SL**	K^+**-SL**	K^+**-SSL**	K^+**-RSSL**	K^+**-SSLE**
Case 1	0	14120	14200	16370	13960
Case 2	0	1215	1311	1311	1315
Case 3	0	30040	14650	14390	14050
Case 4	0	4090	9765	9638	9113

find spectrum opportunities for potential users. As expected, K-SL algorithm does not incur reconstruction failure, but its regret is high. Also, in Case 4, due to the selection of the lower number of channels than the optimal subset size, K^+-SL faces a lesser number of reconstruction failures but incurs high regret. The K^+-SSLE algorithm incurs the lowest number of reconstruction failures and lower regret (for large N), indicating accurate learning of channel statistics and subset size.

3.2 System Model: Markovian Decision Process

The signal model considered in this section is similar to the signal model discussed in Section 3.1, except each channel follows an independent stationary Markovian channel statistics. Thus, the channel statistics of n^{th} channel is based on the transition probability, $p_{u,v}(n) = \mathbb{P}(s_n(t_s) = v | s_n(t_s - 1) = u)$ where $u, v \in \{0, 1\}$ are the vacant and occupied states of the channel. Hence,

the instantaneous probability of vacancy, $\boldsymbol{\omega}$, at t_s^{th} time slot is defined as

$$\omega_{t_s+1}(n) = \begin{cases} \hat{p}_{10}(n), & \text{if } n \in \beta, \hat{s}_n(t_s) = 1, \zeta_{\mathbf{s}_\beta} = 0 \\ \hat{p}_{00}(n), & \text{if } n \in \beta, \hat{s}_n(t_s) = 0, \zeta_{\mathbf{s}_\beta} = 0 \\ \phi_{t_s+1}(n), & \text{if } n \notin \beta \text{ or } \zeta_{\mathbf{s}_\beta} = 1 \end{cases} \tag{3.20}$$

where $\omega_{t_s+1}(n)$ is the updated instantaneous probability of n^{th} channel, $\phi_{t_s+1}(n) = (1 - \omega_{t_s}(n))\hat{p}_{10}(n) + \omega_{t_s}(n)\hat{p}_{00}(n)$ and $\hat{p}_{uv}(n)$ is the estimated transition probability. In the next section, two algorithms, which are the extension of K^+-SSLE, have been proposed for Markovian statistics.

3.2.1 K^+- ϵ SSLE

As shown in Algorithm 4, the K^+- ϵ SSLE algorithm consists of two phases: 1) Exploration phase to learn the spectrum statistics of all N channels and 2) Exploitation phase to exploit $|\beta|$ best channels. The algorithm explores channels with the probability ϵ and exploits with the probability $(1 - \epsilon)$ as shown in Algorithm 4 (line 3), where the value of ϵ is calculated as

$$\epsilon = 1 - \min\left\{1, \frac{t}{\mathcal{M}}\right\} \tag{3.21}$$

where $\mathcal{M} < P$. The higher the value of P, the higher is the number of times each band is explored. The value of $\mathcal{M}$ depends on the minimum gap between statistics of any two channels and is chosen empirically.

Similar to K^+-SSLE, the exploration phase is executed till all the channels

are sensed W times, i.e. till $T_c(n) < W \; \forall \; n \in [N]$. In the exploration phase (line 3-12), the K^+- ϵ SSLE algorithm learns the transition probability, p_{uv}, by sequentially selecting K bands for two consecutive time slots. As shown in the Subroutine 5 (Markov_Characterizaton), by choosing the same channels in the consecutive time slots (i.e. $iter = 2$), the characterization phase learns the transition probability. It first estimates the status, $\hat{\mathbf{s}}_\beta$ via Eq. 3.8. After determining $\hat{\mathbf{s}}_\beta$ for two consecutive time slots, the transition counters, $C^n_{u,v}$, which keep the count of u to v state transition are updated for every $n \in \{1, 2, ..., N\}$ channels. Based on $C^n_{u,v}$, the transition probability, $\hat{p}_{u,v}(n)$, and the immediate probability of vacancy, $\boldsymbol{\omega}$, are updated as shown in the Eq. 3.22 and 3.20, respectively.

$$\hat{p}_{u,v}(n) = \frac{C^n_{u,v}}{C^n_{u,v} + C^n_{u,u}} \tag{3.22}$$

The exploitation phase (line 14-19) is executed either with a probability of $1 - \epsilon$ or when $T_c(n) > W$. Based on the learnt statistics, $\hat{\boldsymbol{p}}_{uv}$, the optimum subset size, $|\beta|$ is determined as (line 14, Algorithm 4)

$$|\beta| = \underset{|\beta'| \geq K}{\arg\max} \sum_{\mathbf{s}_{\beta'} \in \mathcal{Q}_\beta} \mathbb{P}(\zeta_{\mathbf{s}_{\beta'}} = 0) \; ||1 - \hat{\mathbf{s}}_{\beta'}||_1 \tag{3.23}$$

where the probability of successful reconstruction is determined as discussed in Eq. 3.2 and the probability of occurrence of $\mathbf{s}_\beta$ is updated with the instantaneous

Algorithm 4 K^{+}-ϵ SSLE algorithm

Initialize: $X_c = [1]_{1\times N}$, T_c=$[1]_{1\times N}$, $\boldsymbol{\omega} = [0.5]_{1\times N}$, $C_{uv} = [1]_{1\times N}$, $\hat{\mathbf{p}}_{uv} = [0.5]_{1\times N}\ \forall\ u, v \in \{0, 1\}$ and $i = 1$

Input: $P, W, K, N, \mathcal{S}, [N]$

Output: β (for digitization)

for $t_s = 1 \ldots P$ **do**
  Set ϵ as per Eq. 3.21
  if (rand $< \epsilon$ and $T_c(n) \leq W\ \forall\ n \in [N]$) **then** ▷ Explore
    Set $|\beta| = K$
    Select a subset, β, via Eq. 3.15 and set $iter = 2$
    $[X_c, T_c, \mathcal{T}(t_s), \hat{\mathbf{s}}_\beta] =$ ***Markov_Characterization***$(\beta, X_c, T_c, N, K, iter)$
    Update C_{uv}, $\hat{\mathbf{p}}_{uv}$ and $\boldsymbol{\omega}_{t_s}$ via Eq. 3.22 and 3.20
    if $i < \lceil \frac{N}{K} \rceil$ **then**
      Set $i = i + 1$
    else
      Set $i = 1$
    end if
  else ▷ Exploit
    Determine the subset size, $|\beta|$, via Eq. 3.23 and $\boldsymbol{\omega}_{t_s}$
    Update the power-set, $\mathcal{S}$, with subsets of size $|\beta|$
    Update $Q_c(n)$ via Eq. 3.25
    Determine $Q_s(v) = \sum_{n\in\mathcal{S}(v)} Q_c(n)\ \forall\ v \in \{1, 2, \cdots, |\mathcal{S}|\}$
    Select a subset, β, of maximum value of Q_s and set $iter = 1$
    $[X_c, T_c, \mathcal{T}(t_s), \hat{\mathbf{s}}_\beta] =$ ***Markov_Characterization***$(\beta, X_c, T_c, N, K, iter)$
  end if
end for

Subroutine 5: Markov_Characterization

Initialize: $\hat{\mathbf{s}}_\beta = NULL$ and $\mathcal{T} = 0$

Input: $\beta, X_c, T_c, N, K, iter$

Output: $T_c, X_c, \mathcal{T}, \hat{\mathbf{s}}_\beta$

for $j = 1\ to\ iter$ **do**
  Perform SNS and determine the status, $\hat{\mathbf{s}}_\beta^j$ via Eq. 3.8
  Determine number of occupied channels, $O_\beta = ||\hat{\mathbf{s}}_\beta^j||_1$
  Determine number of vacant channels, $V_\beta = ||1 - \hat{\mathbf{s}}_\beta^j||_1$ and store their indices in β_v
  if $O_\beta \leq K$ **then** ▷ Reconstruction Success
    $\mathcal{T} = \mathcal{T} + V_\beta/N$ and $X_c(n) = X_c(n) + 1\ \forall\ n \in \beta_v$
  else ▷ Reconstruction Failure
    $\mathcal{T} = \mathcal{T}$
  end if
  $T_c(n) = T_c(n) + 1\ \forall\ n \in \beta$
  $\hat{\mathbf{s}}_\beta = [\hat{\mathbf{s}}_\beta; \hat{\mathbf{s}}_\beta^j]$
end for

probability of vacancy, $\boldsymbol{\omega}_{t_s}$ as

$$\mathbb{P}(\mathbf{s}_\beta) = \prod_{n\in\beta} ((1 - \mathbf{s}(n))\boldsymbol{\omega}_{t_s}(n) + \mathbf{s}(n)(1 - \boldsymbol{\omega}_{t_s}(n))) \tag{3.24}$$

Now, similar to K^+-SSLE, the power-set, $\mathcal{S}$, of possible subset is reduced to the subsets of size $|\beta|$ and the subset, β, is selected based on the updated value of Q_c and Q_s where the value of Q_c can be updated via upper confidence bound (UCB) as

$$Q_c(n) = \frac{X_c(n)}{T_c(n)} + \sqrt{\frac{\gamma_{ucb} \log(t_s)}{T_c(n)}} \tag{3.25}$$

where $X_c(n)$ denotes the reward collected over the n^{th} channel till time slot t_s and $T_c(n)$ denotes the number of times n^{th} channel is selected for digitization till time slot t_s and γ_{ucb} is the exploration coefficient. At the end, the reward/throughput, $\mathcal{T}$, is determined as shown in Subroutine 5.

3.2.2 K^+-BSSLE (K^+- Blind SSLE)

The previous learning algorithm suffers from three drawbacks: 1) All channels are selected uniformly in the exploration phase leading to the frequent selection of sub-optimal bands, 2) Need prior knowledge of the difference in statistics to determine the minimum duration of the exploration phase, and 3) When learning of transition probabilities is difficult, i.e. when bands do not switch states frequently, the duration of the exploration phase is significantly longer. The proposed K^+-BSSLE algorithm overcomes these drawbacks. The proposed algorithm is based on the observation that the transition probability based selection always offers higher throughput than the stationary probability based selection.

In the beginning, K^+-BSSLE sets $|\beta| = K$ and sequentially chooses all channels according to Eq. 3.15 (line 3) for once. Then similar to K^+-ϵ SSLE, K^+-

Algorithm 5 K^+-BSSLE

Initialize: $X_c = [1]_{1\times N}$, T_c=$[1]_{1\times N}$, $\boldsymbol{\omega} = [0.5]_{1\times N}$, $C_{uv} = [1]_{1\times N}$, $\hat{\mathbf{p}}_{uv} = [0.5]_{1\times N}$ $\forall\, u, v \in \{0, 1\}$
Input: $P, K, N, \mathcal{S}, [N]$
Output: β (for digitization)

1: **for** $t_s = 1 \ldots P$ **do**
2: **if** $t_s < \lceil N/K \rceil$ **then**
3: Set $|\beta| = K$
4: Select a subset, β, via Eq. 3.15 and set $iter = 2$
5: $[X_c, T_c, \mathcal{T}(t_s), \hat{\mathbf{s}}_\beta] =$ ***Markov_Characterization***$(\beta, X_c, T_c, N, K, iter)$
6: Update $C_{uv}, \hat{\mathbf{p}}_{uv}$ and $\boldsymbol{\omega}_{t_s}$ via Eq. 3.22 and 3.20
7: **else**
8: Update $Q_c(n)$ via Eq. 3.25
9: Update β_1 with best K channels as per Q_c
10: Update β_2 with best K channels as per $\boldsymbol{\omega}_{t_s}$
11: **if** $\beta_1 != \beta_2$ **then**
12: Set $|\beta| = K$
13: Select a subset, β, via Eq. 3.15 and set $iter = 2$.
14: **else**
15: Determine the subset size, $|\beta|$, via Eq. 3.23 and $\boldsymbol{\omega}_{t_s}$
16: Update the power-set, $\mathcal{S}$, with subsets of size $|\beta|$
17: Determine $Q_s(v) = \sum_{n\in\mathcal{S}(v)} Q_c(n)$ $\forall\, v \in \{1, 2, \cdots, |\mathcal{S}|\}$
18: Select a subset, β, of maximum value of Q_s and set $iter = 1$
19: **end if**
20: $[X_c, T_c, \mathcal{T}(t_s), \hat{\mathbf{s}}_\beta] =$ ***Markov_Characterization***$(\beta, X_c, T_c, N, K, iter)$
21: Update $C_{uv}, \hat{\mathbf{p}}_{uv}$ and $\boldsymbol{\omega}_{t_s}$ via Eq. 3.22 and 3.20
22: **end if**
23: **end for**

BSSLE uses Markov_Characterization subroutine to learn the transition channel statistics, $\boldsymbol{p}_{uv}$, and instantaneous vacancy probability (line-5 and 6).

After the initial phase, the algorithm can be in one of the two states: 1) State 1 (line 11): Learning is not accurate, and hence, $|\beta| = K$. This means, reconstruction is always successful, but throughput is not optimal. 2) State 2 (line 15): Learning is sufficiently accurate, and hence, $|\beta| \geq K$. In this case, reconstruction can fail, but optimal throughput may be achieved.

In each time slot, the algorithm identifies the state based on the parameters, β_1 (line 9) and β_2 (line 10). The parameter β_1 refers to the K best chan-

nels selected based on the highest value of channel quality index, $Q_c(n) \sim Beta(X_c(n), T_c(n)) \; \forall \; n \in [N]$. The parameter β_2 refers to the K best channels selected based on the highest value of the learned immediate vacancy probability, $\omega_{t_s}(n)$. When both parameters select identical channels, the algorithm switches to State 2. There it estimates $|\beta|$ via Eq. 3.23 (line 15) followed by the reduction in the size of power-set, $\mathcal{S}$ and then it selects the best subset having the highest value of subset quality index, Q_s. Otherwise, it goes to State 1 and hence, $|\beta| = K$. Then, $|\beta|$ channels are chosen based on the Q_c (line 16). The same process is repeated in each time slot.

3.2.3 Simulation Results: Markovian Decision Process

This section compares the performance analysis of the proposed K^+-ϵSSLE and K^+-BSSLE algorithms for Markovian channel distribution. The regret is calculated as the difference between the throughput achieved by the oracle policy, referred to as ideal policy (IP) and the proposed algorithms. To check the performance of stationary probability based channel subset selection under the Markovian channel model, the comparison is done with an ideal stationary (IS). IS assumes the prior knowledge of the stationary probability, i.e. probability of vacancy, $\boldsymbol{p}_v = \frac{\boldsymbol{p}_{10}}{\boldsymbol{p}_{01}+\boldsymbol{p}_{10}}$, and determines the subset size via Eq. 3.14 with $\mathbb{P}(\mathbf{s}_\beta)$ given as:

$$\mathbb{P}(\mathbf{s}_\beta) = \prod_{n \in \beta} ((1 - \mathbf{s}(n))\boldsymbol{p}_v(n) + \mathbf{s}(n)(1 - \boldsymbol{p}_v(n))) \tag{3.26}$$

The simulation results presented here are averaged over ten independent ex-

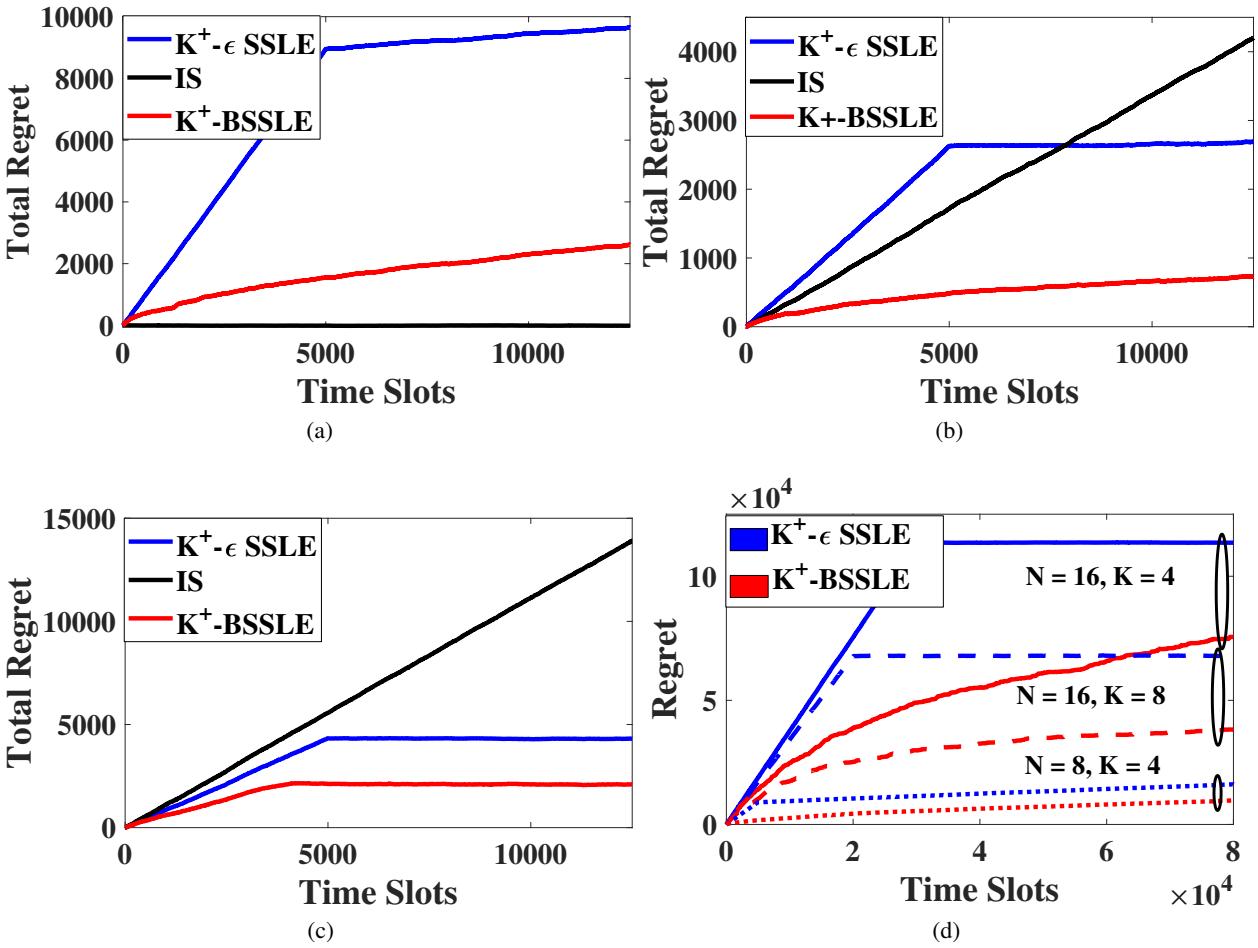

Figure 3.6: Comparison of total regret with respect to IP [63] at 20 dB SNR for (a) Case 1 (b) Case 2, (c) Case3 (d) Case 1 with different values of N and K.

periments and compared for different sets of spectrum statistics given as:

Case 1: $\mathbf{p}_{10} = [0.95\ 0.9\ 0.85\ 0.8\ 0.75\ 0.7\ 0.6\ 0.5]$,

$\mathbf{p}_{01} = [0.05\ 0.1\ 0.15\ 0.2\ 0.25\ 0.3\ 0.4\ 0.5]$

Case 2: $\mathbf{p}_{10} = [0.45\ 0.425\ 0.4\ 0.375\ 0.35\ 0.325\ 0.3\ 0.275]$,

$\mathbf{p}_{01} = [0.2\ 0.225\ 0.25\ 0.275\ 0.3\ 0.325\ 0.35\ 0.375]$

Case 3: $\mathbf{p}_{10} = [0.95\ 0.9\ 0.85\ 0.8\ 0.75\ 0.7\ 0.65\ 0.6]$,

$\mathbf{p}_{01} = [0.95\ 0.9\ 0.85\ 0.8\ 0.75\ 0.7\ 0.65\ 0.6]$

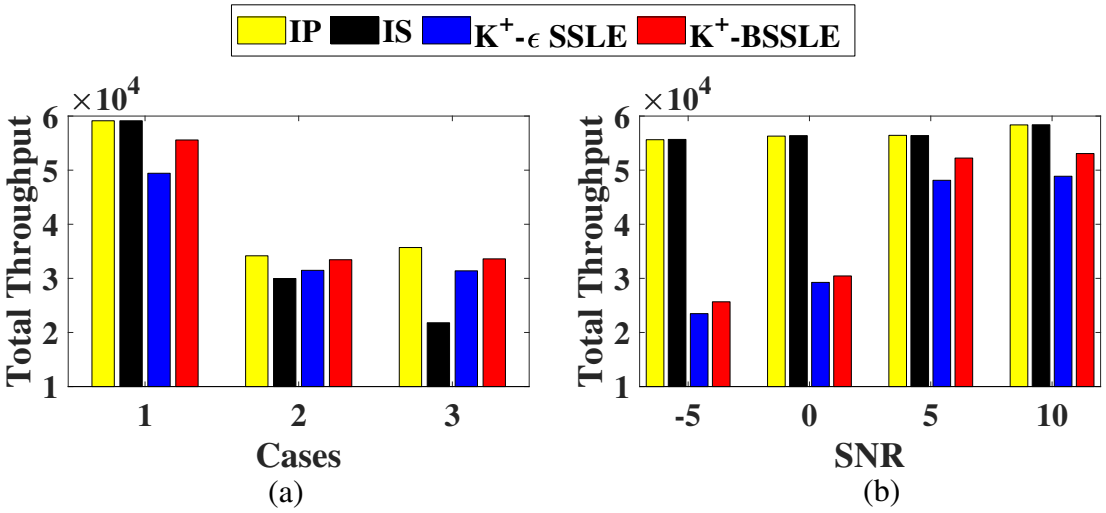

Figure 3.7: (a)Total throughput comparison for different cases and time horizon of 20,000 slots, and (b) Total throughput comparison for various values of SNRs with statistics in Case 1.

From the spectrum statistics, we can observe that Case 1 corresponds to the sparse spectrum whereas, Case 2 and Case 3 correspond to the non-sparse spectrum. However, Case 3 offers sparsity in the transition characteristics due to higher p_{01} and p_{10}. The regret comparison is shown in Fig. 3.6 and it can be observed that: 1) Positive regret indicates that the transition probability based selection in IP offers the highest throughput in all cases, 2) IS algorithm does not perform well in Case 2 and 3, i.e. when the spectrum is non-sparse, and thus, stationary probability based channel selection is not optimal, and 3) Proposed K^+-BSSLE offers lower regret (i.e. higher throughput) than K^+-ϵSSLE in all three cases. Next, the regret comparison is done for different values of N and K in Fig. 3.6(d). Since the learning time increases with an increase in N and decrease in K, the total regret of all three algorithms also increases with an increase in N and decrease in K. The K^+-BSSLE offers better performance with a larger N validating the efficacy of the proposed learning approach.

Since the throughput is an important parameter in wireless communications,

we compare the actual throughput of various algorithms for different cases in Fig. 3.7(a) and different SNRs in Fig. 3.7(b). As expected, the goverall throughput is highest in Case 1 due to the sparse spectrum. At low SNRs, the energy detector performs poorly, which leads to inaccurate learning and lower throughput for K^+-BSSLE and K^+-ϵSSLE. However, the performance improves with SNR. Nevertheless, in all cases, K^+-BSSLE offers better throughput than K^+-ϵSSLE.

3.3 Experimental Set-Up

A hardware testbed, as shown in Fig. 3.8, is developed to validate the effectiveness of the proposed learning and decision-making algorithms in the real radio signal. Two National Instruments (NI) based USRP-2922 with VERT900 antennas are used for the wireless transmission and reception of a multi-band signal. Baseband signal processing for both transmitter and receiver is performed using the LabView environment from NI. Since the Markovian channel model is more practical than the Bernoulli channel distribution, the validation is performed for K^+-ϵSSLE and K^+-BSSLE algorithms. Next, the transmitter model and receiver model are discussed in detail.

3.3.1 Transmitter Model

The task of the transmitter is to generate a multi-band signal such that each frequency band evolves as an independent Markovian chain followed by its transmission over the desired carrier frequency. As shown in Fig. 3.9, the transmitter

Figure 3.8: USRP testbed for validating the proposed learning and decision making algorithms.

consists of three blocks: 1) The first block configures the transmission parameters such as IQ sampling rate, carrier frequency, antenna gain and transmission port of USRP, 2) The second block generates the multi-band signal and 3) The third block continuously transmits the signal at the specified IQ sampling rate and the desired carrier frequency. An orthogonal frequency division multiplexing (OFDM) waveform has been used for the generation of multi-band signal. Sub-carriers of OFDM are divided into the desired number of frequency bands. For example, as shown in Fig. 3.10, for 1024-point OFDM signal, eight bands are formed by combining 112 sub-carriers in a band with two sub-carriers as a guard band. Depending upon the transition probability of each channel, either data or null is transmitted over the respective sub-carriers. To maintain synchronization between transmitter and receiver, the first frequency band switches between occupied and vacant states at every alternate time slot.

3.3.2 Receiver Model

The task of the receiver is to tune the analog front-end of the USRP to the desired carrier frequency and perform learning and subset selection for the non-

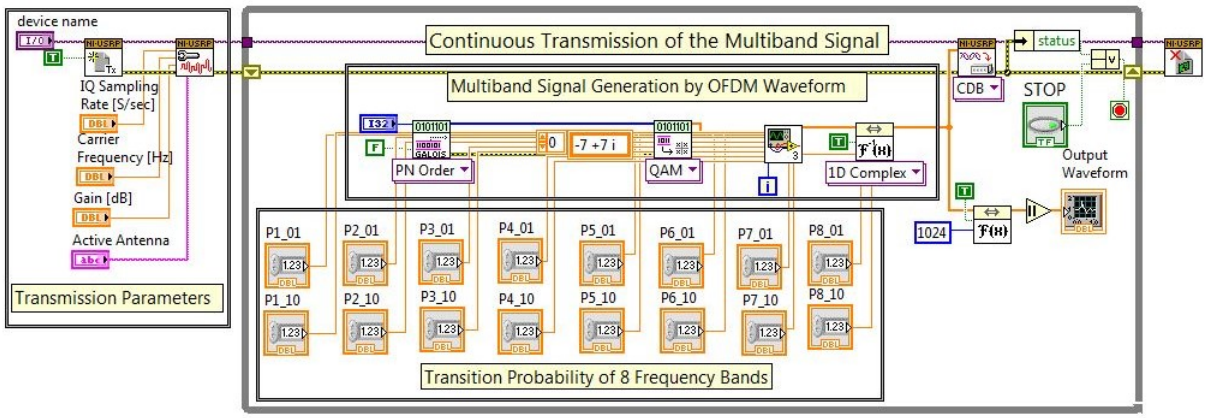

Figure 3.9: Block diagram of the transmitter model.

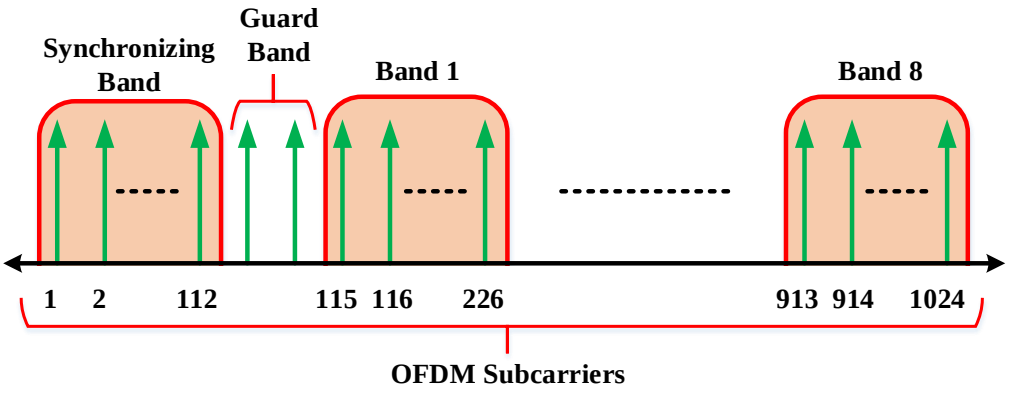

Figure 3.10: Multiband signal formation from OFDM waveform.

contiguous SNS. Similar to the transmitter, the receiver configures the receiver parameters like IQ sampling rate, reception frequency, antenna gain and reception port of the USRP, which aid in the continuous reception of the multi-band signal. As shown in Fig. 3.11, energy detection is performed on the first frequency band to achieve synchronization between the receiver and transmitter. Then as discussed in Section 3.2.1 and 3.2.2, the proposed K^{+}-ϵSSLE and K^{+}-BSSLE algorithms are implemented on the received synchronized signal to learn the spectrum statistics and select the best channel subset.

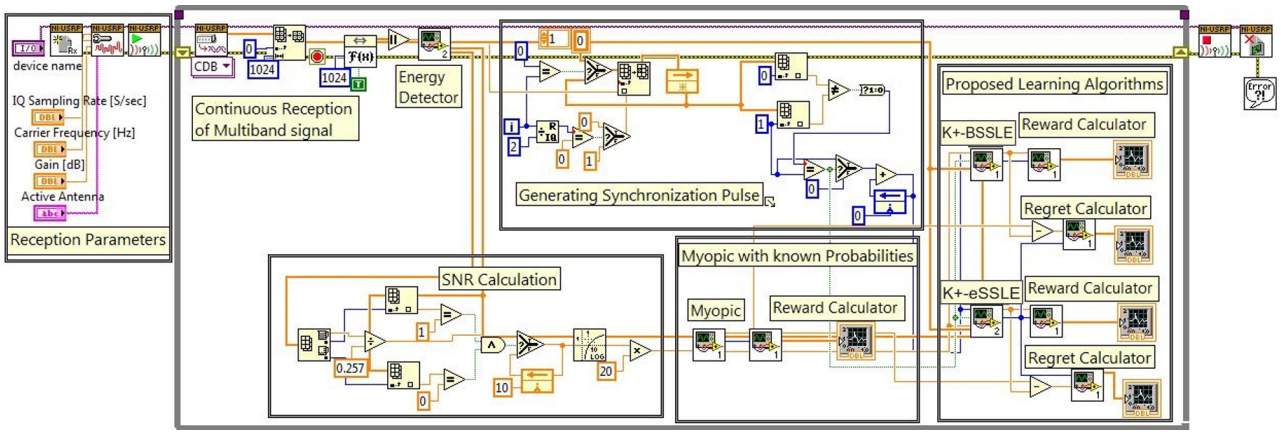

Figure 3.11: Block diagram of the receiver model.

3.3.3 Experimental Analysis

Performance comparison of the K^+-ϵSSLE and K^+-BSSLE algorithms in terms of the throughput and regret is shown in Fig. 3.12. The transmitter and receiver antenna gains are set to $0\ dB$ and $10\ dB$, respectively. Two spectrum statistics are considered for the analysis:

Case 1: $\mathbf{p}_{10} = [0.95\ \ 0.9\ \ 0.85\ \ 0.8\ \ 0.75\ \ 0.7\ \ 0.65\ \ 0.6]$

$\mathbf{p}_{01} = [0.05\ \ 0.1\ \ 0.15\ \ 0.2\ \ 0.25\ \ 0.3\ \ 0.35\ \ 0.4]$

Case 2: $\mathbf{p}_{10} = [0.95\ \ 0.9\ \ 0.85\ \ 0.8\ \ 0.75\ \ 0.7\ \ 0.65\ \ 0.6]$

$\mathbf{p}_{01} = [0.95\ \ 0.9\ \ 0.85\ \ 0.8\ \ 0.75\ \ 0.7\ \ 0.65\ \ 0.6]$

It can be observed from Fig. 3.12 that the throughput of IP is maximum, followed by those of K^+-BSSLE and K^+-ϵSSLE. This happens because IP has the prior knowledge of spectrum statistics, and thus it always selects the optimal subset size $|\beta^*|$ and optimal subset. Whereas K^+-BSSLE has a higher throughput than K^+-ϵSSLE, validating the simulation results presented in Sec-

tion 3.2.3. Similar observations can be verified from regret plots in Fig. 3.12 where instantaneous regret becomes zero (i.e. no increase in cumulative regret) after initial learning and accurate estimation of $|\beta|$. Zero instantaneous regret guarantees the convergence of the K^+-BSSLE and K^+-ϵSSLE to the IP, which is the desired requirement of the proposed algorithm. This also validates the functionality of the proposed algorithms in the real-radio environment compared to existing simulation-based analysis. Note that the throughput achieved by all the algorithms is higher for Case 1 than Case 2. It occurs because the spectrum in Case 1 is more sparse and hence offers higher transmission opportunities than Case 2. This is evident from the stationary probability of vacancy, $\boldsymbol{p}_v = \frac{\boldsymbol{p}_{10}}{\boldsymbol{p}_{10}+\boldsymbol{p}_{01}}$, which is higher in Case 1 than Case 2.

3.4 Summary

In this chapter, a novel channel subset selection algorithms, namely $K-$SL ($K-$Subset Learning), K^+-SSL (K^+-Shared Subset Learning), K^+-SSLE

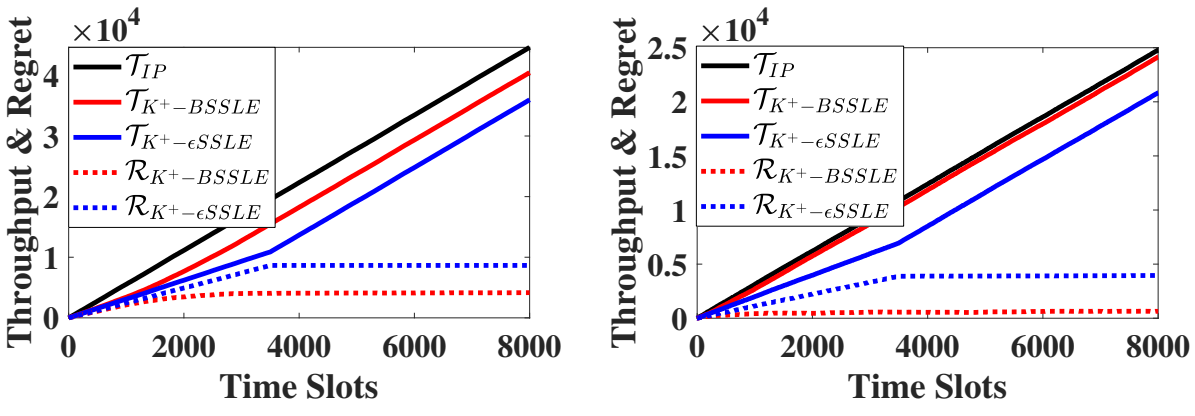

Figure 3.12: Throughput, $\mathcal{T}$ and Regret, $\mathcal{R}$ achieved by the proposed $K^+ - \epsilon$SSLE and K^+-BSSLE for (a) Case 1, and (b) Case 2.

(K^+-SSL with subset size estimation) for the Bernoulli channel distribution model, and $K^+ - \epsilon$SSLE and K^+-BSSLE (K^+-Blind SSLE) for Markovian decision process channel model, under the feedback loss condition are presented. The feedback loss arises due to reconstruction (or characterization) failure, which occurs whenever the number of occupied channels is higher than the number of ADCs, K, of a sub-Nyquist sampling (SNS) set-up.

To show that the subset selection problem is learnable, the $K-$SL algorithm selecting a subset having K best channels is proposed. But since the optimal size of the selected channel subset, which results in maximum throughput, is always greater than K, the $K-$SL algorithm is extended to K^+-SSL algorithm, where a subset size can range from K to the total number of channels, N. Due to the analysis of every channel subset sharing a common channel with the selected subset, K^+-SSL is computationally complex. Further, the complexity of K^+-SSL increases with N. To reduce the complexity, we proposed K^+-SSLE. At the beginning of every time slot, it first determines the optimal channel subset's size and then only analyses the subsets of the calculated subset size. The simulation results show that the proposed K^+-SSLE achieves the minimum regret. The gap between the regret of K^+-SSLE and other algorithms increases with N. It is also studied that the performance of all algorithms, including ideal policy, which always selects optimal channel subset, increases with an increase in K and decreases with an increase in N.

To have more similarity with the real radio signal, where a channel occupancy status depends on its previous state, we have presented the $K^+ - \epsilon$SSLE

and K^+-BSSLE algorithms. Similar to the K^+-SSLE, $K^+ - \epsilon$SSLE and K^+-BSSLE algorithms determine the size of the optimal channel subset. To have accurate learning of channel statistics, $K^+ - \epsilon$SSLE algorithm explores the channel subsets of K with the ϵ probability. It calculates the optimal subset size for remaining time slots and selects the best subset based on the learnt statistics. For avoiding the linear regret collected during the exploration phase of $K^+ - \epsilon$SSLE algorithm, the K^+-BSSLE algorithm is proposed. If the subset selected via transitional and stationary quality indexes are different, then K^+-BSSLE selects a subset of size K. Otherwise, it selects a subset of size ranging from K to N. For the validation of $K^+ - \epsilon$SSLE and K^+-BSSLE algorithms on the real-radio signals, an USRP-hardware testbed is developed in the latter part of the chapter. It is shown that the proposed K^+-BSSLE algorithm offers the minimum regret.

In the next chapters, the wideband signal characterization techniques utilizing the proposed channel subset learning algorithm to perform non-contiguous SNS are discussed.

Chapter 4

Reconfigurable and Intelligent Ultra-Wideband Angular Sensing

The non-contiguous sub-Nyquist sampling (SNS) based wideband spectrum analyzer (WSA) needs to be reconfigurable and intelligent. The reconfigurability allows the WSA to select non-contiguous channels for digitization. At the same time, online learning and decision making based intelligence enable the WSA to learn spectrum statistics and choose the frequency bands (or channels) to maximize the throughput. Since beamforming and MIMO are de-facto standards in next-generation networks, WSA should perform spectrum sensing in temporal and spatial domains. This chapter focuses on ultra-wideband angular spectrum sensing (UWASS) on the ultra-wideband non-contiguous spectrum (UWNS) not only in the time domain but in the spatio-temporal domain, i.e. along with the identification of vacant and occupied frequency bands in the frequency domain, the determination of the direction of arrival (DoA) of occupied bands is also performed in the spatial domain. To perform UWASS , we first discuss a

novel antenna array and SNS based wideband receiver architecture. Later we discuss the efficacy of the proposed UWASS over state-of-the-art approaches via hardware complexity comparison and simulation results.

4.1 Signal Model

Consider a wideband signal consisting of a finite number of far-field, uncorrelated and narrowband transmissions. The wideband signal, $x(t)$, at time t is given as

$$x(t) = \sum_{i=1}^{M} c_i(t) e^{j2\pi f_i t} + \eta(t) \tag{4.1}$$

where M denotes the unknown number of narrowband/active transmissions at time t s.t. $M \leq N$, $c_i(t)$ is the amplitude of the i^{th} active transmission of a carrier frequency, f_i, and $\eta(t)$ is an additive white Gaussian noise. Similar to [24, 26, 63], the following assumptions have been made on $x(t)$.

1. The spectrum of $x(t)$ is bandlimited to f_{max} and is divided into N frequency bands (or channels) of uniform bandwidth $B = \frac{f_{max}}{N}$.
2. Each active transmission, $c_i(t)$, has a maximum possible bandwidth of $B\ Hz$ and occupies orthogonal frequency bands.
3. The status of N frequency bands evolves as an independent two-state Markovian chain where the two states are vacant and busy.

A time-slotted communication has been assumed where the status of all frequency bands remains static for a time slot, t_s. Let $\mathbf{s} = [s_n(t_s)]_{n=1}^{N}$ be a bi-

nary support vector denoting the vacant and busy status of frequency bands, i.e. $s_n(t_s) = 0$ (or 1) implies the vacant (or busy) status of n^{th} frequency band for a time slot, t_s.

4.2 Proposed Ultra-Wideband Angular Sensing (UWASS)

The proposed UWASS approach aims to select a subset of non-contiguous frequency bands from the wideband spectrum, sample and digitize them via SNS followed by digital reconstruction and the estimation of carrier frequencies and DoAs of occupied bands with an objective to maximize the throughput. The process is repeated in each time slot, and it involves four blocks as shown in Fig. 4.1: 1) Multi-antenna non-contiguous SNS, 2) Reconstruction and characterization, 3) Joint angular spectrum sensing and 4) Learning and Decision Making (LDM).

The SNS block consists of L antennas, out of which the first antenna has K branches, whereas other antennas have a single branch. Each branch digitizes a set of frequency bands chosen by the LDM block. Let β be a vector storing the indexes of these selected frequency bands. Using the digitized samples, $\mathbf{y}_{1,k}[n]$, obtained from the $k \in \{1, \cdots, K\}$ branches of the first antenna, the reconstruction and characterization block determines the status, $\mathbf{s}_\beta \in \mathbf{s}$, of selected frequency bands. The output of all antennas, $\mathbf{y}_{l,1}[n], l \in \{1, L\}$, along with the estimated status, $\hat{\mathbf{s}}_\beta \in \mathbf{s}$ is then utilized by the joint angular spectrum sensing block to estimate the carrier frequency, f_i and corresponding DoA, θ_i

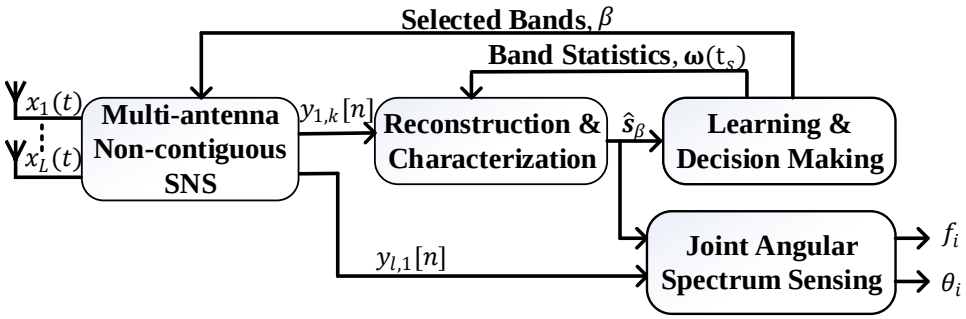

Figure 4.1: Proposed UWASS sensing model.

for active transmission in β. Simultaneously, by using $\hat{\mathbf{s}}_\beta$ and learned frequency band statistics, the LDM block updates β to be used in the subsequent time slot. Next, the functioning of each block is discussed in detail.

4.2.1 Multi-antenna Non-contiguous SNS

The proposed receiver architecture, shown in Fig. 4.2, considers a planar antenna array, which includes various possible geometries such as L-shaped, rectangular, circular, etc. [136]. From Fig. 4.2, it can be observed that the first antenna of an antenna array has K analog branches (where $K \ll N$) and other antennas have a single branch. The signal received at the l^{th} antenna can be written as

$$x_l(t) = \sum_{i=1}^{M} c_i(t + \tau_l(\theta_i))e^{j2\pi f_i(t+\tau_l(\theta_i))} + \eta_l(t) \tag{4.2}$$

Due to the narrowband signal assumption, Eq. 4.2 can be approximated as

$$x_l(t) = \sum_{i=1}^{M} c_i(t)e^{j2\pi f_i(t+\tau_l(\theta_i))} + \eta_l(t) \tag{4.3}$$

where θ_i is DoA of the i^{th} active transmission, $\tau_l(\theta_i)$ is the time delay observed at the l^{th} antenna with respect to the reference antenna (i.e. the first antenna),

and it depends on θ_i and geometry of the antenna array.

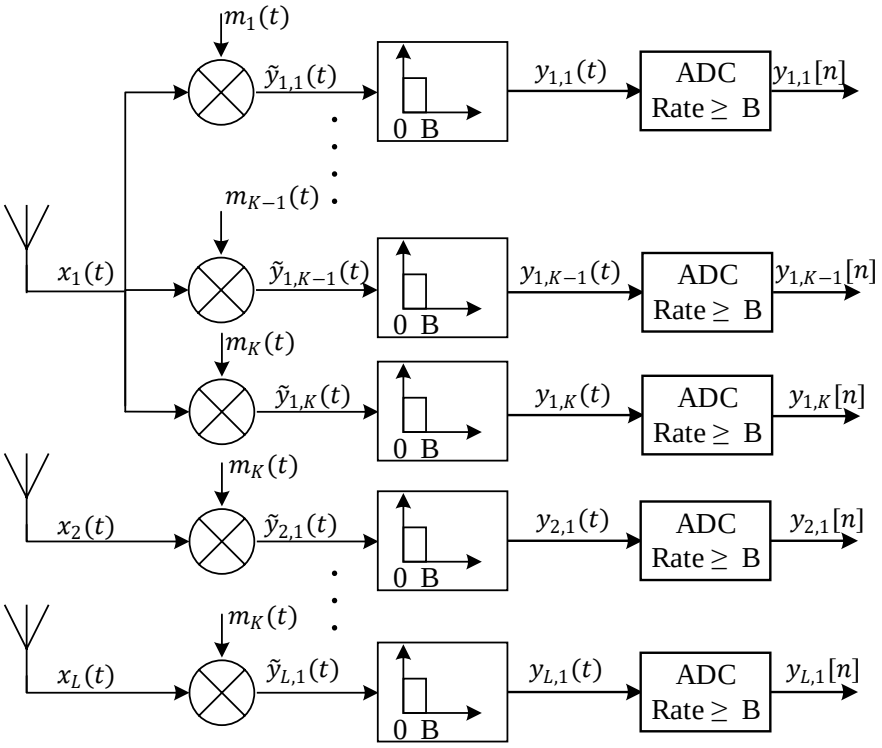

Figure 4.2: Proposed multi-antenna non-contiguous SNS architecture.

To perform SNS over non-contiguous frequency bands, the finite rate of innovation (FRI) based architecture has been considered [62]. Since all K branches of the first antenna observe the same signal, $x_1(t)$, the low rate samples, $y_{1,k}(t)$, obtained at these branches are a function of center frequencies, f_i only. Thus, the samples $y_{1,k}(t)$ of first antenna branches are utilized to identify busy frequency bands in β. To perform SNS over β frequency bands, the wideband signal, $x_1(t)$, received at the first antenna is passed through a unique mixing function, $m_k(t) = \sum_{n\in\beta} \alpha_{k,n} e^{-j2\pi(n-1)Bt}$ of all K branches. Under the noiseless case, the Fourier transform of the mixed signal, $\tilde{y}_{1,k}(t) = x_1(t)m_k(t)$, pro-

duced at the k^{th} branch of the first antenna can be written as

$$\tilde{Y}_{1,k}(f) = \int_{-\infty}^{\infty} x_1(t)\ m_k(t)\ e^{-j2\pi ft} dt \tag{4.4}$$

Since, $m_k(t) = \sum_{n\in\beta} \alpha_{k,n} e^{-j2\pi(n-1)Bt}$, the Eq. 4.4 can be expanded as

$$\tilde{Y}_{1,k}(f) = \int_{-\infty}^{\infty} x_1(t)\ \sum_{n\in\beta} \alpha_{k,n}\ e^{-j2\pi(f+(n-1)B)t} dt \tag{4.5}$$

As summation is a linear operator, it can be taken outside the integration. Thus, Eq. 4.5 can be re-written as

$$\tilde{Y}_{1,k}(f) = \sum_{n\in\beta} \alpha_{k,n} \int_{-\infty}^{+\infty} x_1(t) e^{-j2\pi(f+(n-1)B)t} dt \tag{4.6}$$

From Eq. 4.6, it can be observed that $\int_{-\infty}^{+\infty} x_1(t) e^{-j2\pi(f+(n-1)B)t} dt$ is the frequency-shifted Fourier transform of $x_1(t)$. Hence, it can be written as

$$\tilde{Y}_{1,k}(f) = \sum_{n\in\beta} \alpha_{k,n} X_1(f + (n-1)B) \tag{4.7}$$

where $X_1(f)$ is the Fourier transform of $x_1(t)$. It can be observed from Eq. 4.7 that the mixed signal, $\tilde{Y}_{1,k}(f)$ is an aliased signal containing shifted and scaled images of all active transmissions in $x(t)$. But it can be noticed that the base-band images (i.e. within $f \in [0, B]$) present in $\tilde{Y}_{1,k}(f)$ belongs to the active transmissions present in β. To filter out the unwanted images present at a higher

frequency, $\tilde{Y}_{1,k}(f)$ is bandlimited by a LPF of bandwidth $B\ Hz$ as

$$Y_{1,k}(f) = \begin{cases} \sum_{n\in\beta} \alpha_{k,n} X_1(f + (n-1)B) & \text{if } f \in \mathcal{F} = [0, B], \\ 0 & \text{if } f \notin \mathcal{F} \end{cases} \tag{4.8}$$

The filtered signal is then digitized via ADC of rate $f_{sns} \geq B$ Hz. The low rate samples, $y_{1,k}[n]$ obtained at the K branches of the first antenna correspond to only β frequency bands. The DTFT of these samples can be written as

$$Y_{1,k}(e^{j2\pi f/B}) = \sum_{n\in\beta} \alpha_{k,n} X_1(f + (n-1)B)\ \forall f \in \mathcal{F} \tag{4.9}$$

Thus, for all K branches above equation can be represented as

$$\mathbf{Y}(f) = \mathbf{A}\ \mathbf{X}_1(f) \qquad f \in \mathcal{F} \tag{4.10}$$

where $\mathbf{Y}(f)$ represents $K \times 1$ vector such that its k^{th} entry is the DTFT of samples obtained at the k^{th} branch of the first antenna, $\mathbf{A}$ is a $K \times |\beta|$ sensing matrix which contains $\alpha_{k,n}$ as its $(k,n)^{th}$ entry and $\mathbf{X}_1(f)$ is a $|\beta|\times 1$ vector containing $X_1(f + (n-1)B)\ \forall\ n \in \beta$. To determine the status of frequency bands, the sub-Nyquist samples are passed to the reconstruction and characterization block.

4.2.2 Reconstruction and Characterization

The aim of this block is to determine the status, $\mathbf{s}_\beta$, of β frequency bands digitized via SNS. To guarantee a unique solution of $\mathbf{s}_\beta$, Eq. 6.3 should satisfy

Theorem 1.

Theorem 1: For the sampling architecture as shown in Fig. 4.2, a unique solution of $\mathbf{s}_\beta$ is possible if

1. $f_{sns} \geq B$
2. Kruskal rank of $\mathbf{A}$ [1], i.e. $krank(\mathbf{A}) > \|\mathbf{s}_\beta\|_0$

Proof: From Eq. 4.7 , it can be observed that $\tilde{Y}_{1,k}(f)$ contains every frequency band of β in the frequency range of $[0, B]$. Thus, to get a single image of these bands in $\mathbf{X}_1(f)$ of Eq. 6.3, $f_{sns} \geq B$ [137]. The second condition follows directly from the unique recovery condition of a sparse infinite measurement vector signal [138, Theorem 11.26] i.e.

$$\|\mathbf{s}_\beta\|_0 \leq \frac{krank(\mathbf{A}) + dim(span(\mathbf{X}_1(f)))}{2} \tag{4.11}$$

As $dim(span(\mathbf{X}_1(f))) = \|\mathbf{s}_\beta\|_0$, hence, $krank(\mathbf{A}) \geq \|\mathbf{s}_\beta\|_0$.

□

To satisfy Theorem 1, the sensing matrix $\mathbf{A}$ is taken as independent and identically distributed (i.i.d.) Gaussian matrix, and an LDM algorithm is designed such that β has at most K busy bands.

We can directly use the energy detector to determine the status of digitized frequency bands when $|\beta| \leq K$. But there is a need for a sparse recovery algo-

[1] A matrix having a Kruskal rank of k is defined as the maximum value of k, such that every k columns of a matrix are linearly independent

rithm in the case of $|\beta| > K$. As discussed in Section II.A, Bayesian algorithms have better recovery accuracy than greedy algorithms (like orthogonal matching pursuit (OMP) [81]) and have lower computational complexity than l_1 norm minimization algorithms (like basis pursuits [79]). However, the only drawback of the Bayesian approach is that it requires prior knowledge of occupancy statistics of frequency bands. Since the LDM block in the proposed UWASS approach aims to learn frequency bands statistics, the Bayesian recovery algorithm becomes a good fit. Hence, we explore the Bayesian matching pursuit (BMP) algorithm [74, 139].

Consider a vector $\boldsymbol{\omega}(t_s)$ storing the immediate probability of vacancy of all N frequency bands for a t_s time slot and can be defined as

$$\boldsymbol{\omega}(t_s) = [\omega_1(t_s), \omega_2(t_s), ..., \omega_N(t_s)] \tag{4.12}$$

where $\omega_n(t_s) = \mathbb{P}[s_n(t_s) = 0]$ is an immediate vacancy probability of the n^{th} band. The BMP algorithm utilizes $\boldsymbol{\omega}(t_s)$, which is updated by the LDM block at every time slot. For mathematical simplicity, the proposed UWASS method considers every frequency band, $X(f + (n-1)B)$ where $f \in \mathcal{F}$ and $n \in [0, N]$, to be generated from a Gaussian distribution, i.e. $X(f+(n-1)B)|s_n \sim \mathcal{N}(0, \sigma_{s_n})\ \forall\, n \in [1, N]$ similar to [63,74,139]. However, the detection method is also applicable to other distribution models. For modeling the sparse signal, we consider $\sigma_{s_n=0} = 0\ \forall\ n \in [1, N]$. With this probability model, the probability

distribution of the sub-Nyquist samples of β frequency bands will become

$$\mathbf{Y}(f)|\mathbf{s}_\beta \sim \mathcal{N}(0, \mathbf{A}\mathbf{R}(s)\mathbf{A}^T) \tag{4.13}$$

where $\mathbf{R}(s) = diag(\{\sigma_{s_n}\}_{n\in\beta})$ is a covariance matrix. Now to determine the status, $\mathbf{s}_\beta$, we can perform maximum a posteriori estimate of $\mathbf{s}_\beta$ as

$$\mathbf{s}_\beta = \underset{\mathbf{s'}_\beta \in\, \mathcal{S}}{\arg\max}\, \mathbb{P}(\mathbf{s'}_\beta|\mathbf{Y}) \tag{4.14}$$

where $\mathcal{S}$ is a set containing all possible values of $\mathbf{s}_\beta$. By applying Bayes rule on the posterior $\mathbb{P}(\mathbf{s}_\beta|\mathbf{Y})$, we get

$$\mathbb{P}(\mathbf{s}_\beta|\mathbf{Y}) = \frac{\mathbb{P}(\mathbf{Y}|\mathbf{s}_\beta)\mathbb{P}(\mathbf{s}_\beta)}{\sum_{\mathbf{s'}_\beta \in\, \mathcal{S}} \mathbb{P}(\mathbf{Y}|\mathbf{s}'_\beta)\mathbb{P}(\mathbf{s}'_\beta)} \tag{4.15}$$

Since $\sum_{\mathbf{s'}_\beta \in\, \mathcal{S}} \mathbb{P}(\mathbf{Y}|\mathbf{s}'_\beta)\mathbb{P}(\mathbf{s}'_\beta)$ remains same for all possible values of $\mathbf{s}_\beta$ in $\mathcal{S}$, estimation of $\mathbb{P}(\mathbf{s}_\beta|\mathbf{Y})$ can be reduced to the estimation of $\mathbb{P}(\mathbf{Y}|\mathbf{s}_\beta)\mathbb{P}(\mathbf{s}_\beta)$. Hence, Eq. 4.14 can be re-written as

$$\hat{\mathbf{s}}_\beta = \underset{\mathbf{s'}_\beta \in\, \mathcal{S}}{\arg\max}\, \mathbb{P}(\mathbf{Y}|\mathbf{s'}_\beta)\mathbb{P}(\mathbf{s'}_\beta) \tag{4.16}$$

For simplification, we convert above maximization in the logarithmic domain

$$\hat{\mathbf{s}}_\beta = \underset{\mathbf{s'}_\beta \in\, \mathcal{S}}{\arg\max}\, \ln \mathbb{P}(\mathbf{Y}|\mathbf{s'}_\beta) + \ln \mathbb{P}(\mathbf{s'}_\beta) \tag{4.17}$$

Let

$$\lambda(\mathbf{s}_\beta) = \ln \mathbb{P}(\mathbf{Y}|\mathbf{s}_\beta) + \ln \mathbb{P}(\mathbf{s}_\beta) \tag{4.18}$$

The above equation can be expanded as

$$\lambda(\mathbf{s}_\beta) = \ln \mathbb{P}(\mathbf{Y}|\mathbf{s}_\beta) + \sum_{n\in\beta} \ln \mathbb{P}(s_n) \tag{4.19}$$

$$= \ln \mathbb{P}(\mathbf{Y}|\mathbf{s}_\beta) + \sum_{n\in\beta} (1 - s_n) \ln \mathbb{P}(s_n = 0) + \sum_{n\in\beta} s_n \ln \mathbb{P}(s_n = 1) \tag{4.20}$$

As an immediate probability of vacancy vector, $\mathbf{\Omega}(t_s)$, defines the probability of vacancy of all N frequency bands, hence, $\mathbb{P}(s_n = 0) = \omega_n$ and $\mathbb{P}(s_n = 1) = 1 - \omega_n$. Therefore,

$$\lambda(\mathbf{s}_\beta) = \ln \mathbb{P}(\mathbf{Y}|\mathbf{s}_\beta) + \sum_{n\in\beta} \ln(\omega_n) + \sum_{n\in\beta} s_n \ln\left(\frac{1-\omega_n}{\omega_n}\right) \tag{4.21}$$

$$\lambda(\mathbf{s}_\beta) = -\frac{K}{2}\ln 2\pi - \frac{1}{2}\ln det(\phi(\mathbf{s}_\beta)) - \frac{1}{2}\mathbf{Y}^T\phi(\mathbf{s}_\beta)^{-1}\mathbf{Y} + \sum_{n\in\beta} \ln(\omega_n) + \sum_{n\in\beta} s_n \ln\left(\frac{1-\omega_n}{\omega_n}\right) \tag{4.22}$$

where $\phi(\mathbf{s}_\beta) = \mathbf{A}\mathbf{R}(\mathbf{s}_\beta)\mathbf{A}^T$. Now, to determine $\mathbf{s}_\beta$, Eq. 4.22 needs to be maximized, and it is performed by employing the proposed BMP algorithm, shown in Algorithm 1. Similar to [74], BMP is a greedy method that works iteratively (line 4-12). For the first iteration, i.e. $i = 0$, it generates $\mathbf{s}_{\beta,j}$ vectors where $j \in \mathcal{J} = \{1, ..., (|\beta| - i)\}$ (line 5) and initialize them to $\hat{\mathbf{s}}_\beta$, i.e. a NULL vector at $i = 0$ (line 6). Note that each entry of $\mathbf{s}_{\beta,j}$ represents the status of the n^{th}

Algorithm 6 Proposed BMP algorithm

1: Input: β (from LDM), ϵ
2: Output: Status of selected bands, $\hat{\mathbf{s}}_\beta$
3: Initialization: Set $i = 0$, error $\geq \epsilon$, $\hat{\mathbf{s}}_\beta = [0]_{|\beta|\times 1}$, $\lambda_p = 0, \mathcal{U} = \varnothing$
4: **while** error$\geq \epsilon$ **do**
5: Generate a set of binary vectors, $\mathbf{s}_{\beta,j}$ of size $|\beta|\times 1$ where $j \in \mathcal{J} = \{1, ..., (|\beta|-i)\}$
6: Initialize $\mathbf{s}_{\beta,j} = \hat{\mathbf{s}}_\beta \; \forall \; j \in \mathcal{J}$
7: Determine a band index, $k_j \in \{1, .., |\beta|\}\backslash\mathcal{U}$ for all $\mathbf{s}_{\beta,j}$ vectors s.t. all k_j are orthogonal.
8: Set $\mathbf{s}_{\beta,j}(k_j) = 1 \; \forall j \in \mathcal{J}$.
9: Find $\hat{\mathbf{s}}_\beta = \arg\max_{\mathbf{s}_{\beta,j}} \lambda(\mathbf{s}_{\beta,j})$ and $\lambda_c = \lambda(\hat{\mathbf{s}}_\beta)$.
10: Update error = $\lambda_c - \lambda_p$ and Set $\lambda_p = \lambda_c$.
11: Update $\mathcal{U} = find(\hat{\mathbf{s}}_\beta == 1)$ and $i = i + 1$.
12: **end while**

frequency band in β. Next, for all $(|\beta|-i)$ vectors, $\mathbf{s}_{\beta,j}$, one frequency band $\in \{1, .., |\beta|\}\backslash\mathcal{U}$ is made busy (i.e. made 1) such that all the selected bands are orthogonal (line 7-8). At the end (line 9-11), $\hat{\mathbf{s}}_\beta$ is determined by maximizing $\lambda(\mathbf{s}_{\beta,j})$ over $\mathbf{s}_{\beta,j}$ followed by updating the error and $\mathcal{U}$ (which contains a set of detected frequency bands). This process is repeated at every iteration until the error becomes less than ϵ.

4.2.3 Joint Angular Spectrum Sensing

The task of the angular spectrum sensing block is to estimate carrier frequencies, f_i, and corresponding DoAs, θ_i, of active transmissions present in β frequency bands. This is accomplished using the estimated status, $\hat{\mathbf{s}}_\beta$ and the sub-Nyquist samples, $y_{l,1}[n]$, i.e. samples generated at the first branch of the first antenna and the rest of the $(L-1)$ antennas. The number of antennas, L, depends on the number of branches in the SNS architecture of the first antenna. It is shown in in Theorem 2 that for K branches at the first antenna, the proposed receiver architecture must have at least $L = K + 1$ antennas for the successful recovery

of f_i and θ_i. Furthermore, it is shown in proposition 1 that in the case of sensing more than K bands, the probability of successful recovery of f_i and θ_i becomes $\mathbb{P}(\zeta_{\mathbf{s}_\beta} = 0)$, where $\zeta_{\mathbf{s}_\beta}$ is a reconstruction/sensing failure event and is described in detail in Chapter 3.

The Fourier transform of the signal, $\tilde{y}_{l,1}(t)$, obtained at the output of mixer of the l^{th} antenna, under the noiseless condition, is given as

$$\tilde{Y}_{l,1}(f) = \int_{-\infty}^{\infty} \sum_{i=1}^{M} c_i(t) e^{j2\pi f_i(t+\tau_l(\theta_i))} \sum_{n\in\beta} \alpha_n e^{-j2\pi(n-1)Bt} e^{-j2\pi ft} dt \tag{4.23}$$

$$= \sum_{i=1}^{M} \sum_{n\in\beta} \alpha_n e^{j2\pi f_i \tau_l(\theta_i)} \int_{-\infty}^{\infty} c_i(t) e^{j2\pi(f_i-(n-1)B)t} e^{-j2\pi ft} dt \tag{4.24}$$

$$= \sum_{i=1}^{M} e^{j2\pi f_i \tau_l(\theta_i)} \sum_{n\in\beta} \alpha_n C_i(f - (f_i - (n-1)B)) \tag{4.25}$$

where $C_i(f)$ is the Fourier transform of an active transmission $c_i(t)$. Note that since $k = 1$, α_n is same for all the antennas. From the above equation, it can be observed that the mixed signal, $\tilde{y}_{l,1}(t)$, contains the images of i^{th} active transmissions at every $f_i - (n-1)B$ position. For illustration, consider a wideband signal, shown in Fig. 4.3(a) where $\beta = \{1, 2, 4, 5, 6, 7, 8, 9\}$, which means all bands except the third one are digitized and, hence, the sparsity of digitized spectrum is 25%. Then, the images of the first active transmission, $c_1(t)$ whose radio frequency representation is $c_1^{rf}(t) = c_1(t)e^{j2\pi f_1 t}$ are present at locations $C_1(f - f_1), C_1(f - (f_1 - B)), C_1(f - (f_1 - 3B))$, $C_1(f - (f_1 - 4B))$ and so on (same is shown in Fig. 4.3(b)). Similarly, the images of active transmissions $c_2(t)$ and $c_3(t)$ are shown in Fig. 4.3(c) and Fig. 4.3(d), respectively. From

Fig. 4.3(e), we can see that only the digitized active transmissions (i.e. present in 2^{nd} and 5^{th} bands) have baseband images in $\mathcal{F} = [0, B\ Hz]$. Then $\tilde{y}_{l,1}(t)$ is passed through a low pass filter (LPF) of bandwidth $B\ Hz$ to remove unwanted images present outside $\mathcal{F}$. Thus the output of the LPF can be written as

$$Y_{l,1}(f) = \sum_{b \in \beta_{busy}} \alpha_b C_b(f - (f_b - (b-1)B)) e^{j2\pi f_b \tau_l(\theta_b)} \quad f \in \mathcal{F} \tag{4.26}$$

where $\beta_{busy} = \{\beta_i \mid \hat{s}_{\beta_i} = 1$ where β_i and $\hat{s}_{\beta_i}$ indicate the i^{th} element of set β and $\hat{\mathbf{s}}_\beta$, respectively$\}$ (For example in Fig. 4.3, $\mathbf{s}_\beta = \{0, 1, 0, 1, 0, 0, 0, 0\}$, so, $\beta_{busy} = \{2, 5\}$) and C_b represents the Fourier transform of an active transmission present in the b^{th} frequency band with f_b and θ_b as its carrier frequency and DoA, respectively. Let $M_\beta = |\beta_{busy}| = ||\mathbf{s}_\beta||_0$ be the number of bands in the set β_{busy}.

The filtered signal, $y_{l,1}(t)$, is then sampled at a low sampling rate of $f_{sns} \geq B$ Hz. Thus, the DTFT of samples obtained at the output of the first branch of every antenna can be represented as

$$\mathbf{Y}_{l,1}(f) = \mathbf{EC}(f) \qquad f \in \mathcal{F} \tag{4.27}$$

where $\mathbf{Y}_{l,1}$ is an $L \times 1$ vector containing DTFT, $Y_{l,1}(e^{j2\pi f/B})$ of samples obtained at the l^{th} antenna, $\mathbf{E}$ is a $L \times M_\beta$ steering matrix with a steering vector, $e(f_b, \theta_b) = [e^{j2\pi f_b \tau_1(\theta_b)}\ ....\ e^{j2\pi f_b \tau_L(\theta_b)}]^T$ as its b^{th} column and $\mathbf{C}(f)$ is a $M_\beta \times 1$ vector containing $\alpha_b C_b(f - (f_b - (b-1)B))$ as its b^{th} entry.

Now, to determine the carrier frequencies and respective DoAs of β_{busy} fre-

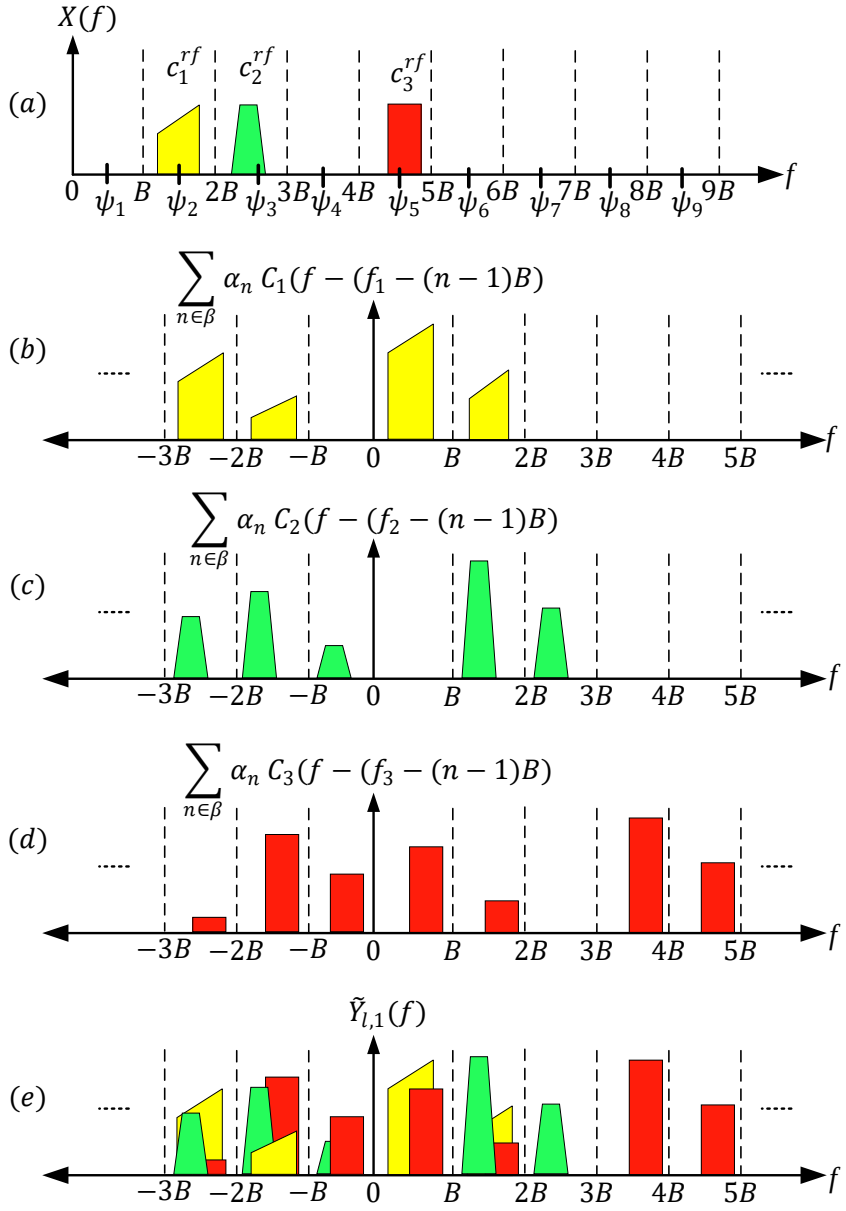

Figure 4.3: $N = 9$ frequency bands with $\beta = \{1, 2, 4, 5, 6, 7, 8, 9\}, s_\beta = \{0, 1, 0, 1, 0, 0, 0, 0\}$ and $c_i^{rf}(t) = c_i(t)e^{j2\pi f_i t}$. (a) Fourier transform of the wideband signal, $x(t)$, (b) Images of first active transmission when passed through the mixing function, (c) Images of second active transmission, (d) Images of third active transmission and (e) Output of the mixer (Note that since β does not include third frequency band, $c_2(t)$ does not appear in $[0, B]$).

quency bands, grids are made in the spatio-temporal domain. Since the carrier frequency of an active transmission will be nearest to the center frequency of its corresponding detected busy frequency band, refining is performed over the center frequency to determine the exact value of carrier frequency. To perform this task, an overcomplete steering matrix, $\mathbf{E}_C$, which contains a steering vector

for every potential value of f_b and θ_b is defined.

Let center frequencies of N frequency bands be denoted by a set $\{\psi_1, \psi_2, ..., \psi_N\}$. Since the spectrum sensing block detects busy frequency bands, a set $\psi_{busy} = \{\psi_b, b \in \beta_{busy}\}$ is formed. For making an over complete steering matrix, $\mathbf{E}_C$, the steering vectors are generated over frequency grid, $\boldsymbol{\psi}_b$, and spatial grid, $\boldsymbol{\theta}$, where $\boldsymbol{\psi}_b = \{(\psi_b - \frac{q}{2}\Delta) .... \psi_b ..... (\psi_b + \frac{q}{2}\Delta)\} \; \forall \; \psi_b \in \psi_{busy}$ and $\boldsymbol{\theta} = [\theta_1, \; \theta_2.....\theta_{180}]$. Here, Δ denotes the frequency grid size, q denotes the number of frequency grids, and θ_{deg} represent deg°.

As the first step in the joint estimation of carrier frequency and DoA, an auto-covariance matrix, $R_{\mathbf{Y}}(f) = \mathbb{E}\left[\mathbf{Y}_{l,1}(f)\mathbf{Y}_{l,1}^H(f)\right]$, of size $L \times L$ is generated. By performing the singular value decomposition on $R_{\mathbf{Y}}(f)$ and observing the eigenvalues, the basis vector corresponding to signal sub-space, say $\mathbf{U}_s$ and its orthogonal noise sub-space, say $\mathbf{U}_n$ can be separated. Since $\mathbf{U}_n$ and $\mathbf{U}_s$ are orthogonal and the potential steering vectors in $\mathbf{E}_C$ and $\mathbf{U}_s$ span the same sub-space, the correlation between $\mathbf{E}_C$ and $\mathbf{U}_n$ will generate nulls at potential values of actual f_b and θ_b. The MUSIC spectrum is generated for every $b \in \beta_{busy}$ as

$$\vec{\mathbf{p}}_b = \frac{1}{\mathbf{E}_C^H(\boldsymbol{\psi}_b, \boldsymbol{\theta}) U_n U_n^H \mathbf{E}_C(\boldsymbol{\psi}_b, \boldsymbol{\theta})} \tag{4.28}$$

where $\mathbf{E}_C(\boldsymbol{\psi}_b, \boldsymbol{\theta}) = [e^{j2\pi\boldsymbol{\psi}_b\tau_1(\boldsymbol{\theta})}..... \; e^{j2\pi\boldsymbol{\psi}_b\tau_L(\boldsymbol{\theta})}]^T$ is a steering matrix corresponding to $\boldsymbol{\psi}_b$ and $\boldsymbol{\theta}$. The maximum value in $\vec{\mathbf{p}}_b$ will corresponds to the carrier frequency and DoA of the first busy frequency band in β_{busy}. Similarly, the MUSIC spectrum for every $b \in \beta_{busy}$ will generate carrier frequencies and DoAs of all

sensed active transmissions. It can be noted that with the proposed approach, the frequency search grid size is reduced to the bandwidth of $M_\beta B$ which is unlike [27] stretches the grid size to the entire Nyquist bandwidth $f_s = NB$. Hence, the proposed approach leads to the reduction in the computational load by $\frac{N}{M_\beta}$ times (where $M_\beta << N$) as compared to the conventional MUSIC algorithm.

Theorem 2: Under the no noise condition, assuming the Theorem 1 holds, the sufficient conditions for the unique estimation of f_i and its corresponding θ_i for the proposed UWASS algorithm are

1. $L \geq K + 1$
2. $krank(\mathbf{E}_C) \geq \|\mathbf{s}_\beta\|_0$

Proof: As with K branches at first antenna, maximum K busy frequency bands can be detected during sensing and reconstruction block. Thus, with MUSIC algorithm, the determination of f_i and their θ_i for K busy bands can be done if the number of antennas, $L \geq K + 1$ [141]. The second condition directly follows from Theorem 1. □

Remark: Note that the proposed UWASS is independent of antenna array arrangement, hence, we employ MUSIC method (which can be generalized to any antenna array geometry) for the estimation of carrier frequencies and their DoAs. However, the proposed approach can also be extended to other approaches like ESPIRIT where one fixes the geometry of the antenna array as described in [25, 29].

Proposition 1: Assume Theorem 1 and Theorem 2 hold for the sensed β frequency bands, then the proposed UWASS method successfully determines f_i and their θ_i of K busy frequency bands with a probability of $\mathbb{P}(\zeta_{\mathbf{s}_\beta} = 0)$.

Proof: When $|\beta|$ increases beyond K then the probability of successful sensing, $\mathbb{P}(\zeta_{\mathbf{s}_\beta} = 0)$, decreases from 1 to $\sum_{i=0}^{K} \mathbb{P}(||s_\beta||_0 = i)$. Since the determination of f_i and corresponding θ_i are possible only if sensing of β frequency bands is successful, the probability of successful determination of f_i and θ_i becomes same as the probability of successful sensing. □

4.2.4 Learning and Decision Making

The learning and decision making (LDM) block aims to determine the optimal number of frequency bands, $|\beta|$ and their locations, β, for the digitization by SNS block at every time slot. The selection of $|\beta|$ and β is to be made to maximise the throughput. This problem is the same as the MPMAB problem discussed in Chapter 3. Hence, the proposed K^+-BSSLE algorithm is employed in the LDM block.

4.3 Simulation Results

This section compares the hardware complexity and performance of the proposed UWASS method with the existing WAS methods [25, 29].

4.3.1 UWASS Architecture Comparison: Complexity

In Table 4.1, the complexity of state-of-the-art UWASS approaches in [25] (referred to as CASCADE) and [29] (referred to as Joint frequency and DOA estimation, JFDE) is compared with the proposed approach. It is assumed that each architecture can digitize a maximum K active transmissions. For such a requirement, the proposed approach requires a fewer number of antennas and ADCs. Furthermore, the proposed approach does not need prior knowledge of the number of active transmissions, M, in the entire wideband spectrum. As expected, existing approaches fail whenever $M > K$. On the other hand, the proposed approach fails only when a number of active transmissions in β (i.e. bands selected by the LDM block) is higher than K. Hence, sensing failure is

Table 4.1: Comparison of UWASS architectures for digitizing K active transmissions.

Characteristics	**CASCADE**	**JFDE**	**Proposed**
SNS Architecture	MWC Low analog BW ADCs	MCS High analog BW ADCs	FRI Low analog BW ADCs
No. of Antennas (L)	$2K+1$	$K+1$	$K+1$
No. of) ADCs (J)	$2K+1$	$2(K+1)$	$2K$
No. of transmissions (M)	Need prior knowledge	Need prior knowledge	No need of prior knowledge
Sensing Failure ($M_\beta > K$)	Yes	Yes	Yes
Sensing Failure ($M > K$)	Yes	Yes	No
Carrier frequency	No constraints	No constraints	Active transmission is confined to a single band

independent of the number of active transmissions in the spectrum, making it feasible in sparse as well in a non-sparse spectrum. The proposed UWASS approach only assumes that the wideband spectrum is divided into multiple bands of B Hz, and each active transmission is confined to a single band. However, the center frequency of the band and transmission may not be the same. Such an assumption is valid since all communication standards either have predefined carrier frequencies or fixed resolutions between adjacent carrier frequencies.

Next, we discuss the computation complexity comparison of the proposed UWASS method with the existing CASCADE and JFDE mehtods.

CASCADE Method: It involves the following five operations:

1) Cross-Covariance of complexity $O(4K^2Q)$
2) Singular Value Decomposition of complexity $O((4K)^3)$
3) Pseudo-Inverse of complexity $O(6K^3)$
4) Eigenvalue Decomposition of complexity $O(K^3)$
5) Matrix multiplication of complexity: $O(7K^2M)$

Hence, the total computational complexity of CASCADE is $O(K^2Q + K^2M + K^3)$. Since $M \leq K$, the complexity can be approximated to $O(K^2Q + K^3)$.

JFDE Method: It involves the following four operations:

1) Correlation of complexity $O(2K^2Q)$.
2) Singular value decomposition of complexity $O(K^3)$.

3) Eigenvalue calculation of complexity $O(K^3)$.

4) MUSIC spectra generation of complexity $O(M\boldsymbol{\theta}K^2)$.

Hence, the total computational complexity of JFDE is $O(M\boldsymbol{\theta}K^2 + K^3 + K^2Q)$ and it can be approximated to $O(\boldsymbol{\theta}K^3 + K^3 + K^2Q)$.

Proposed UWASS Method: As shown in Fig. 4.1, the proposed method involves the following three tasks:

1) Reconstruction and characterization task uses the fast Bayesian matching pursuit algorithm of complexity $O(KMNQ)$

2) Joint angular spectrum sensing involves the following operations

   2.1) Correlation of complexity $O(2K^2Q)$

   2.2) Singular value decomposition of complexity $O(K^3)$.

   2.3) MUSIC spectra generation of complexity $O(M\boldsymbol{\theta}K^2)$

   Thus, the total complexity of the second task is $O(K^2Q + K^3 + M\boldsymbol{\theta}K^2)$

3) Learning and decision making (LDM) task has the complexity of $O(P)$

The LDM algorithm aims to learn the spectrum statistics and utilize the learnt statistics to select the optimal channel subset. Hence, it selects the best channel subset at every time slot and performs reconstruction and characterization followed by joint angular spectrum sensing tasks to determine the DoA and carrier frequency of occupied bands in the selected channel subset. Hence, for every time slot, the computation complexity of the proposed method is

$O(KMNQ+K^2Q+K^3+M\boldsymbol{\theta}K^2) \approx O(K^2NQ+K^2Q+K^3+\boldsymbol{\theta}K^3)$. To determine the carrier frequency and DoA at every time slot, CASCADE and JFDE methods have the complexity of $O(K^2Q + K^3)$ and $O(\boldsymbol{\theta}K^3 + K^3 + K^2Q)$, respectively. From the complexity analysis, we can say that the CASCADE method has the lowest complexity. Due to the presence of an additional K^2NQ term, the proposed UWASS method has higher complexity than JFDE. Thus we can say that the proposed method has higher computation complexity than CASCADE and JFDE methods. This is a minor penalty paid to perform blind UWASS compared to the existing non-blind UWASS methods, which require prior knowledge of the number of active transmissions in the spectrum.

4.3.2 UWASS Architecture Comparison: Performance

In this sub-section, the performance comparison of the proposed UWASS method is done with [25] and [29]. The considered spectrum has $N = 16$ frequency bands of spectrum statistics:

$$\mathbf{p}_{10} = [0.95\ 0.9\ 0.85\ 0.8\ 0.75\ 0.7\ 0.65\ 0.6\ 0.55\ 0.5\ 0.45\ 0.6\ 0.65\ 0.7\ 0.75\ 0.8]$$

$$\mathbf{p}_{01} = [0.05\ 0.1\ 0.15\ 0.2\ 0.25\ 0.3\ 0.35\ 0.4\ 0.45\ 0.5\ 0.55\ 0.4\ 0.35\ 0.3\ 0.25\ 0.2]$$

Three performance metrics are used for the performance analysis: 1) Normalized carrier frequency estimation error (NCEE), 2) Normalized DoA estimation error (NDEE), and 3) Total throughput. Parameters, NCEE and NDEE, are calculated as:

$$NCEE = \frac{1}{M}\sum_{i=1}^{M}\frac{|f_i - \hat{f}_i|}{f_s} \tag{4.29}$$

$$NDEE = \frac{1}{M}\sum_{i=1}^{M}\frac{|\theta_i - \hat{\theta}_i|}{180^\circ} \tag{4.30}$$

These metrics are compared for different values of SNRs, number of ADCs, J and number of samples, Q. In Fig. 4.4, the comparison is done in the terms of above three performance metrics for different values of SNRs ranging from $0-50\ dB$ along with $J \in \{10, 14\}$ and $Q = 512$.

Note that [25] and [29] fail whenever the number of active transmissions, M, is more than 4 for $J = 10$. On the other hand, failure in the proposed UWASS method depends on the bands selected by the LDM block. Overall, the proposed method offers lower error and higher throughput than others. Even though [26] offers lower NCEE at $0\ dB$, its throughput is inferior to the proposed method.

Next, we perform the comparison for different number of ADCs with $20\ dB$ SNR and $Q = 256$. As shown in Fig. 4.5, the proposed method offers better performance at all J. At lower J (fewer ADCs), the performance of the proposed method is significantly better than others. For instance, to achieve a throughput of $7,600$, the proposed method requires four antennas, whereas [25] and [29] require five and eleven antennas, respectively. Thus, the proposed method is both power and cost efficient. Hence, it is preferred, especially when the number of resources (area, power) is limited.

In Fig. 4.6, the effect of Q on the performance of all three methods is analyzed. As expected, the performance improves as Q increases. Moreover, at a lower Q of 256 samples, the proposed method offers 26% to 8% lower NCEE

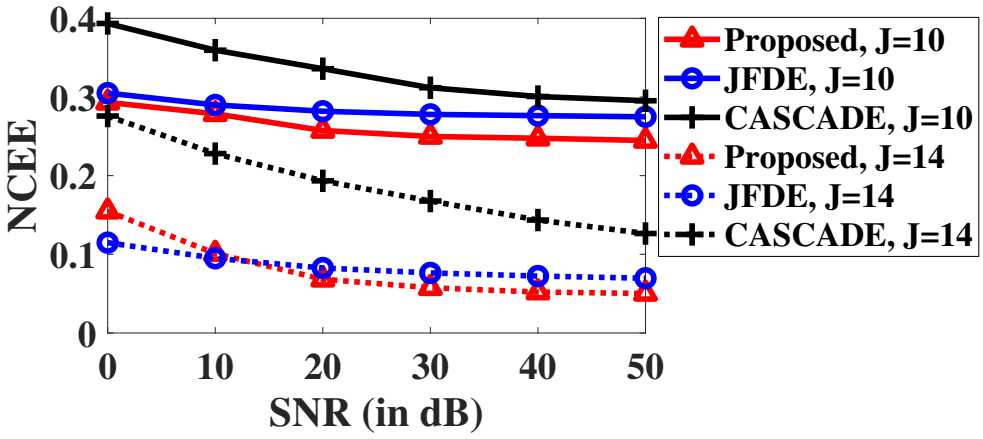

(a)

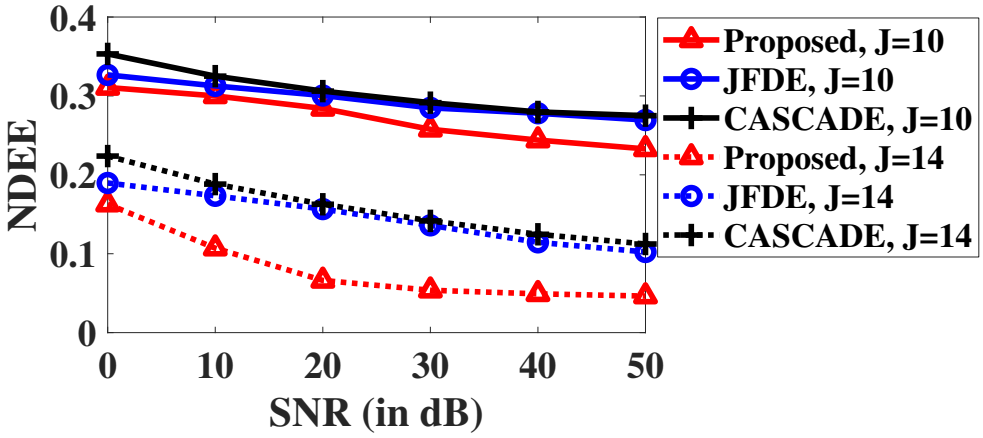

(b)

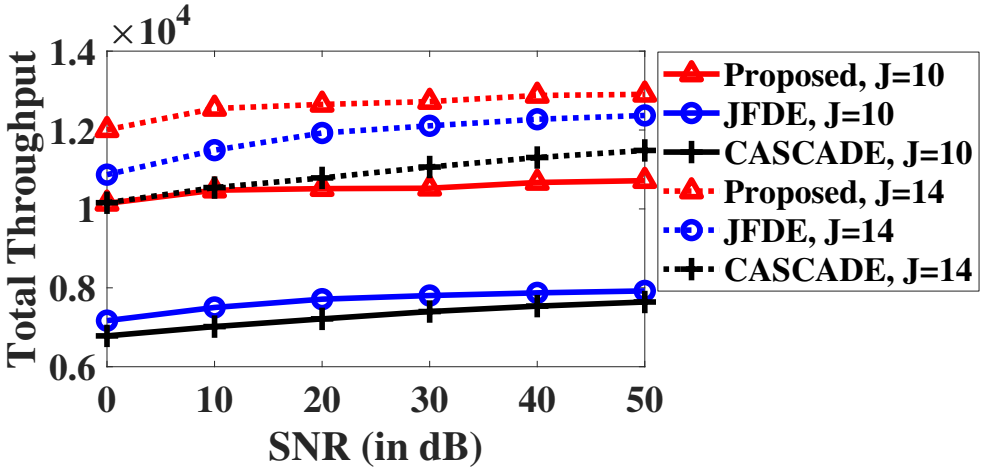

(c)

Figure 4.4: (a) NCEE, (b) NDEE, and (c) Total throughput for different values of SNRs, $J \in \{10, 14\}$ and $Q = 512$.

and 10% to 8% lower NDEE as compared to [25] and [29]. Hence, in practice, the proposed method enables faster sensing, which allows the receiver to adapt to the dynamically changing spectrum quickly. Also, fewer samples can lead to

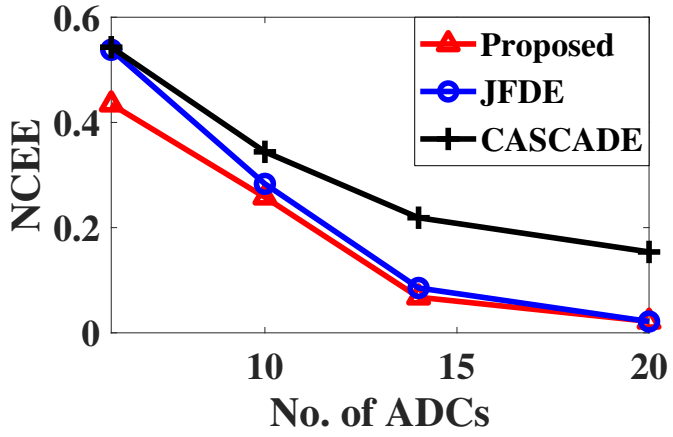

(a)

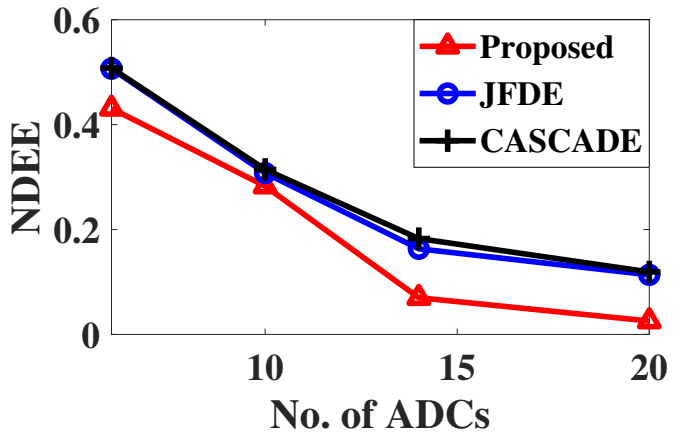

(b)

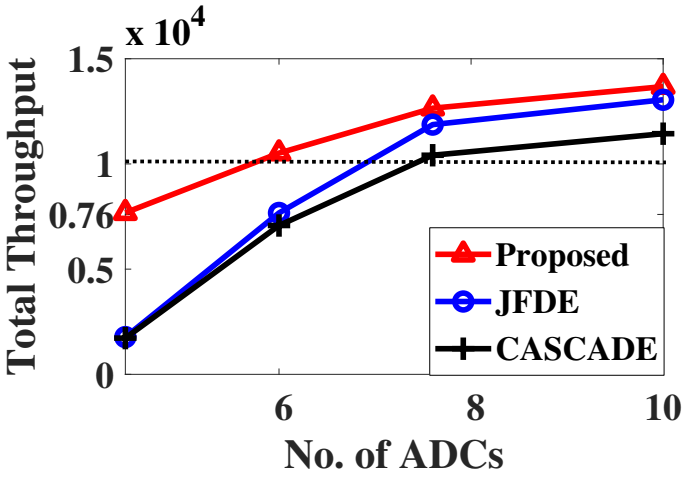

(c)

Figure 4.5: (a) NCEE, (b) NDEE, and (c) Total throughput for different values of ADCs, J, with 20 dB SNR and $Q = 256$.

significant savings in power and area requirements.

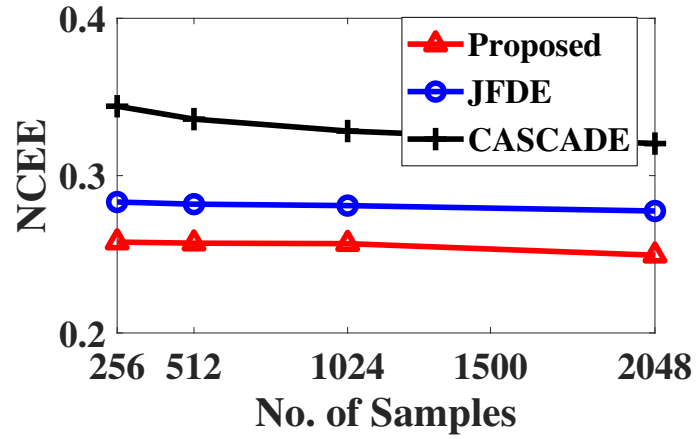

(a)

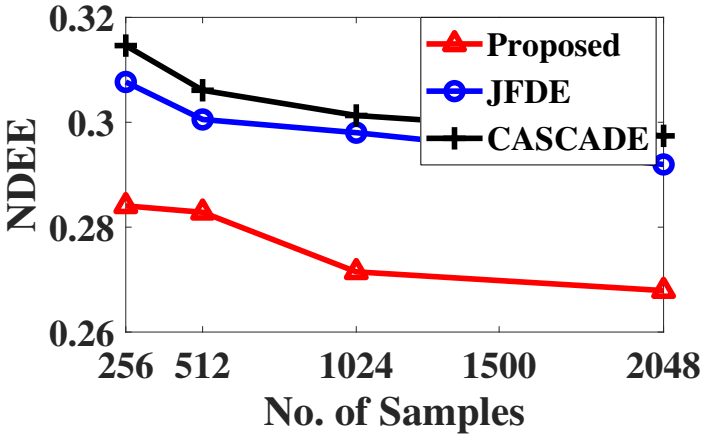

(b)

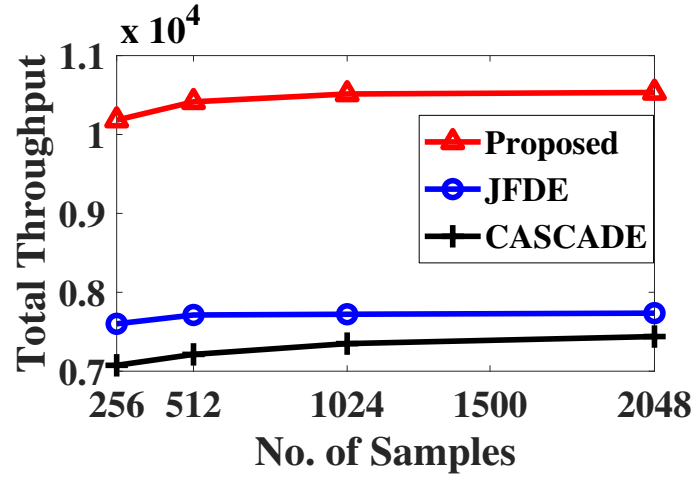

(c)

Figure 4.6: (a) NCEE, (b) NDEE, and (c) Total throughput for different number of samples, Q, with 20 dB SNR and $J = 10$.

4.4 Summary

In this chapter, an intelligent and reconfigurable multi-antenna wideband receiver architecture capable of ultra-wideband angular spectrum sensing (UWASS

) is designed to determine the transmission opportunity in both spatial and temporal domains. Here, the reconfigurable architecture is introduced by performing finite rate of innovation based non-contiguous sub-Nyquist sampling. At the same time, the intelligence of selecting non-contiguous channels is achieved via the channel subset selection algorithm discussed in the previous chapter. Due to the intelligence and non-contiguous digitization, the proposed wideband receiver is independent of the number of active transmissions in the spectrum.

The sub-Nyquist samples produced at the output of the wideband receiver are utilized to determine the status of selected frequency bands. A Bayesian matching pursuit algorithm is introduced, which takes the sub-Nyquist samples, and spectrum statistics learnt via the channel subset selection algorithm, to determine the occupancy status of selected frequency bands. The information of occupied frequency bands is then utilized to jointly estimate their carrier frequency and direction of arrival (DoA). The carrier frequency and DoA are determined by applying the multiple signal classification (MUSIC) algorithm with a double grid structure on the possible frequency and DoA range.

In the latter part of the chapter, we compared the architecture and performance of the proposed UWASS approach with the existing multi-coset sampling (MCS) and modulated wideband converter (MWC). It is shown that the proposed UWASS requires a lesser number of ADCs and does not need prior knowledge of the number of active transmissions. Also, the proposed UWASS incurs a lesser number of sensing failures as compared to the other two wideband angular sensing architectures. It is also observed that due to the non-contiguous

digitization, the proposed UWASS has lower normalized carrier frequency and DoA error for different values of antennas, analog to digital converter (ADCs) and signal to noise ratio (SNR). In the next chapter, we develop a multi-antenna USRP testbed to validate the proposed UWASS in a real radio environment.

Chapter 5

Reconfigurable and Intelligent UWASS: Prototype Design and Validation

The performance analysis of various ultra-wideband angular spectrum sensing (UWASS) approaches in the real-radio environment is critical to their practical realization. However, there is limited work in this direction. For instance, the hardware prototypes of SNS in [61, 73] are state-of-the-art, but they consider wideband spectrum sensing only in the temporal domain. The extension of the temporal to spatial sensing demands multi-antenna transceivers which significantly increases the design complexity. Few prototypes to estimate the DoA of a user signal via multi-antenna receiver have been discussed in [123–130]. All these works are focused on the narrowband spectrum and employ Nyquist-sampling based digitization. The main objective of this chapter is to design and develop an end-to-end prototype demonstrating reconfigurable and intelligent UWASS along with the experimental validation in the real-radio environment. In the proposed prototype, all baseband algorithms are realized using LabVIEW

NXG and USRPs for over the air communication.

5.1 Proposed Prototype Design

Various building blocks of the proposed prototype of reconfigurable and intelligent UWASS are shown in Fig. 5.1. The prototype consists of three modules: 1) Dynamic Wireless traffic generator, 2) Phase reference generator, and 3) UWASS receiver. The design details of each module are presented in the subsequent sections. The hardware units, i.e. USRPs and octo-clock, are shown using yellow-coloured blocks with a dotted border. USRPs are used for the transmission and reception of the wireless RF signals, while the octo-clock is used for clock synchronization at the receiver. The blue-coloured blocks with dashed border correspond to various signal processing, machine learning and wireless physical layer algorithms of the proposed UWASS, and they are realized using LabVIEW NXG.

Dynamic wireless traffic generator module emulates the multi-directional multi-user traffic in the wideband spectrum. For each user, LTE based SC-FDMA is used for baseband waveform modulation at the physical layer. The traffic of each user is beam-formed to a chosen direction via directional HORN-antennas integrated with USRPs. The transmit direction may change over time, distinct for each user and is chosen randomly. However, while performing the experiment, the dynamic wireless traffic generator is geometrically fixed by the HORN antenna locations, and the receiver antenna array is rotated to gener-

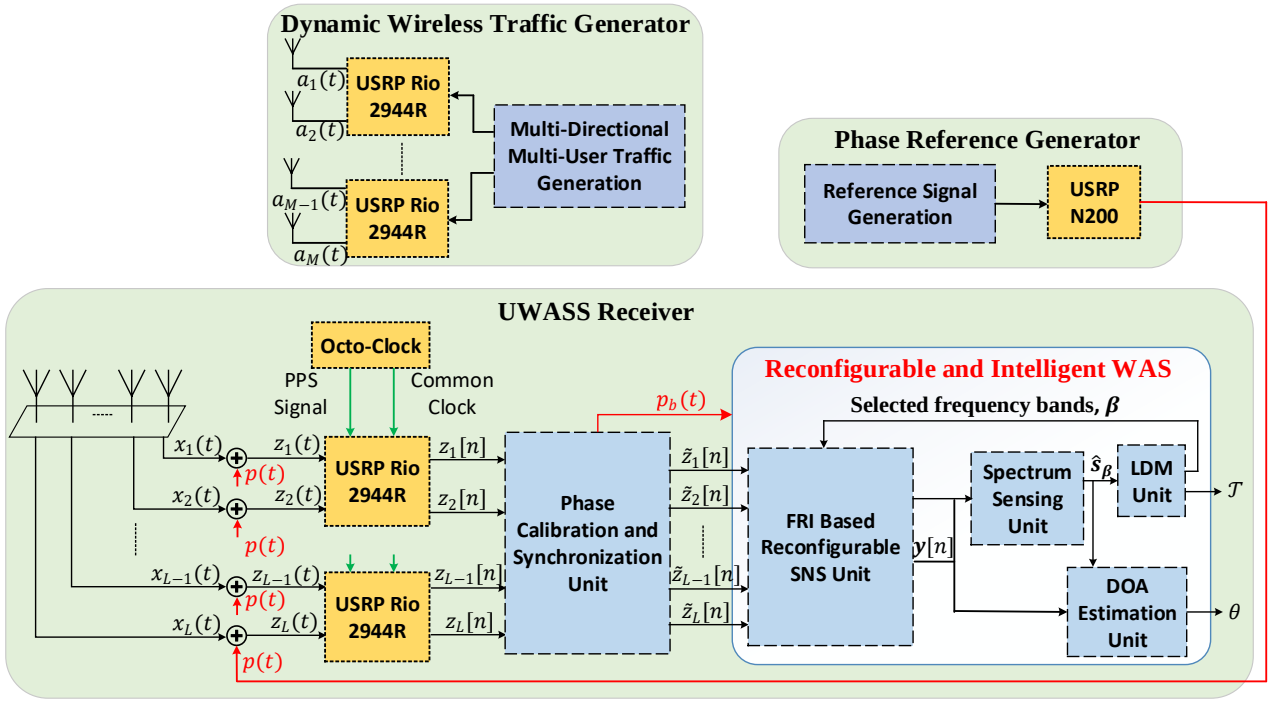

Figure 5.1: Proposed UWASS prototype consisting of 1) Dynamic wireless traffic generator, 2) Phase reference generator, and 3) UWASS receiver.

ate different DoAs. Since single NI-USRP 2944R has two transmitter/receiver ports, $M/2$ USRPs and M directional antennas are needed for the transmission of RF signal, $a_m(t)$, where $m \in \{1, 2, ..., M\}$, in M directions. Furthermore, the carrier frequencies of users vary dynamically according to the probability distribution, which maintains the sparsity of the wideband spectrum. Similar to the UWASS work discussed in Chapter 4, time-slotted communication is considered here. The time-slotted communication makes the carrier frequency and beam-direction of each user constant over a given time slot, t_s, and may change them dynamically from one slot to another.

The UWASS receiver receives the multi-directional multi-user traffic signal, $x_l(t)$ where $l \in \{1, 2, .., L\}$ and L is the number of antennas at the receiver, via the designed sparse antenna array (SAA). Since the received signal phase

is critical for accurate DoA estimation, the phase reference generator module generates the reference signal, $p(t)$, combined with $x_l(t)$ and is responsible for performing phase calibration among the signals received at various antennas. $L/2$ number of NI-USRPs 2944R are used for digitizing the L combined signals, $z_l(t)$. These USRPs receive the common clock signal and pulse per second (PPS) signal from the octo-clock unit to synchronize their local oscillators and ADCs. The signals, $z_l[n]$, received from the USRPs are digitized and downconverted to the desired sampling rate.

In the baseband operation of UWASS, five tasks are performed in every time-slot, t_s: 1) Phase calibration and synchronization, 2) FRI based reconfigurable SNS, 3) Spectrum sensing, 4) DoA estimation and, 5) Learning and decision making (LDM). Since UWASS requires the phase information of the signals impinging on the antenna array, the phase calibration of $z_l[n]$ removes the phase offset produced due to the independent RF channels of the receiver USRPs. Subsequently, the filtering operation is performed to remove the reference signal, $p(t)$, and other synchronization signals to obtain the user data signal, $\tilde{z}_l[n]$, for subsequent digitization and characterization. The USRP performs digitization of the entire received signal at the Nyquist rate. Hence, to perform non-contiguous UWASS over the selected frequency bands, a set of desired frequency bands, β, storing the indices of selected frequency bands, are extracted from $\tilde{z}_l[n]$ via FRI based reconfigurable SNS. The samples, $\mathbf{y}[n]$, correspond to the sub-Nyquist samples of frequency bands present in β. $\mathbf{y}[n]$ is passed to the spectrum sensing unit to determine the occupancy status vector,

$\hat{\mathbf{s}}_\beta \in \{0,1\}^{|\beta|}$, of β frequency bands, followed by the DoA estimation for the busy frequency bands. At the same time, the learning and decision making unit updates the learned parameters and selects the β frequency bands to be digitized in the subsequent time slot.

5.2 Multi-User Traffic and Phase Reference Generation

This section discusses the design details of dynamic wireless traffic and phase reference generator modules.

5.2.1 Dynamic Wireless Traffic Generator

The dynamic wireless traffic generator, shown in Fig. 5.2, consists of three sub-blocks. The first sub-block is the uncorrelated SC-FDMA signal generator. As shown in Fig. 5.2, it generates a multiband signal, $u(t)$, which consists of $N+2$ frequency-bands, out of which one is reserved for the phase reference signal (more details are given in the next sub-Section) and another is reserved for the

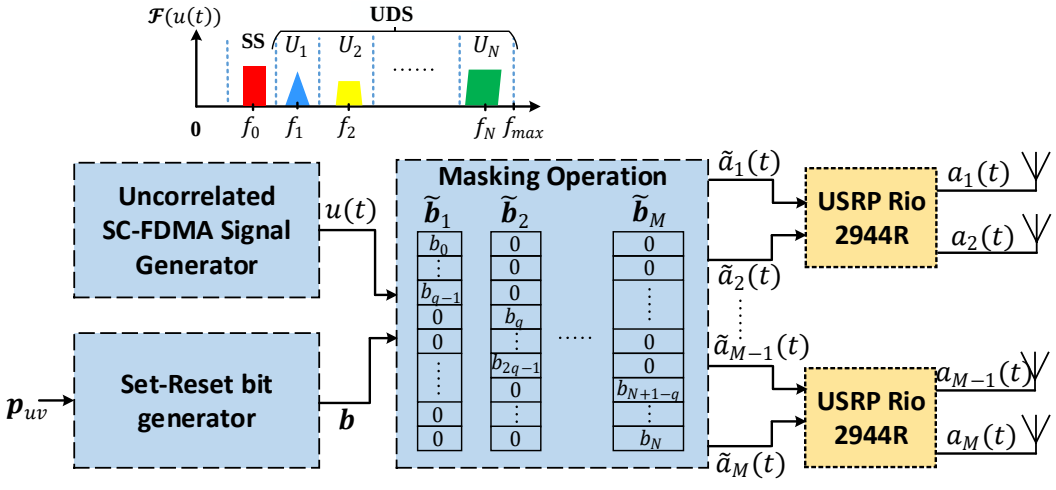

Figure 5.2: Dynamic wireless traffic generator.

synchronization signal (SS). The remaining N frequency bands (i.e. U_1 to U_N) are used for the user data communication and referred to as a user data signal (UDS). Similar to the synchronization burst in the 4G/5G, the SS is used for frame and symbol synchronization over the downlink. The SC-FDMA signal generator block first generates the $N+1$ uncorrelated LTE SC-FDMA signals, $c_i(t)$ where $i \in \{0, 1, ..., N\}$, for SS and U_1 to U_N frequency bands, and then modulates them to a carrier frequency of f_i. The bandwidth, B, of each SC-FDMA signal, i.e. each user, can be varied between $1.4\ MHz - 20MHz$, similar to 4G. Mathematically,

$$u(t) = \sum_{i=0}^{N} c_i(t) e^{j2\pi f_i t} \tag{5.1}$$

The second block is the set-reset bit generator block, and it generates a binary status vector, $\mathbf{b} = [b_0, b_1, ..., b_N]$, consisting of masking bits for SS and U_1 to U_N frequency bands. The occupancy of U_1 to U_N frequency bands is decided based on the independent Markovian decision process (MDP). In MDP, the immediate occupancy status depends on the transition probabilities of each of the N frequency bands. Let $\mathbf{p}_{uv}$, where $u, v \in \{0, 1\}$ denotes the {vacant, busy} status, be a vector storing the transition probabilities of N frequency bands. Thus, $\mathbf{p}_{uv}$ is an input to the second block. However, the status of these N frequency bands changes only when the masking bit of the SS i.e. b_0 changes its status. To achieve this, the masking bit, b_0 is implemented as a square wave of 50% duty cycle. So, whenever the status of b_0 changes, the masking bits $b_i\ \forall\ i \in \{1, ..., N\}$ are updated according to the input $\mathbf{p}_{uv}$.

Since the designed multi-user traffic signal generates the directional traffic only in M directions, the third block, which performs masking operation, generates M masking vectors, $\tilde{\mathbf{b}}_m \in \{0,1\}^N \ \forall \ m \in \{1,2,...,M\}$ such that the output signals, $\tilde{a}_m(t)$, contain the information of bands $\{SS, U_1, .., U_{q-1}\}$, $\{U_q, .., U_{2q-1}\}$, ..., $\{U_{N+1-q}, ..., U_N\}$, where $q = \frac{N+1}{M}$. Thus, $\tilde{\mathbf{b}}_m = [\mathbf{0}_{1\times(m-1)q}$, $b_{(m-1)q}, ..., b_{mq-1}, \mathbf{0}_{1\times(N+1-mq)}]$ where $\mathbf{0}_{1\times q}$ denotes a $1 \times q$ size vector of zeros. Mathematically, the output signal, $\tilde{a}_m(t)$, of this block is written as

$$\tilde{a}_m(t) = \sum_{q=0}^{N} \tilde{\mathbf{b}}_m(q) c_q(t) e^{j2\pi f_q t} \tag{5.2}$$

where $\tilde{\mathbf{b}}_m(q)$ denotes the q^{th} entry of $\tilde{\mathbf{b}}_m$.

Now, the M channels of $\frac{M}{2}$ NI-USRP 2944R receive the signal $\tilde{a}_m(t), \ \forall \, m \in \{1,2,...,M\}$ from the processing unit. Then they transmit the up-converted RF signals, $a_m(t) \ \forall \ m \in \{1,2,...,M\}$, over the air via M HORN antennas. Refer to Appendix A for the LabVIEW NXG based implementation flow graph of the dynamic wireless traffic generator.

5.2.2 Phase Reference Generator

The UWASS receiver, shown in Fig. 5.1, receives the multi-directional multi-user traffic signal, $x_l(t)$ where $l \in \{1,2..,L\}$, from a sparse antenna array of size L. The output of the antenna array is passed through independent AFE of the receiver USRPs for digitization. Since the AFE introduces phase distortion, we add a phase reference signal (PRS), $p(t)$, which can be used later to compen-

sate for this distortion [135]. In the designed prototype, the signal received from the antenna is combined with PRS via SMA cables. PRS is generated entirely independent of the dynamic wireless traffic generator at the transmitter. Note that in the existing 4G/5G system, there is a separate phase-tracking reference signal (PTRS) which is used to phase synchronize base-station and mobile terminals. As discussed in the next section, the prototype also has a similar signal and $p(t)$ is an additional signal to overcome the phase distortion of the receiver USRPs. The reference signal, $p(t)$, is based on the sinusoidal wave, as shown in Fig. 5.3, where two sinusoidal signals of carrier frequency $200\ kHz$ and a phase shift of $0°$ and $90°$ are generated. These in-phase and quadrature-phase sinusoidal signals are then combined and passed through the USRP N200 for the baseband to RF conversion followed by interfaced with UWASS receiver via SMA cables.

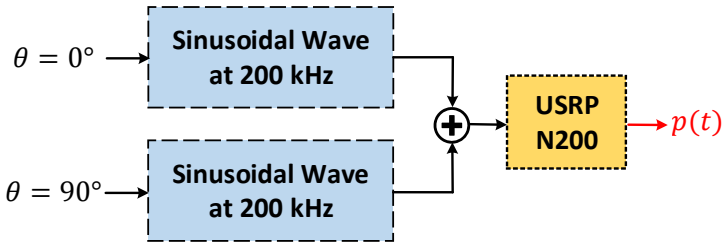

Figure 5.3: Phase reference signal generator.

5.3 UWASS Receiver

The UWASS receiver, shown in Fig. 5.1, receives the multi-directional multi-user traffic signal, $\mathbf{x}(t)$, from the antenna array of size L. The received signal is then combined with $p(t)$. The resultant signal, $\mathbf{z}(t)$, is passed through the

NI-USRP 2944R for digitization and downconversion to obtain the multiband signal, $\mathbf{z}[n]$, as shown in Fig. 5.1 and Fig. 5.4. The signal $\mathbf{y}[n]$ consists of three types of signals (also referred to as channels in 3GPPP 3G/4G standards): 1) Phase reference signal (PRS), $p(t)$ equivalent to PTRS in 4G/5G, 2) Synchronization signal (SS) equivalent to a primary synchronization signal (PSS) and secondary synchronization signal (SSS) in 4G/5G and 3) Multi-directional user-data signal (UDS) similar to physical downlink shared channel (PDSCH) in 4G/5G. The distance between adjacent antennas of L-antenna array is carefully chosen to be integer multiple of $d = \frac{c}{2f_t}$, where c is the speed of light and f_t is the transmission frequency. This results in a sparse antenna array of length $L_s > L$, which in turn leads to a higher number of active DoA estimations for a given L. Refer to Section 5.3.2.2 for more details. To characterize UDS, as shown in Fig. 5.1, the design of the UWASS receiver consists of two units: 1) Phase calibration and synchronization unit, and 2) Reconfigurable and Intelligent WAS unit. Refer to Appendix B for the LabVIEW NXG based implementation flowgraph of the UWASS receiver.

5.3.1 Phase Calibration and Synchronization Unit

The phase calibration and synchronization unit, as explained in Fig. 5.4, consists of 1) Synchronization block, 2) Phase offset calculation block and 3) Phase calibration block. The first task of the synchronization block is to detect the SS signal and identify the slot boundary. Based on the slot boundary, it generates the pulse signal, $p_b(t)$, which is needed for WAS unit to differentiate between

adjacent time slots and learn the spectrum statistics, i.e. $\mathbf{p}_{uv}$. In the proposed prototype, the SS signal is first filtered via band pass filter of cut-off frequencies f_{prs} and $f_r = f_{prs} + B$ followed by an energy detection based approach to detect its status (vacant/occupied) and generate an appropriate pulse signal. The second task of the synchronization block is to filter $\mathbf{z}[n]$ to obtain the UDS signal $\tilde{\mathbf{z}}^f[n]$ and forward it to the phase calibration block.

The phase offset calculation block generates the phase offset vector, $\boldsymbol{\phi} \in \mathbb{R}^{1\times L}$, containing phase offset at L receiver channels. $\boldsymbol{\phi}$ is used by phase calibration block to eliminate the phase distortions caused by the different AFE of $L-$channels receiver USRPs. The PRS, $p(t)$, is filtered out from $\mathbf{z}[n]$ via LPF of cut-off frequency f_{prs} to determine $\boldsymbol{\phi}$. The phase information of the filtered reference signal corresponds to the phase offset, $\boldsymbol{\phi}$.

Next, the phase calibration block receives the filtered UDS, $\tilde{\mathbf{z}}^f[n]$ and the phase offset, $\boldsymbol{\phi}$, to perform phase calibration on $\tilde{\mathbf{z}}^f[n]$. Here, the contribution of phase offset is removed from $\tilde{\mathbf{z}}^f[n]$. For the l^{th} signal, the phase calibration is

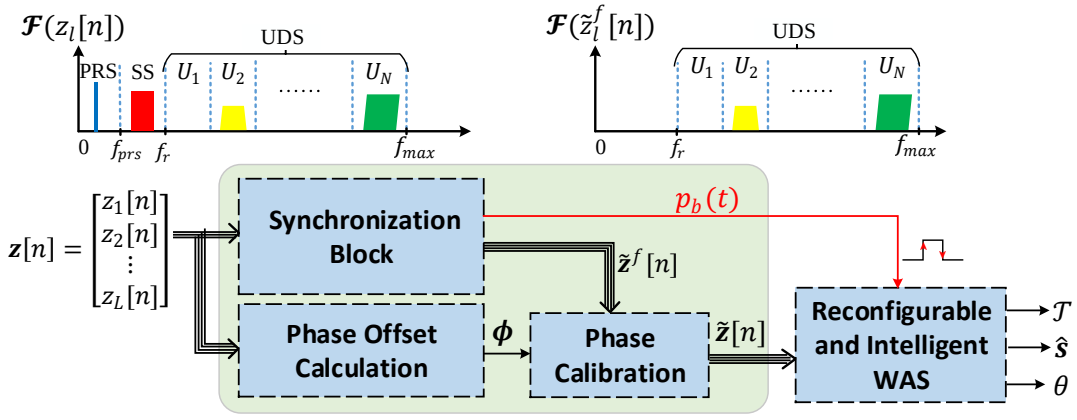

Figure 5.4: Phase calibration and synchronization unit of the UWASS receiver.

performed as

$$\tilde{z}_l[n] = \tilde{z}_l^f[n]e^{-j\phi_l} \tag{5.3}$$

Hence, the phase of $\tilde{\mathbf{z}}[n]$ only contains the phase information introduced by the sparse antenna array. The signal, $\tilde{\mathbf{z}}[n]$, is then passed to the reconfigurable and intelligent WAS block for subsequent baseband processing and learning tasks.

5.3.2 Reconfigurable and Intelligent WAS Unit

The signal, $\tilde{\mathbf{z}}[n]$, received from the phase calibration and synchronization unit, comprises of the wideband spectrum samples. The signal $\tilde{\mathbf{z}}[n]$ is passed through FRI based SNS architecture, as shown in Fig. 5.5, to realize the reconfigurable SNS. Mathematically, the wideband signal consisting of transmission from multiple users at the l^{th} AFE can be represented as

$$\tilde{z}_l[n] = \sum_{q=1}^{N} s_q(t_s)c_q[n]e^{j2\pi f_q(n+\tau_l(\theta_q))} + \eta_l[n] \tag{5.4}$$

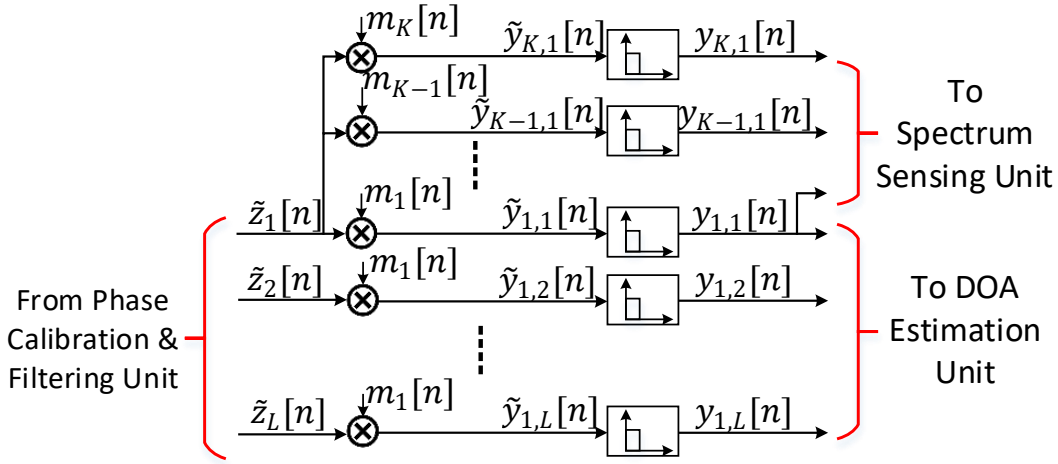

Figure 5.5: FRI based reconfigurable SNS.

where $s_q(t_s) \in \mathbf{b}$ is the transmission/occupancy status of q^{th} frequency band at a time instant t_s, with $s_q(t_s) = 0$ denotes no transmission, and $s_q(t_s) = 1$ denotes the transmission of active SC-FDMA signal. Note that as discussed in Section 5.2.1, $s_q(t_s)$ is unknown at the receiver. For the simplicity of notations, let $s_q(t_s)$ be denoted by s_q. $c_q[n]$ is a discrete-time SC-FDMA signal transmitted at the q^{th} frequency band of a center frequency, f_q, θ_q is the direction of arrival of $c_q[n]$, $\tau_l(\theta_q)$ is the time difference between the reception of signal, $c_q[n]$ at the l^{th} antenna and the reference antenna, and $\eta_l[n]$ is the additive white Gaussian noise at the l^{th} received signal. Note that $\tau_l(\theta_q)$ is dependent on θ_q and the antenna array structure. The DTFT of $\tilde{z}_l[n]$ is given as

$$\tilde{Z}_l(e^{j2\pi f}) = \sum_{q=1}^{N} s_q e^{j2\pi f_i \tau_l(\theta_i)} C_q(e^{j2\pi(f-f_q)}) + \eta_l(e^{j2\pi f}) \tag{5.5}$$

where $C_i(e^{j2\pi f})$ is the DTFT of $c_i[n]$. To generate samples corresponding to a set of specific frequency bands (of indices are stored in β), $\tilde{z}_l[n] \; \forall \; l \in \{1, .., L\}$, is passed through a mixing unit. The mixing function, $m_k[n]$, is defined as

$$m_k[n] = \sum_{i \in \beta} \alpha_{k,i} e^{-j2\pi((i-1)B + f_r)n} \tag{5.6}$$

where $\alpha_{k,i}$ is a mixing coefficient and is generated randomly from Gaussian distribution, f_r is the frequency offset due to PRS and SS, and B is the bandwidth of a frequency band or an SC-FDMA signal. It can be noted that the system model considered in this chapter incorporates the impairments due to practical hardware implementation. Hence, PRS is required due to which the

mixing function introduces an additional $e^{-j2\pi f_r n}$ term as compared to the mixing function used in the UWASS method discussed in Chapter 4. Thus, under the noiseless condition, the DTFT of the output of the mixing unit will become

$$\tilde{Y}_{k,l}(e^{j2\pi f}) = \sum_{n=-\infty}^{+\infty} \sum_{q=1}^{N} s_q c_q[n] e^{j2\pi f_q(n+\tau_l(\theta_q))} \sum_{i\in\beta} \alpha_{k,i} e^{-j2\pi((i-1)B+f_r)n}\ e^{-j2\pi f n} \tag{5.7}$$

$$= \sum_{q=1}^{N} e^{j2\pi f_q \tau_l(\theta_q)} s_q \sum_{i\in\beta} \alpha_{k,i} \sum_{n=-\infty}^{+\infty} c_q[n] e^{-j2\pi(f-(f_q-(i-1)B-f_r))n} \tag{5.8}$$

$$= \sum_{q=1}^{N} e^{j2\pi f_q \tau_l(\theta_q)} s_q \sum_{i\in\beta} \alpha_{k,i} C_q(e^{j2\pi(f-(f_q-(i-1)B-f_r))}) \tag{5.9}$$

For illustration, consider a scenario as shown in Fig. 5.6(a) where $N = 8$ and at a given time slot, t_s, $\mathbf{b} = \{0, 0, 1, 0, 0, 1, 0, 1\}$ and $\beta = \{1, 2, 3, 4, 5, 7, 8\}$. Let $\mathcal{N}_{busy}$ be a set containing the indices of the busy frequency band in $\tilde{\mathbf{z}}[n]$, and $\beta_{busy} = \beta \cap \mathcal{N}_{busy}$ contains busy bands of β. This means $\mathcal{N}_{busy} = \{3, 6, 8\}$ and $\beta_{busy} = \{3, 8\}$. Thus, as discussed in Eq. 5.9, $\tilde{Y}_{k,l}(e^{j\omega})$ will contain the contribution of only those bands for which $s_i = 1$ where $s_i \in \mathbf{b}$, i.e. for $\mathcal{N}_{busy}$ frequency bands. Therefore, Eq. 5.9 is written as

$$\tilde{Y}_{k,l}(e^{j2\pi f}) = \sum_{q\in\mathcal{N}_{busy}} e^{j2\pi f_q \tau_l(\theta_q)} \sum_{i\in\beta} \alpha_{k,i} C_q(e^{j2\pi(f-(f_q-(i-1)B-f_r))}) \tag{5.10}$$

Fig. 5.6(b)-(d) show Eq. 5.10 for all $i \in \mathcal{N}_{busy}$ (i.e. $i \in \{3, 6, 8\}$), and it can be observed that only for β_{busy} bands, i.e. U_3 and U_8, C_i is present in the frequency range $\mathcal{B} = [0, B]$. However, it is noticed from Fig. 5.6(e) that Eq. 5.10 contains

images outside $\mathcal{B}$. Thus, after applying LPF on $\tilde{Y}_{k,l}(e^{j2\pi f})$ over $\mathcal{B}$, the DTFT of the output is

$$Y_{k,l}(e^{j2\pi f}) = \sum_{q \in \beta_{busy}} e^{j2\pi f_q \tau_l(\theta_q)} \alpha_{k,q}\, C_q(e^{j2\pi f}) \tag{5.11}$$

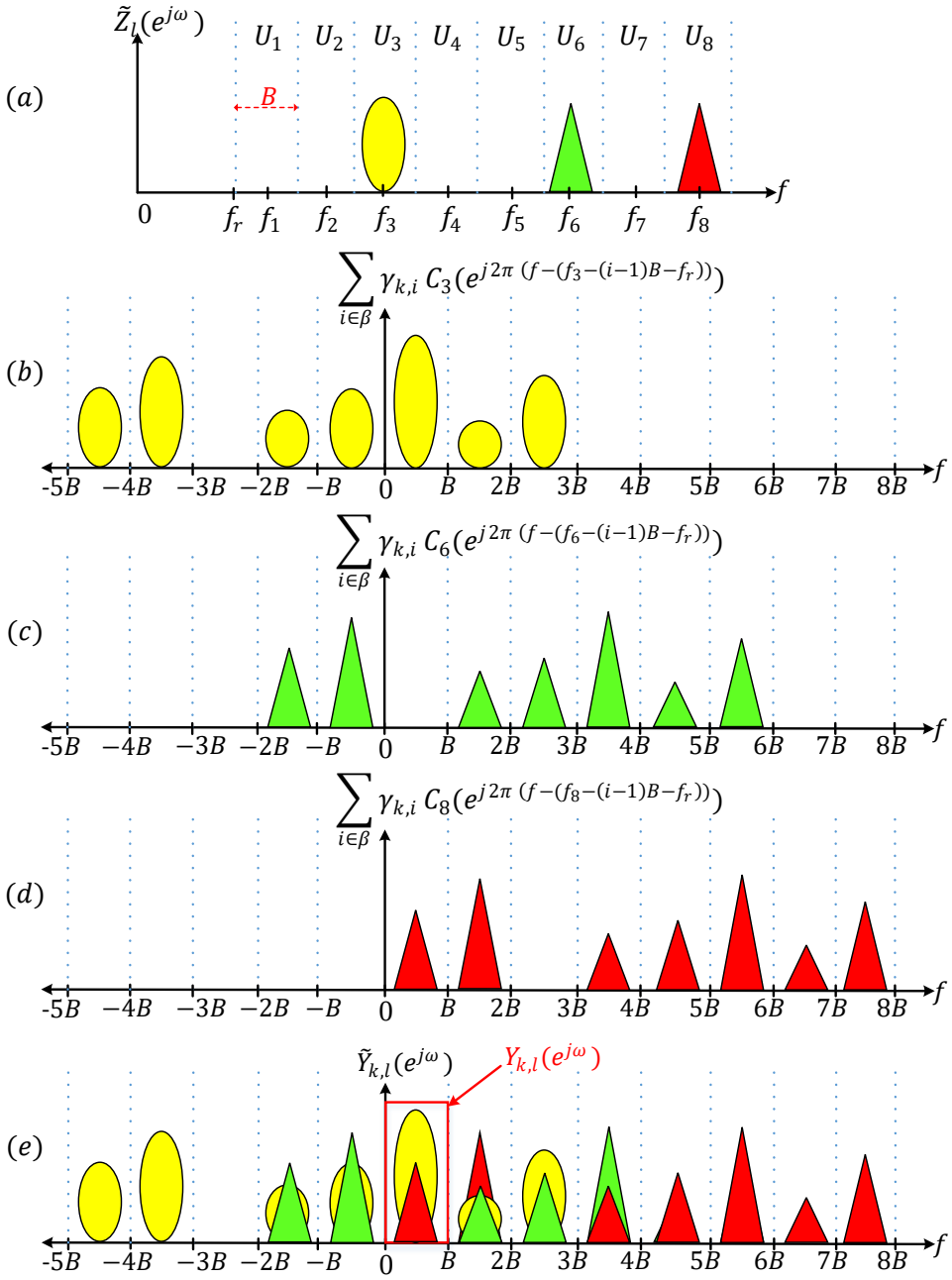

Figure 5.6: DTFT of the (a) l^{th} output of phase calibration and synchronization unit i.e. $\tilde{y}_l[n]$, (b) $\tilde{z}_{k,l}[n]$ for $i = 3$ in Eq. 5.10, (c) $\tilde{z}_{k,l}[n]$ for $i = 6$ in Eq. 5.10, (d) $\tilde{z}_{k,l}$ for $i = 8$ in Eq. 5.10 and (e) $\tilde{z}_{k,l}[n]$ and output of LPF $z_{k,l}[n]$ (in red box).

Now, to perform WAS, the samples $y_{k,1}[n]\ \forall\ k \in \{1, ..., K\}$ are passed to the spectrum sensing unit to determine the estimated status, $\hat{\mathbf{s}}_\beta$ of β frequency bands selected by LDM algorithm and digitized by reconfigurable SNS. Further, the samples $y_{1,l}\ \forall\ l \in \{1, .., L\}$ are passed to the DoA estimation unit to estimate the DoA of detected busy bands in β.

5.3.2.1 Spectrum Sensing Unit

The aim of spectrum sensing (SS) unit is to estimate the status, $\mathbf{s}_\beta \in \{0, 1\}^{|\beta|}$, of β frequency bands. Since SS uses the output, $y_{k,l}[n]$ where $k \in \{1, ..., K\}$ and $l = 1$, Eq. 5.11 can be represented as

$$Y_{k,1}(e^{j2\pi f}) = \sum_{q \in \beta_{busy}} \alpha_{k,q} \tilde{C}_q(e^{j\omega}) \equiv \sum_{q \in \beta} \alpha_{k,q} \tilde{C}_q(e^{j\omega}) \tag{5.12}$$

where $\tilde{C}_q(e^{j2\pi f}) = e^{j2\pi f_q \tau_1(\theta_q)}\ C_q(e^{j2\pi f})\ \forall\ q \in \beta_{busy}$ and is 0 otherwise. For all values of k, Eq. 5.12 can be written in the matrix form as

$$\mathbf{Y_k} = \boldsymbol{\alpha}\tilde{\mathbf{C}} \tag{5.13}$$

where $\boldsymbol{\alpha}$ is a $K \times |\beta|$ matrix with $\alpha_{k,q}$ as its $\{k, q\}^{th}$ entry and $\tilde{\mathbf{C}} \in \mathbb{C}^{|\beta| \times Q}$ is a sparse matrix with $|\beta_{busy}|$ non-zero rows and Q samples. Thus, the estimation of $\mathbf{s}_\beta \in \{0, 1\}^{|\beta|}$ from Eq. 5.13 can be treated as compressive sensing problem. The LDM learns the spectrum statistics, i.e. the prior probability, $\mathbf{p}_{uv}$, which makes the BMP algorithm best fit for the determination of $\tilde{\mathbf{C}}$. But BMP also requires the knowledge of probability distribution function of $P(\tilde{\mathbf{C}}|\mathbf{s})$. As SC-

FDMA signal is transmitted in the multi-user traffic, this parameter is unknown for the considered signal model. Hence, we apply the OMP algorithm [81] to determine the estimated status, $\hat{\mathbf{s}}_\beta \in \{0,1\}^{|\beta|}$, of β frequency bands.

5.3.2.2 DoA Estimation Unit

This unit aims to estimate the DoA of detected busy frequency bands, i.e. β_{busy}. To perform this task, DoA unit utilizes the estimated status, $\hat{\mathbf{s}}_\beta$ and the samples $y_{1,l}\ \forall\ l \in \{1,...,L\}$. For the DoA estimation, Eq. 5.11 can be rewritten as

$$Y_{1,l}(e^{j2\pi f}) = \sum_{q \in \beta_{busy}} e^{j2\pi f_q \tau_l(\theta_q)} D_q(e^{j2\pi f}) \tag{5.14}$$

where $D_q(e^{j2\pi f}) = \alpha_{1,q}\ C_i(e^{j2\pi f})$. All $l \in \{1,...,L\}$ can be represented in the matrix form as

$$\mathbf{Y}_l = \mathbf{E}\ \mathbf{D} \tag{5.15}$$

where $\mathbf{E}$ is a $L \times |\beta_{busy}|$ steering matrix with $e^{j2\pi f_q \tau_l(\theta_q)}$ as its $\{l,q\}^{th}$ entry and $\mathbf{D} \in \mathbb{C}^{|\beta_{busy}| \times Q}$ contains $D_q(e^{j2\pi f})$ as q^{th} row.

The proposed UWASS receiver uses minimum sparse ruler of length L_s to design sparse antenna array. Thus, with L number of physical antennas, the proposed UWASS allows DoA estimation of $L_s - 1$ busy bands where $L < L_s$. For example, as shown in Fig. 5.7, for $L = 3$ and 4 physical antennas, the total number of actual antennas that can be utilized for DoA estimation will be 4 and 6, respectively [77].

For the purpose of exposition, consider $L = 4$ antennas for sparse antenna

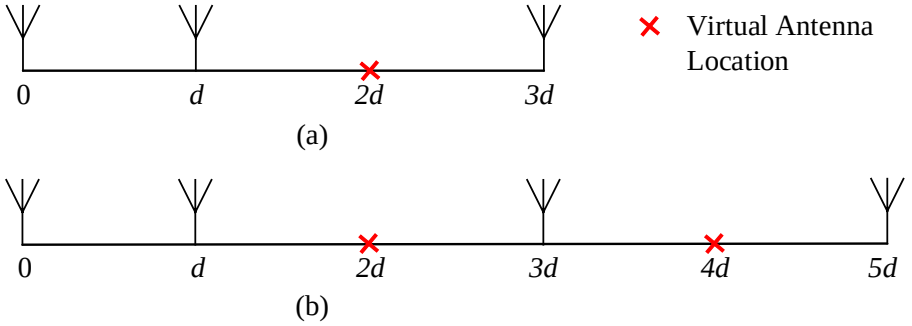

Figure 5.7: Sparse antenna array arrangement for (a) $L = 3$ and (b) $L = 4$.

arrangement. Therefore, $\tau_l(\theta_i) = \frac{d_l}{c} cos(\theta_i)$, where $d_l = [0\ d\ 3d\ 5d]$. Thus, the steering matrix $\mathbf{E}$ for sparse array will be

$$\mathbf{E} = \begin{bmatrix} 1 & 1 & \cdots & 1 \\ e^{j2\pi f_1 \frac{d}{c} cos(\theta_1)} & e^{j2\pi f_2 \frac{d}{c} cos(\theta_2)} & \cdots & e^{j2\pi f_M \frac{d}{c} cos(\theta_M)} \\ e^{j2\pi f_1 \frac{3d}{c} cos(\theta_1)} & e^{j2\pi f_2 \frac{3d}{c} cos(\theta_2)} & \cdots & e^{j2\pi f_M \frac{3d}{c} cos(\theta_M)} \\ e^{j2\pi f_1 \frac{5d}{c} cos(\theta_1)} & e^{j2\pi f_2 \frac{5d}{c} cos(\theta_2)} & \cdots & e^{j2\pi f_M \frac{5d}{c} cos(\theta_M)} \end{bmatrix} \tag{5.16}$$

Now, in order to estimate more DoAs than the number of antennas, L, the procedure similar to [77] is followed. But, here, DoA estimation is performed at sub-Nyquist rate and in contrast to [77], both temporal and spatial sparsity is explored. So, the auto-correlation of $\mathbf{Y}_l$ will be

$$\mathbf{R}_{y,y} = \int_{f \in \mathcal{B}} \mathbf{Y}_l(e^{j2\pi f}) \mathbf{Y}_l^H(e^{j2\pi f}) df \qquad = \mathbf{E}\mathbf{D}\mathbf{D}^H\mathbf{E}^H \tag{5.17}$$

$$= \mathbf{E}\mathbf{R}_{d,d}\mathbf{E}^H \tag{5.18}$$

Since the SC-FDMA signals transmitted at every frequency band are uncorrelated, $\mathbf{R}_{d,d}$ is a diagonal matrix. Hence, by applying Kronecker and Khatri-Rao

properties of vectorization on Eq. 5.18 , we get

$$vec(\mathbf{R}_{y,y}) = \mathbf{E}^* \otimes \mathbf{E}\ vec(\mathbf{R}_{d,d}) \tag{5.19}$$

$$= \mathbf{E}^* \odot \mathbf{E}\, \boldsymbol{p}_d \tag{5.20}$$

where $\boldsymbol{p}_d = diag(\mathbf{R}_{d,d})$, and $\otimes$ and $\odot$ are Kronecker and Khatri-Rao operators. The $\mathbf{E}^* \odot \mathbf{E}$ is a $L^2 \times M$ matrix, but it contains $L^2 - (2L_s - 1)$ redundant rows. Thus by removing the redundant rows and re-arranging Eq. 5.20 in the ascending order of steering vector, we get

$$\begin{bmatrix} r_{-(L_s-1)} \\ \vdots \\ r_0 \\ \vdots \\ r_{L_s-1} \end{bmatrix} = \underbrace{\begin{bmatrix} e^{j2\pi f_1 \frac{-(L_s-1)d}{c} cos(\theta_1)} & \dots & e^{j2\pi f_M \frac{-(L_s-1)d}{c} cos(\theta_M)} \\ \vdots & \vdots & \vdots \\ 1 & \dots & 1 \\ \vdots & \vdots & \vdots \\ e^{j2\pi f_1 \frac{(L_s-1)d}{c} cos(\theta_1)} & \dots & e^{j2\pi f_M \frac{(L_s-1)d}{c} cos(\theta_M)} \end{bmatrix}}_{\mathbf{E}_{new}} \boldsymbol{p}_d \tag{5.21}$$

where $\mathbf{E}_{new}$ is a steering matrix of size $(2L_s - 1) \times M$. Now, similar to [77], L_s vectors are generated for every $\mathbf{r}_{l_s} = [r_{l_s-(L_s-1)}, \cdots, r_{l_s-1}, r_{l_s}]^T \ \forall \ l_s = \{0, \cdots, L_s - 1\}$. Subsequently, a sample average of the auto-correlation of these vectors is calculated as

$$\mathbf{R}_{L_s} = \frac{1}{L_s} \sum_{l_s=0}^{L_s-1} \mathbf{r}_{l_s} \mathbf{r}_{l_s}^H \tag{5.22}$$

Finally, MUSIC algorithm [141] is applied on $\mathbf{R}_{L_s}$ to determine the DoAs of β_{busy} frequency bands.

Note that once the status, $\hat{\mathbf{s}}_\beta \in \{0,1\}^{|\beta|}$, is estimated in the SS unit, the next task is to determine the carrier frequency of the user for which $\hat{\mathbf{s}}_\beta = 1$. For simplicity of our analysis, the carrier frequency of an SC-FDMA signal is considered in the U_i frequency band is same as its center frequency, i.e. $f_i = f_r + i\frac{B}{2} \; \forall \; i \in \{1,2,....,N\}$. However, as done in Chapter 4, this assumption can be removed by applying the MUSIC algorithm on the possible sets of carrier frequencies of β_{busy} frequency bands.

Now to determine $\theta_i \; \forall \; i \in \beta_{busy}$, the MUSIC algorithm is applied. Here an over-complete steering matrix, $\mathbf{E}_c$, is generated where θ varies from $0°$ to $180°$ with a grid size of $0.5°$ for every f_i. Then the MUSIC spectrum is generated as

$$P(\theta) = \frac{1}{\mathbf{e}(\theta)^H \mathbf{V}_n \mathbf{V}_n^H \mathbf{e}(\theta)} \tag{5.23}$$

where $\mathbf{e}(\theta)$ is a steering vector of $\mathbf{E}_c$ for a particular θ, and $\mathbf{V}_n$ is the noise subspace of the auto-correlation of $\mathbf{R}_{L_s}$. The peaks in the MUSIC spectrum correspond to the DoAs of transmissions present in the sensed spectrum. For example, two and three peaks in the MUSIC spectrums shown in Fig. 5.8 denote two busy bands with DoAs $18°$ and $62°$, and three busy bands with DoAs $42°$, $87°$ and $145°$, respectively.

5.3.2.3 LDM Unit

To sense a large number of frequency bands, the size of the selected subset, β, should be as large as possible. But as discussed in Chapter 4, for ULA antenna arrangement, the UWASS incurs characterization failure if the number of busy

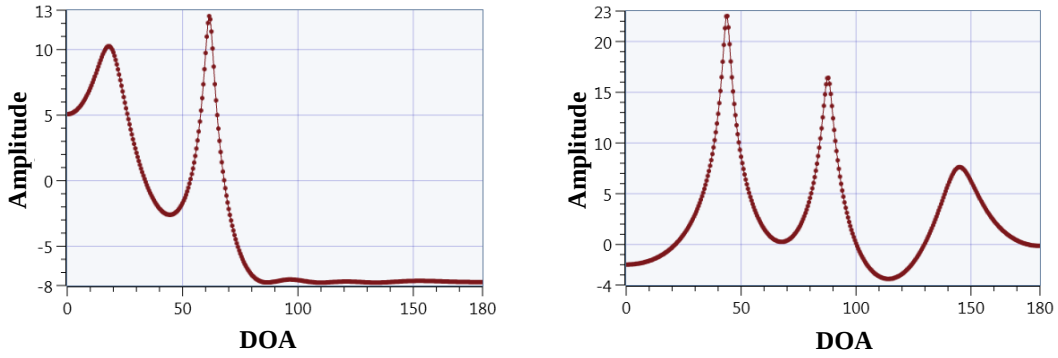

(a) (b)

Figure 5.8: MUSIC spectrum (a) For two directional users and (b) For three directional users.

bands, i.e. $|\beta_{busy}| \geq L$. In the case of the proposed sparse UWASS and as mentioned in Lemma 1, $|\beta_{busy}| < L_s$ for the successful sensing of $\hat{\mathbf{s}}_\beta$ and θ_i of β_{busy} bands.

Lemma 1: If L_s is the length of the minimum sparse ruler then under the noiseless condition, the perfect recovery of the occupancy status and DoA of β_{busy} bands is possible only if

1. $K \geq L_s - 1$
2. $||\mathbf{s}_\beta||_0 < L_s$ i.e. $|\beta_{busy}| < L_s$

In order to learn the spectrum statistics and determine the best subset, three MPMAB algorithms: 1) Ideal Policy (IP) 2) K^+-ϵSSLE and 3) K^+-BSSLE have been integrated in the proposed UWASS testbed.

5.4 Experimental Performance and Complexity Analysis

This section presents extensive experimental results in real-radio conditions using the proposed testbed along with the hardware complexity analysis. The

prototype setup in Fig. 5.9 demonstrates the UWASS receiver and phase reference generator while a dynamic wireless traffic generator is placed at distant locations to generate multi-directional multi-user traffic. As shown in Fig. 5.10, for all the results presented in this section, the dynamic wireless traffic generator module consists of two NI-USRP 2944R with $M = 3$ active transmission directions via three directional HORN-antennas DP240-AB. Since the phase reference generator module outputs a common reference signal, $p(t)$, to all the AFE of the receiver, only one Ettus USRP N200 is used. The UWASS receiver module consists of two NI-USRP 2944R to provide four AFEs integrated with $L = 4$ omni-directional VERT2450 antennas of the phase antenna array. For sparse antenna array (SAA) arrangement, the antenna spacing, $d_l = ld$ where $l \in \{1, 2, 3\}$, is considered to be integer multiple of $d = \frac{c}{2f_t} = \frac{3\times10^8}{2\times2.4\times10^9}$. Various parameters of different blocks of the proposed prototype are given in Table 5.1.

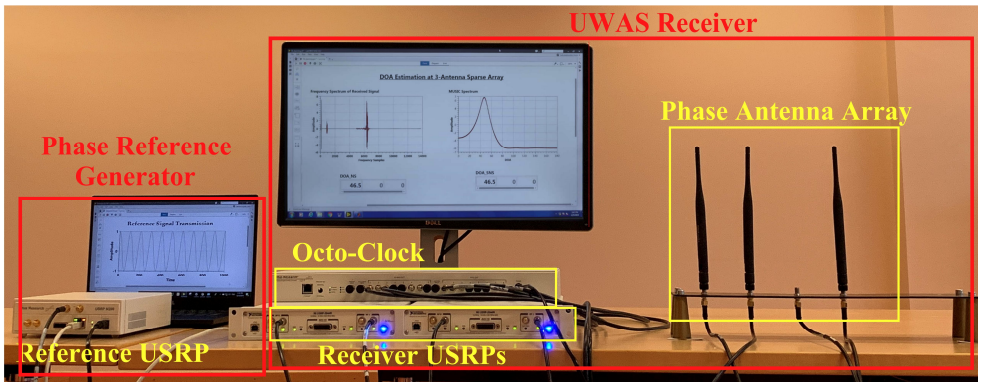

Figure 5.9: Proposed prototype setup consisting of phase reference generator and UWASS receiver.

The effect of antenna array arrangement, i.e. ULA [140] (work presented in Chapter 4) and proposed SAA based UWASS on the throughput for various MPMAB algorithms, are compared in Fig. 5.11. The analysis is done with a

receiver gain of 10 dB for both antenna array arrangements. 2, 3 and 4 antenna ULA are considered, and they are referred to as 2-ULA, 3-ULA and 4-ULA, respectively. For sparse arrangement, 3 and 4 antenna sparse array are considered, and they are referred to as 3-SAA and 4-SAA, respectively. For 3-SAA, antennas are placed at location $\{0, 1, 3\}$ whereas for 4-SAA, antennas are present at locations $\{0, 1, 3, 5\}$, thereby enabling the sensing for 3 and 5 directional signals, respectively. Due to the increase in the number of antennas from 2-ULA to the 4-SAA array, the throughput of the intelligent UWASS also increases. Furthermore, since the number of possible antennas in the 4-ULA and 3-SAA are the same (i.e. 4), the throughput of all LDM methods also remains the same for both 4-ULA and 3-SAA antenna arrangement.

The hardware analysis of the proposed UWASS is compared with [140] (referred to as Proposed-ULA) and [77] (referred to as NS-SAA) in Fig. 5.12. Note that the proposed UWASS methods discussed in Chapter 4 and this Chapter are referred as Proposed-ULA and Proposed-SAA, respectively. Since [77] assumes the prior knowledge of the carrier frequency, for the fair comparison

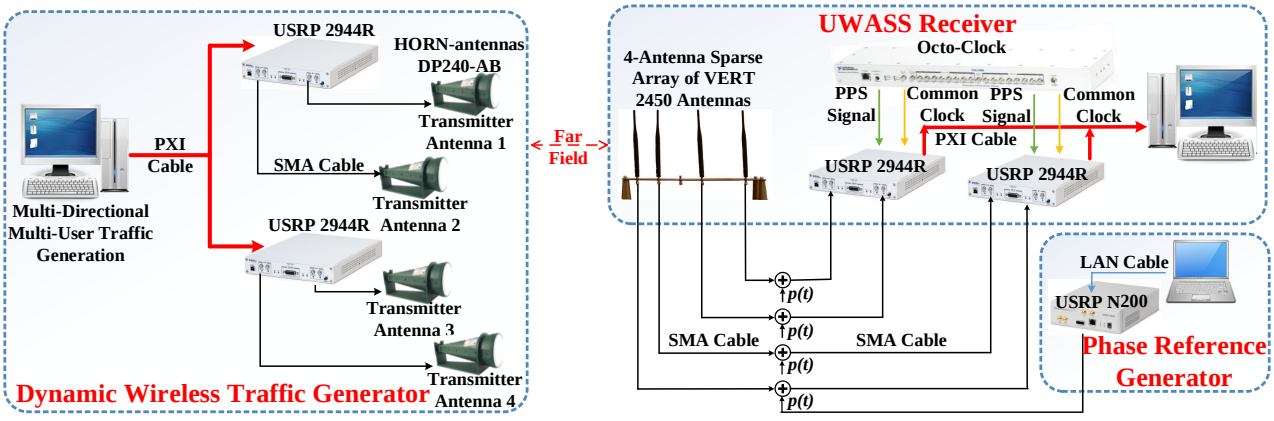

Figure 5.10: Graphical representation of the experimental set-up.

Table 5.1: Transmission and reception parameters.

Parameters		Value
Dynamic Wireless Traffic Generator Module	N	8
	M	3
	B	1.4 MHz
	f_r	1.4 MHz
	Guard Band	400 MHz
	f_{max}	13 MHz
	Resource blocks in SC-FDMA	6
	Antenna Gain	0 dB
	IQ Sampling Rate	13 $Msps$
	Transmission Frequency, f_t	2.4 GHz
Phase Reference Module	Carrier frequency	200 kHz
	f_{prs}	400 kHz
	Antenna Gain	0 dB
	IQ Sampling Rate	13 $Msps$
	Transmission Frequency, f_t	2.4 GHz
UWASS Receiver Module	L	2, 3 and 4
	L_s	4 and 6
	K	3 and 5
	Common Clock	10 MHz
	PPS Signal	1 pulse/second
	Antenna Gain	0 dB, 2 dB, 6 dB and 10 dB
	IQ Sampling Rate	13 $Msps$
	Reception Frequency, f_t	2.4 GHz

with [140] and proposed work, an energy detector is applied to determine the status of frequency bands followed by the DoA estimation method presented in [77]. Note that similar to the spectrum occupancy detection algorithms used in the proposed work and [140], the performance of the energy detector improves with an increase in antenna gain. It can be observed from Fig. 5.12(a)

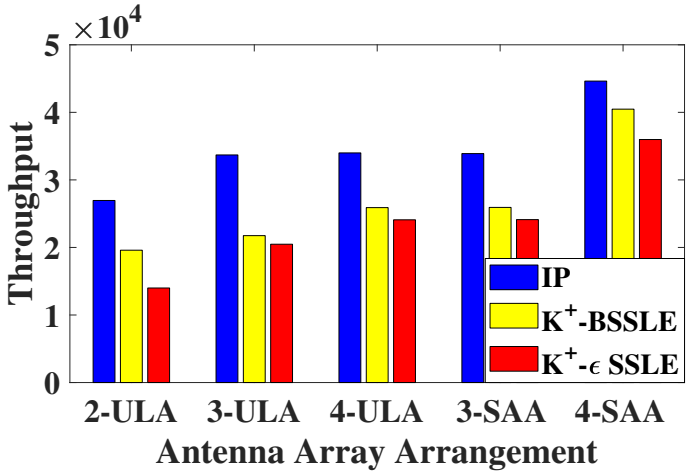

Figure 5.11: Throughput achieved by the MPMAB algorithms for various arrangements of the antenna array.

that the number of characterization failures is highest for NS-SAA [77], followed by Proposed-ULA [140] and the proposed-SAA method. This happens because NS-SAA uses the Nyquist sampling (NS) method for UWASS. Since it senses all frequency bands, characterization failure occurs whenever the number of busy frequency bands in the spectrum is higher or equal to the total number of antennas. Whereas proposed-ULA and the proposed-SAA works employ reconfigurable SNS based UWASS, which dynamically selects a set of frequency bands for sensing and allows learning and decision making unit to ensure that the number of busy bands in the sensed spectrum is less than the total number of antennas.

Fig. 5.12(b) shows the comparison of total throughput achieved by NS-SAA [77], Proposed-ULA [140] and proposed-SAA methods. Since the proposed-SAA method and NS-SAA can sense a higher number of frequency bands than [140], they receive higher throughput. The proposed method achieves a higher throughput than NS-SAA [77] because it faces higher number of charac-

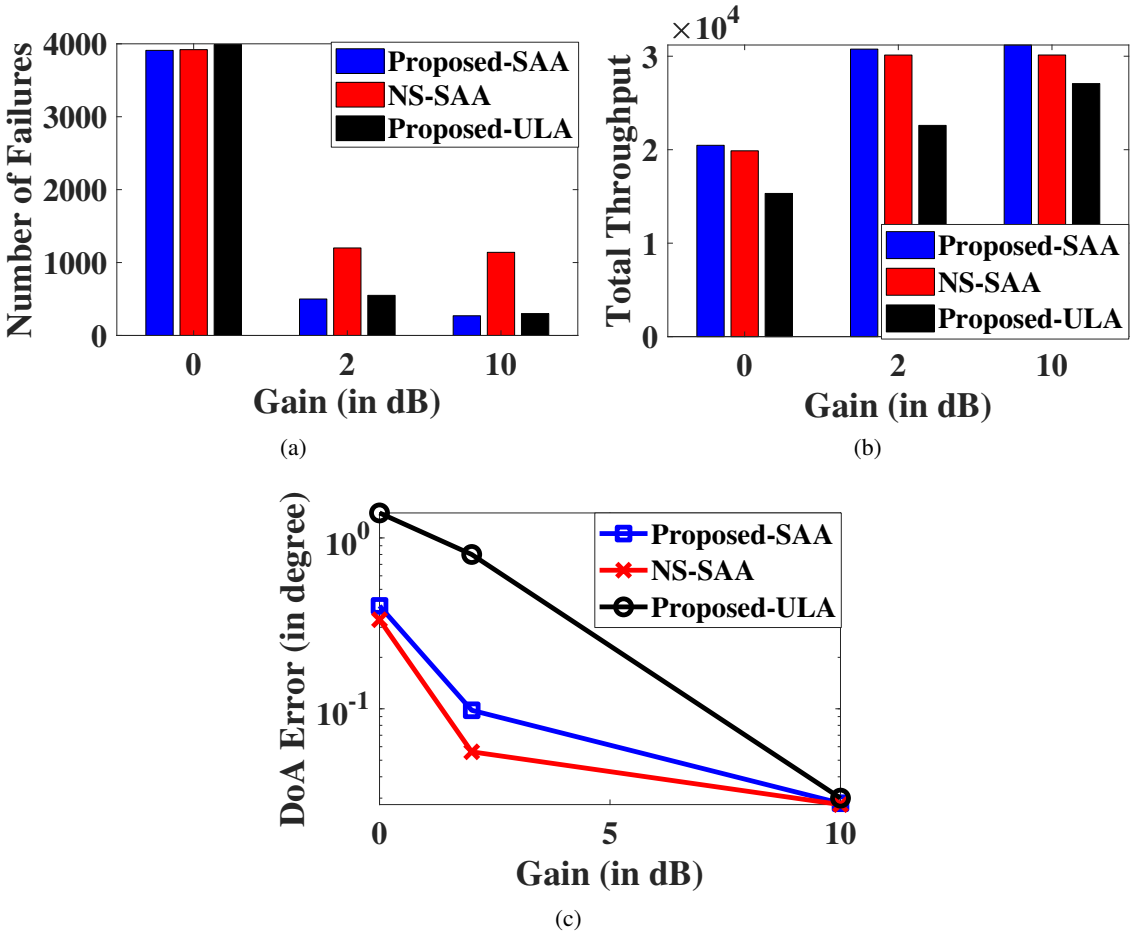

Figure 5.12: Comparison of the proposed reconfigurable UWASS with [140] and [77] for different values of receiver antenna gain (a) Throughput, (b) Number of characterization failure and (c) DOA Estimation Error.

terization failures, as discussed in Fig. 5.12(a), which leads to lower throughput than the proposed method. The DoA estimation error is shown in Fig. 5.12(c). Since the total number of antennas in the proposed-ULA is less than that of NS-SAA and proposed-SAA methods, the DoA error is highest for proposed-ULA. The DoA error of the proposed method is slightly higher than NS-SAA, and it happens because NS-SAA works on the Nyquist samples, whereas the proposed method works on the sub-Nyquist samples.

Note that the DoA estimation error reported in Fig. 5.12(c) does not consider the DoA estimation error incurred due to the reconstruction failure. As dis-

cussed in Section 4.3.2, the DoA estimation error performance of the proposed UWASS method is better than the state-of-the-art wideband angular spectrum sensing methods when the effect of reconstruction failure is included in the DoA error performance analysis.

Next, the DoA estimation error of the UWASS receiver is compared with ULA and sparse array for the different number of directional user signals and sampling methods, i.e. SNS and Nyquist sampling (NS). At the transmitter, the DoA of each user is randomly selected. The DoA estimation errors for one, two and three directional user signals are shown in Fig. 5.13-5.15, respectively. It can be validated that the DoA estimation error decreases with an increase in the number of antennas. As 4-SAA creates two more virtual antennas, the DoA error is minimum for 4-SAA arrangement. It is also validated that the DoA estimation error increases when the number of directional users increases from 1 to 3. Furthermore, since the strength of the received signal increases with antenna gain, the DoA estimation error decreases significantly. Similarly, with an increase in the gain, the performance of SNS based UWASS approaches to NS based UWASS.

The deviation in DoA measurement, Δ, is shown in Fig. 5.16(a)-(c) for one, two and three directional user signals, respectively. For one user, the deviation of SNS and NS based WAS is the same; hence, the deviation for only one case, i.e. NS based WAS, is shown. It is observed that for one user signal, the deviation becomes zero for 4-ULA and 4-SAA. When the number of DoA sources increased from 1 to 3, the deviation becomes non-zero, and since 4-SAA creates a

total of 6-antennas, the deviation is minimum for the 4-SAA case. Furthermore, for a given number of antennas, the deviation increases with the number of user signals. For example, for the 3-ULA arrangement, the deviation increases as $2^0, 7^0$ and 15^0 when the number of user signals increases from one, two and three, respectively.

The value of actual DoA and estimated DoA for different antenna array arrangements of the reconfigurable UWASS is shown in Table 5.2. It can be observed that there is a difference between the true and estimated value of DoA. This difference is maximum for 3-SAA than 4-ULA and 4-SAA. It happens due to the antenna pattern fluctuations, which depend on the hardware equipment

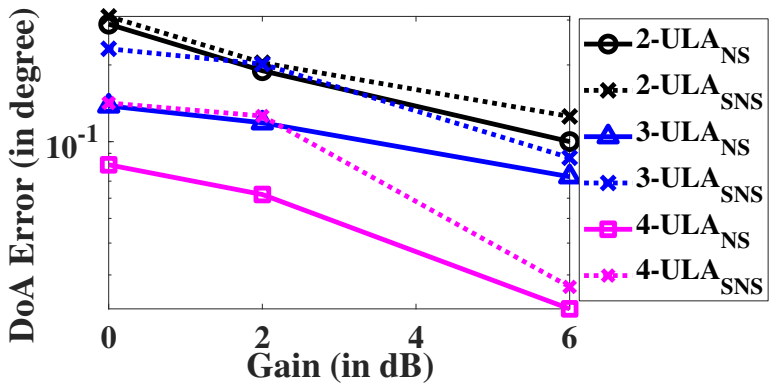

(a)

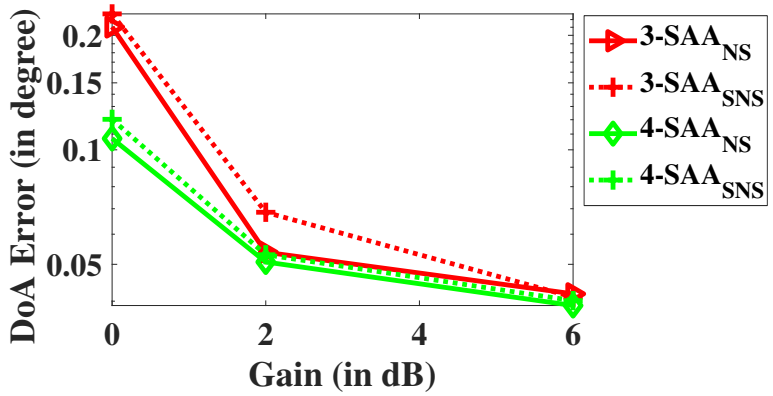

(b)

Figure 5.13: DoA estimation error in case of single directional user signal for (a) ULA antenna arrangement and (b) SAA arrangement.

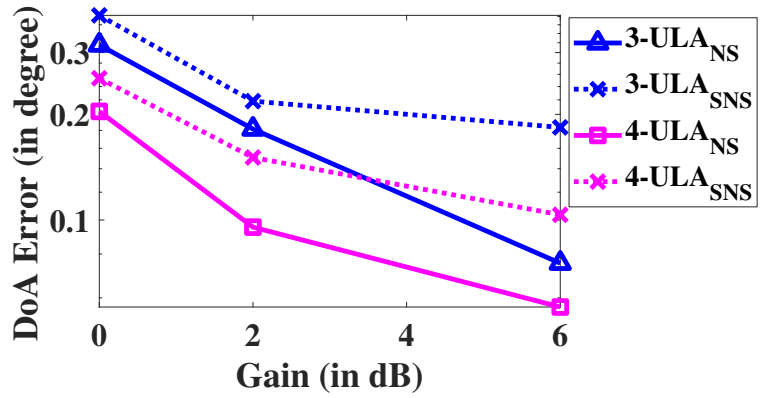

(a)

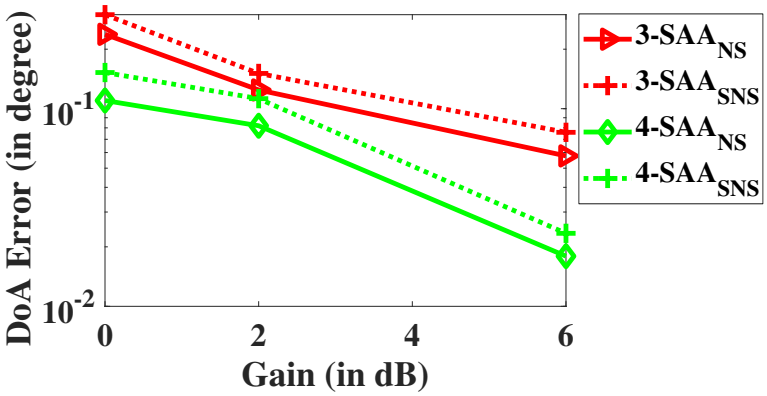

(b)

Figure 5.14: DoA estimation error in case of two directional user signals for (a) ULA antenna arrangement and (b) SAA arrangement.

surrounding the antenna array. Furthermore, it is also observed that the difference between the true and estimated DoA is smaller for 4-SAA when compared to 4-ULA. The happens because 4-ULA provides 4 antennas for DoA estima-

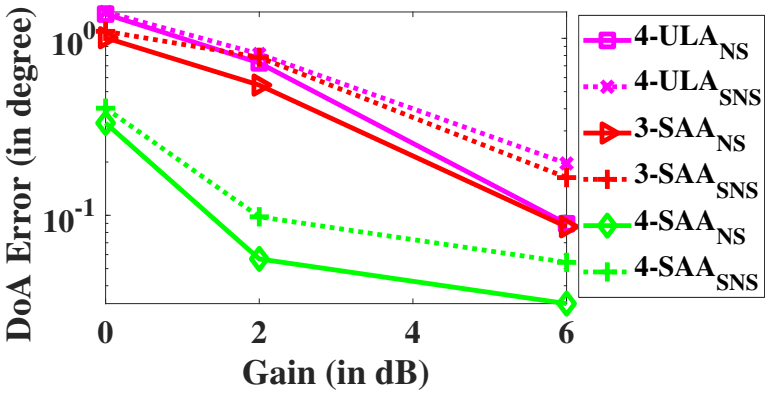

Figure 5.15: DoA estimation error for three directional user signals.

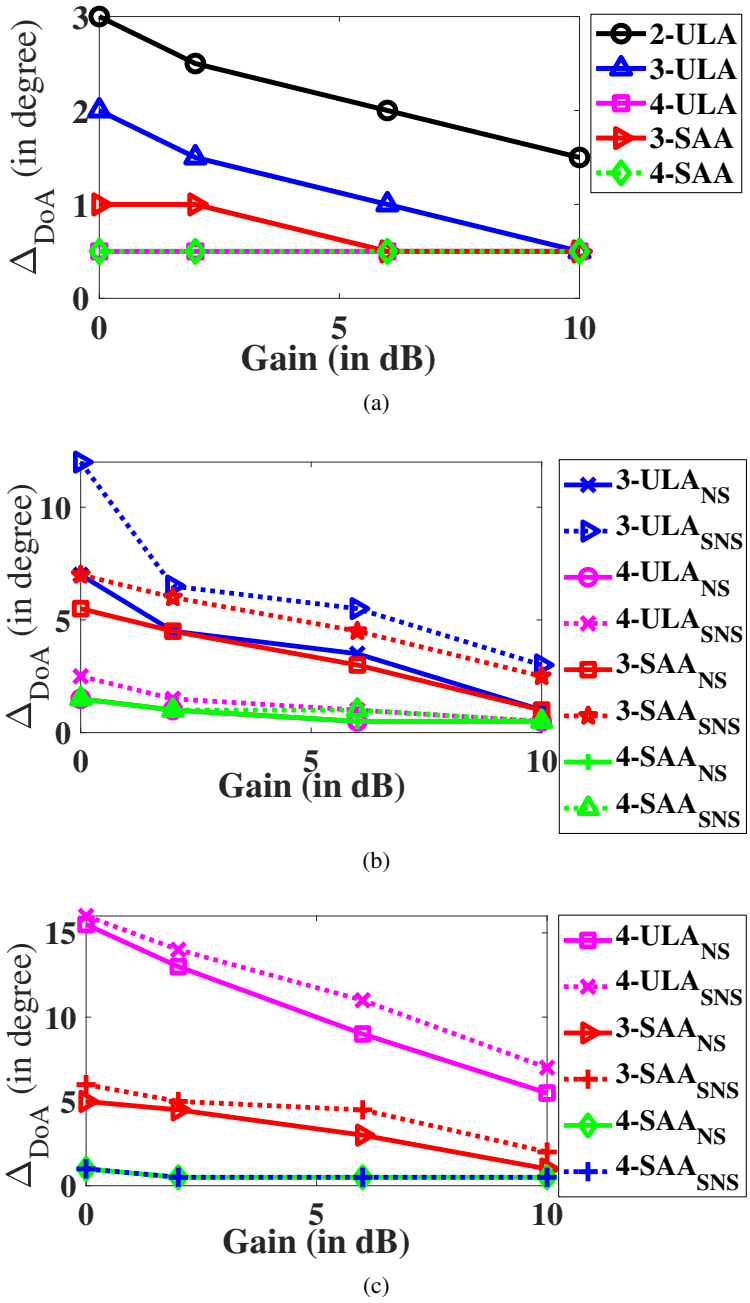

Figure 5.16: The deviation in DoA measurement for (a) One directional user signal, (b) Two directional user signals and (c) Three directional user signals.

tion, whereas 4-SAA provides total 6 antennas (i.e. 4 actual and 2 virtual antennas). Due to an increase in the total number of antennas, 4-SAA gives the best performance.

Table 5.2: True and estimated DoAs for different antenna array.

True DoA Angle	Antenna Array Arrangement		
	4-ULA	3-SAA	4-SAA
0°	0°	0°	0°
30°	34.59°	33.97°	31.57°
52°	54.28°	60.89°	53.81°
110°	114.30°	116.83°	112.44°
155°	156.37°	161.73°	157.74°
180°	180°	180°	180°

5.4.1 Hardware Complexity Analysis

This section compares the hardware complexity of the proposed and existing UWASS methods [23–27, 29, 140] when implemented on the AFE. Table 7.2 compares the hardware complexity of these UWASS methods for seven different parameters. For M number of users in the wideband spectrum, the number of antennas and ADCs required in all approaches is given in the first two rows. It can be observed that the proposed approach, along with [24] and [26] offer a lower number of antennas and ADCs compared to other approaches [23, 25, 27, 29, 140]. This results in a huge savings in the AFE, which consumes significant area and power of the wireless receiver and offers limited flexibility and upgradability. Although compared to [24] and [26], the proposed UWASS utilizes a slightly higher number of antennas and ADCs, the analog bandwidth of ADCs used in [24] and [26] is equal to the Nyquist rate. In contrast, the analog bandwidth in our proposed UWASS is N times lower. Furthermore, unlike [26], the proposed approach does not require a precise delay element in AFE making it possible to realize in hardware for UWASS.

Next, the comparison of characterization failure is made. As shown in the fifth row of Table 5.3, UWASS approaches in [23–25] and [26,27] incur failures whenever $M \geq L$ and $M \geq L_s$, respectively, i.e. whenever the number of active transmissions/users in the wideband spectrum is higher than the number of antennas. Since the wideband spectrum ranges over a few GHz, and L can have a limited value ranging from $1-64$, the probability of characterization failure is very high in existing methods due to the contiguous sensing approach. This is because the wideband spectrum may have users from other services such as narrowband IoT, WLAN and applications in the unlicensed spectrum. Due to the augmentation of LDM with non-contiguous digitization, the characterization failure in the proposed reconfigurable SNS does not depend on the occupancy of the wideband spectrum. Instead, the characterization failure happens when $\beta_{busy} \geq L_s$ and hence, the design of the LDM unit is critical in the proposed approach. The only limitation of the proposed UWASS method is that a user can be present only in a single frequency band and thus limits its carrier frequency. But this assumption is valid and practical as per 3GPP communication standards where carrier frequencies can take only predefined values as per the defined carrier frequency raster.

5.4.2 Hardware Feasibility of Proposed UWASS

This work uses the USRP based hardware prototype for developing the UWASS testbed. Since the USRPs have inbuilt ADC tightly integrated with antennas, SNS is employed at the received digitized signal to perform UWASS at a sub-

Table 5.3: Hardware complexity comparison of different UWASS approaches.

Characteristics	**[23]**	**[24]**	**[25]**	**[26]**	**[27]**	**Proposed ULA**	**Proposed SAA**
Number of Antennas	$M+1$	$M+1$	$2M+1$	$4M/K$	$< M+1$	$M+1$	$< M+1$
Number of ADCs	$2M+1$	$M+1$	$2M+1$	$4M+K-1/K$	$< (M+1)K$	$2M-1$	$< 2M-1$
Analog BW of ADCs	High	High	Low	High	High	Low	Low
Precise delay	Required	Not Required	Not Required	Required	Required	Not Required	Not Required
Characterization Failure ($M \geq L$)	Yes	Yes	Yes	Only if $M \geq L_s$	Only if $M \geq L_s$	No	No
Characterization Failure ($\beta_{busy} \geq L$)	Yes	Yes	Yes	Yes	Yes	Yes	Only if $\beta_{busy} \geq L_s$
Constraint on f_i	No	No	No	No	No	Yes	Yes

Nyquist rate. To enable SNS on the frequency bands spaced across an ultra-wideband RF signal, the AFE similar to [61] needs to be designed. The AFE of these two differs mainly in the generation of the mixing function. This is not challenging since it requires minor changes in the RTL code of the generator. Furthermore, the proposed UWASS is capable of performing non-contiguous wideband sensing and DoA estimation of the occupied frequency bands, whereas [61] only performs contiguous wideband spectrum sensing. Thus, to develop end-to-end hardware without USRP, AFE integration with a multi-antenna array and its calibration is also an important task.

5.5 Summary

In this chapter, a multi-antenna USRP testbed is developed to perform wideband angular spectrum sensing over a non-contiguous wideband spectrum. To the best of our knowledge, it is the first work that demonstrates wideband angular sensing on the sub-Nyquist sampled non-contiguous spectrum. To generate an M-directional traffic signal, $\frac{M}{2}$ NI-USRP 2944 are used as a transmitter. The directional traffic signal is generated in the form of a multiband signals whose occupancy status follows the unknown Markovian decision process. Similar to 5G, an uncorrelated single carrier frequency divison multiple access (SC-FDMA) is transmitted on each occupied frequency band of a multiband signal.

Next, we discussed the design of a wideband receiver to perform ultra-wideband angular spectrum sensing (UWASS). The multi-antenna receiver USRPs receives the multiband traffic signal. But since the received signal passes through the different analog front ends of the receiver USRP ports, a random phase offset is added to each received signal. A phase synchronization signal is combined with the output of the receiver antennas to monitor and remove these phase offsets continuously. Then finally, the phase calibration is performed on the output signal of the receiver USPRs followed by the implementation of an intelligent reconfigurable UWASS.

As the proposed UWASS can be applied to any antenna array, the experiment is performed for uniform linear antenna array (ULA) and sparse antenna array (SAA) with L number of physical antennas. The SAA antenna arrangement is

discussed in the latter part of the chapter to sense more than $L-1$ signals. Finally, in the end, the experimental analysis is performed in terms of throughput, number of failures and deviation in the DoA estimation for different antenna array configurations. As expected, the performance of SAA is better than ULA due to higher number of total antennas, and it improves with an increase in L.

In the next chapter, we discuss another wideband signal characterization that determines the modulation schemes of the occupied frequency bands at sub-Nyquist rate.

Chapter 6

Automatic Modulation Classification for Wideband Spectrum Analyzer

An automatic modulation classifier (AMC) aims to estimate the modulation scheme of the received signal blindly. As discussed in the previous chapters, future generation wideband receiver requires sub-Nyquist sampling (SNS) based wideband spectrum characterization. This chapter focuses on determining one of the characteristics, i.e. the modulation scheme of the detected occupied frequency bands from the sub-Nyquist samples of a wideband spectrum. Due to recent advances in the classification accuracy of deep learning based classifiers, here, we explored the performance of deep learning based AMC (DLMC) on the sub-Nyquist sampled wideband spectrum. Firstly, we discuss the DLMC to determine the modulation scheme of every detected occupied band sequentially. The performance of the proposed sequential AMC is validated on the USRP hardware testbed. A single unified pipeline to simultaneously determine the occupancy status and modulation schemes of all occupied frequency bands

is presented in the latter part of the chapter.

6.1 Signal Model

Consider a wideband spectrum consisting of multiple disjoint (i.e. distinct central frequency) narrowband signals of maximum possible bandwidth, $B\ Hz$. Mathematically, the received wideband signal, $y(t)$, can be modelled as

$$x(t) = \sum_{i=1}^{M} h_i(t) * c_i(t) e^{j2\pi(f_i+f_d)t} + \eta(t) \tag{6.1}$$

where M is the maximum possible number of narrowband signals in $x(t)$, $c_i(t)$ is the i^{th} modulated narrowband signal of carrier frequency f_i, $h_i(t)$ is the channel response faced by the i^{th} signal, f_d is the Doppler frequency, $\eta(t)$ is additive white Gaussian noise (AWGN) and $*$ is a convolution operator. The modulated narrowband signal, $c_i(t)$, can be represented as

$$c_i(t) = \sum_{v=1}^{V} g(t - vT_s) b_v^m \tag{6.2}$$

where $g(t)$ is the impulse response of a root raised cosine pulse shaping filter, T_s is the symbol period, b_v^m is the v^{th} modulated symbol of m^{th} modulation scheme and V is the length of symbol sequence. Similar to the assumptions made in previous chapters, the following realistic assumptions have been made on the wideband signal:

1. The received wideband spectrum, $X(f)$, of Nyquist frequency, f_s, is divided into N frequency bands of bandwidth, $B = \frac{f_s}{N}$.

2. The bandwidth of a narrowband signal, $c_i(t)$, does not exceed $B\ Hz$.

6.2 Proposed Sequential DLMC

The proposed classifier consists of two main stages: 1) Digitization and 2) Classification. As shown in Fig. 6.1, the digitization stage digitizes the wideband signal, $x(t)$, via SNS based RF to digital conversion block followed by the reconstruction of the Nyquist rate signal, $\hat{x}[n]$, from the sub-Nyquist samples, $\mathbf{y}[n]$. The output is then passed to the deep learning based AMC (DLMC), which identifies the modulation schemes of various occupied frequency bands in the digitized signal. We employ non-contiguous SNS and orthogonal matching pursuit (OMP) to perform digitization and reconstruction, respectively [81]. For determining the modulation schemes, DLMC is applied sequentially on all the reconstructed occupied frequency bands. The CNN [103] and LSTM neural networks [142] are widely used for classification in signal processing and have shown good modulation classification accuracy on Nyquist sampled data. Hence, this work explores the performance of these DL classifiers on the sub-Nyquist sampled data.

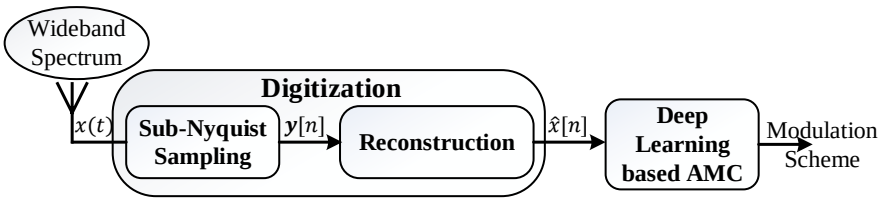

Figure 6.1: Block diagram of the proposed SNS-AMC.

6.3 Implementation Details and Dataset Generation

The DL models work in two modes: 1) Offline training mode and 2) Online inference mode (i.e. testing mode). Offline training mode provides the learned network parameters, which are then used by the inference mode to determine the modulation schemes of the signals present in the occupied frequency bands. The implementation details of the CNN and LSTM classifiers are given below:

6.3.1 CNN Model

Similar to [103], the CNN model consists of three convolution layers with 256, 80 and 32 filters of size 1×3, 2×3 and 3×3, respectively. The model also has 2 fully connected (FC) layers with 256 and 7 neurons, respectively. All layers have a ReLU activation function except the last dense layer, which has a softmax activation function [143]. Regularization technique like dropout of 60% is used to prevent the model from overfitting.

6.3.2 LSTM model

The architecture of the LSTM network model is similar to that used in [142]. It consists of two LSTM layers and a dense layer with seven neurons. This dense layer has a softmax activation function. Here, dropout of 50% and batch normalization are used in the LSTM layers.

6.3.3 Dataset Generation

The dataset is generated synthetically using the MATLAB tool. It consists of seven widely used modulation schemes: BPSK, QPSK, 16-QAM, 64-QAM, 128-QAM, 256-QAM and 8-PAM. The dataset is keyed by both modulation schemes and signal to noise ratio (SNR). The SNR range from $-10\,dB$ to $25\,dB$ at a step size of $5\,dB$ is considered. The datasets used for comparison are:

$\mathbf{D_{IQ}}$: The time-domain IQ sample vectors of a narrowband signal extracted from the reconstructed wideband signal are considered. The length of IQ samples is 256 units. The IQ sample vector is separated into two vectors containing in-phase and quadrature-phase components. Hence, the dataset has a shape of 2×256 where the in-phase and quadrature-phase components form the two rows, respectively.

$\mathbf{D_{AP}}$: It comprises time-domain amplitude-phase vectors (i.e. polar representation of IQ samples) of a narrowband signal extracted from the reconstructed wideband signal. The length of the vector is 256 units. The data has a shape of 2×256, where the amplitude and phase parts form two rows. The amplitude is l-2 normalized, and phase (in radians) is normalized between the range -1 and 1 [142].

Furthermore, in each case, two types of wireless channels are considered: 1) AWGN ($\mathbf{D_{IQ1}}$ and $\mathbf{D_{AP1}}$) and 2) AWGN channel and Rayleigh fading ($\mathbf{D_{IQ2}}$ and $\mathbf{D_{AP2}}$). Each dataset consists of $112,000$ examples, out of which 75% (i.e $84,000$ examples) is used for training and remaining (i.e $28,000$ examples) is

used for testing.

6.4 Performance Analysis

This section analyzes the proposed sequential DLMC over various datasets that correspond to different channel conditions. Classification accuracy of the proposed CNN based DLMC and LSTM based DLMC is compared with other classifiers in Fig. 6.2. It can be observed that the accuracy of the proposed DLMC, i.e. CNN_{SNS} and $LSTM_{SNS}$ (trained on the sub-Nyquist samples) approaches to CNN_{NS} and $LSTM_{NS}$ (trained on the Nyquist samples) with an increase in SNR.

Classification accuracy of CNN_{SNS} and $LSTM_{SNS}$ on dataset $\mathbf{D_{IQ1}}$, CNN_{NS} and $LSTM_{NS}$ (trained on the Nyquist IQ samples), and other machine learning classifiers (trained on higher order cumulants obtained from the sub-Nyquist samples) are shown in Fig. 6.2(a). It is observed that at high SNR, both CNN_{SNS} and $LSTM_{SNS}$ achieves an accuracy of 100%, whereas at a low SNR of $-10\,dB$, CNN_{SNS} obtains an accuracy of 63.5% and $LSTM_{SNS}$ obtains 56.5%.

Classification accuracy on dataset $\mathbf{D_{AP1}}$ is shown in Fig. 6.2(b). Here, it can be observed that the performance of $LSTM_{SNS}$ remains the same as it was on dataset $\mathbf{D_{IQ1}}$, whereas the performance of CNN_{SNS} degrades. The applicability of $LSTM_{SNS}$ and CNN_{SNS} models on dataset $\mathbf{D_{IQ2}}$ and $\mathbf{D_{AP2}}$ is shown in Fig. 6.2(c). Here, it can be observed that due to the time dependency of samples during flat fading scenario, $LSTM_{SNS}$ performs better than CNN_{SNS}

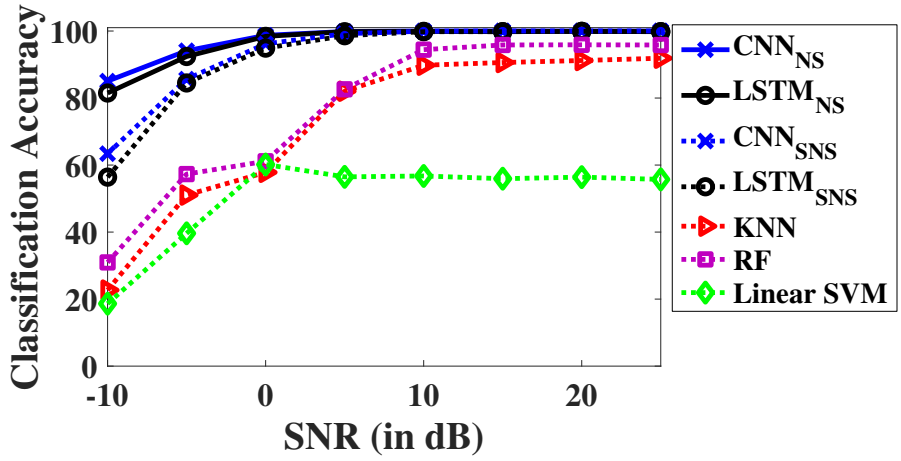

(a)

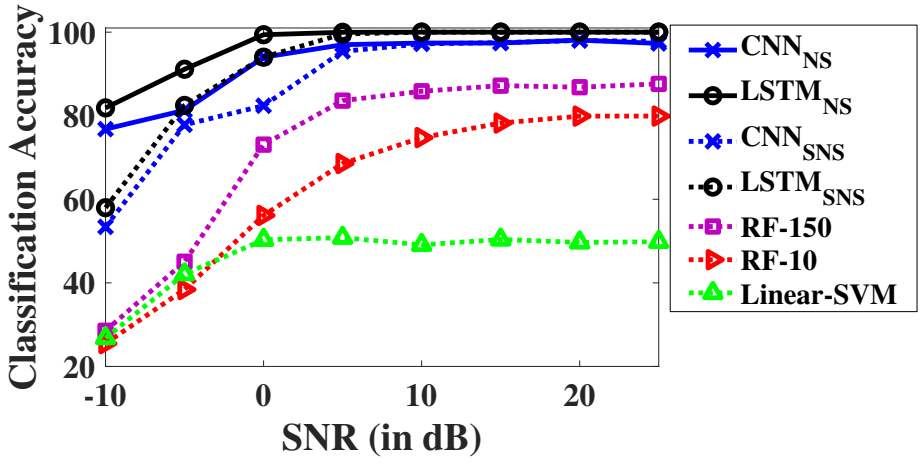

(b)

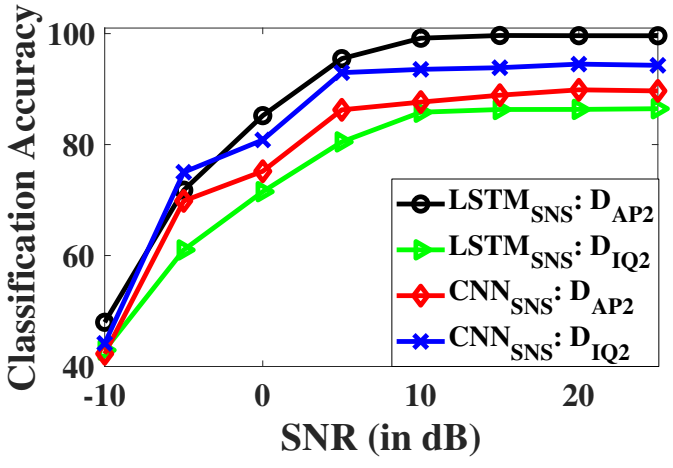

(c)

Figure 6.2: Classification accuracy of the proposed CNN_{SNS} and $LSTM_{SNS}$ for (a) Dataset $\mathbf{D_{IQ1}}$, (b) Dataset $\mathbf{D_{AP1}}$ and (c) $\mathbf{D_{IQ2}}$ and $\mathbf{D_{AP2}}$.

and achieves the highest average classification accuracy of 87.3% on dataset $\mathbf{D_{AP2}}$. Whereas for dataset $\mathbf{D_{IQ2}}$, the CNN_{SNS} model performs better than $LSTM_{SNS}$ but its average accuracy is 83.6%, i.e., less than the accuracy of $LSTM_{SNS}$ on dataset $\mathbf{D_{AP2}}$. Hence, for the hardware validation, the proposed $LSTM_{SNS}$ model is used.

6.5 Experimental Analysis

A USRP testbed has been developed to validate the performance of the proposed DLMC on the real-time dataset. As shown in Fig. 6.3 , the testbed consists of two NI-USRP 2922 with VEERT900 antennas to perform wireless RF transmission and reception. The baseband signal processing for both the transmitter and receiver is performed in the LabVIEW environment. The transmission/reception parameters used in the testbed are: Carrier frequency of $935MHz$ and IQ sampling rate of $1\ Msps$. Since $LSTM_{SNS}$ performs better than CNN_{SNS}, next we discuss the performance analysis of the proposed $LSTM_{SNS}$ on the experimental dataset.

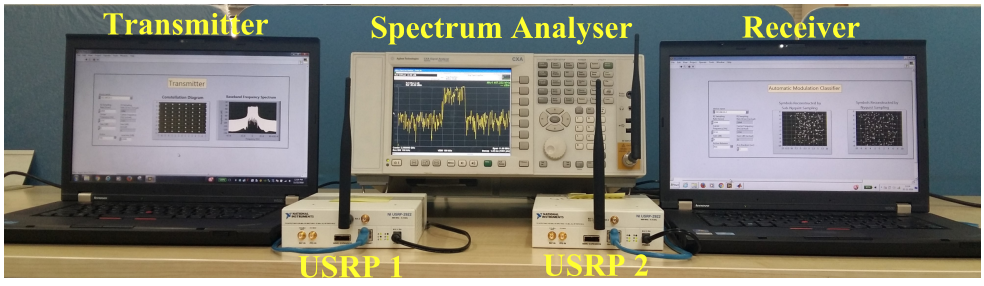

Figure 6.3: USRP testbed of the proposed SNS based DLMC.

Similar to the synthetic dataset, the following datasets consisting of amplitude-

phase components of the signal reconstructed from the sub-Nyquist samples are considered:

D_{H1}: It consists of the line of sight (LoS) and multi-path signals generated in the indoor environment.

D_{H2}: It consists of only multi-path signal components.

Classification accuracy of the proposed $LSTM_{SNS}$ is compared with other machine learning classifiers for a transmitting range of $1m$ to $70m$. It can be observed in Table 6.1 that the $LSTM_{SNS}$ outperforms machine learning classifiers. Furthermore, due to the presence of a LoS signal, the performance for dataset **D_{H1}** is higher than the dataset **D_{H2}** for all classifiers.

Table 6.1: Average % classification accuracy for dataset **D_{H1}** and dataset **D_{H2}**.

Modulation Classifier	**Average % Classification Accuracy**							
	Distance = $1m$		**Distance =** $10m$		**Distance =** $40m$		**Distance =** $70m$	
	D_{H1}	**D_{H2}**	**D_{H1}**	**D_{H2}**	**D_{H1}**	**D_{H2}**	**D_{H1}**	**D_{H2}**
$LSTM_{SNS}$	100	99	99	99	99	98	97	92
RF-150	96	95.7	95.9	95.5	90	57.3	67	38.7
RF-10	85.4	78	79.8	72.7	64	40	40.7	25.8
DT	69.5	56.9	63.4	50.6	47	35.8	31.2	23.5

6.6 Proposed Unified Model for DLMC

The proposed unified model for DLMC provides an end-to-end pipeline to simultaneously determine occupancy status and modulation schemes of all occu-

pied frequency bands. The architecture of the proposed unified model, as shown in Fig. 6.4, can be divided into three sections: 1) AFE for analog signal conditioning, 2) SNS for digitization, and 3) DFE comprising of the proposed DL based reconstruction and classification.

The main task of AFE is to perform impedance matching, low noise amplification and equalization on the received RF wideband signal, $x^{'}(t)$ [61]. For the simplicity of analysis, we assume the output, $x(t)$, of AFE is approximately the same as $x^{'}(t)$. The next step is SNS based digitization using multiple low-speed ADCs. As discussed in Chapter 2, various SNS architectures like MCS and MWC can be used to digitize contiguous wideband spectrum and FRI-based SNS for non-contiguous spectrum. The DTFT of sub-Nyquist samples, $y[n]$, can be represented as

$$\mathbf{Y}(f) = \mathbf{A}\mathbf{X}(f) \qquad \forall\, f \in [0, B] \tag{6.3}$$

where $\mathbf{A}$ is a $K \times N$ sensing matrix corresponding to the used SNS architecture and $\mathbf{X}(f)$ contains $X(f - nB)$ as the n^{th} row with $n \in \{1, 2, ..., N\}$ and $f \in$

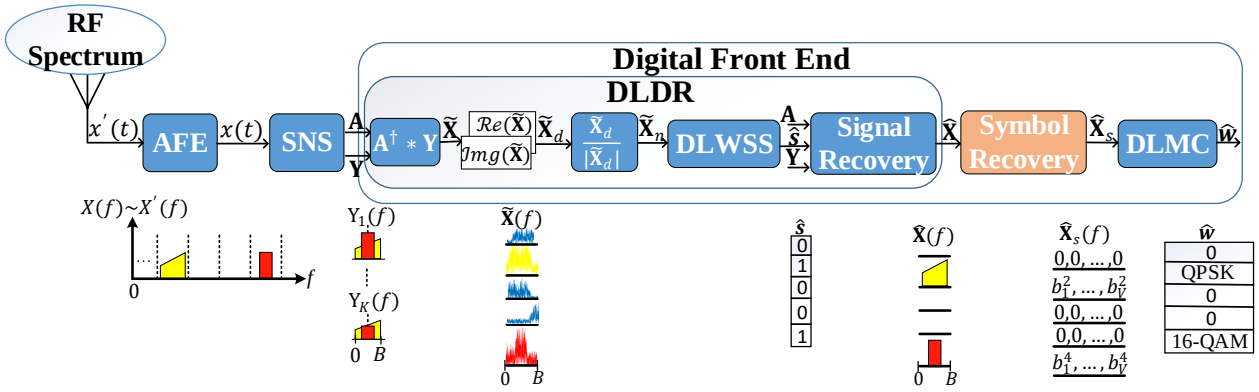

Figure 6.4: Proposed deep learning based architecture for end-to-end unified model of DLMC.

$[0, B]$. Here $K << N$ is the number of ADCs used in the SNS, and N is the number of sensed frequency bands that, in the contiguous sensing case, is the same as the total number of bands in $x(t)$.

Since the sampling rate of each ADC is $B << f_s$, all N frequency bands get aliased at the baseband, i.e. in the frequency range of $[0, B]$ as shown in Fig. 6.4. The aliased sub-Nyquist samples, $\mathbf{Y}(f)$, and the SNS specific sensing matrix, $\mathbf{A}$, are passed to the proposed unified DLMC, which identifies the vacant bands and the modulation scheme of occupied bands. The unified model for DLMC consists of three stages: 1) DL based digital reconstruction (DLDR) and 2) (Optional) Symbol recovery and 3) DL based modulation classification (DLMC). Various operations in three stages are shown in Fig. 6.4 and described using Algorithm 7.

The sub-Nyquist samples, $\mathbf{Y}(f)$, and sensing matrix, $\mathbf{A}$, are inputs (line 1), while the occupancy status, $\hat{\mathbf{s}}$, and identified modulation schemes, $\hat{\mathbf{w}}$, of occupied bands are the outputs (line 2). The inputs, $\mathbf{Y}(f)$ and $\mathbf{A}$ are first processed to obtain a pseudo-reconstructed signal, $\tilde{\mathbf{X}}(f)$, (line 3), as

$$\tilde{\mathbf{X}}(f) = \mathbf{A}^{\dagger}\mathbf{Y}(f) \tag{6.4}$$

where † denotes the pseudo-inverse operator. Since $\tilde{\mathbf{X}}(f)$ is a complex signal of dimension $N \times Q$ and can not be feed to the DL model directly, $\tilde{\mathbf{X}}(f)$ is reshaped to a higher dimensional matrix, $\tilde{\mathbf{X}}_d(f)$, of size $N \times Q \times 2$ (line 4), where the third dimension represents the real and imaginary values of $\tilde{\mathbf{X}}(f)$.

Algorithm 7 Proposed Unified model for DLMC

Input: $\mathbf{A}, \mathbf{Y}(f)$
Output: $\hat{\mathbf{s}}, \hat{\mathbf{w}}$

1: $\tilde{\mathbf{X}}(f) \leftarrow \mathbf{A}^{\dagger}\mathbf{Y}(f)$
2: $\tilde{\mathbf{X}}_d(f) \leftarrow$ Concatenate$(\tilde{\mathbf{X}}_{real}(f), \tilde{\mathbf{X}}_{img}(f))$
3: $\tilde{\mathbf{X}}_n(f) \leftarrow$ Normalize$(\tilde{\mathbf{X}}_d(f))$
4: $\phi_{ss} \leftarrow$ DLWSS$(\tilde{\mathbf{X}}_n(f), \mathbf{s})$ ▷ Training mode
5: $\hat{\mathbf{s}} \leftarrow DLWSS(\tilde{\mathbf{X}}_n(f), \phi_{ss})$ ▷ Inference mode
6: $\mathbf{A}_{new} \leftarrow$ Select columns of $\mathbf{A}$ corresponding to occupied bands
7: Determine $\hat{\mathbf{X}}(f)$ according to Eq. 6.5
8: $\hat{\mathbf{X}}_s \leftarrow$ Symbol Recovery of $\hat{\mathbf{X}}(f)$ ▷ Optional Step
9: $\phi_c \leftarrow$ DLMC$(\hat{\mathbf{X}}_s, \mathbf{w})$ ▷ Training mode
10: $\hat{\mathbf{w}} \leftarrow$ DLMC$(\hat{\mathbf{X}}_s, \phi_c)$ ▷ Inference mode

For the faster convergence of the training process, the higher dimensional pseudo-reconstructed matrix, $\tilde{\mathbf{X}}_d(f)$, is normalized between $[0, 1]$ (line 5). The normalized matrix, represented by $\tilde{\mathbf{X}}_n(f)$, is fed to DL based wideband spectrum sensing (DLWSS) block. The DLWSS is based on a CNN and its architecture along with the ablation study is discussed later in Section 6.7. The output of the DLWSS is $\hat{\mathbf{s}}$ which contains the status of each digitized frequency band. Note that $\hat{s}_n = 0\ (or\ 1)$ denotes that n^{th} band is vacant (or occupied).

The offline training mode of DLWSS provides the learned network parameters, ϕ_{ss} (line 6), which are then used to determine occupancy status, $\hat{\mathbf{s}}$ (line 7) of frequency bands in the digitized spectrum, $\tilde{\mathbf{X}}_n(f)$. Since the reconstruction noise is very high in the pseudo-reconstructed signal, $\tilde{\mathbf{X}}(f)$, we perform the signal reconstruction (line 8-9), and the corresponding architecture is shown in Fig. 6.5. Here, the occupancy status vector, $\hat{\mathbf{s}}$, determined by the DLWSS block, the sub-Nyquist samples, $\mathbf{Y}(f)$ and the sensing matrix $\mathbf{A}$ are taken as inputs. First, we generate a new sensing matrix $\mathbf{A}_{new}$ by selecting the columns of $\mathbf{A}$ corresponding to the occupied frequency bands (line 8) followed by the recon-

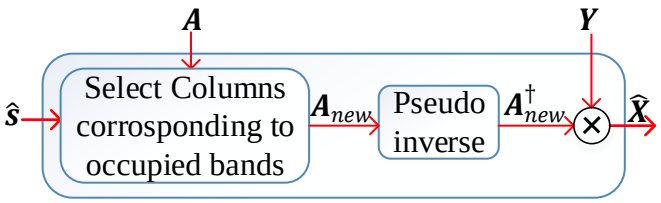

Figure 6.5: Wideband signal recovery in the DLDR block.

struction of the wideband signal (line 9). Mathematically, the reconstruction step can be written as

$$\hat{\mathbf{X}}(f) = \begin{cases} \mathbf{A}_{new}^{\dagger}\mathbf{Y}(f) & \text{for occupied bands,} \\ 0 & \text{for vacant bands} \end{cases} \tag{6.5}$$

where $\hat{\mathbf{X}}(f)$ is the reconstructed wideband signal, $\mathbf{A}_{new}$ is of size $K \times ||\hat{\mathbf{s}}||_0$ and $\mathbf{Y}(f)$ is the DTFT of sub-Nyquist samples. For the simplicity of analysis, we refer $\tilde{\mathbf{X}}_n(f), \hat{\mathbf{X}}(f)$ and $\mathbf{Y}(f)$ as $\tilde{\mathbf{X}}_n, \hat{\mathbf{X}}$ and $\mathbf{Y}$, respectively.

After reconstruction, the next step is the modulation classification of all the occupied bands present in the digitized wideband spectrum. As discussed before, the proposed DLMC performs simultaneous multi-band classification instead of sequential single band classification discussed previously. In this direction, we consider two scenarios:

6.6.1 Scenario 1

In the first scenario, symbol recovery is employed on each occupied frequency band before the modulation classification. The output of this block, as shown in Fig. 6.4, is represented as $\hat{\mathbf{X}}_s$ and is of size $N \times V$ where V is the number of modulated symbols and b_v^m is the v^{th} modulated symbol of m^{th} modulation scheme.

To recover the modulation symbols from $\hat{\mathbf{X}}$, we first perform the interpolation on $\hat{\mathbf{X}}$ of every occupied band followed by the root raised cosine filtering. Depending on the requirement, the modulated symbols are represented in two forms: 1) Real and imaginary, and 2) Amplitude and phase. This is followed by the proposed narrowband DL-based modulation classifier (NDLMC) that explores a new formulation of the cross-entropy loss function to simultaneously classify multiple frequency bands in the wideband signal compared to the sequential single band classification in existing approaches [54, 55, 100–103, 108, 109]. Thus, the proposed approach is more sophisticated than a Velcro approach of stacking multiple classifiers in parallel.

6.6.2 Scenario 2

Since the symbol recovery on each occupied frequency band incurs significant computational complexity, direct classification of the reconstructed wideband signal, $\hat{\mathbf{X}}$ via new wideband DLMC (WDLMC), is discussed later in Section 6.8. Another benefit of WDLMC is its architecture similarity with DLWSS making the complete architecture a good candidate for reconfigurable platforms such as Zynq SoC.

6.7 Proposed DLWSS Architecture

The proposed DLWSS is based on CNN[1]. The existing DL based iterative spectrum sensing methods [82–84] handle a single band at a time and involve com-

[1]The CNN is preferred over LSTM based on in-depth study and comparison for a wide variety of DLWSS datasets.

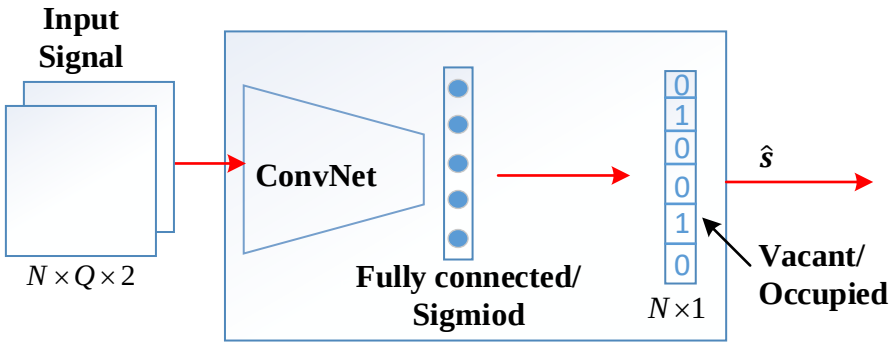

Figure 6.6: CNN architecture for DLWSS.

puting the residual, solving a least-squares problem at each iteration until convergence. Thus, they have high computational and time complexity. The proposed DLWSS generates the status of all bands simultaneously and does not require any prior knowledge of the sparsity of the spectrum. CNN is chosen for this task since it is good at capturing spatial correlation in input signals which is important for the considered signal model. Furthermore, parameter sharing allows them to operate with fewer parameters enabling the network to be memory efficient and a good candidate for hardware realization.

The CNN architecture for DLWSS and its ablation study are shown in Fig. 6.6 and Fig. 6.7, respectively. As discussed in Section 6.6, offline training is performed first to learn the network parameters, ϕ_{ss}, followed by testing real-time pseudo-reconstructed signal in the inference/testing mode. Algorithm 8 shows the offline training process with the dataset, $\mathbf{D}_{WSS} = \{(\tilde{\mathbf{X}}_{n,1}, \mathbf{s}_1), (\tilde{\mathbf{X}}_{n,2}, \mathbf{s}_2), \ldots\ldots, (\tilde{\mathbf{X}}_{n,U}, \mathbf{s}_U)\}$ where U denotes the number of observations (or examples) over which training is performed. $\tilde{\mathbf{X}}_{n,u} \in \mathfrak{R}^{N \times Q \times 2}$ is the u^{th} normalized and pseudo-reconstructed signal and $\mathbf{s}_u \in \{0,1\}^{N \times 1}$ is the label of u^{th} observation indicating actual occupancy status of all N frequency bands of $\tilde{\mathbf{X}}_{n,u}$ (line 5-7).

The training process involves minimizing a loss function, which is a measure of inconsistency between the predicted and actual label. Since more than one frequency band can be occupied in a wideband spectrum, the problem is formulated as a multi-label binary classification with binary cross-entropy as the training loss function. It is calculated as

$$L_{BCE}(\mathbf{p}_{\hat{\mathbf{s}}}, \mathbf{s}) = -\sum_{i=1}^{N} \mathbf{s}(i) \log \mathbf{p}_{\hat{\mathbf{s}}}(i) + (1 - \mathbf{s}(i)) \log(1 - \mathbf{p}_{\hat{\mathbf{s}}}(i)) \tag{6.6}$$

where $\mathbf{s}(i) \in \mathbf{s}$ is the actual occupancy status of i^{th} frequency band and $\mathbf{p}_{\hat{\mathbf{s}}}(i)$ is the predicted occupancy probability of i^{th} frequency band (line 8). Furthermore, the learnable network parameters, ϕ_{ss}, are optimized using a stochastic gradient descent algorithm such that the training loss, L_{BCE}, is minimized. Mathematically, it is represented as

$$\phi_{ss} = \phi_{ss} - \xi \nabla_{\phi_{ss}} L_{BCE} \tag{6.7}$$

where ξ is the learning rate. Here, the loss gradients, $\nabla_{\phi_{ss}} L_{BCE}$, are backpropagated and used to update the learnable network parameters at each iteration (line 9). This process is repeated until the validation loss no more decreases (i.e. until the model converges). The final output is the optimized parameters, ϕ_{ss}. After the training mode, the CNN model is used in the inference mode to find the occupancy status of unknown wideband spectrum in real-time.

The ablation study of the DLWSS CNN model is shown in Fig. 6.7. The experiments are performed for different network depths and filter settings. The

Algorithm 8 DLWSS Training Mode

Input: Dataset$=\{\tilde{\mathbf{X}}_{n,u}, \mathbf{s}_u\}\forall u \in \{1, U\},\ \xi,\ t=0$
Output: ϕ_{ss} **Initialize**: $\phi_{ss} = \mathcal{N}(0,1)$

1: **while** not converge **do**
2: $t = t+1$
3: Sample batch of data-points $\{\tilde{\mathbf{X}}_{n,u}, \mathbf{s}_u\}$
4: $\hat{\mathbf{s}} \leftarrow CNN(\tilde{\mathbf{X}}_{n,u}, \phi_{ss})$
5: Calculate L_{BCE} as per Eq. 6.6
6: Update ϕ_{ss} as per Eq. 6.7
7: **end while**

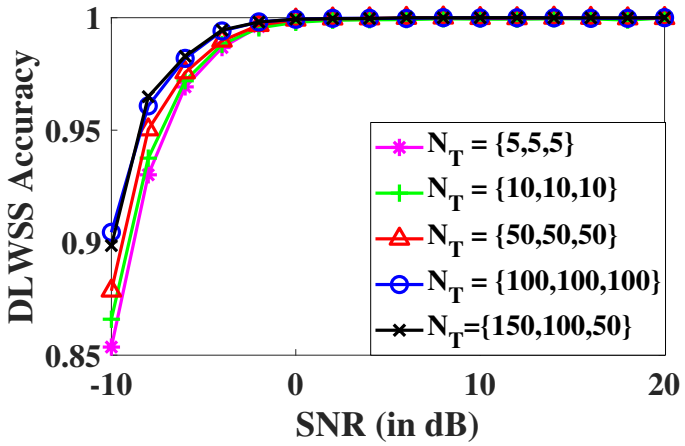

Figure 6.7: Classification accuracy of CNN based DLWSS for different values of $n-taps$.

filters used are of the form $1\times\ n-taps$ where $n-taps$ denote the width of the convolution filter in all layers. The number of filters is fixed to 64 in all layers to perform the ablation for filter size. It is observed that filters with a larger width perform better as compared to those with a smaller width and saturates when the width is increased further. The same has been shown in Fig. 6.7 for three-layer CNN. Here, N_T tells the $n-taps$ values for the three layers of CNN. The best classification accuracy is obtained when $N_T = \{150, 100, 51\}$. Furthermore, then the filter sizes are fixed to the best case, and the number of filters is varied in each layer. The best performing CNN architecture is shown in Table 6.2. The same architecture has been selected for the rest of the discussion.

6.8 Proposed DLMC Architecture

As discussed in Section 6.6, to perform DLMC, two scenarios have been considered: 1) NDLMC, and 2) WDMLC. Their corresponding architectures are presented below.

6.8.1 CNN Architecture for NDLMC

As shown in Fig. 6.4, the output of the DLDR block, $\hat{\mathbf{X}}$, is processed via symbol recovery to obtain $\hat{\mathbf{X}}_s$ of size $N \times V$. Three types of datasets are considered in the literature: 1) IQ (in-phase and quadrature-phase) samples [100, 101, 103], 2) AP (amplitude-phase) samples [102], and 3) Constellation diagram images of modulation schemes [17] to perform AMC on this processed baseband spectrum. Since the received wideband spectrum is represented using complex samples, IQ and AP datasets are readily available in the wireless receiver without additional processing in the physical layer compared to the constellation image based processing. Hence, we restrict the discussion to IQ and AP samples of $\hat{\mathbf{X}}_s$. Furthermore, our models are designed considering the various studies which show that the CNN and LSTM models are more suited for IQ and AP

Table 6.2: CNN architecture for the proposed DLWSS.

Layers	Filter Size	Number of Filters	Output Dimension
Input	–	–	$N \times Q \times 2$
Conv/relu	1x150	256	$N \times 150 \times 256$
Conv/relu	1x100	128	$N \times 51 \times 128$
Conv/relu	1x51	64	$N \times 1 \times 64$
Custom pool	–	–	$N \times 1 \times 64$
FC/sigmoid	–	–	N

samples, respectively, [100–103].

Algorithm 9 shows the steps involved in the training of NDLMC. Inputs to this classifier are $\hat{\mathbf{X}}_s$ and the labels of modulation schemes, $\mathbf{w}$. Since W modulation schemes are considered for the classification for each of the N frequency bands, the output of the classifier is a vector, $\hat{\mathbf{h}}_w$ of un-normalized log probabilities and has the size of $1 \times W$. The values in vector $\hat{\mathbf{h}}_w$ are converted into probabilities by applying a softmax activation function, which for a particular frequency band, is calculated as

$$\hat{\mathbf{p}}_w(i) = \mathbf{softmax}(\hat{\mathbf{h}}_w(i)) = \frac{exp(\hat{\mathbf{h}}_w(i))}{\sum_j exp(\hat{\mathbf{h}}_w(j))} \tag{6.8}$$

where $\hat{\mathbf{p}}_w(i)$ is the predicted probability of the i^{th} modulation scheme for a frequency band. Thus for all N bands, this gives an output vector of size $N \times W$ (line 5-7). Next, similar to the CNN modelling for DLWSS, to optimize the learnable network parameters for the modulation scheme classifiers, we use a stochastic gradient descent algorithm to minimize the training loss. As the training loss for a particular frequency band depends on the status of the band, we define it as the categorical cross entropy if the band is occupied and zero if the band is vacant. Mathematically, loss of the n^{th} frequency band can be defined as

$$L_n = \begin{cases} -\sum_i \mathbf{p}_w(i) log(\hat{\mathbf{p}}_w(i)) & \text{if } \hat{\mathbf{s}}(n) = 1, \\ 0 & \text{if } \hat{\mathbf{s}}(n) = 0 \end{cases} \tag{6.9}$$

where $\hat{\mathbf{s}}(n)$ is the estimated occupancy status (i.e. 0 for vacant and 1 for occu-

Algorithm 9 NDLMC Training Mode

Input: Dataset= $\{\hat{\mathbf{X}}_{s,u}, \mathbf{w}_u\}\ \forall\ u \in \{1, U\}\ \xi,\ t = 0$
Output: ϕ_c
Initialize: $\phi_c = \mathcal{N}(0, 1)$

1: **while** not converge **do**
2: $t = t + 1$
3: Sample batch of observations $\{\hat{\mathbf{X}}_{s,u}, \mathbf{w}_u\}$
4: $\hat{\mathbf{w}} \leftarrow$ Classifier$(\hat{\mathbf{X}}_{s,u}, \phi_c)$
5: Calculate L_c as per Eq. 6.10
6: Update ϕ_c as per Eq. 6.11
7: **end while**

pied) of the n^{th} band, and $\mathbf{p}_w(i)$ and $\hat{\mathbf{p}}_w(i)$ are the actual and predicted probability of the i^{th} modulation scheme for the n^{th} frequency band.

To determine the complete loss function (line 8), we concatenate the estimated band status vector, $\hat{\mathbf{s}}$ with the detected modulation scheme vector, $\hat{\mathbf{w}}$, and it can be expressed as

$$L_c = \sum_{n=1}^{N} -\hat{\mathbf{s}}(n) \left(\sum_{i} \mathbf{p}_w(i) \log \hat{\mathbf{p}_w}(i) \right) \tag{6.10}$$

where $\hat{\mathbf{s}}(n)$ is the n^{th} entry of $\hat{\mathbf{s}}$. Now, similar to DLWSS, the network learnable parameter, ϕ_c, is updated as (line 9)

$$\phi_c = \phi_c - \xi \nabla_{\phi_c} L_c \tag{6.11}$$

The next step is to finalize the architectures of the CNN model. Since the proposed NDLMC is the first work that handles simultaneous classification of multiple bands of a wideband signal in a single forward pass, we perform an ablation study to decide the NDLMC architecture.

To start with the ablation study, we first establish a simple baseline CNN

model (referred to as $CNN_{Baseline}$) and discuss it in detail. As the proposed NDLMC aims to classify all frequency bands in the multiband input simultaneously, we need deeper and more complex architectures to capture spatial correlation in the signal. However, deeper models result in vanishing gradients, making it difficult for the network to learn optimal parameters. Thus, in addition to $CNN_{Baseline}$, we analyze four approaches, namely: 1) Network in Network(NiN) [144], 2) Inception network [145], 3) Residual network (ResNet) [146], and 4) Densenet network [147], to enhance the AMC performance. These models enable us to capture better spatial correlation, which is integral for simultaneous multiband classification. Also, they alleviate the gradient vanishing issues to a large extent allowing us to train deeper models. Note that in the proposed setup, the final outcome is of the form $N \times (W + 1)$, comprising the status of N bands and modulation schemes of occupied bands.

The $CNN_{Baseline}$ architecture is shown in Table 6.3. We studied the classification performance to decide our baseline model architecture for different filter sizes (i.e. $n - taps$), number of filters and depth of the network. Fig. 6.8 (a) shows the classification performance for various values of $n - taps$, (N_T). We notice that smaller filters (i.e. for $N_T = 3, 5$) perform better than the larger filters. This is an important observation as it is not valid in the case of WDLMC discussed later. Thus, we use small filter sizes with $N_T = 3$ in the $CNN_{Baseline}$.

Furthermore, the results obtained by varying the number of filters are very similar to the ones obtained in [101]. Thus, 64 number of filters is considered for further analysis as it is efficient from both computation, memory and perfor-

Table 6.3: $CNN_{Baseline}$ architecture for NDLMC.

Layers	Filter Size	Number of Filters	Output Dimension
Input	-	-	$N \times V \times 2$
Conv/relu	1×3	64	$N \times V \times 64$
Conv/relu	1×3	64	$N \times V \times 64$
Conv	1×1	$W + 1$	$N \times V \times (W + 1)$
Custom pool/softmax	-	-	$N \times (W + 1)$

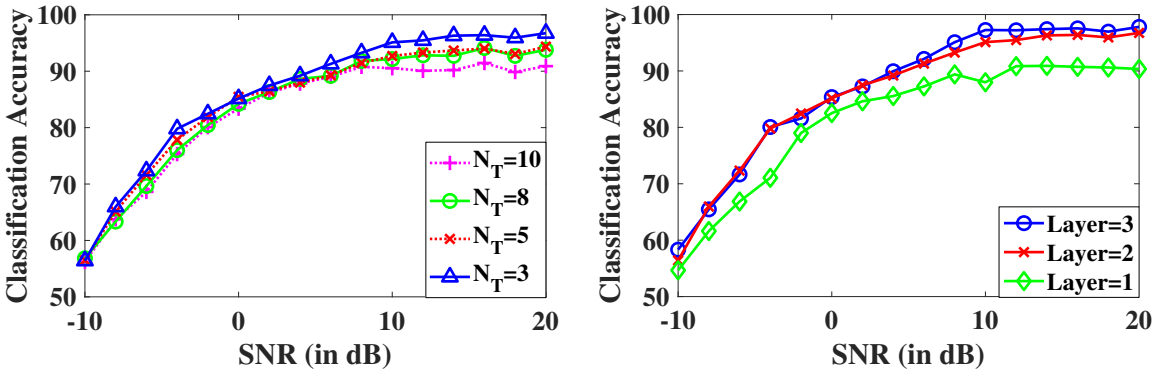

(a) (b)

Figure 6.8: Ablation study for $CNN_{Baseline}$ on IQ samples for different values of (a) $n - taps$, and (b) Layers.

mance point of view. Also, as shown in Fig. 6.8 (b), we observe no significant performance improvements when we increase the number of layers with a 1×3 filters beyond 2. Hence, the $CNN_{Baseline}$ has two convolution layers with 1×3 filter size, a convolution layer of filter size 1×1, and a custom average pool/-softmax activation layer at the end. The last convolution layer of filter size 1×1, along with the custom pool layer aim to match the dimension of the output label (i.e. $W + 1$) and it is performed by averaging the input along the column dimension (i.e. V). Note that the softmax activation layer associates the output with the probability of occurrence of every modulation scheme.

Next, we extend the proposed baseline model for NiN [144], Inception network [145], ResNet [146], and Densenet network [147] and their performance

Table 6.4: Modulation classification accuracy of various variants of CNN model for NDLMC and WDLMC.

DLMC Methods	Classifiers	AWGN					Rician Fading with Doppler					Rayleigh Fading with Doppler				
		$-10\ dB$	$-6\ dB$	$0\ dB$	$4\ dB$	$14\ dB$	$-10\ dB$	$-6\ dB$	$0\ dB$	$4\ dB$	$14\ dB$	$-10\ dB$	$-6\ dB$	$0\ dB$	$4\ dB$	$14\ dB$
NDLMC	**Baseline**	56.4	72.3	85.1	89.2	96.4	45.4	59.3	72.6	74.7	77.1	43.2	58.7	71	71	76.8
	NiN	58.4	72.3	84.5	91.7	99.9	45.1	59.7	72.9	78.1	89.1	44.02	59.4	74.1	79.1	89.6
	ResNet	58.5	72.9	84.6	91.4	99.9	45.9	61.6	74.5	79.1	89.7	46.2	61.2	73.4	79	89.1
	Densenet	57.1	72.9	85.3	90.2	99.8	46.8	61.8	75.9	79.8	90	45.8	60.9	73.5	79	90
	Inception-SNS	**59**	**73.7**	**84.4**	**91.7**	**99.8**	**47.5**	**62.3**	**74.8**	**79.8**	**89.4**	**45.3**	**61.6**	**73.4**	**78.5**	**90.3**
	Inception-NS	68.6	81.5	90.1	97.7	100	54.6	68.3	79.5	86	93.5	57.2	68.6	78.3	83.3	91.1
WDLMC	**CNN-SNS**	42	49.7	67.1	75.4	82.7	34.8	39.7	45.9	52.6	52	34.3	37.9	42.1	46	47.7
	CNN-NS	43.8	58.1	74.5	79.1	83.2	34.4	44.7	50.2	51.5	53.2	33.1	42.1	45.4	47.8	48.3

analysis for different channel conditions, i.e. AWGN, Rayleigh and Rayleigh with a Doppler shift is shown in Table 6.4. It can be observed that Inception offers better performance than other architectures, and hence, it is chosen for the NDLMC task with IQ-samples as input. Note that the performance of NDLMC improves if Nyquist sampling is used. Table 6.5 and Fig. 6.9 show the corresponding architecture of Inception model for NDLMC and Inception block.

In addition to the CNN architecture, we also design a novel LSTM based architecture for NDLMC. Similar to the proposed CNN based NDLMC, it si-

Table 6.5: Architecture of Inception model for NDLMC.

Layer	Output dimension
Input	$N \times V \times 2$
Inception Block	$N \times V \times 192$
Inception Block	$N \times V \times 192$
1×1 Conv/Relu	$N \times V \times (W+1)$
Custom pool/softmax	$N \times (W+1)$

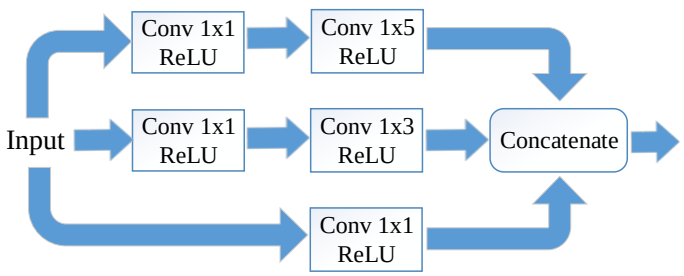

Figure 6.9: Architecture of Inception block.

multaneously classify various frequency bands of a multiband. The proposed LSTM based NDLMC architecture with ablation study are discussed in the next sub-section.

6.8.2 LSTM Architecture for NDLMC

Various studies in the literature have shown that the LSTM based architecture offers slightly better performance for datasets with AP samples [102]. We have also explored LSTM architecture with AP samples for NDLMC and WDLMC tasks with SNS based digitization. The proposed novel architecture, shown in Fig. 6.10, consists of N parallel (one for each frequency band) neural network based prediction modules and these modules share the learned parameters. Note that the *LSTM block* in Fig. 6.10 comprises V LSTM cells. Thus, the proposed architecture can directly process a signal of dimension $N \times V \times 2$. With reference to NS based LSTM classifier in [102], the proposed architecture can process the multi-band signal simultaneously without increasing the weight complexity.

For this architecture, we perform the ablation study for selecting the appropriate value of the hidden state vector (HSV) hyper-parameter [102]. As shown in Fig. 6.11, we choose HSV of 64 as it offers better performance than HSV$= 32$ and lower computational time than HSV$= 128$.

Note that both the proposed CNN and LSTM models employ weight sharing and do not use any special training strategy for optimization other than the

proposed multiband classification loss. Hence, the proposed NDLMC method has time and computational complexity comparable to any other recently single band classification models at training and test times [100–103].

6.8.3 CNN Architecture for WDLMC

Next, we consider AMC of the wideband spectrum directly from the reconstructed wideband signal, $\hat{\mathbf{X}}$ (i.e. raw samples). The training of the WDLMC follows the same approach as that of NDLMC in algorithm 9 except that $\hat{\mathbf{X}}$ is used instead of $\hat{\mathbf{X}}_s$ in Line 1. In the end, we have estimated network learnable parameters, ϕ_c, via the steepest descent method (line 8-9). To decide the architecture for the CNN classifier for WDLMC, we conduct an ablation study, as shown in Fig. 6.12. We further design the architecture such that it is similar to

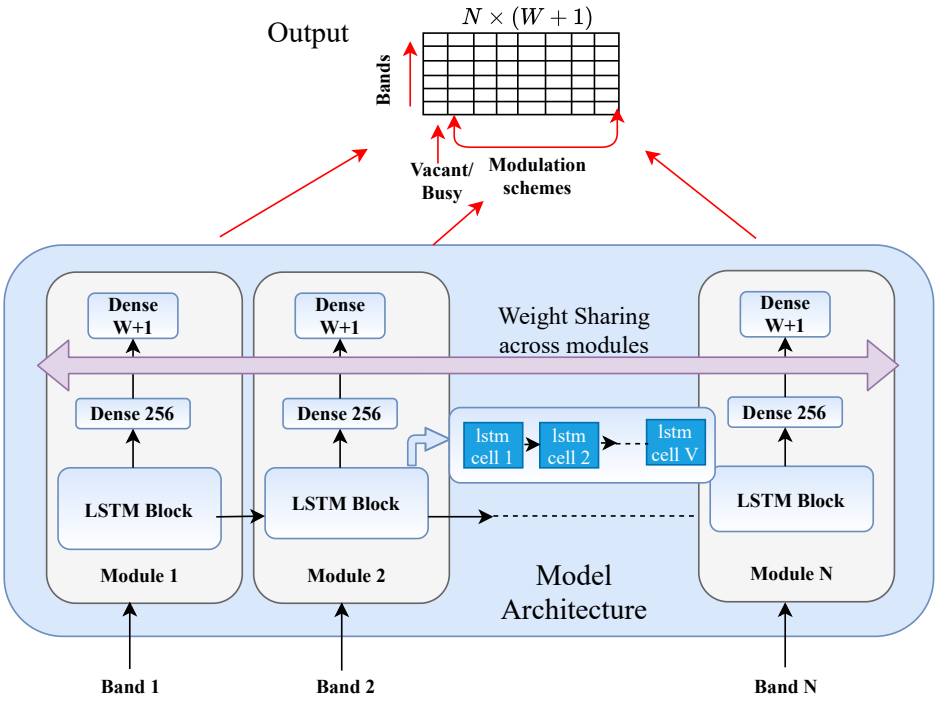

Figure 6.10: LSTM architecture for NDLMC.

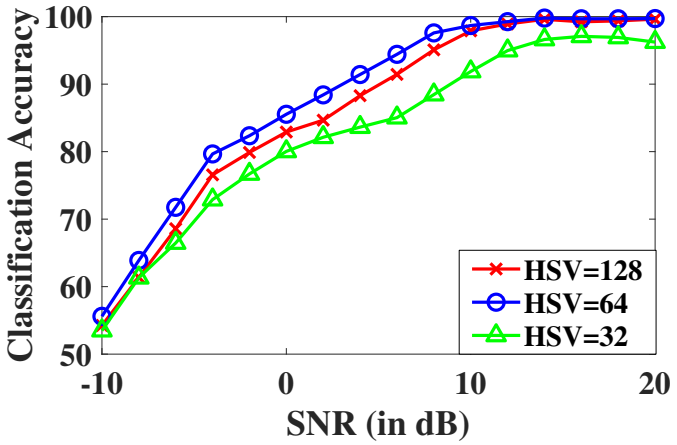

Figure 6.11: Ablation study of LSTM based NDLMC on AP samples of $\hat{\mathbf{X}}_s$.

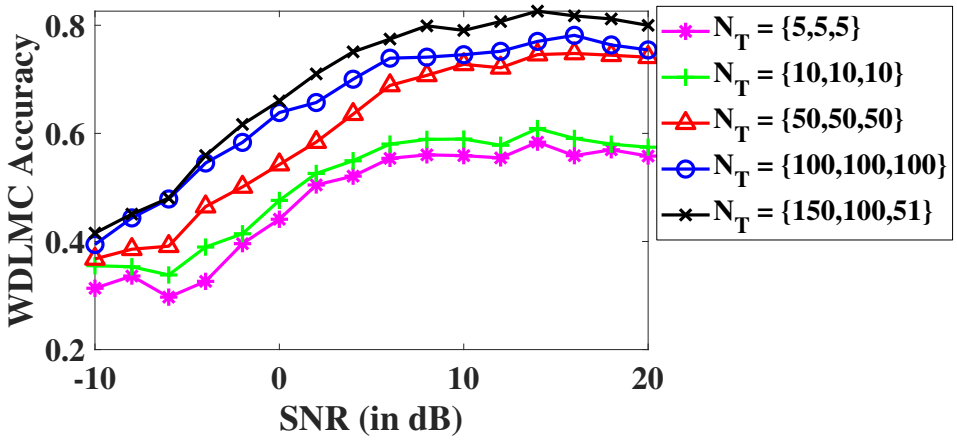

Figure 6.12: Ablation study of CNN based WDLMC architecture for different values of n-taps.

DLWSS architecture, enabling the proposed model well-suited for realization on the reconfigurable hardware. The chosen WDLMC architecture is given in Table 6.6. Note that the additional convolution layer of filter size 1 in the architecture is to match the output of the model to the dimensions of the ground-truth label, which is $N \times (W + 1)$.

The performance of WDLMC for different wireless channels is shown in the last rows of Table 6.4, along with its performance for Nyquist sampled data. Notice that the performance of the proposed architecture for Nyquist and sub-Nyquist sampled data becomes almost identical as SNR increases showing the

Table 6.6: CNN architecture for the proposed WDLMC.

Layers	**Filter Size**	**Number of Filters**	**Output Dimension**
Input			$N \times Q \times 2$
Conv/ReLu	1×150	256	$N \times 150 \times 256$
Conv/ReLu	1×100	128	$N \times 51 \times 128$
Conv/ReLu	1×51	64	$N \times 1 \times 64$
Conv/ReLU	1×1	$W + 1$	$N \times 1 \times (W + 1)$
Custom pool/softmax			$N \times (W + 1)$

strength of the proposed signal reconstruction and classification methodology. As expected, the performance of WDLMC is lower than NDLMC, especially for wireless channels with Rayleigh and Rician fading. This indicates that the design of WDLMC architectures for these channels is itself a challenging research problem. This problem is important from the architecture perspective as the design of intelligent and reconfigurable physical layer is one of the critical research areas. In this direction, the significant similarity between our proposed WDLMC and DLWSS architecture in terms of number of layers, number of filters and size makes the proposed unified model of DLMC well-suited for realization on the reconfigurable hardware. For example, via dynamic partial reconfiguration capability of Zynq SoC, on-the-fly switch between DLWSS and WDLMC can significantly reduce area and power complexity and cost benefits due to the reduction in the chip area. Thus, the proposed WDLMC approach is a novel state-of-the-art contribution in the design of a reconfigurable wideband spectrum analyzer.

In the next sub-section, we show the performance of the proposed LSTM based WDLMC architecture.

6.8.4 LSTM Architecture for WDLMC

We use the LSTM architecture shown is Fig. 6.10 for WDLMC. However, every LSTM block consists of Q LSTM cells. Thus, the architecture takes the direct wideband signal of dimension $N \times Q \times 2$ as input. We perform an ablation study for the different sizes of HSV as shown in Fig. 6.13. It is found that similar to the NDLMC case, HSV$= 64$ gives better performance.

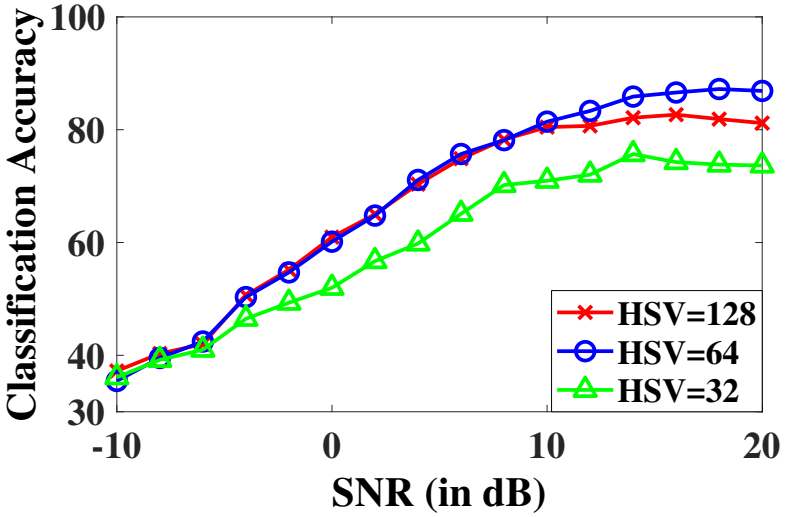

Figure 6.13: Ablation study of LSTM based WDLMC on the dataset $\hat{\mathbf{X}}$.

6.9 Simulation Setup

In this section, we discuss the proposed datasets for training and verification of DLWSS and DLMC. The proposed datasets are generated synthetically using MATLAB and are the only available datasets for SNS based wideband spectrum characterization. Each dataset is keyed with a modulation scheme and SNR. We consider seven widely used modulation schemes (BPSK, QPSK, 16-QAM, 64-QAM, 128-QAM, 256-QAM, 8-PAM) and SNR ranging from $-10\ dB$ to $20\ dB$

with an interval of 2 dB. We consider $N = 14$ frequency bands and FRI based SNS for digitization consisting of 7 ADCs and hence, has a compression ratio of 0.5. For every characterization, we take $Q = 299$ samples from each ADC. To ensure the considered datasets resemble real-world conditions and our model can generalize well to different channel variations, we consider various versions of datasets for Rayleigh and Rician fading channels with a Doppler shift. Next, we explain the details of the dataset. All datasets are free and available online at [148].

6.9.1 $\mathbf{D}_{\mathbf{WSS}}$: DLWSS Dataset

The $\mathbf{D}_{\mathbf{WSS}}$ dataset is generated using the complex-valued normalized pseudo reconstructed signal, $\tilde{\mathbf{X}}_n$ of size $N \times Q \times 2$. For generating this dataset, real and complex parts of $\tilde{\mathbf{X}}$ are separated and then normalized in the range $[0, 1]$ as shown in Fig. 6.4. Since this dataset is used for spectrum sensing, the label, $\mathbf{s}$ of each frequency band will either be vacant (i.e. $\mathbf{s}(n) = 0$) or occupied (i.e. $\mathbf{s}(n) = 1$) for n^{th} frequency band.

6.9.2 $\mathbf{D}_{\mathbf{NMC}}$: NDLMC Dataset

The $\mathbf{D}_{\mathbf{NMC}}$ dataset uses $\hat{\mathbf{X}}_s$, which is generated by passing the reconstructed wideband signal via symbol recovery. It is different from [102, 103], where a single frequency band is considered compared to N bands simultaneously in our dataset depicting a real wideband spectrum. Thus, the label, $\hat{\mathbf{w}}$ is of size $N \times 1$, where its i^{th} entry, $\hat{\mathbf{w}}(i) \in \{0, 1, ..., W\}$. Here, $\hat{\mathbf{w}}(i) = 0$ denotes

that the i^{th} frequency band is vacant and $\hat{\mathbf{w}}(i) \in \{1, ..., W\}$ denotes that the i^{th} frequency band is occupied with any one of the W modulations schemes. For performance analysis in various scenarios, $\mathbf{D_{NMC}}$ is further divided into two sections: 1) $\mathbf{D_{NMC\_IQ}}$: Time domain IQ samples of $\hat{\mathbf{X}}_s$, and 2) $\mathbf{D_{NMC\_AP}}$: Time domain amplitude-phase samples (i.e. polar representation of IQ samples) of $\hat{\mathbf{X}}_s$.

Each dataset has a shape of $N \times V \times 2$, where $V = 256$ is the number of modulated symbols. In $\mathbf{D_{NMC\_IQ}}$, the two vectors of the third dimension denote in-phase and quadrature-phase components of $\hat{\mathbf{X}}_s$. We normalize this dataset in the range [0,1] before passing it to the DL models. Similarly, in $\mathbf{D_{NMC\_AP}}$, amplitude and phase form two vectors of the third dimension. The amplitude is normalized via l_2 norm, and phase (in radians) is normalized in the range $[-1, 1]$ as in [102].

Furthermore, in each case, we consider three types of wireless channels: 1) AWGN ($\mathbf{D_{NMC\_IQ1}}$ and $\mathbf{D_{NMC\_AP1}}$), 2) AWGN channel and Rayleigh fading with a Doppler shift ($\mathbf{D_{NMC\_IQ2}}$ and $\mathbf{D_{NMC\_AP2}}$), and 3) AWGN channel and Rician fading with a Doppler shift ($\mathbf{D_{NMC\_IQ3}}$ and $\mathbf{D_{NMC\_AP3}}$).

6.9.3 $\mathbf{D_{WMC}}$: WDLMC Dataset

The $\mathbf{D_{WMC}}$ dataset is generated directly from the complex valued reconstructed wideband signal, $\hat{\mathbf{X}}$ of size $N \times Q$. This dataset is also separated into real and imaginary parts and hence, it is of size $N \times Q \times 2$. Since the dataset

classifies the modulation schemes of all N frequency bands, the dataset $\mathbf{D_{WMC}}$ has labels, $\hat{\mathbf{w}} \in \{0, 1, .., W\}$ as in $\mathbf{D_{NMC}}$. Likewise, we consider three types of wireless channels: 1) AWGN ($\mathbf{D_{WMC1}}$), 2) AWGN channel and Rayleigh fading with a Doppler shift ($\mathbf{D_{WMC2}}$), and 3) AWGN channel and Rician fading with a Doppler shift ($\mathbf{D_{WMC3}}$).

6.9.4 Training Parameters and Tools

The neural networks are implemented using Keras [149] with Tensorflow back-end on Nvidia Cuda enabled Quadro P4000 GPU. The weights of the models are initialized using default Keras initializers. We use an Adam optimizer whose parameters are set as $\beta_1 = 0.9$ and $\beta_2 = 0.999$ [150].

6.10 Performance Comparison

In this section, we present results to compare the performance of the proposed architectures with the state-of-the-art works in literature. From a wireless communication perspective, we consider two parameters: 1) Spectrum sensing accuracy, which in turn guarantees accurate spectrum reconstruction from sub-Nyquist samples, 2) Modulation classification accuracy for a wide range of SNRs and wireless channels.

6.10.1 Spectrum Sensing Performance Analysis on D_{WSS}

In Fig. 6.14, we compare the spectrum sensing accuracy of the proposed DLWSS architecture with the conventional OMP based approach [81], which, unlike DLWSS, requires the prior knowledge of the number of occupied frequency bands. The analysis is performed for three different wireless channels. As expected, DLWSS outperforms OMP at low SNRs. Furthermore, at a low SNR of -10 dB, the accuracy is 5.02%, 5.53% and 3.04% higher than OMP for AWGN, Rayleigh and Rician fading channels, respectively. Thus, as discussed in Section 6.7, the proposed DLWSS method, in addition to being more efficient and less computationally intensive than OMP based spectrum sensing, DLWSS also improves the performance. Furthermore, switching from OMP to DLWSS based spectrum reconstruction also allows a reconfigurable architecture via a single unified pipeline due to similarity between DLWSS, NDLMC and WDLMC building blocks.

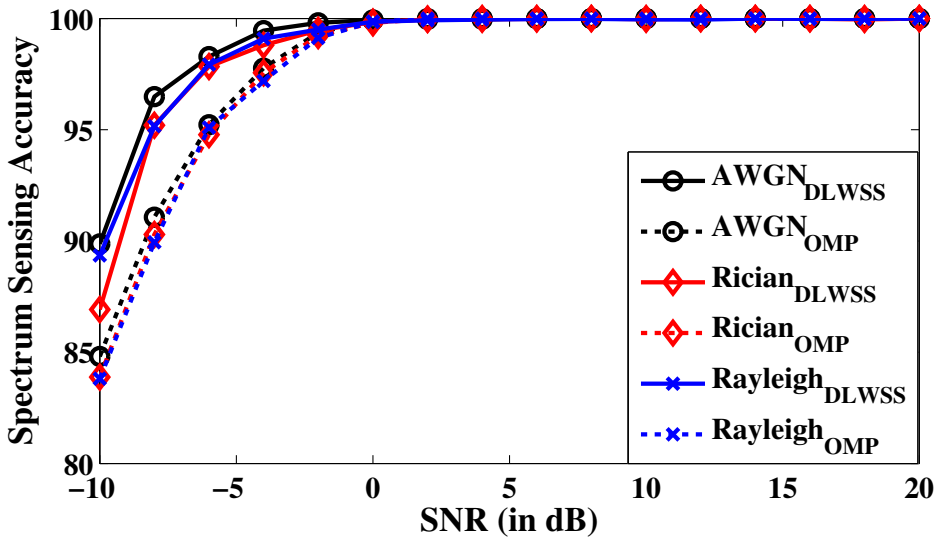

Figure 6.14: Spectrum sensing accuracy of the proposed DLWSS and existing OMP method for various channel models.

6.10.2 Modulation Classification Accuracy Comparison

For modulation classification, we compare the performance of the proposed NDLMC and WDLMC architectures for various IQ and AP datasets discussed in Section 6.9. We consider the comparison with various approaches such as SVM classifier with linear function kernel (referred as P-SVM) and random forest with 10 and 150 trees in [102, 103] (referred as P-RF10/150). Since these approaches demand Nyquist-sampled signal, we apply the proposed DLWSS based DLDR for reconstruction. Furthermore, these approaches cannot characterize the multiband signal directly. Hence, we sequentially pass the detected occupied bands via symbol recovery compared to simultaneous classification in the proposed approach. Thus, only occupied frequency bands were considered while calculating modulation classification accuracy. In addition, we also considered the SVM classifier (with radial basis kernel) used in [55], but its performance is similar to P-RF150. Hence, it is not included in the plots.

The CNN_{NS} approach in Fig. 6.15 and Fig. 6.18 denotes the proposed NDLMC and WDLMC applied on the symbols obtained from the Nyquist samples (NS) and directly on the wideband NS of signal, $\mathbf{X}$, respectively. Also, CNN_{NS} requires prior knowledge of occupied frequency bands [103]. In contrast, CNN_{OMP} represents NDLMC (for Fig. 6.15) and WDLMC (for Fig. 6.18), applied on the signal reconstructed via OMP instead of DLWSS. Similarly, the $LSTM_{NS}$ approach in Fig. 6.19 is the proposed WDLMC applied directly on the NS.

Note that the NS approach needs additional signal processing operation before classification.

6.10.2.1 $\mathbf{D_{NMC\_IQ}}$

The modulation classification accuracy of the proposed NDLMC on the CNN classifier for AWGN, Rayleigh and Rician channels for dataset $\mathbf{D_{NMC\_IQ}}$ are shown in Fig. 6.15 (a) and (b). As shown in Fig. 6.15 (a), for AWGN channel, i.e., with a dataset $\mathbf{D_{NMC\_IQ1}}$, the average accuracy is 88.95% and 96.42% for the SNR range of -10 dB to 20 dB and 0 dB to 20 dB, respectively. At high SNR, the accuracy of the proposed NDLMC architecture is the same as NS based approaches while this is not true for $CNN_{Baseline}$ approach. As discussed before, $CNN_{Baseline}$ also demands additional complex signal processing between the reconstruction and classification stages. Next, in Fig. 6.15 (b), we consider the challenging Rayleigh and Rician wireless channels and corresponding classification accuracy for datasets $\mathbf{D_{NMC\_IQ2}}$ and $\mathbf{D_{NMC\_IQ3}}$, respectively. Here, $Rayleigh_{NS}$ and $Rician_{NS}$ use the CNN classifier on the symbols obtained from the NS of the received wideband signal. Overall, the average accuracy of $Rayleigh_{NDLMC}$ and $Rician_{NDLMC}$ is 77.40% and 77.72%, respectively, along with closed match between SNS and NS approaches.

To understand the classifier performance and inter-class discrepancies better, we analyze the confusion plots of the proposed NDLMC for CNN classifier at an SNR of 0 dB and 18 dB for all three channel models in Fig. 6.16. For all the channel models, at an SNR of 18 dB, we can see a sharp diagonal with

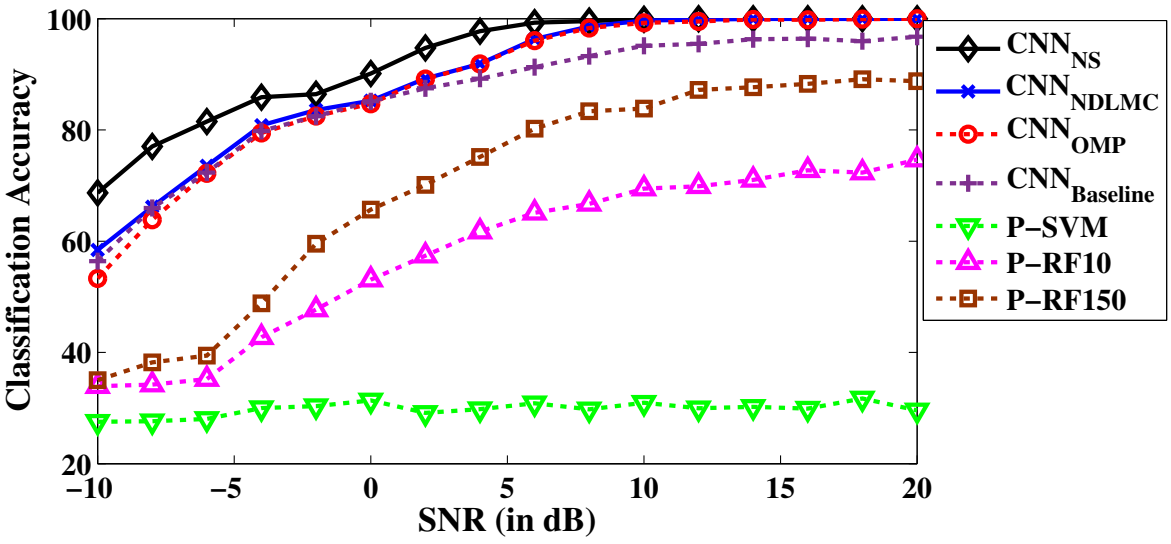

(a)

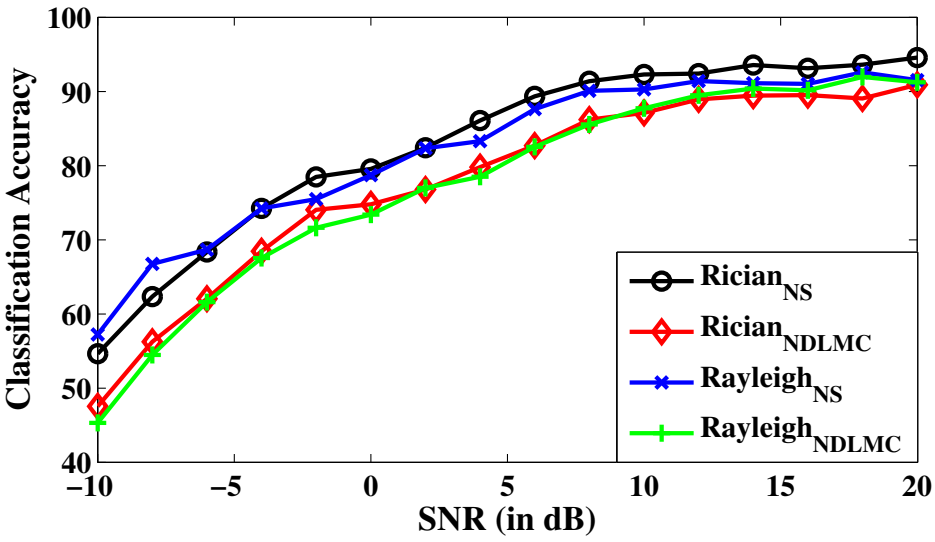

(b)

Figure 6.15: Modulation classification accuracy of (a) CNN based NDLMC and other classification methods for the dataset $\mathbf{D}_{\text{NMC\_IQ1}}$ (i.e. IQ samples of AWGN channel) (b) CNN based NDLMC and NS NDLMC on Rayleigh (i.e. dataset $\mathbf{D}_{\text{NMC\_IQ2}}$) and Rician (i.e. dataset $\mathbf{D}_{\text{NMC\_IQ3}}$) channel models.

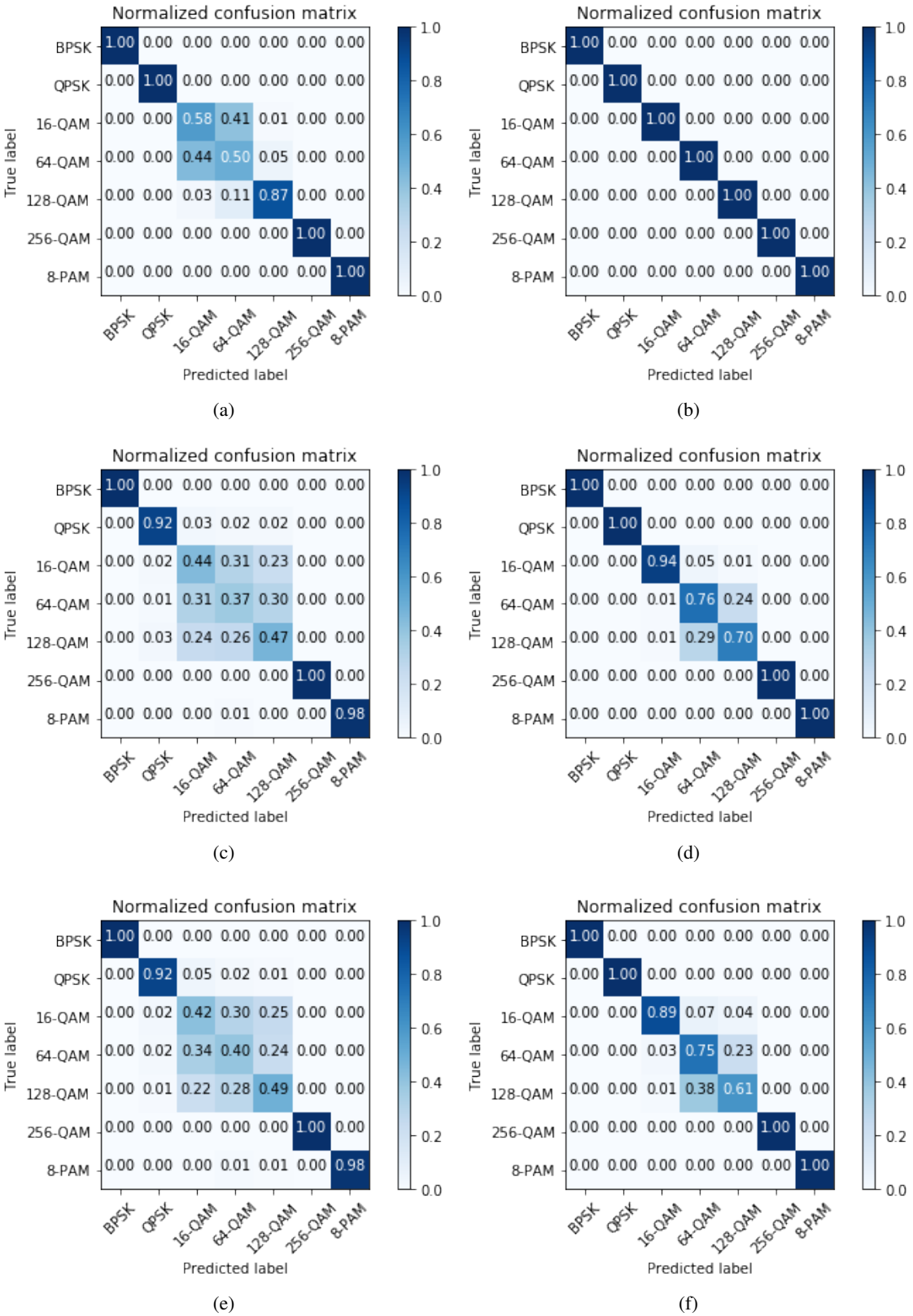

Figure 6.16: Confusion plots of NDLMC for (a) AWGN channel i.e. $\mathbf{D}_{\mathbf{NMC\_IQ1}}$ at SNR = 0 dB (b)AWGN channel i.e. $\mathbf{D}_{\mathbf{NMC\_IQ1}}$ at SNR = 18 dB (c) Rayleigh channel i.e. $\mathbf{D}_{\mathbf{NMC\_IQ2}}$ at SNR = 0 dB (d) Rayleigh channel i.e. $\mathbf{D}_{\mathbf{NMC\_IQ2}}$ at SNR = 18 dB (e) Rician channel i.e. $\mathbf{D}_{\mathbf{NMC\_IQ3}}$ at SNR = 0 dB (f) Rician channel i.e. $\mathbf{D}_{\mathbf{NMC\_IQ3}}$ at SNR = 18 dB.

almost perfect classification except for 16-QAM and 64-QAM. As the SNR reduces, the sharpness of the diagonal further reduces in the 16/64/128-QAM region. Since a similar observation is also valid for NS based classifier, we observed that classification of QAM schemes at low SNR is challenging, and there is a scope for improvement. Nonetheless, the proposed solution offers better performance than existing state-of-the-art approaches [55, 101–103] and directions for future work.

6.10.2.2 $\mathbf{D_{NMC\_AP}}$

The modulation classification accuracy of the proposed NDLMC on the LSTM classifier for AWGN, Rayleigh and Rician fading channel models are shown in Fig. 6.17 (a) and (b). As shown in Fig. 6.17 (a), for the AWGN channel with dataset $\mathbf{D_{NMC\_AP1}}$, the average accuracy is 87.96% and 95.83% for the SNR range of -10 dB to 20 dB and 0 dB to 20 dB, respectively. Similar to NDLMC on the CNN classifier, at a SNR of 10 dB, its classification accuracy becomes 100%. Fig. 6.17 (b) shows the classification accuracy for Rayleigh and Rician fading channels for dataset $\mathbf{D_{NMC\_AP2}}$ and $\mathbf{D_{NMC\_AP3}}$, respectively. The average accuracy for the Rayleigh fading channel is 76.4%, whereas it is 79.66% for the Rician fading channel. Note that $Rayleigh_{NS}$ and $Rician_{NS}$ use the LSTM classifier of the architecture shown in Fig. 6.10 on the symbols recovered from the Nyquist samples of a wideband signal.

Since LSTM and CNN perform best in AP and IQ dataset, the Table 6.7 shows the average classification performance comparison of NDLMC when

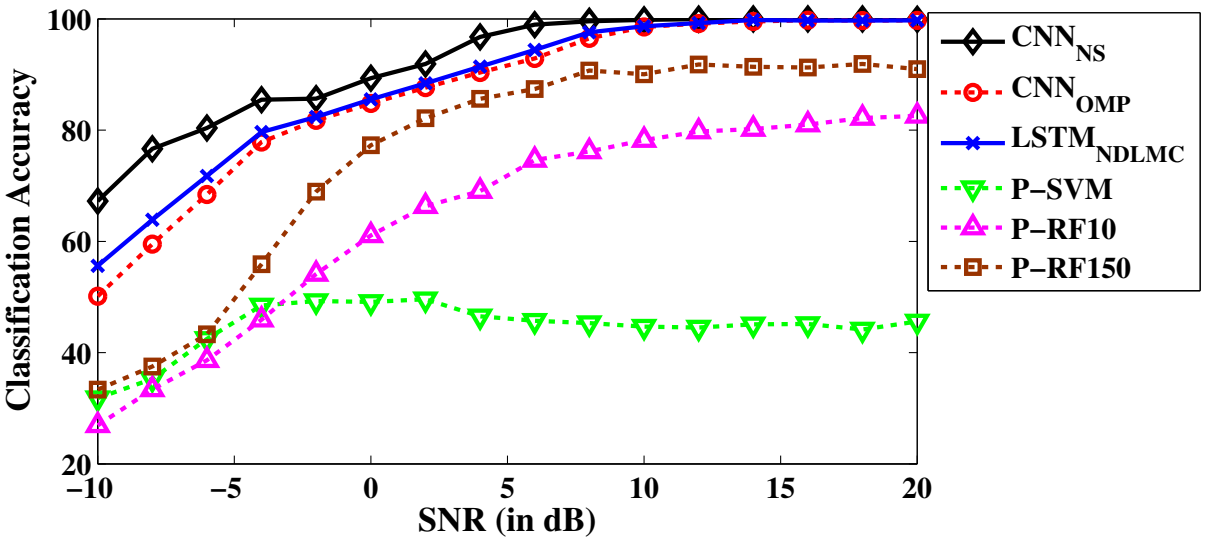

(a)

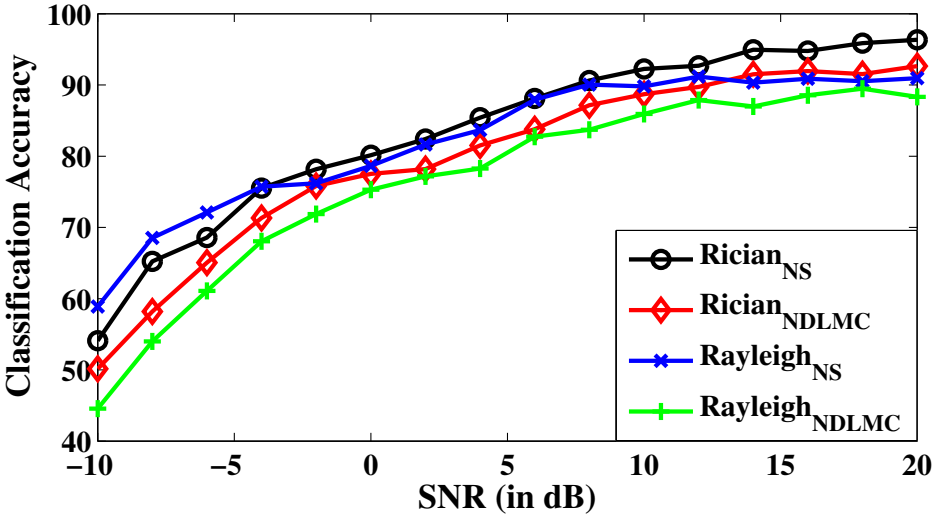

(b)

Figure 6.17: Classification accuracy of LSTM based NDLMC on AP samples for (a) AWGN channel i.e. $\mathbf{D}_{\mathbf{NMC\_AP1}}$ (b) Rayleigh channel i.e. $\mathbf{D}_{\mathbf{NMC\_AP2}}$ and Rician channel $\mathbf{D}_{\mathbf{NMC\_AP3}}$.

CNN classifier and LSTM classifier are used on dataset $\mathbf{D}_{NMC_{IQ}}$ and $\mathbf{D}_{NMC_{AP}}$, respectively. It is observed that the classification accuracy of NDLMC with CNN and LSTM classifier is almost same for AWGN and Rayleigh fading channel whereas LSTM classifier performs better than CNN classifier for Rician fading channel.

Table 6.7: Average percentage classification accuracy comparison of $\mathbf{LSTM_{NDLMC}}$ on $\mathbf{D_{NMC\_AP}}$ and $\mathbf{CNN_{NDLMC}}$ on $\mathbf{D_{NMC\_IQ}}$.

Method	AWGN	Rayleigh	Rician
$\mathbf{LSTM_{NDLMC}}$	88	76.4	79.9
$\mathbf{CNN_{NDLMC}}$	88.7	77.7	77.4

6.10.2.3 WDLMC

Next, we consider the WDLMC scenario for the same three channels. The corresponding results are shown in Fig. 6.18 (a) and (b) for dataset $\mathbf{D_{WMC}}$. Since the direct wideband signal classification has not been done in the literature, there is no baseline architecture for comparison. As shown in Fig. 6.18 (a), for the AWGN channel, i.e. for dataset $\mathbf{D_{WMC1}}$, the average accuracy of the CNN based WDLMC is 70% and 78% for SNR range of -10 dB to 20 dB and 0 dB to 20 dB, respectively. At high SNR, the accuracy of the proposed architecture is the same as NS based approach, i.e. CNN_{NS}.

Classification performance of datasets $\mathbf{D_{WMC2}}$ and $\mathbf{D_{WMC3}}$ is shown in Fig. 6.18 (b). Here $Rayleigh_{NS}$ and $Rician_{NS}$ use CNN classifier directly on the wideband signal, $x(t)$. Although the performance of the proposed SNS based WDLMC approaches to that of Nyquist sampling based DLMC (i.e. $Rayleigh_{NS}$ and $Rician_{NS}$) but as expected, both NS and SNS based modulation classifier performance is lower than the NDLMC based classification as shown in Fig. 6.15 (b). This is a small penalty incurred to reduce the complexity of additional signal processing between reconstruction and classification stages, along with making the architecture reconfigurable.

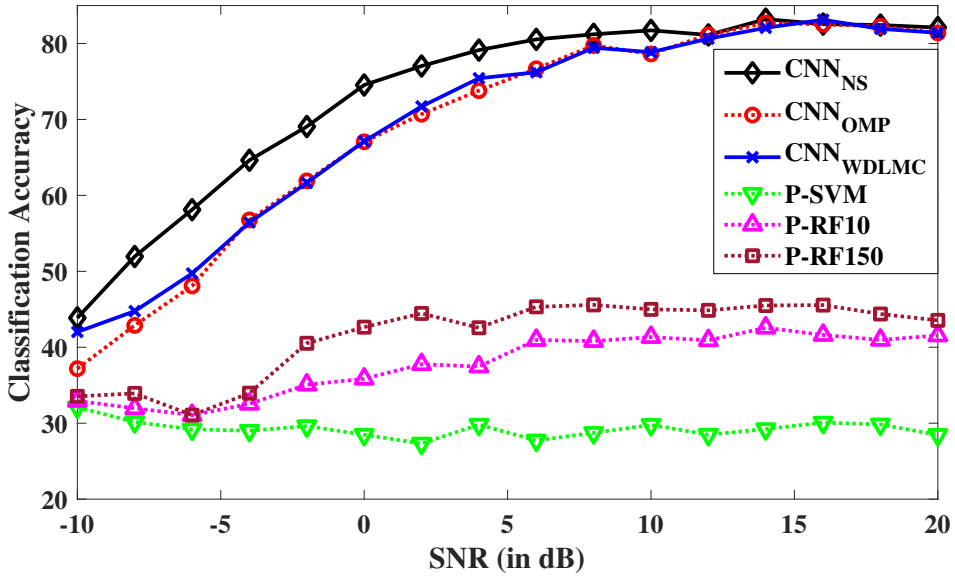

(a)

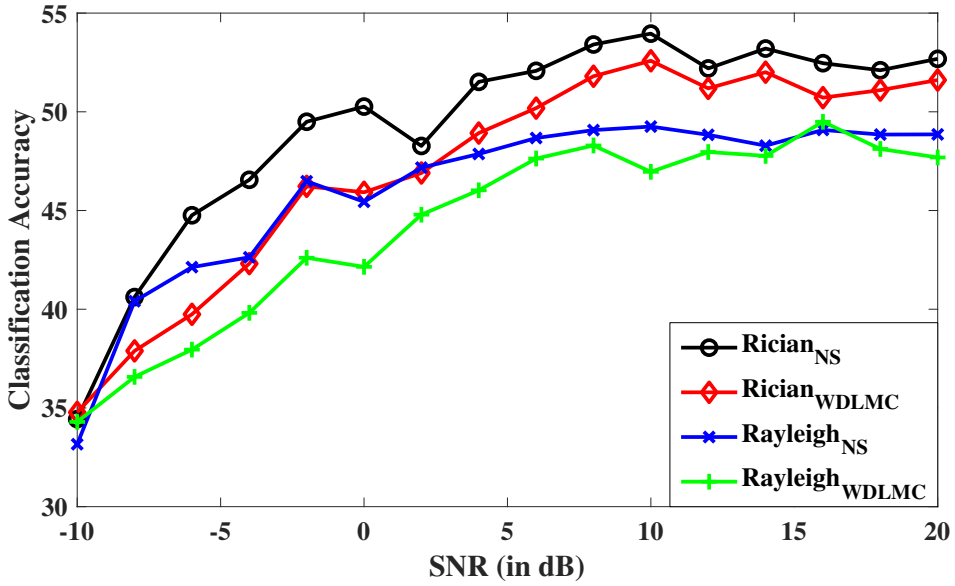

(b)

Figure 6.18: Modulation classification accuracy of (a) CNN based WDLMC and other classification methods for the dataset $\mathbf{D_{WMC1}}$ (i.e. AWGN channel) (b) CNN based WDLMC and NS WDLMC on Rayleigh (i.e. the dataset $\mathbf{D_{WMC2}}$) and Rician (i.e. the dataset $\mathbf{D_{WMC3}}$) channel models.

Next, we show the classification performance comparison of LSTM based WDLMC and other algorithms on the reconstructed wideband signal, $\hat{\mathbf{X}}$. Here, $LSTM_{WDLMC}$ and CNN_{WDLMC} represent the performance of the LSTM and CNN, respectively, on the signal $\hat{\mathbf{X}}$. As shown in Fig. 6.19, the average accuracy of $LSTM_{WDLMC}$ for the AWGN channel, i.e. for dataset $\mathbf{D_{WMC1}}$ is

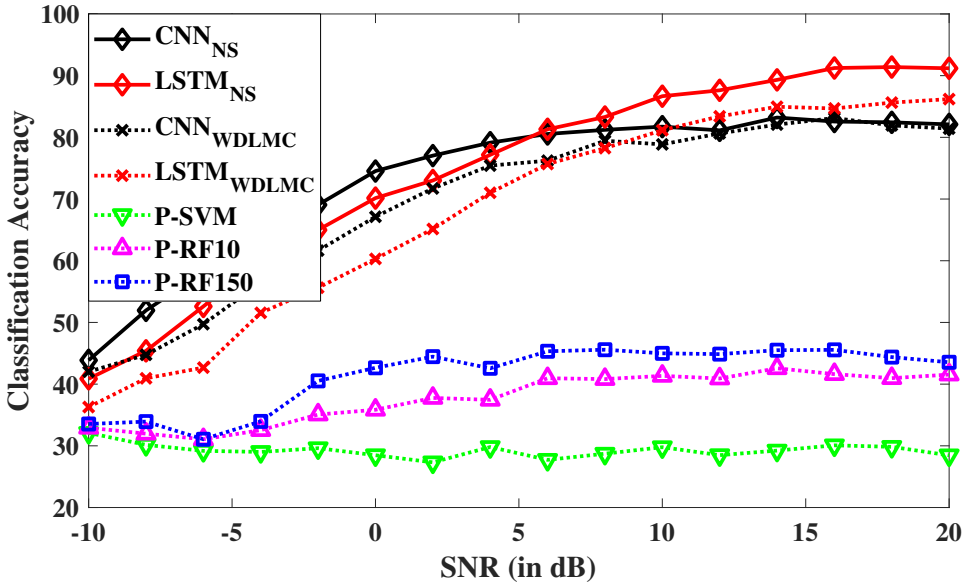

Figure 6.19: Modulation classification accuracy of CNN based WDLMC (i.e. CNN_{NS} for Nyquist samples and CNN_{WDLMC} for SNS) and LSTM based WDLMC (i.e. $LSTM_{NS}$ for Nyquist samples and $LSTM_{WDLMC}$ for SNS) on AWGN channel i.e. dataset $\mathbf{D_{WMC1}}$.

67.7% for the SNR range of -10 dB to 20 dB, which is poorer than that of the CNN_{WDLMC} model (i.e. 70%). Note that the performance of the proposed CNN_{WDLMC} model is better than the $LSTM_{WDLMC}$, especially at low SNR. However, at a very high SNR, i.e. above 12 dB, the performance of $LSTM_{WDLMC}$ is found to be slightly better than CNN_{WDLMC}.

To summarize, LSTM based WDLMC does not significantly improve performance compared to CNN based WDLMC. Moreover, CNN based WDLMC offers higher accuracy at lower SNR. Thus, we conclude that CNN based classifier is the preferred approach for SNS based unified DLMC and offers reconfigurable architecture due to similarity with DLWSS block.

6.11 Summary

In this chapter, another wideband signal characterization parameter, i.e., the identification of the modulation schemes of the occupied frequency bands, is presented. Two deep learning based modulation classification (DLMC) models, i.e., 1) Sequential DLMC model and 2) Unified DLMC model, which use sub-Nyquist samples, are proposed.

A sequential determination of the modulation schemes of occupied frequency bands is performed in the sequential DLMC model. It uses the recovered symbols of an occupied frequency band, which is reconstructed from the sub-Nyquist samples. Two deep learning methods, the convolutional neural network (CNN) on the in phase-quadrature phase (IQ) samples and long short term memory (LSTM) on the amplitude-phase (AP) samples of the recovered symbols, are explored. The classification accuracy of the proposed DLMC is compared with the machine learning (ML) classifiers and the Nyquist sampled dataset. It is observed that the proposed DLMC has higher classification accuracy than ML classifiers, and their accuracy approaches that of Nyquist sampled signal with an increase in signal to noise ratio (SNR). As for the Rayleigh fading channel, the LSTM classifier has 4.2% higher classification accuracy than the CNN classifier. Hence, the experimental analysis of the LSTM based DLMC is performed on the developed USRP-testbed.

A unified DLMC model allows simultaneous determination of the occupancy status of all frequency bands and modulation schemes of occupied bands. Here,

the sub-Nyquist samples are passed directly to the CNN based deep learning wideband spectrum sensing (DLWSS) classifier to determine the occupancy status of all frequency bands simultaneously. Then the wideband signal is reconstructed to classify the modulation scheme of all occupied bands simultaneously. We considered two scenarios of the unified DLMC model. The narrowband DLMC (NDLMC) used the recovered symbols of all frequency bands. To remove the extra overhead of the interpolation and filtering operations of NDLMC, the wideband DLMC directly passed the reconstructed wideband signal to the classifier.

The performance of both DLMCs is verified for CNN and LSTM classifiers. For NDLMC, it is observed that both classifiers have comparable performance. Whereas for WDLMC, CNN offers 2.3% higher classification accuracy than LSTM for low SNR. Furthermore, it is noticed that, as expected, NDLMC has higher classification accuracy than WDLMC. But since WDLMC avoids the extra overhead of interpolation and filtering operations of NDLMC, and both DLWSS and WDLMC have a similar architecture of CNN classifier, the CNN classifier is the preferable choice of the proposed unified DLMC.

Chapter 7

Conclusions and Future Works

In this chapter, a brief synopsis of the contributions as well as conclusions of the work presented in this thesis is done. Some directions for future work in this research area are also identified.

7.1 Conclusions

This thesis addressed the challenges of non-contiguous ultra-wideband spectrum characterization. The analysis of an ultra-wideband spectrum requires a very high Nyquist rate analog to digital converter (ADC), which is area, power and cost hungry. To overcome this issue, the current implementations either perform serial digitization and analysis of every desired frequency bands (i.e. channels) or apply multiple low rate ADCs in parallel to individually digitize and analyze each frequency band. The serial frequency band analysis approach can not be applied in the next-generation wireless network, requiring ultra-reliable low latency communication. Also, the parallel ADCs approach follows a Velcro

approach that is not reconfigurable and hardware inefficient due to the sparse nature of a wideband spectrum.

By utilizing the sparse characteristics of a wideband spectrum, the existing works propose sub-Nyquist sampling (SNS) techniques for the digitization of a wideband signal via low rate ADCs. The multi-coset sampling (MCS) and modulated wideband converter (MWC) are state-of-the-art SNS techniques and have been studied to perform wideband signal characterization. But these SNS and their corresponding characterization techniques are applicable on a contiguous wideband spectrum. Since the next-generation wireless network works on a non-contiguous ultra-wideband spectrum, the existing characterization techniques can not be applied. For example, to support various use cases of 5G, non-contiguous spectrum bands such as 700, 3300-4200, 4400-5000, 2500-2690, 2300-2400, 5925-7125 MHz, and 24.25-29.5 and 37-43.5 GHz are being explored. Also, IEEE 802.15.4 for industrial internet-of-things (IIoT) networks have channels in three non-contiguous ranges: 1) One channel in 250-740 MHz, 2) Four channels in 3.1-4.8 GHz, and 3) Eleven channels in 6 - 11.6 GHz. To deal with this issue, finite rate of innovation (FRI) based SNS technique has been studied recently, but it requires an intelligence unit to determine a set of channels to perform digitization and characterization.

The first contribution of this thesis is a channel subset selection algorithms for Bernoulli channel distribution [J5]. Unlike the existing learning algorithms, the proposed algorithms are the first of their kind, which has considered feedback loss due to reconstruction failure. It is shown that throughput achieved by

the proposed algorithms increases with an increase in the number of ADCs but decreases with an increase in the number of channels, N, in a wideband spectrum. Furthermore, among all the proposed algorithms, the K^+-SSLE (K^+- Shared Subset Learning via channel estimation) performs the best due to channel subset size estimation. Also, the regret gap between K^+-SSLE and other algorithms increases with an increase in N.

Next, we have proposed subset learning algorithms for the Markovian decision process channel model, and it is the second contribution of the thesis [J2,J3]. The $K^+ - \epsilon$SSLE algorithm performing exploration by selecting subsets of size K with ϵ probability and exploitation by selecting subsets of size between K and N with a probability $1 - \epsilon$, was studied in [J2]. It is shown that the regret achieved by $K^+ - \epsilon$SSLE saturates with time slots indicating selection of best subset. In [J3], we have proposed K^+-BSSLE (i.e. K^+-Blind SSLE) for the learning and decision making unit. Unlike the $K^+ - \epsilon$SSLE, the K^+-BSSLE algorithm does not require prior knowledge of the minimum gap between channel statistics (i.e. probability of vacancy). It is shown that, since the K^+-BSSLE, performs the exploitation based on the transitional and stationary quality index, the K^+-BSSLE has a lower regret than the $K^+ - \epsilon$SSLE algorithm. By developing the USRP hardware testbed, the performance of the proposed algorithms is also validated on the real-radio signal.

By utilizing the proposed channel subset selection algorithm, ultra-wideband signal characterization is performed in the rest of the work. The development of an SNS based intelligent reconfigurable ultra-wideband angular spectrum

sensing (UWASS) receiver is the third contribution of the thesis [J2,C1]. The proposed UWASS is able to determine the carrier frequency and direction of arrival (DoA) jointly, Unlike the existing SNS based wideband angular sensing, the proposed UWASS is independent of the number of active transmissions in the spectrum. Thus, it faces a lower number of characterization failures as compared to the existing methods. Furthermore, to determine the occupancy status of channels selected by the $K^{+}-$BSSLE algorithm, the occupancy statistics learnt by the $K^{+}-$BSSLE are used as an input to the Bayesian matching pursuit algorithm. Finally, to determine the characteristics of the occupied frequency band, a double grid approach is applied to the frequency bands and DoAs. The simulation results showed that as the proposed UWASS faces a lesser number of failures, it has lower normalized DoA and carrier frequency estimation error and higher throughput than the existing wideband angular sensing methods. The work presented in [J2] is applicable for any uniform antenna array configuration. In [C1], we extended the UWASS for the sparse antenna array configuration and performed rank enhancement on the received non-contiguous sub-Nyquist sampled data followed by joint estimation of carrier frequency and DoA.

A multi-antenna USRP hardware testbed was developed to validate the functionality of the proposed intelligent reconfigurable UWASS method, and it is the fourth contribution of the thesis [J1,D1,D2]. Multiple transmitter USRPs are used to generate a multi-directional multi-band wireless traffic signal. Depending on the occupancy probability of every frequency band, an SC-FDMA signal is transmitted over each occupied band. Among the wireless multi-directional

multi-band traffic signal, a phase synchronization signal is also received by every antenna of the developed multi-antenna receiver. The proposed intelligent and reconfigurable UWASS technique [J2] and its extension for sparse antenna array are then implemented on the LabVIEW tool for validation. The experimental analysis is done for throughput, DoA Estimation Error and Deviation from true DoA for various antenna gain values and antenna array configurations. It is shown that throughput achieved by 4-antenna sparse antenna array is higher than 4-antenna uniform linear array, and it happened due to the addition of 2 virtual antennas at the sparse array. It is also proved that the DoA estimation error decreases with an increase in the number of antennas.

In the next works, the identification of another wideband spectrum characterization parameter, i.e. modulation schemes, is performed. An intelligent SNS based sequential automatic modulation classifier (AMC) is explored in [P1], and it is the fifth contribution of the thesis. Here, recovered symbols of every occupied frequency band are passed sequentially to a long short term memory (LSTM), and convolution neural network (CNN) based deep learning modulation classifiers (DLMC). The performance comparison is made with existing machine learning based SNS-AMC [J4, C5]. It is shown that the proposed SNS-DLMC has 29.5% higher classification accuracy at $-10\ dB$ and 16.3% higher average accuracy than the machine learning based random forest classifier. Since the performance of LSTM based DLMC (LSTM-DLMC) is 4.2% higher than the CNN based DLMC, the validation of only LSTM-DLMC is performed on the developed USRP hardware testbed. Similar to the simulation

results, it is observed that the classification accuracy of the proposed SNS based LSTM-DLMC approaches to the Nyquist sampling based LSTM-DLMC with an increase in antenna gain (or SNR, for simulation results).

To simultaneously determine the occupancy status and modulation schemes of occupied bands, a unified DLMC model is proposed in [J6], and it is the sixth contribution of the thesis. The proposed unified DLMC is the first to provide an end-to-end model for deep learning based wideband spectrum sensing (DLWSS), followed by reconstruction and DLMC. CNN model is utilized to perform DLWSS simultaneously on all frequency bands, and its comparison is made with the conventional orthogonal matching pursuit (OMP) algorithm. At a low SNR of $-10\ dB$, the proposed DLWSS has 5%, 5.53% and 3%higher classification accuracy than OMP for AWGN, Rayleigh and Rician fading channel models. Two different DLMC techniques are proposed in [J6], i.e. Narrowband DLMC (NDLMC) and Wideband DLMC (WDLMC), to perform simultaneous AMC on all occupied frequency bands. It is shown that since the recovered symbols of all frequency bands are passed to DLMC, the NDLMC has higher classification accuracy than the WDLMC, which directly used the reconstructed wideband signal for DLMC. But since WDLMC avoids the extra overhead of interpolation and filtering operations and has the similar CNN architecture to DLWSS, the CNN based WDLMC is a preferable choice for developing an end-to-end prototype of unified DLMC.

For an easy evaluation, the summary of comparison between the existing and proposed subset learning algorithms presented in this thesis is given in Table

Table 7.1: Comparison of various subset learning (SL) algorithms.

Proposed SL Algorithms	**Subset Size,** $\lvert\beta\rvert$	**Number of Subsets,** $\lvert\mathcal{S}\rvert$	**Estimate of** $\lvert\beta\rvert$	**Subset updates in each slot**	**Complexity**
K**-SL**	K	$C(N,K)$	No	One i.e. β subset	Lowest
K^+**-SL**	K to N	$2^N - \sum_{k=0}^{K-1} C(N,k)$	No	One i.e. β subset	High
K^+**-SSL**	K to N	$2^N - \sum_{k=0}^{K-1} C(N,k)$	No	All	Highest
K^+**-RSSL**	K to N	• $2^N - \sum_{k=0}^{K-1} C(N,k)$ • Reduces by 50% after W rounds	No	All	High
K^+**-SSLE**	• K for W slots • K to N	• Depends on $\lvert\beta\rvert$	Yes	One i.e. β subset	Low
$K^+\epsilon$**-SSLE**	• K with ϵ probability • K to N with $1-\epsilon$ probability	• $C(N,K)$ • Depends on $\lvert\beta\rvert$	Yes	One i.e. β subset	Low
K^+**-BSSLE**	K to N	• Depends on $\lvert\beta\rvert$	Yes	One i.e. β subset	Low

7.1. Similarly, the summary of comparison between existing wideband angular sensing and UWASS presented in this thesis is given in Table 7.2.

7.2 Future Works

In this thesis, subset learning algorithms for non-contiguous channels selection, SNS based UWASS technique for carrier frequency and DoA estimation, and SNS based DLMC to identify the modulation schemes of occupied channels were proposed. Along with these low-rate wideband spectrum characterization, USRP hardware testbeds were also developed for the validation of the proposed wideband spectrum characterization techniques. Some research problems to

Table 7.2: Hardware complexity comparison of different UWASS approaches.

UWASS Techniques	**Number of Antennas**	**Number of ADCs**	**Analog BW of ADCs**	**Precise Delay**	**Sensing Failure**	
					$M \geq L$	$\beta_{busy} \geq L$
[23]	$M+1$	$2M+1$	High	Required	Fails	Fails
[24]	$M+1$	$M+1$	High	Not Required Required	Fails	Fails
[25]	$2M+1$	$2M+1$	Low	Not Required	Fails	Fails
[26]	$\frac{4M}{K}$	$\frac{4M+K-1}{K}$	High	Required	Fails when $M \geq L_s$	Fails
[27]	$< M+1$	$< (M+1)K$	High	Required	Fails when $M \geq L_s$	Fails
[J2]	$M+1$	$2M-1$	Low	Not Required	Does not Fail	Fails
[C1]	$< M+1$	$< 2M$	Low	Required	Does not Fail	Fails when $\beta_{busy} \geq L_s$
[J1]	$< M+1$	$< 2M-1$	Low	Not Required	Does not Fail	Fails when $\beta_{busy} \geq L_s$

pursue the discussed work further are discussed in the following sub-sections.

7.2.1 Wideband Spectrum Characterization Under Frequency Hopping Signal Model

Frequency hopping (FH) is widely used in wireless standards to mitigate interference, channel fading and jamming effects. The exiting wideband spectrum characterization techniques studied in the previous chapters consider a simple scenario where users transmit only at a particular frequency. But in the FH signal model, users switch their carrier frequencies many times throughout their transmission period, hence, reduces the sparsity. For example, let there are FH users, as shown in Fig. 7.1. If the sensing time is for only 3 time slots, then out of 8 available frequencies, only 2 are occupied. But if the sensing time is

8 time slots, then 5 out of 8 frequencies becomes occupied, making the signal non-sparse. Thus, the SNS based low rate digitization can not be applied even when the number of active transmissions is sparse in a single time slot.

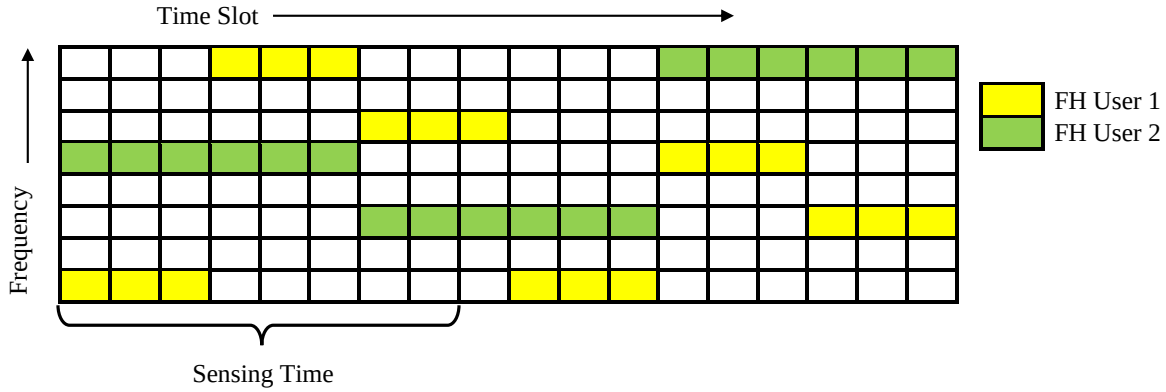

Figure 7.1: Spectrum utilization under FH use case.

The existing SNS based digitization and signal reconstruction technique either requires the prior knowledge of frequency hopping interval or performs reconstruction of the spectrum at every time slot, increasing the signal processing time and hence, sensing time. Hence, there is a need for an efficient SNS and characterization technique for an FH signal model.

7.2.2 Task based Quantization for Massive-Multiple Input Multiple Output

The massive MIMO (mMIMO) system has a large number of antennas and thus the number of ADCs in the analog front end. The power and cost of mMIMO systems depend on the operating signal bandwidth and the number of quantization bits required by the ADCs. By applying the SNS based digitization, the work focused in the thesis, considers the operating signal bandwidth aspect. However, there is a need to look into the low-level quantization. But with a lesser value of quantization bits, the quantization noise gets added to the digi-

tally converted signal. This permanently distorts the information present in the actual signal.

Recently, a task based quantization is being studied [151]. Instead of performing characterization on the recovered signal, it aims to jointly develop a quantization system and characterization task module. To perform this, it uses the prior knowledge of statistical model relating the input analog signal and output characterization task. However, the ADCs considered in the task based quantization use the wideband signal as an input. Thus, there is a need for a power and cost efficient digitization technique that consider both, the input signal bandwidth and the number of quantization bits, aspects to perform characterization in mMIMO system.

References

[1] M. Labib, V. Marojevic, J. H. Reed and A. I. Zaghloul, "Extending LTE into the Unlicensed Spectrum: Technical Analysis of the Proposed Variants," in *IEEE Communications Standards Magazine*, vol. 1, no. 4, pp. 31-39, Dec. 2017.

[2] F. Liu, C. Masouros, A. P. Petropulu, H. Griffiths and L. Hanzo, "Joint Radar and Communication Design: Applications, State-of-the-Art, and the Road Ahead," in *IEEE Transactions on Communications*, vol. 68, no. 6, pp. 3834-3862, June 2020.

[3] M. K. Waidhuba, S. S. Tiang, S. Manzoor and M. V. Hong, "A Wireless Backhaul using a Massive MIMO - 5G NR HetNet design; at Sub-6GHz and MillimetreWave Frequencies," in *IEEE International Conference on Smart Computing & Communications (ICSCC)*, pp. 1-5, Sep. 2019, Sarawak, Malaysia.

[4] W. S. H. M. W. Ahmad et al., "5G Technology: Towards Dynamic Spectrum Sharing Using Cognitive Radio Networks," in *IEEE Access*, vol. 8, pp. 14460-14488, Jan. 2020.

[5] H. Hu, H. Gao, Z. Li and Y. Zhu, "A Sub 6GHz Massive MIMO System for 5G New Radio," in *IEEE 85th Vehicular Technology Conference (VTC Spring)*, pp. 1-5, Nov. 2017, Sydney, Australia.

[6] I. Dolińska, M. Jakubowski and A. Masiukiewicz, "Interference comparison in Wi-Fi 2.4 GHz and 5 GHz bands," in International Conference on Information and Digital Technologies (IDT), pp. 106-112, Sept. 2017, Zilina, Slovakia.

[7] P. C. Sofotasios, E. Rebeiz, L. Zhang, T. A. Tsiftsis, D. Cabric and S. Freear, "Energy Detection Based Spectrum Sensing Over $\kappa-\mu$ and $\kappa-\mu$ Extreme Fading Channels," in *IEEE Transactions on Vehicular Technology*, vol. 62, no. 3, pp. 1031-1040, March 2013.

[8] A. Singh, M. R. Bhatnagar and R. K. Mallik, "Performance of an Improved Energy Detector in Multihop Cognitive Radio Networks," in *IEEE Transactions on Vehicular Technology*, vol. 65, no. 2, pp. 732-743, Feb. 2016.

[9] F. Salahdine, H. E. Ghazi, N. Kaabouch and W. F. Fihri, "Matched filter detection with dynamic threshold for cognitive radio networks," in *International Conference on Wireless Networks and Mobile Communications (WINCOM)*, pp. 1-6, Jan. 2016, Marrakech, Morocco.

[10] D. Cabric, S. M. Mishra and R. W. Brodersen, "Implementation issues in spectrum sensing for cognitive radios," in *IEEE Conference Record of the Thirty-Eighth Asilomar Conference on Signals, Systems and Computers*, pp. 772-776, March 2015, Pacific Grove, USA.

[11] Y. Qu, X. Li, R. Zhou, V. Chakravarthy and Z. Wu, "Software-Defined Radio Based Automatic Blind Hierarchical Modulation Detector via Second-Order Cyclostationary Analysis and Fourth-Order Cumulant," in *IEEE Military Communications Conference (MILCOM)*, pp. 441-446, Nov 2013, USA.

[12] Y. Zhao, Y. Wu, J. Wang, X. Zhong and L. Mei, "Wavelet transform for spectrum sensing in Cognitive Radio networks," in *International Conference on Audio, Language and Image Processing*, pp. 565-569, Jan. 2015, Shanghai, China.

[13] K. Hassan, I. Dayoub, W. Hamouda, M. Berbineau, "Automatic modulation recognition using wavelet transform and neural networks in wireless systems," in *EURASIP Journal on Advances in Signal Processing*, July 2010.

[14] S. A. Alvi, M. S. Younis, M. Imran, F. Amin, "A log-likelihood based cooperative spectrum sensing scheme for cognitive radio networks," in *Elsevier: Procedia Computer Science*, vol. 37, pp. 196-202, Jan 2014.

[15] W. Wei and J. M. Mendel, "Maximum-likelihood classification for digital amplitude-phase modulations," in *IEEE Transactions on Communications*, vol. 48, no. 2, pp. 189-193, Feb. 2000.

[16] H. Huang et al., "Deep Learning for Physical-Layer 5G Wireless Techniques: Opportunities, Challenges and Solutions," in *IEEE Wireless Communications*, vol. 27, no. 1, pp. 214-222, Feb. 2020.

[17] S. Peng et al., “Modulation Classification Based on Signal Constellation Diagrams and Deep Learning,” in *IEEE Transactions on Neural Networks and Learning Systems*, vol. 30, no. 3, pp. 718-727, March 2019.

[18] Texas Instruments, “Analog-to-Digital Converters”, [Online], Available: https://www.ti.com/data-converters/adc-circuit/overview.html

[19] Y. Kim et al., “New Radio (NR) and its Evolution toward 5G-Advanced,” in *IEEE Wireless Communications*, vol. 26, no. 3, pp. 2-7, June 2019.

[20] H. Sun, A. Nallanathan, C. Wang and Y. Chen, “Wideband spectrum sensing for cognitive radio networks: a survey,” in *IEEE Wireless Communications*, vol. 20, no. 2, pp. 74-81, April 2013.

[21] M. Mishali and Y. C. Eldar, “Wideband Spectrum Sensing at Sub-Nyquist Rates [Applications Corner],” in *IEEE Signal Processing Magazine*, vol. 28, no. 4, pp. 102-135, July 2011.

[22] G. Hattab and D. Cabric, “Distributed Wideband Sensing-Based Architecture for Unlicensed Massive IoT Communications, ” in *IEEE Transactions on Cognitive Communications and Networking*, vol. 5, no. 3, pp. 819-834, Sept. 2019.

[23] A. A. Kumar, S. G. Razul and C. S. See, “Carrier frequency and direction of arrival estimation with nested sub-nyquist sensor array receiver,” in *23rd European Signal Processing Conference (EUSIPCO)*, 2015, pp. 1167-1171, Nice, France.

[24] F. Wang, J. Fang, H. Duan and H. Li, "Phased-Array-Based Sub-Nyquist Sampling for Joint Wideband Spectrum Sensing and Direction-of-Arrival Estimation," in *IEEE Transactions on Signal Processing*, vol. 66, no. 23, pp. 6110-6123, Dec. 2018.

[25] S. Stein Ioushua, O. Yair, D. Cohen and Y. C. Eldar, "CaSCADE: Compressed Carrier and DOA Estimation," in *IEEE Transactions on Signal Processing*, vol. 65, no. 10, pp. 2645-2658, May 2017.

[26] A. A. Kumar, M. G. Chandra and P. Balamuralidhar, "Joint frequency and 2-D DOA recovery with sub-Nyquist difference space-time array," in *25th European Signal Processing Conference (EUSIPCO)*, pp. 400-404, Oct. 2017, Kos, Greece.

[27] D. D. Arianandа and G. Leus,"Compressive joint angular-frequency power spectrum estimation," in *21st European Signal Processing Conference (EUSIPCO 2013)*, pp. 1-5, May. 2013, Marrakech, Morocco.

[28] L. Liu and P. Wei, "Joint DOA and Frequency Estimation With Sub-Nyquist Sampling in the Sparse Array System," in *IEEE Signal Processing Letters*, vol. 25, no. 9, pp. 1285-1289, Sept. 2018.

[29] A. A. Kumar, S. G. Razul and C. S. See, "An efficient sub-Nyquist receiver architecture for spectrum blind reconstruction and direction of arrival estimation," in *IEEE International Conference on Acoustics, Speech and Signal Processing (ICASSP)*, pp. 6781-6785, Florence, Italy.

[30] Z. Tian and G. B. Giannakis, "A Wavelet Approach to Wideband Spectrum Sensing for Cognitive Radios," in *1st International Conference on Cognitive Radio Oriented Wireless Networks and Communications*, pp. 1-5, May 2007, Mykonos, Greece.

[31] T. Yu, S. Rodriguez-Parera, D. Marković and D. Čabrić, "Cognitive Radio Wideband Spectrum Sensing Using Multitap Windowing and Power Detection with Threshold Adaptation," in *IEEE International Conference on Communications*, pp. 1-6, July 2010, Cape Town, South Africa.

[32] T. Yu, O. Sekkat, S. Rodriguez-Parera, D. Markovic and D. Cabric, "A Wideband Spectrum-Sensing Processor With Adaptive Detection Threshold and Sensing Time," in *IEEE Transactions on Circuits and Systems I: Regular Papers*, vol. 58, no. 11, pp. 2765-2775, Nov. 2011.

[33] D. D. Ariananda and G. Leus, "Compressive Wideband Power Spectrum Estimation," in *IEEE Transactions on Signal Processing*, vol. 60, no. 9, pp. 4775-4789, Sept. 2012.

[34] C. Yen, Y. Tsai and X. Wang, "Wideband Spectrum Sensing Based on Sub-Nyquist Sampling," in *IEEE Transactions on Signal Processing*, vol. 61, no. 12, pp. 3028-3040, June 2013.

[35] D. Cohen and Y. C. Eldar, "Sub-Nyquist Sampling for Power Spectrum Sensing in Cognitive Radios: A Unified Approach," in *IEEE Transactions on Signal Processing*, vol. 62, no. 15, pp. 3897-3910, Aug. 2014.

[36] D. Cohen and Y. C. Eldar, "Sub-Nyquist Cyclostationary Detection for Cognitive Radio," in *IEEE Transactions on Signal Processing*, vol. 65, no. 11, pp. 3004-3019, June 2017.

[37] D. Cohen, E. Rebeiz, V. Jain, Y. C. Eldar and D. Cabric, "Cyclostationary feature detection from sub-Nyquist samples," in *4th IEEE International Workshop on Computational Advances in Multi-Sensor Adaptive Processing (CAMSAP)*, pp. 333-336, Jan. 2012, San Juan, USA.

[38] Z. Tian, Y. Tafesse and B. M. Sadler, "Cyclic Feature Detection With Sub-Nyquist Sampling for Wideband Spectrum Sensing," in *IEEE Journal of Selected Topics in Signal Processing*, vol. 6, no. 1, pp. 58-69, Feb. 2012.

[39] D. Romero and G. Leus, "Wideband Spectrum Sensing From Compressed Measurements Using Spectral Prior Information," in *IEEE Transactions on Signal Processing*, vol. 61, no. 24, pp. 6232-6246, Dec. 2013.

[40] D. Cohen, E. Rebeiz, Y. C. Eldar and D. Cabric, "Cyclic spectrum reconstruction and cyclostationary detection from sub-Nyquist samples," in *IEEE 14th Workshop on Signal Processing Advances in Wireless Communications (SPAWC)*, pp. 425-429, Sept. 2013, Darmstadt, Germany.

[41] E. Rebeiz, V. Jain and D. Cabric, "Cyclostationary-based low complexity wideband spectrum sensing using compressive sampling," in *IEEE International Conference on Communications (ICC)*, 2012, pp. 1619-1623.

[42] E. Rebeiz, P. Urriza and D. Cabric, “Optimizing Wideband Cyclostationary Spectrum Sensing Under Receiver Impairments,” in *IEEE Transactions on Signal Processing*, vol. 61, no. 15, pp. 3931-3943, Aug. 2013.

[43] E. Rebeiz and D. Cabric, “How wideband receiver nonlinearities impact spectrum sensing,” in *IEEE Global Conference on Signal and Information Processing*, pp. 1178-1181, Feb. 2014, Austin, USA.

[44] Z. Quan, S. Cui, H. V. Poor and A. H. Sayed, “Collaborative wideband sensing for cognitive radios,” in *IEEE Signal Processing Magazine*, vol. 25, no. 6, pp. 60-73, Nov. 2008.

[45] J. J. Meng, W. Yin, H. Li, E. Hossain and Z. Han, “Collaborative Spectrum Sensing from Sparse Observations in Cognitive Radio Networks,”in *IEEE Journal on Selected Areas in Communications*, vol. 29, no. 2, pp. 327-337, Feb. 2011.

[46] H. Sun, A. Nallanathan, J. Jiang, D. I. Laurenson, C. Wang and H. V. Poor, “A Novel Wideband Spectrum Sensing System for Distributed Cognitive Radio Networks,” in *IEEE Global Telecommunications Conference (GLOBECOM)*, pp. 1-6, Jan. 2012, Houstan, USA.

[47] H. Sun, A. Nallanathan, S. Cui and C. -X. Wang, “Cooperative Wideband Spectrum Sensing Over Fading Channels,” in *IEEE Transactions on Vehicular Technology*, vol. 65, no. 3, pp. 1382-1394, March 2016.

[48] A. López-Parrado and J. Velasco-Medina, “Cooperative Wideband Spectrum Sensing Based on Sub-Nyquist Sparse Fast Fourier Trans-

form," in *IEEE Transactions on Circuits and Systems II: Express Briefs*, vol. 63, no. 1, pp. 39-43, Jan. 2016.

[49] L. Chen, N. Zhao, Y. Chen, F. R. Yu and G. Wei, "Over-the-Air Computation for Cooperative Wideband Spectrum Sensing and Performance Analysis," in *IEEE Transactions on Vehicular Technology*, vol. 67, no. 11, pp. 10603-10614, Nov. 2018.

[50] B. Khalfi, A. Zaid and B. Hamdaoui, "When machine learning meets compressive sampling for wideband spectrum sensing," in *13th International Wireless Communications and Mobile Computing Conference (IWCMC)*, pp. 1120-1125, July 2017, Valencia, Spain.

[51] A. Fehske, J. Gaeddert and J. H. Reed, "A new approach to signal classification using spectral correlation and neural networks," in *IEEE International Symposium on New Frontiers in Dynamic Spectrum Access Networks(DySPAN)*, pp. 144-150, Dec. 2005, Baltimore, USA.

[52] E. Rebeiz and D. Cabric, "Blind modulation classification based on spectral correlation and its robustness to timing mismatch," in *MILCOM 2011 Military Communications Conference*, pp. 277-282, Jan. 2012, Baltimore, USA.

[53] D. Cohen, L. Pollak and Y. C. Eldar, "Carrier frequency and bandwidth estimation of cyclostationary multiband signals," in *IEEE International Conference on Acoustics, Speech and Signal Processing (ICASSP)*, pp. 3716-3720, May 2016, Shanghai, China.

[54] S. Ramjee, S. Ju, D. Yang, X. Liu, A. E. Gamal and Yonina C. Eldar, "Fast Deep Learning for Automatic Modulation Classification," in *arXiv preprint arXiv:1901.05850*, Jan 2019.

[55] H. Joshi, S. J. Darak and Y. Jouet, "Spectrum Blind Recovery and Application in Non-uniform Sampling Based Automatic Modulation Classifier," in *Springer: Circuits, Systems, and Signal Processing*, vol. 37, no. 8, pp. 3457-3486, Aug. 2018.

[56] M. Mishali and Y. C. Eldar, "Sub-Nyquist Sampling," in *IEEE Signal Processing Magazine*, vol. 28, no. 6, pp. 98-124, Nov. 2011.

[57] H. J. Landau, "Sampling, data transmission, and the Nyquist rate," in *Proceedings of the IEEE*, vol. 55, no. 10, pp. 1701-1706, Oct. 1967.

[58] R. Venkataramani and Y. Bresler, "Sub-Nyquist sampling of multiband signals: perfect reconstruction and bounds on aliasing error," in *Proceedings of the 1998 IEEE International Conference on Acoustics, Speech and Signal Processing (ICASSP)*, pp. 1633-1636 vol. 3, May 1998, WA, USA.

[59] M. Mishali and Y. C. Eldar, "Blind Multiband Signal Reconstruction: Compressed Sensing for Analog Signals," in *IEEE Transactions on Signal Processing*, vol. 57, no. 3, pp. 993-1009, March 2009.

[60] M. Mishali and Y. C. Eldar, "From Theory to Practice: Sub-Nyquist Sampling of Sparse Wideband Analog Signals," in *IEEE Journal of Selected Topics in Signal Processing*, vol. 4, no. 2, pp. 375-391, April 2010.

[61] M. Mishali, Y, C. Eldar, O. Dounaevsky and E. Shoshan, "Xampling: Analog to Digital at Sub-Nyquist Rates," in *IET Circuits, Devices Systems*, vol. 5, no. 1, pp. 8-20, Jan. 2019.

[62] K. Gedalyahu, R. Tur and Y. C. Eldar, "Multichannel Sampling of Pulse Streams at the Rate of Innovation," in *IEEE Transactions on Signal Processing*, vol. 59, no. 4, pp. 1491-1504, April 2011.

[63] S. Bagheri and A. Scaglione, "The Restless Multi-Armed Bandit Formulation of the Cognitive Compressive Sensing Problem," in *IEEE Transactions on Signal Processing*, vol. 63, no. 5, pp. 1183-1198, March 2015.

[64] C. Vogel and H. Johansson, "Time-interleaved analog-to-digital converters: status and future directions," in *IEEE International Symposium on Circuits and Systems*, pp. 4-3389, Kos, Greece.

[65] J. A. Tropp, J. N. Laska, M. F. Duarte, J. K. Romberg and R. G. Baraniuk, "Beyond Nyquist: Efficient Sampling of Sparse Bandlimited Signals," in *IEEE Transactions on Information Theory*, vol. 56, no. 1, pp. 520-544, Jan. 2010.

[66] F. Li, D. Yu, H. Yang, J. Yu, H. Karl and X. Cheng, "Multi-Armed-Bandit-Based Spectrum Scheduling Algorithms in Wireless Networks: A Survey," in *IEEE Wireless Communications*, vol. 27, no. 1, pp. 24-30, February 2020.

[67] A. Slivkins, "Introduction to multi-armed bandits," in *arXiv preprint arXiv:1904.07272*, April 2019.

[68] S. J. Darak and M. K. Hanawal, "Multi-Player Multi-Armed Bandits for Stable Allocation in Heterogeneous Ad-Hoc Networks," in *IEEE Journal on Selected Areas in Communications*, vol. 37, no. 10, pp. 2350-2363, Oct. 2019.

[69] W. Chen and Y. Wang and Y. Yuan,'Multi-Armed Bandit: General Framework and Applications," in *Proceedings of Machine Learning Research (PMLR)*, vol. 28, no. 1, pp. 151-159, Georgia, USA.

[70] J. Komiyama and J. Honda and H. Nakagawa, "Optimal Regret Analysis of Thompson Sampling in Stochastic Multi-armed Bandit Problem with Multiple Plays," in *International Conference on Machine Learning*, pp. 1152-1161, June 2015, Lille, France.

[71] S. Agrawal and N. Goya, "Analysis of Thompson Sampling for the Multi-armed Bandit Problem," in *Proceedings of Machine Learning Research*, vol. 23, pp. 39.1-39.26, June 2012,

[72] V. Anantharam, P. Varaiya and J. Walrand, "Asymptotically efficient allocation rules for the multiarmed bandit problem with multiple plays-Part I: I.I.D. rewards," in *IEEE Transactions on Automatic Control*, vol. 32, no. 11, pp. 968-976, Nov. 1987.

[73] H. Joshi, S. J. Darak, A. A. Kumar and R. Kumar, "Throughput Optimized Non-Contiguous Wideband Spectrum Sensing via Online Learning and Sub-Nyquist Sampling," in *IEEE Wireless Communications Letters*, vol. 8, no. 3, pp. 805-808, June 2019.

[74] P. Schniter, L. C. Potter and J. Ziniel, "Fast bayesian matching pursuit," in *IEEE Information Theory and Applications Workshop*, pp. 326-333, 2008, San Diego, USA.

[75] W. Chen, Y. Wang, Y. Yuan and Q. Wang, "Combinatorial Multi-Armed Bandit and Its Extension to Probabilistically Triggered Arms," in *The Journal of Machine Learning Research*, vol. 7, no. 1, Jan. 2016.

[76] S. Wang and W. Chen, "Thompson Sampling for Combinatorial Semi-Bandits," in Proceedings of Machine Learning Research, vol. 18, pp. 5114-5122, July 2018.

[77] E. Crespo Marques, N. Maciel, L. Naviner, H. Cai and J. Yang, "A Review of Sparse Recovery Algorithms," in *IEEE Access*, vol. 7, pp. 1300-1322, Dec. 2018.

[78] J. D. Blanchard, M. Cermak, D. Hanle and Y. Jing, "Greedy Algorithms for Joint Sparse Recovery," in *IEEE Transactions on Signal Processing*, vol. 62, no. 7, pp. 1694-1704, April1 2014.

[79] J. F. C. Mota, J. M. F. Xavier, P. M. Q. Aguiar and M. Puschel, "Distributed Basis Pursuit," in *IEEE Transactions on Signal Processing*, vol. 60, no. 4, pp. 1942-1956, April 2012.

[80] Y. Arjoune, N. Kaabouch, H. E. Ghazi and A. Tamtaoui, "Compressive sensing: Performance comparison of sparse recovery algorithms," *IEEE Computing and Communication Workshop and Conference*, pp. 1-7, Jan. 2017, Las Vegas, USA.

[81] T. T. Cai and L. Wang, "Orthogonal Matching Pursuit for Sparse Signal Recovery With Noise," in *IEEE Transactions on Information Theory*, vol. 57, no. 7, pp. 4680-4688, July 2011.

[82] Hamid Palangi and Rabab Ward and Li Deng,"Convolutional Deep Stacking Networks for distributed compressive sensing, " in *Elsevier: Signal Processing*, vol. 131, pp. 181-189, Feb. 2017.

[83] H. Palangi, R. Ward and L. Deng, "Using deep stacking network to improve structured compressed sensing with Multiple Measurement Vectors, " in *IEEE International Conference on Acoustics, Speech and Signal Processing*, pp. 3337-3341, Oct. 2013, Vancouver, Canada.

[84] H. Palangi, R. Ward and L. Deng, "Distributed Compressive Sensing: A Deep Learning Approach," in *IEEE Transactions on Signal Processing*, vol. 64, no. 17, pp. 4504-4518, Sept. 2016.

[85] P. Qi, Z. Li, H. Li, T. Xiong, "Blind Sub-Nyquist Spectrum Sensing With Modulated Wideband Converter," in *IEEE Transactions on Vehicular Technology*, vol. 67, no. 5, pp. 4278-4288, Jan. 2018.

[86] Mustafa Al-Ani, Bashar I. Ahmad, Andrzej Tarczynski, "Non-compressive wideband spectrum sensing with sub-Nyquist sampling rates," in *Asilomar Conference on Signals Systems and Computers*, pp. 1483-1487, May 2014, Pacific Grove, USA.

[87] A. Tsakmalis, S. Chatzinotas, B. Ottersten, "Automatic Modulation Classification for adaptive Power Control in cognitive satellite communica-

tions," in *7th Advanced Satellite Multimedia Systems Conference and the 13th Signal Processing for Space Communications Workshop (ASM-S/SPSC)*, pp. 234-240, Oct. 2014, Livorno, Italy.

[88] W. A. Gardner, "Signal interception: a unifying theoretical framework for feature detection," in *IEEE Transactions on Communications*, vol. 36, no. 8, pp. 897-906, Aug. 1988.

[89] A. V. Dandawate and G. B. Giannakis, "Statistical tests for presence of cyclostationarity," in *IEEE Transactions on Signal Processing*, vol. 42, no. 9, pp. 2355-2369, Sept. 1994.

[90] A. Hazza, M. Shoaib, S. A. Alshebeili and A. Fahad, "An overview of feature-based methods for digital modulation classification," in *International Conference on Communications, Signal Processing, and their Applications (ICCSPA)*, pp. 1-6, March 2013, Sharjah, United Arab.

[91] J. L. Xu, W. Su and M. Zhou, "Likelihood-Ratio Approaches to Automatic Modulation Classification," in *IEEE Transactions on Systems, Man, and Cybernetics, Part C (Applications and Reviews),* vol. 41, no. 4, pp. 455-469, July 2011.

[92] D. Chang, P. Shih, "Cumulants-based modulation classification technique in multipath fading channels," in *IET Communications*, vol. 9, no. 6, pp. 828-835, 2015.

[93] B. Ramkumar, “Automatic modulation classification for cognitive radios using cyclic feature detection,” in *IEEE Circuits and Systems Magazine*, vol. 9, no. 2, pp. 27-45, Second Quarter 2009.

[94] 1. Z. Wu, S. Zhou, Z. Yin, B. Ma and Z. Yang, “Robust Automatic Modulation Classification Under Varying Noise Conditions”, in *IEEE Access*, vol. 5, pp. 19733-19741, Aug. 2017.

[95] M. W. Aslam, Z. Zhu and A. K. Nandi, ”Automatic Modulation Classification Using Combination of Genetic Programming and KNN,” in *IEEE Transactions on Wireless Communications*, vol. 11, no. 8, pp. 2742-2750, Aug. 2012.

[96] K. Triantafyllakis, M. Surligas, G. Vardakis and S. Papadakis, “Phasma: An automatic modulation classification system based on Random Forest,” in *IEEE International Symposium on Dynamic Spectrum Access Networks (DySPAN)*, pp. 1-3, May 2017, Baltimore, USA.

[97] K. Zhang, E. L. Xu, Z. Feng, P. Zhang, “A Dictionary Learning Based Automatic Modulation Classification Method,” in *IEEE Access*, vol. 6, pp. 5607-5617, Jan. 2018.

[98] A. Fehske, J. Gaeddert and J. H. Reed, “A new approach to signal classification using spectral correlation and neural networks,” in *IEEE International Symposium on New Frontiers in Dynamic Spectrum Access Networks*, pp. 144-150, Dec. 2005, Baltimore, USA.

[99] B. Kim, J. Kim, H. Chae, D. Yoon and J. W. Choi, "Deep neural network-based automatic modulation classification technique," in *IEEE International Conference on Information and Communication Technology Convergence (ICTC)*, pp. 579-582, Dec. 2016.

[100] T. J. O'Shea, T. Roy and T. C. Clancy, "Over-the-Air Deep Learning Based Radio Signal Classification," in *IEEE Journal of Selected Topics in Signal Processing*, vol. 12, no. 1, pp. 168-179, Feb. 2018.

[101] N. E. West and T. O'Shea, "Deep architectures for modulation recognition," in *IEEE International Symposium on Dynamic Spectrum Access Networks (DySPAN)*, pp. 1-6, May 2017, Baltimore, USA.

[102] S. Rajendran, W. Meert, D. Giustiniano, V. Lenders and S. Pollin, "Deep Learning Models for Wireless Signal Classification With Distributed Low-Cost Spectrum Sensors," in *IEEE Transactions on Cognitive Communications and Networking*, vol. 4, no. 3, pp. 433-445, Sept. 2018.

[103] T. J. O. Shea, J. J. Corgan and T. C. Clancy,"Convolutional Radio Modulation Recognition Networks," in *International Conference on Engineering Applications of Neural Networks*, pp. 213-226, Sep 2016, Aberdeen, United Kingdom.

[104] J. Zhang, Y. Li, J. Yin, "Modulation classification method for frequency modulation signals based on the time–frequency distribution and CNN," in *IET Radar Sonar & Navigation*, vol. 12, no. 2, pp. 244-249, Oct. 2017.

[105] S. Zheng, P. Qi, S. Chen and X. Yang, "Fusion Methods for CNN-Based Automatic Modulation Classification," in *IEEE Access*, vol. 7, pp. 66496-66504, May 2019.

[106] Z. Zhang, C. Wang, C. Gan, S. Sun and M. Wang, "Automatic Modulation Classification Using Convolutional Neural Network With Features Fusion of SPWVD and BJD," in *IEEE Transactions on Signal and Information Processing over Networks*, vol. 5, no. 3, pp. 469-478, Sept. 2019.

[107] Y. Wang, J. Yang, M. Liu and G. Gui, "LightAMC: Lightweight Automatic Modulation Classification via Deep Learning and Compressive Sensing," in *IEEE Transactions on Vehicular Technology*, vol. 69, no. 3, pp. 3491-3495, March 2020.

[108] C. W. Lim and M. B. Wakin, "Automatic modulation recognition for spectrum sensing using nonuniform compressive samples," in *IEEE International Conference on Communications (ICC)*, pp. 3505-3510, Nov. 2012, Ottawa, Canada.

[109] L. Zhou and H. Man, "Wavelet Cyclic Feature Based Automatic Modulation Recognition Using Nonuniform Compressive Samples," in *IEEE 78th Vehicular Technology Conference*, pp. 1-6, Jan 2014, Las Vegas, USA.

[110] C. Moy, A. Nafkha and M. Naoues, "Reinforcement learning demonstrator for opportunistic spectrum access on real radio signals," in *IEEE International Symposium on Dynamic Spectrum Access Networks (DySPAN)*, pp. 283-284, Dec 2015, Stockholm, Sweden.

[111] L. Besson, R. Bonnefoi and C. Moy, "GNU Radio Implementation of MALIN: Multi-Armed bandits Learning for Internet-of-things Networks," in *IEEE Wireless Communications and Networking Conference (WCNC)*, pp. 1-6, April 2019, Marrakesh, Morocco.

[112] J. Manco-Vasquez, C. Moy, F. Bader,"GNU Radio implementation for Multiuser Multi-Armed Bandit learning algorithms in IoT networks," in *European GNU Radio Days*, Jun 2019, Besancon, France.

[113] R. Kumar, A. Yadav, S. J. Darak and M. K. Hanawal, "Trekking based distributed algorithm for opportunistic spectrum access in infrastructure-less network," in *IEEE International Symposium on Modeling and Optimization in Mobile, Ad Hoc, and Wireless Networks (WiOpt)*, pp. 1-8, May 2018, Shanghai, China.

[114] D. Bao, L. De Vito and S. Rapuano, "A Histogram-Based Segmentation Method for Wideband Spectrum Sensing in Cognitive Radios," in *Transactions on Instrumentation and Measurement*, vol. 62, no. 7, pp. 1900-1908, July 2013.

[115] M. Hamid, N. Björsell, W. Van Moer, K. Barbé and S. B. Slimane, "Blind Spectrum Sensing for Cognitive Radios Using Discriminant Analysis: A Novel Approach," in *IEEE Transactions on Instrumentation and Measurement*, vol. 62, no. 11, pp. 2912-2921, Nov. 2013.

[116] S. Yarkan, "A Generic Measurement Setup for Implementation and Performance Evaluation of Spectrum Sensing Techniques: Indoor Environ-

ments," in *IEEE Transactions on Instrumentation and Measurement*, vol. 64, no. 3, pp. 606-614, March 2015.

[117] W. A. Jerjawi, Y. A. Eldemerdash and O. A. Dobre, "Second-Order Cyclostationarity-Based Detection of LTE SC-FDMA Signals for Cognitive Radio Systems," in *IEEE Transactions on Instrumentation and Measurement*, vol. 64, no. 3, pp. 823-833, March 2015.

[118] D. Capriglione, G. Cerro, L. Ferrigno and G. Miele, "Effects of Real Instrument on Performance of an Energy Detection-Based Spectrum Sensing Method," in *IEEE Transactions on Instrumentation and Measurement*, vol. 68, no. 5, pp. 1302-1312, May 2019.

[119] Z. Yan, Z. Ma, H. Cao, G. Li and W. Wang, "Spectrum Sensing, Access and Coexistence Testbed for Cognitive Radio using USRP," in *IEEE International Conference on Circuits and Systems for Communications*, pp. 270-274, June 2008, Shanghai, China.

[120] S. Li, H. Zhu, Z. Gao, X. Guan and K. Xing, "YouSense: Mitigating entropy selfishness in distributed collaborative spectrum sensing," in *Proceedings IEEE INFOCOM*, pp. 2535-2543, July 2013, Turin, Italy.

[121] X. Wang, S. Chaudhari, M. Laghate and D. Cabric, "Wideband spectrum sensing measurement results using tunable front-end and FPGA implementation," in *51st Asilomar Conference on Signals, Systems, and Computers*, pp. 499-503, April 2018, Pacific Grove, USA.

[122] H. Hassanieh, L. Shi, O. Abari, E. Hamed, D. Katabi, “GHz-wide sensing and decoding using the sparse Fourier transform,” in *IEEE INFOCOM - IEEE Conference on Computer Communications*, pp. 2256-2264, July 2014, Toronto, Canada.

[123] A. M. Tonello and D. Inserra, “Radio positioning based on DoA estimation: An implementation perspective,” in *IEEE International Conference on Communications Workshops (ICC)*, pp. 27-31, Oct 2013, Budapest, Hungary.

[124] D. Inserra, A. M. Tonello, “A multiple antenna wireless testbed for the validation of DoA estimation algorithms,” in *AEU - International Journal of Electronics and Communications*, vol. 68, no. 1, pp. 10-18, Jan 2014.

[125] Y. Xie, C. Peng, X. Jiang and S. Ouyang, “Hardware design and implementation of DoA estimation algorithms for spherical array antennas,” in *IEEE International Conference on Signal Processing, Communications and Computing (ICSPCC)*, pp. 219-223, Dec. 2014, Guilin, China.

[126] X. Cai, X. Yin and A. P. Yuste, “Direction-of-arrival estimation using single antenna in high-speed-train environments,” in *IEEE European Conference on Antennas and Propagation (EuCAP)*, pp. 1-4, June 2016, Davos, Switzerland.

[127] B. H. Fleury, M. Tschudin, R. Heddergott, D. Dahlhaus and K. Ingeman Pedersen, “Channel parameter estimation in mobile radio environments us-

ing the SAGE algorithm," in *IEEE Journal on Selected Areas in Communications*, vol. 17, no. 3, pp. 434-450, March 1999.

[128] B. Rares et al., "Experimental Evaluation of AoA Algorithms using NI USRP Software Defined Radios," in *17th IEEE RoEduNet Conference: Networking in Education and Research (RoEduNet)*, pp. 1-6, Nov. 2018, Cluj-Napoca, Romania.

[129] A. A. Hussain, N. Tayem, A. Soliman and R. M. Radaydeh, "FPGA-Based Hardware Implementation of Computationally Efficient Multi-Source DOA Estimation Algorithms," in *IEEE Access*, vol. 7, pp. 88845-88858, July 2019.

[130] S. A. Alawsh, O. A. Al Khazragi, A. H. Muqaibel and S. N. Al-Ghadhban, "Sparse direction of arrival estimation using sparse arrays based on software-defined-radio platform," in *10th IEEE International Conference on Electrical and Electronics Engineering (ELECO)*, pp. 671-675, Jan 2018, Bursa, Turkey.

[131] National Instruments, "Automatic Modulation Classification using Cyclic Feature Detection with NI USRP" 2017, [Online], Available: https://forums.ni.com/t5/Software-Defined-Radio/Automatic-Modulation-Classification-using-Cyclic-Feature/ta-p/3503648?profile.language=en

[132] S. Foulke, J. Jagannath, A. Drozd, T. Wimalajeewa, P. K. Varshney and W. Su, "Multisensor Modulation Classification (MMC): Implementation Con-

siderations - USRP Case Study," in *IEEE Military Communications Conference*, pp. 1663-1668, Nov. 2014, Baltimore, MD, USA.

[133] M. Laghate, S. Chaudhari and D. Cabric, "USRP N210 demonstration of wideband sensing and blind hierarchical modulation classification," in *IEEE International Symposium on Dynamic Spectrum Access Networks (DySPAN)*, pp. 1-3, May 2017, Baltimore, MD, USA.

[134] J. Jagannath et al., "Artificial Neural Network Based Automatic Modulation Classification over a Software Defined Radio Testbed," in *IEEE International Conference on Communications (ICC)*, pp. 1-6, July 2018, Missouri, USA.

[135] National Instruments, "USRP 2945 and USRP 2955 Direction Finding" 2017, [Online], Available: https://forums.ni.com/t5/Software-Defined-Radio/USRP-2945-and-USRP-2955-Direction-Finding/tap/3585793?profile.language=en

[136] P. S. Naidu, "Sensor array signal processing," in *2nd ed., CRC Press*, USA, June 2009.

[137] F Gensun, "Whittaker–Kotelnikov–Shannon Sampling Theorem and Aliasing Error," in *Journal of Approximation Theory*, vol. 85, no. 2, pp. 115-131, May 1996.

[138] Y. C. Eldar, "Sampling theory: Beyond bandlimited systems," in *1st ed., Cambridge University Press*, UK, April 2015.

[139] M. Masood and T. Y. Al-Naffouri, "Sparse Reconstruction Using Distribution Agnostic Bayesian Matching Pursuit," in *IEEE Transactions on Signal Processing*, vol. 61, no. 21, pp. 5298-5309, Nov. 2013.

[140] H. Joshi, S. J. Darak and A. A. Kumar, "Low-Complexity Reconfigurable and Intelligent Ultrawideband Angular Sensing," in *IEEE Systems Journal*, vol. 14, no. 4, pp. 4931-4942, Dec. 2020.

[141] K. Lee, Y. Bresler and M. Junge, "Subspace Methods for Joint Sparse Recovery," in *IEEE Transactions on Information Theory*, vol. 58, no. 6, pp. 3613-3641, June 2012.

[142] S. Rajendran, W. Meert, D. Giustiniano, V. Lenders and S. Pollin, "Deep Learning Models for Wireless Signal Classification With Distributed Low-Cost Spectrum Sensors," in *IEEE Transactions on Cognitive Communications and Networking*, vol. 4, no. 3, pp. 433-445, Sept. 2018.

[143] D. Campbell, R. A. Dunne and N. A. Campbell, "On The Pairing Of The Softmax Activation And Cross-Entropy Penalty Functions And The Derivation Of The Softmax Activation Function," in *Proc. 8th Aust. Conf. on the Neural Networks*, vol. 181, p. 185, June 1997, Melbourne, Australia.

[144] M. Lin, Q. Chen and S. Yan, "Network In Network," in *International Conference on Learning Representations*, AB, Canada, April 2014.

[145] C. Szegedy et al., "Going Deeper with Convolutions," in *Proceedings of the IEEE conference on computer vision and pattern recognition*, pp. 1-9, Oct. 2015, Boston, USA.

[146] K. He, X. Zhang, S. Ren and Jian Sun, “Deep Residual Learning for Image Recognition,” in *Proceedings of the IEEE conference on computer vision and pattern recognition*, pp. 770-778, June 2016, Las Vegas, USA .

[147] G. Huang, Z. Liu, L. V. D. Maaten and K. Q. Weinberger,“Densely Connected Convolutional Networks,” in *IEEE conference on computer vision and pattern recognition*, pp. 4700-4708, July 2017, Hawaii, United States.

[148] H. Joshi, “ASCW_Dataset” 2020, [Online], Available: https://drive.google.com/open?id=1uAzu-RbNNMu38SLnMLS77Vf75DuW17RZ

[149] F. Chollet Keras, “Keras Release 2.6.0 ” 2021, [Online], Available: https://github.com/fchollet/keras

[150] D. P. Kingma and J. Ba, “Adam: A Method for Stochastic Optimization,” in *International Conference on Learning Representations (ICLR)*, May 2015, San Diego, USA.

[151] N. Shlezinger and Y. C. Eldar, “Task-Based Quantization with Application to MIMO Receivers,” in *Commun. Inf. Syst.*, vol. 20, pp. 131-162, Feb. 2020.

Appendix A

In this section, we describe the LabVIEW-NXG block diagram of the dynamic wireless traffic generator module. The functionality of this module, as shown in Fig. 2, can be divided into six sub-blocks. The first sub-block creates the transmission session for the specified USRP device Ids and defines the transmission parameters like transmission frequency, IQ sampling rate, antenna gain, RF channel number and transmission port. The second sub-block generates a multiband signal, $x_u(t)$, of ten frequency bands. The first band is a NULL band and is reserved for the phase reference signal, $p(t)$, whereas the second band is reserved for the synchronization signal (SS). The rest of the eight bands, i.e. U_1 to U_8, carries the user data signal (UDS). In $x_u(t)$, the SS and U_1 to U_8 frequency bands consist of uncorrelated LTE SC-FDMA signals of bandwidth, $B = 1.4\ MHz$.

Since the occupancy status of U_1 to U_8 frequency bands vary according to probability statistics, we make the transition probabilities, i.e. $\mathbf{p}_{01}$ and $\mathbf{p}_{10}$, as user-defined parameters in the sub-block 3. As we consider $N = 8$ frequency bands, the size of vectors $\mathbf{p}_{10}$ and $\mathbf{p}_{10}$ is 1×8 and the same is shown in sub-block 3. The multiband signal, $x_u(t)$ from sub-block 2 and $\mathbf{p}_{uv}$, where

$u, v \in \{0, 1\}$, from sub-block 3 are utilized by the sub-block 4 to generate an M-directional multi-user traffic signal. The sub-block 4 generates the masking bits for U_1 to U_8 according to $\mathbf{p}_{uv}$. However, the masking operation is performed when the SS changes its status. While designing, we consider $M = 3$. Hence, masking is performed such that three directional output signals of sub-block 4 contain the information of $\{SS,\ U_1,\ U_2\}$, $\{U_3,\ U_4,\ U_5\}$ and $\{U_6,\ U_7,\ U_8\}$ frequency bands. These directional multi-user signals are then passed to the sub-block 5, which is responsible for the real-time transmission of these signals via three channels of the two NI-USRP 2944R transmitters. Finally, the sub-block 6 closes the transmitter session for the specified device Ids.

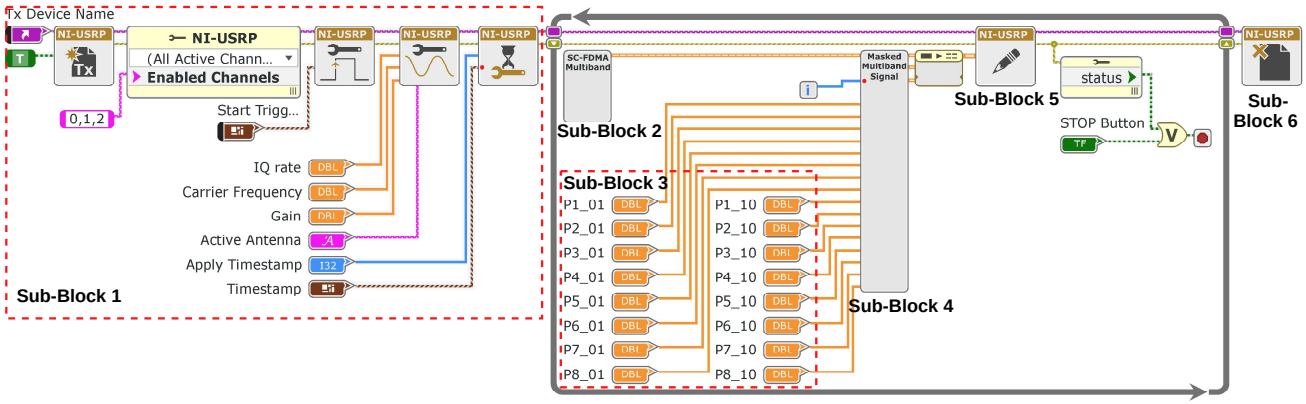

Figure 2: LabVIEW block diagram of dynamic wireless traffic generator module.

Appendix B

Here, we present the LabVIEW-NXG block diagram of the UWASS receiver module. As shown in Fig. 3, the design of the receiver module for UWASS consists of nine sub-blocks. The sub-block 1 creates the receiver session for the specified USRP device Ids and configures the receiver USRPs parameters like receiver channel sequence, external reference clock signal and PPS signal, antenna ports, antenna gains, reception carrier frequency, IQ sampling rate and timestamp. Once these parameters are initialized, sub-blocks 2 to 8 run continuously in two while loops. The first while loop performs the continuous reception of the RF wideband signal, $\mathbf{y}[n] = \mathbf{x}[n] + p[n]$ in sub-block 2. Since while designing UWASS receiver we consider $L = 4$ antenna array, $\mathbf{y}[n] = [y_1[n]\ y_2[n]\ y_3[n]\ y_4[n]]^T$ consists of signals received via four channels of two NI-USRP 2944R. The sub-block 3 stores the received $\mathbf{y}[n]$ into the queue via enqueue operation.

Now, the second while loop first performs the dequeue operation in sub-block 4. Here it extracts the four-channel data from the queue. Next, in sub-block 5, the synchronization signal from the received $\mathbf{y}[n]$ is used to detect the change of status of U_1 to U_8 bands. As discussed in Section V-A, to per-

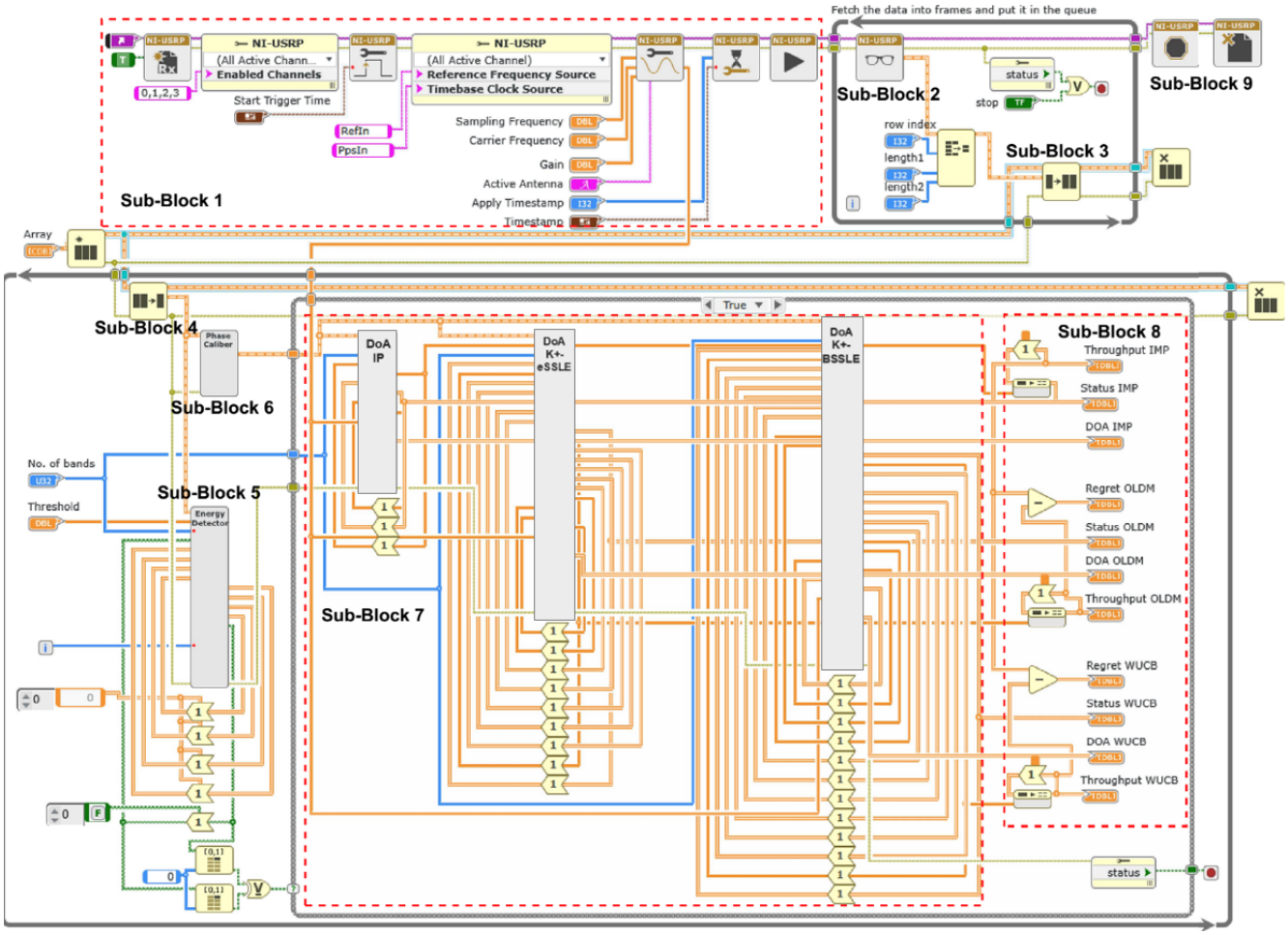

Figure 3: LabVIEW block diagram of UWASS receiver module.

form this, we filter out the SS band from $\mathbf{y}[n]$ and check the status of the SS band via energy detector. It generates a pulse signal, $p_b(t)$, whenever the SS band changes its status, which thereby tells the change of status of U_1 and U_8 bands. Along with the execution of sub-block 5, sub-block 6 determines the phase offset and performs phase calibration, as discussed in Section V-A. In this sub-block, the received phase reference signal (PRS) is extracted from $\mathbf{y}[n]$. The phase of received PRS corresponds to the phase offset, $\boldsymbol{\phi}$, incurred in the received UDS due to the independent channel noise of the receiving channels of USRP-2944R. This phase offset is removed from the received UDS signal, and

the phase calibrated UDS signal, $\tilde{\mathbf{y}}[n]$ is passed to the sub-block 7.

Note that the sub-blocks 7 and 8 perform execution whenever the sub-block 5 generates the pulse signal, $p_b(t)$. The sub-block 7 implements the reconfigurable and intelligent UWASS unit via various LDM methods. Here, each LDM method determines the $|\beta|$ and β, as discussed in Section V-B3 and [63,73,140], followed by the digitization and UWASS of β frequency bands. The sub-block 8 calculates and displays the final output, i.e. throughput (total number of vacant opportunities), occupancy status of frequency bands and DoA of occupied bands. Finally, the sub-block 9 closes the receiver session, which is created by the sub-block 1.